A Digital Tracking Calorimeter for Proton Computed Tomography

Helge Egil Seime Pettersen

Dissertation for the degree of philosophiae doctor (PhD)
at the University of Bergen, Norway

February 2018

Date of defense: 29.05.2018

Scientific environment

The author has carried out the research reported in this dissertation at the Department of Oncology and Medical Physics at Haukeland University Hospital, Bergen, Norway (with his co-supervisor Odd Harald Odland), at the Department of Physics and Technology at the University of Bergen, Norway (with his supervisor Dieter Röhrich), and at the Department of Electrical Engineering at the Western Norway University of Applied Sciences, Bergen, Norway (with his co-supervisor Ilker Meric).

Acknowledgements

List of abbreviations

ALICE *A Large Ion Collider Experiment* at CERN

ALPIDE *ALICE PIxel DEtector*

AGORFIRM *AGOR Facility for Irradiations of Materials*

C++ *A programming language*

CBCT *Cone Beam Computed Tomography*

CERN *European Organization for Nuclear Research*

CMOS *Complementary metal–oxide–semiconductor*, active pixel detectors with integrated electronics.

CPU *Central Processing Unit*

CSDA *Continuous Slowing Down Approximation* of the proton range.

CT *Computed Tomography*

DAQ *Data Acquisition*

DTC *Digital Tracking Calorimeter*, a detector concept described in this work.

ENC *Equivalent Noise Charge*

FDK The volumetric CT reconstruction algorithm by *Feldkamp, Davis, and Kress*.

FLUKA *FLUktuirende KAskade*, a Monte Carlo software application

FoCal *Forward Calorimeter*, a future electromagnetic shower calorimeter for the ALICE experiment.

FPGA *Field Programmable Gate Array*, a device for high speed data processing.

GATE *Geant4 Application For Tomographic Emission*, a Monte Carlo software application that simplifies the usage of Geant4.

GUI *Graphical User Interface*

HU *Hounsfield Unit*, the mass attenuation of photons in x-ray CT.

LAP *Laser Accelerated Protons*

I/O *Input/Output from/to a file or terminal*

ICRU *International Commission on Radiation Units and Measurements*

IMPT *Intensity Modulated Proton Therapy*

ITS The *Inner Tracking System* of the ALICE experiment.

KVI-CART *Kernfysisch Versneller Instituut – Center for Advanced Radiation Technology*

LET *Linear Energy Transfer*

LUT *Look-Up-Table*

MAPS *Monolithic Active Pixel Sensor*

MC *Monte Carlo*, a computer simulation tool for interactions between particles and pre-defined geometries

MCNP (6) *Monte Carlo N-Particle* code (version 6), a Monte Carlo application.

MCS *multiple Coulomb scattering*

eV *Electron volt, the kinetic energy of an electron accelerated by one volt.*

MIMOSA23 *Minimum Ionizing MOS Active Pixel Sensors* — version 23

MLP *Most Likely Path* of a proton through the imaged object

MPV *Most Probable Value* of a distribution.

MRI *Magnetic Resonance Imaging*

NI *Nuclear Interaction*

PCB *Printed Circuit Board*

PET *Positron Emission Tomography*

PID *Particle Identification*

PMMA *PolyMethyl MethAcrylate* or *Perspex*

PSTAR *Proton STopping power And Range tables*

SRIM *Stopping and Range of Ions in Matter*, a computer program.

RMS *Root Mean Square*

ROOT Object-oriented data analysis software package written at CERN.

RSP *Relative Stopping Power* (relative to water)

SSD *Silicon Strip Detectors*

SV *Sensitive Volume*, a volume to be scored in a MC simulation.

TPS *Treatment Planning System*

UiB *University of Bergen*

WEPL *Water Equivalent Path Length* — a material factor that, multiplied by the material's thickness, yields the Water Equivalent Thickness.

WET *Water Equivalent Thickness* — a material's thickness when converted to thickness in water.

Abstract

Cancer is a destructive disease, in which tumor cells grow out-of-control, halting organ function. Its treatment is threefold: Radical surgery, chemotherapy and radiation therapy. Their relative usage is determined by cancer type, stage, organs at risk adjacent to the tumor and progression.

There has been a significant increase in the number of cancer patients treated with radiation therapy using particle therapy in the recent decades worldwide. Short term and long term treatment-induced side effects are reduced when applying particle therapy due to the superior dose conformality compared to conventional radiation therapy using photons. The particle species commonly applied during particle therapy is the proton.

Proton therapy as of today is performed with the delivery of pre-calculated dose plans for each patient: the applied dose plans are made based on x-ray computed tomography (CT) images. The CT images are reconstructed based upon photon interaction with matter, thus a conversion is required for calculating the Relative Stopping Power for how the protons traverse and deposit dose in the patient's body during proton therapy. This conversion procedure introduces range uncertainties typically in the order of 2%–3%, corresponding to 4–6 mm at a treatment depth 20 cm into the patient.

A proton CT system would yield a means of direct calculation of the RSP map in the patient. During a proton CT scan, a high-energy proton beam is directed at the patient and the proton beam must have sufficient energy to completely pass through the patient being imaged. The protons' residual energies are measured after they have traversed through the patient and into a detector behind to the patient. The information about the residual energy from each proton can then be used, together with the proton's estimated path through the patient, as a basis for reconstructing a volumetric RSP.

In this thesis, the feasibility of using a purely pixel-based detector, a so-called Digital Tracking Calorimeter (DTC), for proton CT purposes is investigated and its performance quantified through experiments and Monte Carlo simulations. The DTC is designed for tracking and measuring the range and energy of individual protons in a proton beam.

The DTC consists of multiple layers of semiconductor pixel sensors with a digital readout, interleaved with a passive absorber material for energy degradation. The sensor chips are considered near optimal for use in the tracking, due to their data processing

capacity at the required readout speed, the high granularity of such a detector system and also due to their short radiation thickness. The requirement to this part of the detector is that it must be able to allow for reconstruction of a large amount of proton tracks in each data readout cycle, enabling high proton rate capabilities.

The DTC was originally designed for the reconstruction of high-energy electromagnetic showers for the Forward Calorimeter project in the ALICE experiment at CERN. The presented prototype forms the basis for a proton CT system using a single pixel-based technology for both tracking and calorimetry. This advantage simplifies the setup and reduces the cost of a proton CT system assembly, and it is a unique feature of the Digital Tracking Calorimeter concept.

Measurement data from the AGORFIRM beamline at KVI-CART in Groningen in the Netherlands and Monte Carlo simulation results are used in order to develop a proton tracking algorithm for the estimation of the residual ranges of a high number of concurrent proton tracks.

The range of the individual protons can with the first prototype be estimated with a range resolution of 6–25 mm Water Equivalent Thickness. This relatively low achieved range resolution is expected due to the original design goal of the prototype. The readout system for this prototype is able to handle a proton intensity of 1 million protons/s by using 500 concurrent proton tracks in each readout frame, which is comparable to present similar prototypes.

A next prototype of the proton CT setup using the DTC is at present in the construction stage. A DTC further optimized for use in a proton CT system will utilize next-generation Monolithic Active Pixel Sensors with larger sensor areas and a hundredfold increase in readout speeds. The developed proton CT analysis framework is applied on a variety of possible DTC geometries for the next prototype. The potential design choices are evaluated on basis of the reached range accuracy and range uncertainty as well as of the track reconstruction efficiency. A design recommendation is reached where the proposed DTC will have 3.5 mm thick aluminum absorber slabs between each sensor layer.

Some of the tools applied in this thesis for the purpose of proton range calculation have been validated through comparison studies: First, different MC programs are compared to each other and to available experimental data. Secondly, the accuracy and usability of several available proton range calculation models are evaluated through their capability of reproducing tabulated energy-range proton values. An accurate model is found and applied throughout this thesis for proton range reconstruction purposes.

Innledning på norsk

Denne teksten ble opprinnelig publisert i *Fra Fysikkens Verden* sammen med D. Röhrich.

Partikkelterapi er en målrettet kreftbehandling som er under planlegging i Norge. Partikkelterapi setter store krav til nøyaktig diagnostikk — og i Bergen jobber en forskningsgruppe med å utvikle protontomografi, som vil bidra til en mer skånsom partikkelterapi.

Stråleterapi

Stråleterapi er en behandling som gis til om lag halvparten av alle kreftpasienter i Norge. Sykehus i Norge har tilbydd stråleterapi i form av høyenergetisk røntgen (og elektroner) siden Haukeland Sykehus fikk installert Odd Dahls van de Graaff-generator, også kjent som "Høyvolten", i 1942. Partiklenes vekselvirkninger ioniserer molekyler i pasienten, og de ladde molekylene ("frie radikaler") kan brekke opp DNA-strukturen i kreftcellene. God stråleterapi er å levere ioniserende stråling primært mot kreftsykdommen, og begrense uønsket bestråling av friskt vev.

De siste tiårene har det vært økning i bruk av protoner og tyngre ioner innen stråleterapi. Ideen om å bruke ioner stammer fra 1946, og mange eksperimentelle fysikklaboratorier har behandlet pasienter siden den gang. Første sykehus-baserte protonsenter ble bygget i 1990 ved Loma Linda utenfor Los Angeles i California. I dag finnes 69 sentre på verdensbasis, og over 150 000 pasienter har fått behandling med protoner og tyngre ioner. Sverige åpnet protonsenteret Skandionkliniken i Uppsala i 2015, og Dansk Center for Partikelterapi i Aarhus satser på å behandle første pasient med protoner i 2018. I Norge utarbeider nå de fire helseregionene en plan for å bygge to sentre for partikkelterapi — i Bergen og i Oslo.
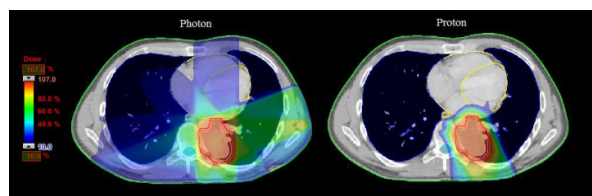
Figur 1: *To behandlingsplaner for en svulst i lungene, her rett under hjertet i lysegrått. Rød farge viser terapeutisk dose. **Venstre:** Konvensjonell stråleterapi med fotoner. Legg merke til "lavdose-badet" i lungene og hjertet. **Høyre:** Protonterapi: Protonstrålen stopper rett etter svulsten, og det blir gitt mindre dose til det omliggende friske vevet. Fra G. M. Engeseth*

ved Haukeland Universitetssykehus.

Innen konvensjonell stråleterapi med fotoner leveres stråledose i en eksponentielt fallende dosegradient gjennom pasienten. Stråleterapauter bestråler pasienten fra ulike vinkler: Da vil man oppnå et område i svulsten med høy dose, og et såkalt lavdose-bad til det friske vevet. Innen konvensjonell stråleterapi med høyenergetisk røntgenstråling leveres stråledose i en eksponentielt fallende dosegradient gjennom pasienten: Det er den naturlige oppførselen til røntgenstråler som gradvis avsetter energi i vevet. Stråleterapeuter bestråler pasienten fra ulike vinkler: Da vil man oppnå et område i svulsten med høy dose, og et såkalt lavdose-bad til det friske vevet. I dag prøver en å erstatte røntgenbestråling med partikkelbestråling der det er mulig. Fordelen med partikkelterapi er at man begrenser strålebruken til det friske vevet, og reduserer risikoen for senskader. Figur 1 sammenlikner to behandlingsplaner, gitt med konvensjonell høyenergetisk røntgen og med protoner. Som kjent er protonet en positivt ladd partikkel med masse om lag som ett hydrogenatom, $1{,}67 \times 10^{-27}$ kg.

Protonets dans mot svulsten

Under partikkelterapi bestråles pasienten med protoner (eller tyngre ioner) som gradvis bremses ned i vevet. Partiklene ioniserer molekyler i bein, fett og muskel: Jo lavere hastighet partiklene har, desto lengre tid har de på ioniseringsprosessen, og jo høyere er energitapet innover i vevet. Re-

sultatet er et skarpt avgrenset område i svulsten med høy ioniseringskraft og dose, hvor alle protonene stopper helt opp. Effekten ble oppdaget i 1903 av W. H. Bragg, og høydose-området kalles for ***Bragg peak***. Dypere enn Bragg peak avgis det praktisk talt ingen dose, siden primærstrålen har blitt bremset ned (for tyngre ioner som karboner, derimot, kan prosjektilene brekke opp i fragmenter med lengre rekkevidde, og da avgis det noe dose bak Bragg peak).

Denne prosessen er formulert i Bethe-likningen, som finner protonets ***stoppekraft*** S (her i ikke-relativistisk tilnærming):

$$S = \frac{4\pi n_e z^2}{m_e v^2} \cdot \left(\frac{e^2}{4\pi\epsilon_0} \right)^2 \cdot \ln \frac{2m_e v^2}{I},$$

hvor n_e og I er hhv. vevets elektrontetthet og gjennomsnittlige ioniseringspotensiale. Videre er m_e elektronets masse, v og z er hhv. hastigheten og ladningen til prosjektilet og e, ϵ_0 er konstantene for hhv. elektronladningen og vakuumpermittiviteten.

En av utfordringene innen partikkelterapi er å beregne hvordan man skal bestråle svulsten. Medisinske fysikere og doseplanleggere på sykehus må finne ikke bare den beste vinkelen å bestråle fra, men også hvilken energi partiklene må ha.

Vevets sammensetning

En protonstråle med en energi på 130 MeV stopper etter 13 cm i fett, 12 cm i muskel eller 7 cm i ben. Da er det viktig å vite hva som ligger mellom strålerøret og svulsten! En liten feilberegning kan føre til store mengder stråling til friskt vev, og

en svulst som slipper unna. Skjelett kan komme inn i partikkelbanen ved puste-bevegelser, pasienten kan ha gått ned en buksestørrelse siden doseplanen ble god-kjent, eller svulsten kan ha krympet siden sist. Slike naturlige hendelser, som ikke en-drer dosenivået med mer enn få prosent un-der fotonterapi, spiller her en stor rolle.

For å kunne beregne nøyaktig hvor pro-tonstrålen stopper i pasienten, trenger man et godt kart over protonets stoppekraft i pasienten. Protonets stoppekraft avhenger, i tillegg til energien, proporsjonalt av elek-trontettheten og logaritmisk av ioniser-ingspotensialet i vevet. Det så vi gjen-nom den tidligere nevnte Bethe-likningen. Den er relativt enkel å beregne analytisk, men krever kjennskap til de to faktorene: Vanligvis leses ioniseringspotensialet ut fra en tabell: for bein, muskel, vann, luft, osv. Hvordan kan man så finne elektrontet-theten? Magnetresonsanstomografi (MRI) måler tettheten av protoner, mens røntgentomografi (eller **røntgen-CT**, for "com-puted tomography") måler dempningskoe-ffisienten for røntgenfotoner. Dempn-ingskoeffisienten er den samlede effekten av fotoelektrisk absorpsjon, Rayleigh- og Comptonspredning, og signalet er sterkt avhengig av atomnummeret til materialet (røntgenfotoner har energier på mellom 20 og 140 keV).

Røntgen-CT

En røntgen-CT fungerer ved å bestråle pasienten med en vifteformet røntgenstråle mens integrerende CMOS-detektorer måler den (varierende) gjenværende intensiteten strålen har etter å ha passert pasienten. Jo mer pasient, jo mindre gjenværende inten-sitet! Både detektor og røntgengenerator roterer rundt pasienten, og etter én rotasjon kan man danne et tynt **snittbilde** av pasien-ten (derav navnet *tomografi*, hvor greske *tomos* betyr snitt). Siden røntgenstråler føl-ger rettlinjede baner blir bilderekonstruk-sjonen relativt enkel.

For å beregne protonets stoppekraft brukes slike snittbilder fra en røntgen-CT: En CT-skanner kalibreres til oppgaven ved å avbilde en 32 cm stor sylindrisk plast-skive med ulike innsatser, alle i forskjel-lige tettheter og materialer med kjent elek-trontetthet. Med Bethe-likningen kan man også beregne innsatsenes stoppekraft. Et slikt objekt kalles for et fantom, og er et vanlig verktøy for å karakterisere, kon-trollere og kalibrere CT-maskiner. Ved å avbilde de ulike innsatsene kan man lage en kalibreringskurve mellom dempningskoe-ffisienten og stoppekraften. Dessverre har ikke denne kurven en enkel form, og det vanlig å anta at den består av stegvise rette linjer: Se Figur 2 for et eksempel på en slik kalibreringskurve. Merk at kurven bare gjelder maskinen (og innstillingen) den er kalibrert for, siden ulikheter i røntgenspek-trum og detektorrespons kan påvirke kali-breringen.
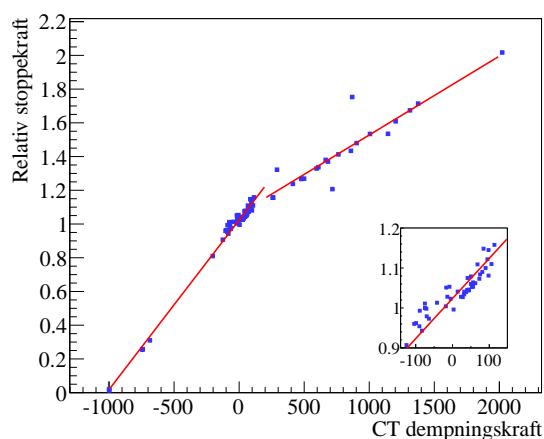
Figur 2: *Kalibrasjonskurven mellom protonets stoppekraft og dempningskraft ("Hounsfield Units"). Laget med data fra U. Schneider et al. Physics in Medicine and Biology 41 (1):111 (1996).*

Denne kalibreringskurven legges så inn i programvaren for behandlingsplanlegging, som omformer pasientens CT-bilder til stoppekraft, og rekkevidden til protoner kan beregnes enkelt. Resultatet av en slik kalibreringsprosess er en total usikkerhet i protonrekkevidden på 2%–3 %. Mesteparten av den usikkerheten kommer fra tabelloppslaget av ioniseringspotensialet.

Den kraftige gradienten til protonstrålen gjør at man i teorien kan bestråle volumer tett opptil kritiske organer som hjerte og synsnerve, men usikkerheten i protonrekkevidden krever økte marginer, dvs. at man øker området som bestråles slik at svulsten er garantert riktig stråledose selv med usikkerhet i beregningene. Det legger begrensninger på hvor tett opptil kritiske organer man kan behandle, og øker den totale dosen til friskt vev. En nøyaktig behandling krever nøyaktig diagnostikk!

Proton-CT

Ideen om å måle vevets sammensetning direkte med protoner har eksistert siden 50-tallet: Dersom en protonstråle har høy nok energi til å komme helt gjennom en pasient, er det også mulig å måle den gjenværende energien til protonene etter de har kommet ut igjen av pasienten. Da kan man regne ut den gjennomsnittlige stoppekraften langs den antatte protonbanen gjennom pasienten. Måler man mange nok ganger, og fra ulike vinkler, slik at de ulike protonbanene dekker hele pasienten kan man rekonstruere et nøyaktig volumkart over stoppekraften til pasienten. Nøyaktigheten øker drastisk i forhold til volumkartet som er beregnet fra røntgen-CT-bildene, og det blir mulig å redusere behandlingsmarginene og følgelig også pasientens senskader.
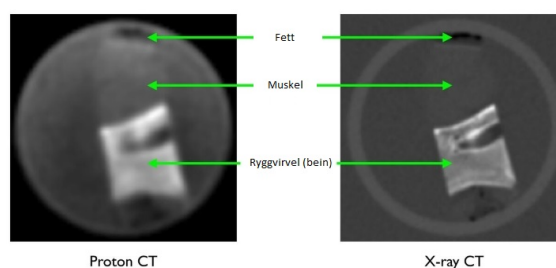
Figur 3: *Et hodefantom rekonstruert med data fra (venstre) en proton CT og (høyre) en røntgen CT. Volumbildet fra proton CT ble rekonstruert ved hjelp av rundt 85 millioner protonbaner. Fra* `http://medicalphysicsweb.org/cws/article/research/68766`

Et proton-CT opptak skjer separat fra selve strålebehandlingen, men siden pro-

tonene ikke stopper i pasienten, blir ikke stråledosen mye høyere enn fra en vanlig røntgen-CT: Bragg peak ender opp i detektoren.

I motsetning til de rettlinjede røntgenstrålene, vil protonene oppleve mange små avbøyninger i form av multippel Coulombspredning mens de flyr gjennom pasienten. For å rekonstruere den nå buede protonbanen må man måle posisjon og retning til hvert enkelt proton både før og etter pasienten. Dette krever et sett med posisjonsdetektorer med høy oppløsning og rask elektronikk. Energien til hvert enkelt proton må også måles, og flere detektorer er foreslått for denne oppgaven: Ulike typer scintillatorer, sammenkoblede ioniseringskamre og sporingskalorimetre.

Flere forskningsgrupper har laget proton-CT-prototyper, og totalt har åtte ulike prototyper blitt konstruert på verdensbasis. Først ut var en gruppe ved Loma Linda, som i dag har publisert gode resultater for sin løsning. Den baserer seg på silisium-stripedetektorer for å spore protonene før og etter pasient, og en plastscintillator segmentert i dybden for å måle den gjenværende protonenergien etter pasienten. Se et eksempel på et rekonstruert hodefantom med data målt i deres detektor i Figur 3.

Proton CT i Bergen

I Bergen foregår nå et samarbeidsprosjekt mellom UiB, Høgskulen på Vestlandet og Haukeland Universitetssykehus med mål om å utvikle et proton-CT-system basert på teknologi fra høyenergifysikk.
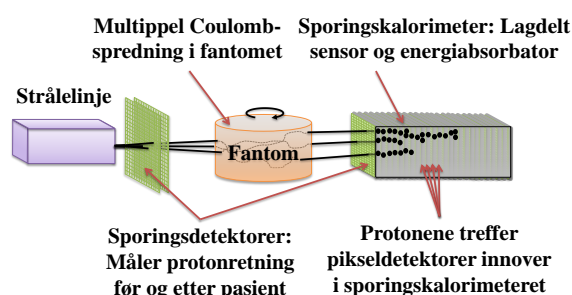
Figur 4: *Oppsettet for en proton CT med sporingskalorimeter.*

En lagdelt pikseldetektor som vist i Figur 4 skal kunne spore tusener av protonbaner samtidig. Den er basert på samplingprinsippet, hvor partikler bremses ned ved hjelp av et absorbatormateriale mellom hvert sensorlag. Den ble opprinnelig utviklet som en prototype på et elektromagnetisk kalorimeter for å telle partikler i foton- og elektrondusjer ved ALICE–eksperimentet ved CERN. Forskningsgruppen i Bergen ønsket å undersøke om sporingskalorimetre kan brukes i en proton-CT.

Ved å bruke data fra sporingskalorimeteret kan vi kombinere rekonstruksjon av samtidige protonbaner og modeller for protonets energiavsetning. Målet er å finne rekkevidden til hvert proton med høy nøyaktighet. Rekkevidden i vann, R, svarer til opprinnelig energi E_0 gjennom Bragg-Kleeman-forholdet

$$R \simeq 0{,}022 E_0^{1,77}.$$
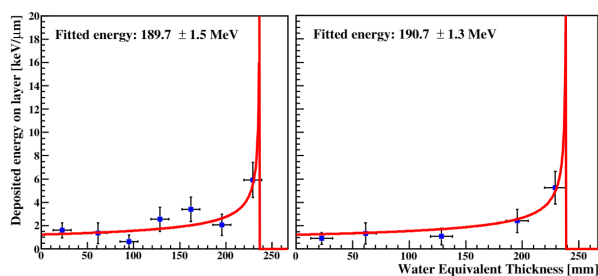
Figur 5: *Energiavsetningen til individu-elle protonbaner, med forventet energi 188 MeV. Hvert datapunkt svarer til dybden hvor protonet har truffet et sensorlag. En Bragg-kurve-modelltilpasning er vist ved den røde kurven.*

I Figur 5 vises energiavsetningen for én protonbane, som har blitt rekonstruert sammen med flere hundre andre protoner i én detektorutlesning. Gjennom studier av både eksperimentelle data målt ved KVI-CART i Groningen, Nederland og Monte Carlo-simuleringer, har vi funnet at prototypen på sporingskalorimeteret svarer til forventningene: En energioppløsning på 4 % av rekkevidden, samt muligheten for å måle 1 million protoner i sekundet.

Veien mot klinikken

I den nære fremtid vil gruppen i Bergen samarbeide om å utvikle, konstruere og evaluere den neste prototypen av sporingskalorimeteret. Samarbeidet med ALICE fortsetter, og detektorbrikker fra ITS-detektoren skal bidra til at den neste prototypen får en meget hurtig og effek-tiv datautlesning og elektronikk. De ulike samarbeidspartnerne er tildelt midler fra TOPPFORSK, Bergens forskningsstiftelse og Helse Vest, og ansetter flere doktor- og postdoktorstipendiater de neste årene med mål om å utvikle prototypen som et klinisk hjelpemiddel.

Når det første partikkelterapisenteret bygges i Norge (og i Bergen) i løpet av de nærmeste årene, enten med protoner eller «fremtidsrettede» tyngre ioner, vil pasienten få tilgang til en skånsom, effektiv og ut-prøvd kreftbehandling. En proton-CT i be-handlingsrommet vil øke treffsikkerheten til en allerede treffsikker behandling gjennom å redusere behovet for å «tippe» på pasientens vev.

Likevel – det er nesten umulig å si når nytt medisinsk utstyr når sitt endelige mål: Pasienten.

Videre lesning

- Poludniowski, G. et al. *Proton Radio-graphy and Tomography with Appli-cation to Proton Therapy.* Br. J. of Radiol. 88, 1053 (2015): 20150134

- Pettersen, H.E.S. et al. *Proton Track-ing in a High-Granularity Digital Tracking Calorimeter for Proton CT Purposes.* Nucl. Instr. and Meth. in Phys. Res. A 860C (2017): 51–61.

- Avhandlingen du nå holder.

Contents

List of Figures

List of Tables

Chapter 1

Introduction

1.1   Proton Therapy

Cancer is a destructive disease, in which tumor cells grow out-of-control, halting organ function. Its treatment is threefold: Radical surgery, chemotherapy and radiation therapy. Recently there has been an important development of immunotherapy, in which the mechanisms of our body enters as a part of the cancer treatment in combination with the other treatment modalities. Their relative usage is determined by cancer type, stage, organs at risk adjacent to the tumor and progression.

In the recent decades, there has been a significant increase in the number of cancer patients treated with proton and carbon ion therapy worldwide. Treatment with protons and ions, referred to as particle therapy, is an alternative to X-ray photon therapy for many cancer patients. More than 174 000 patients have been treated with particles worldwide per 2017 (Jermann, 2017). The increase in the number of patients treated with particle therapy during the recent decades is due to a tremendous development of facilities and medical-technical equipment.

Many hospitals are now considering particle therapy when planning their future radiation therapy departments: this is in part due to the emergence of novel, more economically feasible clinical particle facilities, and in part motivated by results from clinical studies that demonstrate improved outcome for many patient groups receiving radiation treatment with proton and carbon ions. The main advantages of particle therapy compared to conventional photon therapy can be said to be threefold:

i) **Less total dose**: The patient undergoing particle therapy will receive less dose to normal tissue and organs around the tumor, compared to the situation during photon therapy. The sparing of normal tissue will reduce the unwanted side effects from the radiation treatment, both in the short run (during treatment and recovery), and in the long run with an expected improvement of the patient's Quality of Life in the
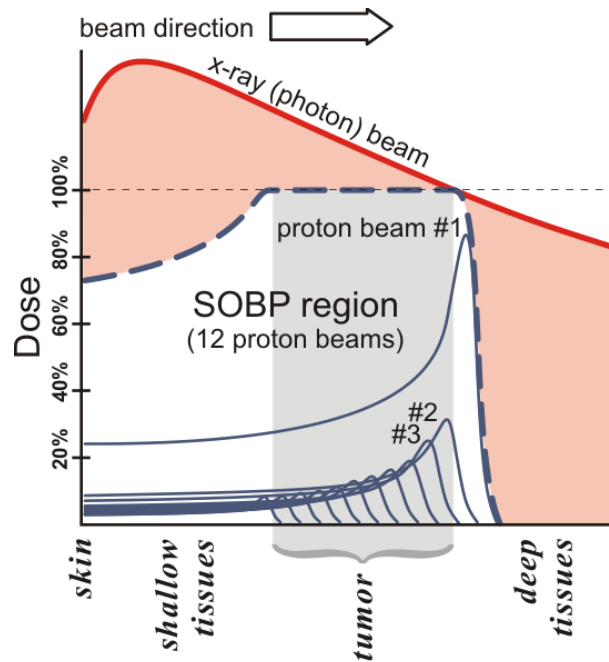
Figure 1.1: *The different depth dose distributions from photons and protons, as a function of depth in water (Filipak, 2012).*

decades post-treatment. This different total dose deposition in the patient can be seen from the different depth dose distributions of the two different radiation types, shown in Fig. 1.1. Put in context, two dose plans using the respective radiation types are compared in Fig. 1.2.

ii) **Improved tumor control**: The improved dose distribution from protons and heavy ions will enable improved tumor control in many situations. This is due to the sharp dose delineation between the tumors to be irradiated and healthy tissue, as well as the possibility coupled to this for an escalation of the dose delivered to the target volume. Compared to photon irradiation there is an enhanced biological effect of heavier ions in tissue in the target volume region where the tumor is located.

iii) **Precise dose delivery**: The delivery techniques emerging in particle therapy yields a more precise dose delivery in the patient than with photon therapy. These delivery techniques include fast scanning particle beams with online feedback loops, which are systems enabling swift adjustment of the particle beam energy and scanning position based upon rapid measurements of the dose deposited in the patient during treatment.

The advantages of particle therapy translate into a significantly reduced number of patients suffering from side effects from their radiation treatment cure (Dionisi and Ben-Josef, 2014; Leeman et al., 2017). Amongst these are a reduction of the number of
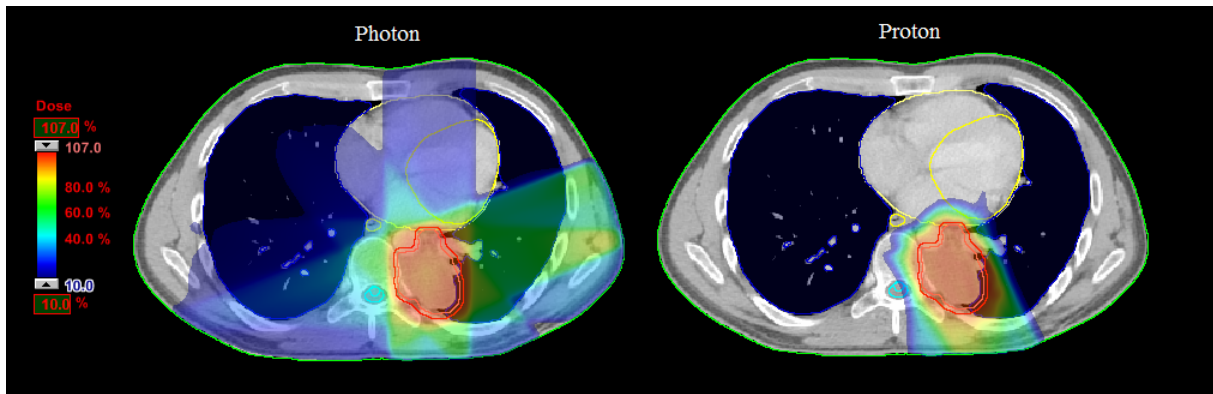
Figure 1.2: *A comparison between two dose plans for irradiation of a paravertebral sarcoma in the lung, overlaid on CT images.* **Left:** *(conventional) Intensity Modulated Radiation Therapy with photons.* **Right:** *Intensity Modulated Proton Therapy. Note the difference in volume between the low dose regions (the so-called low dose bath) visualized as blue areas, substantially smaller in the proton plan. Both plans are from G. M. Engeseth at Haukeland University Hospital, the plans are made using the Aria (version 11) dose planning system (Varian Medical Systems, CA, USA).*

patients developing secondary cancers from the irradiation, a reduction of damage to normal tissue and less damage to nearby organs.

This is of special concern for children, who, in their growth phase in life, are especially sensitive to radiation exposure, and in situations with tumors located critically near sensitive organs – relevant examples are found in the head and neck region and around the central nervous system, as well as for breast and lung cancers.

There is a continuous ongoing international effort with clinical studies and clinical research in order to obtain improved knowledge about the clinical effect and efficacy of particle therapy compared to photon therapy. The process of demonstration of the relative use of particle therapy will last for decades to come since the core advantages of particle therapy is the potential for reduction of unwanted side effects, often not visible until years and decades post-treatment.

In Norway, the health regions are presently planning for two regional particle therapy facilities in Oslo and Bergen, with the aim of clinical startup within the next 5–8 years (Ministry of Finance, 2017). A research room will be built in each of these facilities, equipped with fixed beamlines and technical equipment dedicated to the research and development of particle therapy.

Participation in this common research and development endeavor will require involvement in both national and international clinical studies, development of advanced treatment techniques and refinement of the required technology for precise delivery of the treatment dose in the patient; optimizing the relation between the clinical dose to the

tumor and the unwanted dose to healthy tissue around this.

Proton Beam Delivery Systems

The pre-defined dose plan is a recipe for how the target volume in the patient should be irradiated with protons: in terms of incident angle, field size, beam intensity and beam energy. A cyclotron or a synchrotron accelerates protons from the ion source up to an energy of (usually) 230 MeV. A system of beam optics ensures that the beam is well defined in terms of spatial and spectral distributions. The beam optics include dipole and quadrupole magnets used to, respectively, bend and focus the beam, beam monitors and a range modulator that adjusts the beam energy downwards (and thus also the range of the protons in the patient). Finally, a so-called *nozzle* is located inside the treatment room, where the beam is shaped laterally in accordance to the dose plan. Two main nozzle types are available, varying in the degree of treatment conformality, i.e. how well the dose can be shaped to the tumor in three dimensions (Das and Paganetti, 2015):

i) The *Double Scattering* technique utilizes a proton beam that is scattered twice to increase the lateral extent of the beam. The energy is first partially degraded with a continuously turning *range modulator wheel*. The wheel degrades the beam differently, depending on its rotational angle: During a full rotation, the span of required proton energies will be attained. The beam is scattered using a lead or tungsten disc, spreading the beam up to 20 mrad. A second scatterer is located 1–2 m downstream, it is shaped to remove the high intensities in the beam core so that the irradiation field is flattened in terms of beam intensity. Finally, a patient-specific lead collimator degrades the beam partially so that the lateral distribution of beam energies match the treatment depth at that spot. Due to the material in front of the patient, the neutron dose from this technique is non-negligible.[*] It is not possible to attain a high conformality of the treatment *proximal* to the tumor, as the field is shaped to the distal edges of the treatment volume.

ii) *Intensity Modulated Proton Therapy* (IMPT) consists of a continuously intensity modulated *pencil beam* that is scanned across the patient using horizontal and vertical magnetic fields. The pencil beam scans across a "depth layer" of the tumor, before the energy is decreased slightly using, for instance, a range modulator *wedge* setup, and the next layer of the tumor is scanned. This method requires a precise pencil beam that can be aimed towards a treatment "spot" in the target volume in the patient. The resulting conformality of the dose distribution is very high, since the dose can be "painted" in accordance to the three-dimensional dose plan.

---

[*]0.1–4 mSv per "treatment Gy" depending on the measurement position (Shin et al., 2009).

Both of the above techniques are in use today, however almost all new and planned therapy facilities are and will be based on the delivery of IMPT (PTCOG, 2017).

The Spread-Out Bragg Peak

A distinction is made between the depth-dose depositions from single proton, from a mono-energetic proton beam and from an energy-modulated proton beam (a so-called Spread-Out Bragg peak). A single proton leaves a large portion of its remaining energy in a sub-mm (*pristine*) Bragg peak area. However, due to the statistical nature of the energy loss process, the actual depth of the end point of a single proton track varies by a few millimeter in the patient — the variation can be approximated by a Gaussian distribution[*] where the standard deviation is approximately 1% of the range. This variation is called *range straggling*. It follows that a mono-energetic proton beam will have an extended Bragg peak area. If the energy-loss curve is convoluted with the statistical range straggling of a proton beam, and combined with the beam fluence, the result is the depth-dose curve for a proton beam: this in contrast to the pristine energy loss curve of a single proton.

In contrast, a clinical proton beam needs to cover an extended tumor area: the final depth dose distribution must be broadened artificially, as seen in Fig. 1.1. This broadening is performed by applying different proton beams with varying energy (range) and intensity. The calculation of the appropriate beam energies and their relative intensities is described in Jette and Chen (2011). Depth-dose distributions originating from a single proton, a proton beam and a spread-out Bragg peak are shown in Fig. 1.3. This distinction is important to have in mind, as many of the discussions and results in this thesis depend on the differences between the three depth-dose deposition types.

1.2 Treatment Accuracy

The proton beam characteristics yield a possibility to deliver a precise dose to a target volume (i.e. the tumor including treatment margins). However, the range of protons in the patient's body is highly sensitive to changes in the patient's anatomy during the treatment course of the radiation. Variations due to anatomical changes, tumor shrinkage and displacement, pockets of gas and air, inter- and intrafractional variations in the patient positioning, will all have immediate consequences for how far a proton traverses into the patient. All this emphasize the need for *robust* dose plans, which takes different uncertainty sources into account and compensates for possible dose displacements during

---

[*]The distribution is slightly asymmetrical towards smaller ranges due to multiple Coulomb scattering.
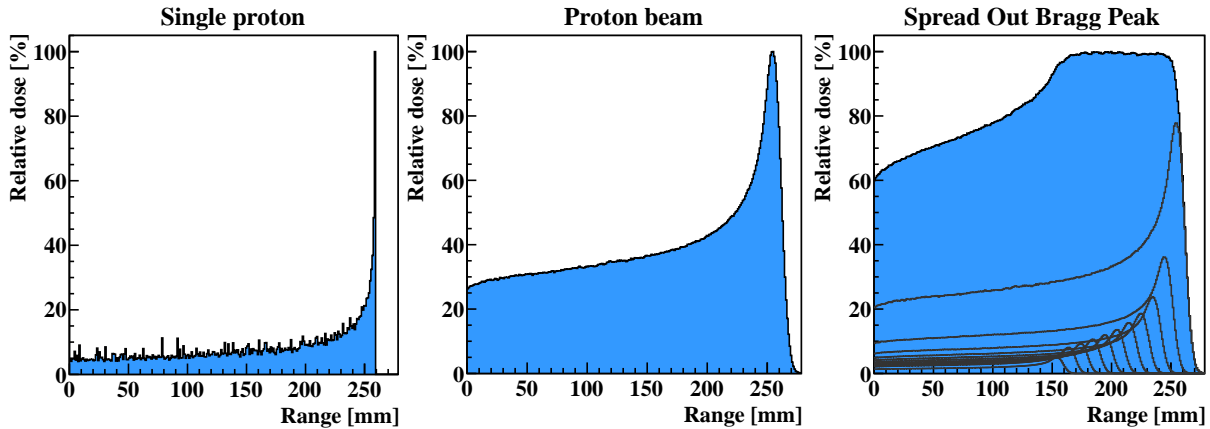
Figure 1.3: *Depth-doses from an individual proton (200 MeV), from a proton beam (200 MeV) displaying the Bragg peak, and from 11 beams in the 150–200 MeV range, producing a Spread-out Bragg peak. The depth-doses were made using the GATE Monte Carlo simulation framework, following the approach in Jette and Chen (2011).*

treatment.

Proton beams irradiate the target volume along different paths and angles in the patient tissue. In order to calculate the beam properties necessary for a precise dose deposition, the measured tissue density, obtained from X-ray CT (known as the mass attenuation), needs to be converted into the *proton stopping power* (or its ratio to the proton stopping power *in water*, called the *Relative Stopping Power* (RSP)). The RSP is the fundamental tissue characteristic that, in addition to the proton beam energy, decides the proton range. Scanner-unique look-up-tables are applied on the X-ray mass attenuation to obtain the electron density, then used together with the energy loss formula (i.e. Bethe's equation) to calculate the proton stopping power (Schneider et al., 1996).

The conversion from X-ray mass attenuation to proton stopping power is associated with an uncertainty inherent to the conversion between the different physical interactions associated with interactions between protons and tissue, and photons and tissue, respectively. These uncertainties, together with small changes in the patient positioning cause large uncertainties: At 20 cm depth, the uncertainty in the proton range is usually 4–6 mm, however it can be up to 1 cm (Paganetti, 2012).

1.2.1 Margins in Dose Planning

A complete dose delivery to a target volume[*] in the presence of uncertainties is made possible through the addition of margins around the tumor volume. Any deviations between the planned treatment and actual treatment conceptually are kept within the treatment

---

[*]Usually meaning at least 95% of the prescribed dose to 98% of the target volume (McGowan et al., 2013).
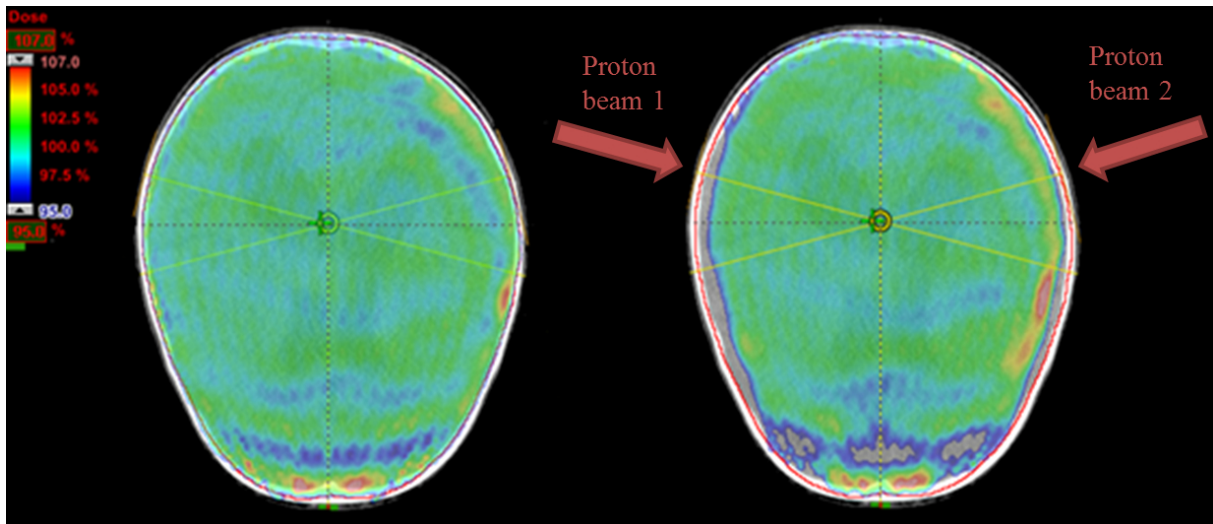
Figure 1.4: *The effect of an increase in the RSP: A comparison between two dose plans for treatment of the central nervous system. **Left:** The nominal treatment plan. **Right:** An artificial 3.5% increase in the RSP. Note the incomplete delivery of the prescribed dose in the peripheral areas distal to the beam. An incomplete delivery is a dose below 95% of the prescribed dose in the target volume (the whole brain). From G. M. Engeseth at Haukeland University Hospital.*

margins.

The total range uncertainty is an important element in the margin that is added to a clinical target volume. Applied margins are typically 2.5%–3.5% of the depth of the Bragg peak plus a fixed part of 1–3 mm. In Table 1.1 the margins that are applied at different proton therapy institutions are shown (Paganetti, 2012). An example of the clinical effect of this uncertainty is shown in Fig. 1.4, where the RSP of brain tissue is artificially increased by 3.5% to illustrate the resulting under-dosage of the target volume.

Greater accuracy implies a more thorough planning and treatment process. Small variations in tissue density, tumor size, patient positioning and even clothing will shift the proton dose distribution considerably. This is not the case in conventional photon radiation therapy, thus the workflow and dose planning methods in proton radiation therapy need to be adjusted accordingly to benefit from the high potential for tumor dose conformality due to the steep dose gradient in the depth distal to the Bragg peak.

1.2.2   Robust and Adaptive Treatment

A robust proton treatment plan takes into account the different scenarios that might potentially degrade the quality of the treatment: Perturbations in the patient positioning, small anatomical changes and errors in the calculated proton stopping power may all substantially increase or decrease the delivered dose in the various regions of a target

Institution	Relative margin	Fixed margin	At 20 cm depth
University of Florida Proton Therapy Institute	2.5%	1.5 mm	6.5 mm
Massachusetts General Hospital	3.5%	1 mm	8 mm
MD Anderson Proton Therapy Center	3.5%	3 mm	10 mm
Loma Linda University Medical Center	3.5%	3 mm	10 mm
Roberts Proton Therapy Center	3.5%	3 mm	10 mm

Table 1.1: *Target volume margins applied at different proton therapy centers. The table displays the relative and fixed part of the applied margin, as well as the total margin (the sum of these two) at 20 cm treatment depth. Data from Paganetti (2012).*

volume. The effect of over- or under dosage is significantly higher in proton therapy than in photon therapy due to the shape of the depth-dose curve.

The robustness of a plan may be evaluated by perturbing all the relevant parameters individually or with a combination thereof: the patient position in (x, y, z) is usually shifted by ± 2–5 mm, and the RSP is increased or decreased by 3%–3.5%. Following the definitions from McGowan et al. (2013), the plan is defined as robust if 95% of the total prescribed dose is still delivered to 98% of the target volume (i.e. a complete dose delivery) and the dose delivered to the various organs-at-risk does not exceed pre-defined limits. Ideally, most of the foreseeable anatomical variations are accounted for in a robust dose plan.

However, when altering individual values in this fashion, hundreds of treatment plans need to be generated and their clinical results must be taken into account in the uncertainty analysis. This is a potentially time-consuming process: one solution is to approximate so-called *pareto* spaces — a strategy for multi-criterion optimization, where the dosimetric outcome of various treatment constraints and strategies are easily assessed — from a handful of perturbed dose plans (Craft et al., 2006).

While the robust planning of radiation treatment aims at mitigating the effect of uncertainties, an *adaptive treatment* should identify any deviations between the prescribed and delivered dose distributions — and recreate the plans based on the updated information (McGowan et al., 2013). Thus all updated information will contribute towards a more accurate treatment (van de Water et al., 2018): Tumor shrinkage, patient weight loss and other changes to the RSP values of the patient's tissue. It is time-demanding to perform full validations of the delivered dose distribution using daily imaging and so-called re-planning of new adaptive dose plans, and therefore the adaptive process is often not fully included in the routine practice.

1.2.3   In-vivo Imaging

In order to reduce the uncertainties in the treatment plan including some measures for determining the patient's organ motion, and also to provide the required information for deciding if an adaptive approach is necessary, online in-vivo imaging can provide information about the patient's anatomy or even dosimetric information about the proton beam during treatment. Different approaches are in use or have been suggested: Adapting Cone Beam Computed Tomography (CBCT) for use in proton treatment situations (Veiga et al., 2017) and using online MRI guidance (Raaymakers et al., 2008). It is also possible to detect secondary particles during treatment such as: Back-to-back photons from position annihilation with post-treatment or on-line Positron Emission Tomography (PET) for imaging of activated isotopes in the treatment volume (Parodi and Enghardt, 2000); prompt-gamma emissions during treatment (Xie et al., 2017); emission of neutrons (Marafini et al., 2017; Meric, 2017) and charged secondaries (Reinhart et al., 2017) during treatment.

As discussed previously, one of the uncertainty sources of the treatment margins is the conversion between the tissue's X-ray mass attenuation and the RSP values in this tissue, a process inducing uncertainties in the 2%–3% range. In this number, about 1.5% is due to the uncertainty of the tissue's mean ionization potential (Paganetti, 2012). A proposed approach is to reduce the uncertainties in the calculation by applying the RSP conversion to images obtained with a Dual Energy CT, a modality with the potential for yielding more accurate electron density measurements compared to regular CT (Zhu and Penfold, 2016). Another approach to reduce this uncertainty is the *proton Computed Tomography* (proton CT) modality — which is the topic of this thesis.

In-vivo imaging strategies as outlined above may all eventually play a role in particle therapy, with the goal in mind of providing improved information for adaptive treatment and for reducing the initial treatment margins.

1.3   Proton Computed Tomography

While protons of therapeutic energies are stopped in the body, protons with higher energies can pass completely through the body and be detected on the distal side, outside of the patient. The idea of proton imaging is that a high energy proton beam is irradiated through the patient just before the treatment, resulting in verification of both patient positioning and enabling proton range calculation (Collins-Fekete et al., 2017). The imaging can be performed as *proton radiography*, where a single projectional image is produced, or as *proton CT*, where different projections from a rotational geometry are combined into a three-dimensional map.

By measuring the residual energy of each proton, the tissue's RSP along the proton's path can be deduced. In essence, these algorithms work by first estimating the individual proton's path through the patient. This is achieved by calculating the Most Likely Path (MLP) using techniques such as Bayesian probabilistic inference (Williams, 2004) from measurements of the proton's position and direction shortly proximal and distal to the patient. Then, the proton's calculated average energy loss is applied along the proton's MLP, before finding the average RSP in each voxel by repeating the process for a large number of protons ($\sim 10^7$) coming from different angles. This last process of mapping individual proton paths to the voxel values is the traditional image reconstruction step, and applying reconstruction algorithms such as MLP-FDK (Rit et al., 2013) or using iterative methods as described in Penfold et al. (2010), a three-dimensional RSP map can be reconstructed.

The RSP map can be used directly in a Treatment Planning System, as a more accurate estimate than the values converted from X-ray CT. Simulations and experimental prototypes of proton CT systems have been used to reconstruct RSP maps that correspond to better than 0.5 mm range accuracy (Petterson et al., 2006). Other kinds of output from this imaging technique are also feasible: attenuation maps applied for measuring the nuclear interaction cross sections (Quiñones et al., 2016), multiple Coulomb scattering maps (Plautz et al., 2014) and proton range straggling distributions (Bopp et al., 2013).

In proton CT, tracking detectors that are placed proximal and distal to the patient yield information needed in order to obtain a measure of the path of each proton through the patient to provide a measure of how and where the protons lose their energy. Telescopic ionization chambers or calorimeters measure, respectively, the remaining range or energy of each individual proton after traversing the patient. The calorimeter is an energy detector with sufficient material to completely stop the protons and record their energy. A clinical proton CT scanner would significantly reduce the 8–10 mm treatment margins applied today (Poludniowski et al., 2015).[*] The dose of such a scan is estimated at 7 mGy, compared to CBCT doses which are in the 1–100 mGy range (Palm et al., 2010).

1.3.1   Adaptive and Robust Proton Therapy with Proton CT

With a proton CT system, a higher accuracy on the RSP measurement is obtained. This will in turn reduce the necessary magnitude of the perturbation in the robustness analysis and by this reduce the applied treatment margins. If proton CT imaging were applied regularly during the treatment course it would also serve as an input to the adaptive

---

[*]The treatment margin at 20 cm depth can be calculated as 3.5% + 1 mm (Paganetti, 2012). If the contribution to the margins from range uncertainties were reduced to from 3.5% to 1.5%, the total uncertainty including patient positioning would be reduced from 8 mm to 4 mm.

treatment process and help decide if a re-planning of the treatment is necessary.

The clinicians and the dose planners will be able to apply margins for the irradiation fields that are at the same time clinically safe in terms of covering the tumor with enough dose, but also limited downwards to the best of knowledge and technology level, thus avoiding unnecessary irradiation of healthy tissue while serving the former purpose.

1.3.2   Proton CT Prototype Systems

Several research groups are (and have been) developing prototype proton CT systems based on different designs. In the current prototypes described in a recent review (Poludniowski et al., 2015), the calorimetry and tracking are based on various technologies, as outlined below.

Tracking detectors

The tracking detectors are used for track reconstruction purposes and MLP estimation. Two tracking planes should be positioned both proximal and distal to the patient, so that a proton passing through each tracking plane is recorded twice: This to reconstruct both position and direction. The two vectors are then used together with information about the patient's position to find the MLP of the proton. To first order, this can be a cubic spline fitted to both vectors, however more sophisticated methods take into account the expected proton scattering power for different tissue types (Wong et al., 2009).

Scintillating Fibers (Naimuddin et al., 2016) or Silicon Strip Detectors (SSD) (Johnson et al., 2013; Taylor et al., 2016a; Scaringella et al., 2013) are the most commonly used technologies for the tracking detectors, which are based on one-dimensional strip readout in several rotated planes for tracking purposes. The SSD readout is very quick, since $\sim m + n$ channels are readout compared to the $\sim mn$ channels in a pixel detector — however the reconstruction of the SSD output into a two-dimensional hitmap is non-trivial if the hit occupancy is high. A Gaseous Electron Multiplier solution has been developed by Bucciantonio et al. (2013).

Residual energy detectors

In addition to the proton's MLP information obtained from the tracking detectors, a proton CT system needs to measure the energy of each proton. The average energy loss of a single proton is then applied along the proton's MLP during the reconstruction process.

Crystal calorimeters such as CsI:Tl (Sadrozinski et al., 2013), YAG:Ce (Scaringella et al., 2014) and NaI:Tl (Saraya et al., 2014), as well as plastic scintillators (Bashkirov et al., 2016), are commonly used in combination with photomultipliers for the energy

measurement. In this case, the number of scintillation photons are counted and calibrated to the total energy deposited by a single proton (its residual energy).

In Bashkirov et al. (2016) a staged calorimeter system has been developed, consisting of five individual plastic scintillators: this technique reduces the range uncertainty markedly. The fractional energy deposition in the last stage can be measured more accurately compared to a measuring the complete energy deposition in a single scintillator.

Poludniowski et al. (2014) are developing a proton CT prototype with a multiple layers of large-area CMOS pixel sensors. They have demonstrated several image reconstruction techniques relying solely on the tracking detectors, such as proton scattering power CT (the degree of scattering inside the patient) (Taylor et al., 2016b).

The slow calorimeters of the first proton CT prototypes caused the total scan time to be in the order of hours (Vanzi et al., 2013). The scan time have since been reduced to minutes (Sadrozinski, 2013), however new and more rapid calorimeters are needed before it is possible to introduce proton CT to the clinic.

1.3.3 The Digital Tracking Calorimeter

Norway is currently preparing for the construction of particle therapy facilities in Oslo and Bergen (Ministry of Finance, 2017). In order to deliver a regional contribution to the highest possible quality of patient treatment, a collaboration between Haukeland University Hospital, the University of Bergen and the Western Norway University of Applied Sciences has been established in an effort, together with international partners, to develop a proton CT system to be used during proton therapy, including the future proton therapy centers in Norway.

The planned proton CT system is to be based on an earlier prototype detector originally designed for High Energy Physics purposes, capable of rapid and precise reconstruction of particles traversing stacks of pixel sensor layers with a digital (1-bit) readout. The detector was made available through the ALICE-FoCal collaboration at the Department of Physics and Technology at UiB (Nooren et al., 2018).

The use of reconstruction of multiple proton tracks for calorimetry — a so-called *Tracking Calorimeter* — is a novel method in terms of proton CT with some similar research being performed by other groups (Esposito et al., 2015; Gehrke et al., 2018). It is expected that this method will greatly increase the rate capabilities, thereby minimizing the scan time for the patient. It may also simplify the proton CT setup since the detector design eliminates the need for the separate proton tracking detectors usually required for proton CT (at least the ones downstream to the patient): The tracking calorimeter already measures the direction and position of individual protons.

So far, five MSc projects (Aadnevik, 2014; Austreim, 2015; Hansen, 2017; Grøttvik,

2017; Schaug, 2017) and five ongoing PhD projects including this work are directly connected to and involved in the proton CT efforts in Bergen.

1.4 Proton Interactions with Matter

The proton is in the context of proton therapy and proton imaging a point-like heavy particle with a unit positive charge.[*] The physical interactions of interest are those happening, mainly electromagnetically, between protons and matter. These interactions can be divided into three main groups in the therapeutic energy range under consideration:[†]
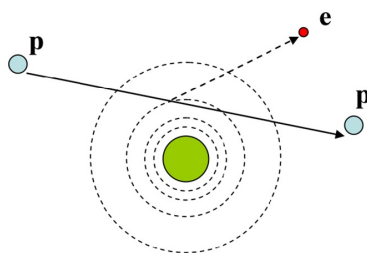
Inelastic Coulomb interactions

Protons ionizing atomic matter through inelastic Coulomb interactions. This is a gradual process as the number of electrons to hit is considerable. The large number of inelastic collisions leads to a continuous energy loss for the protons. Since the electron mass is very low compared to the proton's, any deflection of the protons can be neglected.
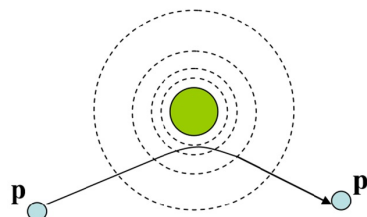
Elastic Coulomb scattering

Protons being deflected by atomic nuclei through elastic coulombic interactions. Due to the kinematics of collisions between protons and nuclei, the protons are deflected a little by each collision, ensuring that the proton's path is curved in a random fashion.
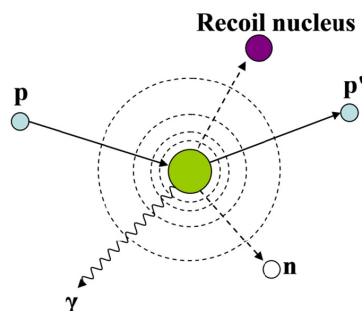
Inelastic nuclear interactions

Protons hitting atomic nuclei head-on, causing inelastic nuclear interactions. Through this process, the original proton is absorbed and secondary particles are ejected: Protons, alphas, photons, neutrons, ^{3}He, deuterons, tritons and more. Approximately 1% of the protons undergo inelastic collisions for each (equivalent) cm of water (Paganetti, 2002).

---

[*]In other contexts, the proton is a complex system consisting of three *quarks* (up, up, down) connected by the *gluons* of the strong force. The seemingly chaotic creation and destruction of virtual quark-antiquark pairs (this to shield the quarks' color charges) are responsible for 99% of the proton's mass. The remaining 1% is due to interactions between the three quarks and the Higgs field.

[†]The figures are reprinted from Newhauser and Zhang (2015) (CC-BY 3.0).

1.4.1   Energy Loss Through the Bethe Equation

The Bethe equation (Bethe, 1930) is a description of the energy loss of charged parti-
cles by interaction with atomic electrons. Following the procedures and formalisms of
Grimes et al. (2017) and Ziegler et al. (2015), we can express the linear energy loss (also
called the stopping power S) in terms of MeV/cm:

$$S = \left\langle -\frac{\mathrm{d}E}{\mathrm{d}x} \right\rangle = \frac{4\pi n z^2}{m_e c^2 \beta^2} \left(\frac{e^2}{4\pi \varepsilon_0^2} \right)^2 \left[f(\beta) - \frac{C}{Z} - \ln\langle I \rangle - \frac{\delta}{2} + z L_1 + z^2 L_2 \right]. \qquad (1.1)$$

Here: n is the electron density of the material, z is the projectile's charge number, m_e is
the electron's mass and β is the relativistic velocity v/c. The model is accurate to proton
energies down to approx. 1 MeV: below that energy, the calculations of the interactions
between the electron shells and the incoming proton are not accurate (Ziegler, 1999).
The various terms and corrections are:

- Fano's calculation of the momentum transferred from the proton to a bound electron
  is summarized in $f(\beta)$ (Fano, 1963). It is defined as

$$f(\beta) = \frac{1}{2} \left(\ln \frac{2 m_e c^2 \beta^2 \Delta E_\mathrm{max}}{1 - \beta^2} \right) - \beta^2, \qquad (1.2)$$

  where ΔE_max is a kinematic term describing the maximum energy transfer from the
  proton to the electron:

$$\Delta E_\mathrm{max} = \left(\frac{2 m_e c^2 \beta^2}{1 - \beta^2} \right) \left(1 + \frac{2 m_e}{m_p (1 - \beta^2)^{1/2}} + \left(\frac{m_e}{m_p} \right)^2 \right)^{-1} \simeq \left(\frac{2 m_e c^2 \beta^2}{1 - \beta^2} \right) \quad (1.3)$$

  Here, m_p is the proton mass. The approximation of Eq. (1.3) is due to the right-
  hand term being very small and introduces and error of below 0.03% in the energy
  range of interest. Combining this, we arrive at

$$f(\beta) \simeq \ln \left(\frac{2 m_e c^2 \beta^2}{1 - \beta^2} \right) - \beta^2. \qquad (1.4)$$

- The mean energy required for ionization of bound electrons is denoted as $\langle I \rangle$. It can
  be calculated using the Local Density Approximation (Ahlen, 1980) and Bragg's
  additivity rule (Thwaites, 1983). However the results are not very accurate (ICRU,
  2016). It is an important factor in the calculation of the proton's stopping power,[*]
  and often the value in water, $\langle I_w \rangle \sim 75$–$80\,\mathrm{eV}$, is assumed for biological tissues.
  However there is still little consensus even on that value (Paul, 2007; Kumazaki
  et al., 2007), with uncertainties in the 10%–15% range (Besemer et al., 2013).

---

[*]In Paganetti (2012) the contribution of I to the range uncertainty is about 1.5%, compared to $\sim$2.4%
when all contributions are added.

- The shell correction C/Z as a correction for the (wrong) assumption that the proton's velocity is far higher than the bound electron's velocity (Fano, 1963). Such corrections must be performed for all the different electron shells around the nuclei. Several attempts have been made at performing accurate calculations of this value using hydrogenic wave functions (Bichsel, 1992), however the results are not very accurate (Ziegler et al., 2015). Another approach is to rearrange Eq. (1.1) and find values for $\langle I \rangle$ and C/Z using experimental values for the stopping power:

$$\ln\langle I \rangle + \frac{C}{Z} = f(\beta) - \left[\frac{S_{\exp} A \beta^2}{\rho K Z z^2} \right] - \frac{\delta}{2} + z L_1 + z^2 L_2. \qquad (1.5)$$

  The result is a correction to the Bethe equation of an order of 1%–6% (less than 1% in the energies and materials relevant to radiotherapy (Grimes et al., 2017)), and the corrections should be accurate to about 1% (Ziegler et al., 2015).

- The density effect correction $\delta/2$ adds a correction which reduces the energy loss at relativistic energies $E > m_p c^2$. Parametrizations or tabulated data may be used to find the magnitudes of the correction (Wyckoff, 1984).

- The zL_1 term is called the Barkas-Andersen correction factor, and describes how the bound electrons slightly rearrange their orbits as a response to the incoming protons. The correction is quite high at low energies, approaching the 10% level at a proton energy of $1\,\mathrm{MeV}$ in a aluminum target. A parametrization is given in Ziegler et al. (2015), which is an empirical fit to experimental data.

- The $z^2 L_2$ is the Bloch-correction, it is necessary to correctly account for a reduction in energy loss at high impact factors (large lateral passing distance between proton and target nuclei), with simple parametrizations by Bichsel (1990).

To summarize, the stopping power of a proton passing through water is visualized in Fig. 1.5 (left). The gradual increase of the stopping power with decreasing energy creates a small area where all remaining energy is deposited (the Bragg peak). The contributions from the various correction terms as discussed above is shown in Fig. 1.5 (right).

It should be noted that by using a proton CT system, the mean value of $S(E)$ in every voxel is measured directly through the average energy loss. This way, all the above-mentioned corrections to Eq. (1.1) are implicitly included. When calculating S from X-ray CT measurements, they must be explicitly accounted for (Schneider et al., 1996), in addition to the several approximations that must be made: no measurements of $\langle I \rangle$, the limited accuracy of some of the above-mentioned corrections and the fact that the relationship between the measured mass attenuation and the required electron density is not one-to-one.
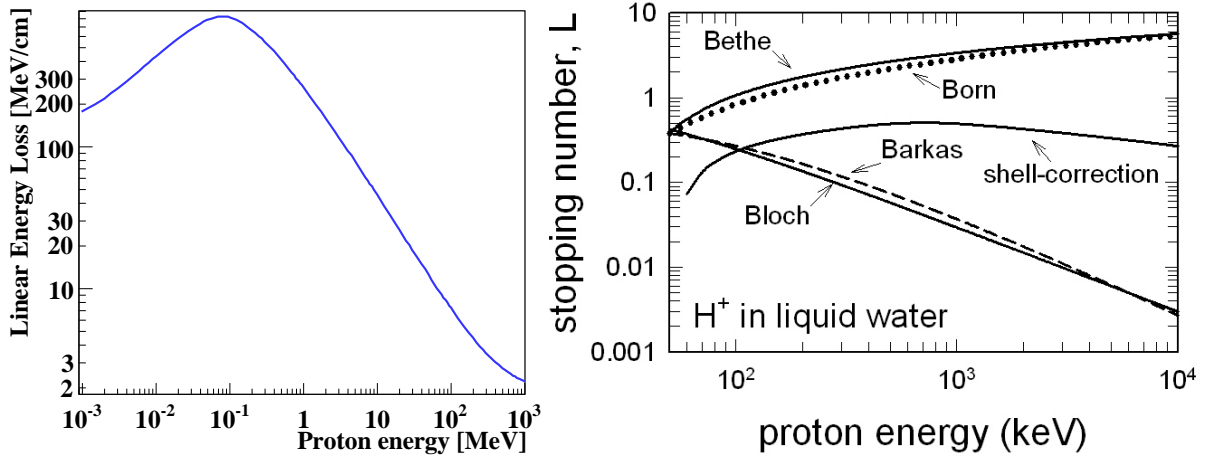
Figure 1.5: *Left: The linear stopping power of protons in water. The underlying data values are from PSTAR. **Right:** Contributions to the stopping power, in units of the stopping number L.* Reprinted with permission from Emfietzoglou et al. (2009).*

1.4.2 Multiple Coulomb Scattering

Protons undergoing elastic interactions with atomic nuclei are deflected gradually for each collision. Following the procedure in Gottschalk (2010), the RMS scattering angle θ_0 for arbitrary thick slabs can be computed from Molière's scattering theory, yielding

$$\theta_0 = \left(\int_0^x \left(\frac{14.1\,\text{MeV}}{pv(x')} \right)^2 \frac{1}{X_0} \mathrm{d}x' \right)^{1/2} \left(1 + \frac{1}{9} \log_{10} \frac{x}{X_0} \right), \tag{1.6}$$

which reduces to the thin-slab Highland formula for small thicknesses x (Highland, 1975):

$$\theta_0 \simeq \frac{14.1\,\text{MeV}}{p_1 v_1} \sqrt{\frac{x}{X_0}} \left(1 + \frac{1}{9} \log_{10} \frac{x}{X_0} \right). \tag{1.7}$$

The different variables introduced here are: x for the slab thickness, X_0 is the radiation length of the material, and pv is the proton's kinematic properties for momentum and velocity. In the simplified equation, it is assumed that the kinematic properties do not change.

1.4.3 The Proton Range

The gradual energy loss of the proton beam ensures that each proton stops in a well-defined area. By integrating the Bethe equation, we obtain the proton range in the so-called *Continuous Slowing Down Approximation* (CSDA). This is the exact path length of the proton, including the angular deflections due to multiple Coulomb scattering, or,

---

*The "stopping number" L refers to the different corrections, L_i, to the Bethe equation of Eq. (1.1). The primary stopping number L_0 is defined as $f(\beta) - C/Z - \ln\langle I \rangle - \delta/2$.

rather, ignoring the effects of the shortening of the projected range due to the scattering. This value is slightly larger than the *projected range*, which is the stopping depth along the proton's original direction.

Due to the complexity of the Bethe equation, such an integration can either be performed numerically (with full knowledge of the different corrections outlined in Section 1.4.1) — yielding data tables such as PSTAR (Berger et al., 2005) or software such as SRIM (Ziegler et al., 2015) — or approximately. In Section 2.2, different approximations of the proton range calculations will be discussed, however for now, a simple and often used approximation can be defined: The range R can be approximated from the initial energy E_0 with

$$R = \alpha E_0^{\,p}, \tag{1.8}$$

with α and p being two parameters found by fitting to experimental data.[*] This approximation is called the Bragg-Kleeman rule (Bragg and Kleeman, 1905).

1.4.4 Water Equivalent Thickness

When a proton is slowed down by traversing through matter, it loses a certain amount of energy. Accordingly, if the proton stops completely in matter, it has thus traversed a certain distance in the material, which is the range, before stopping. The *Water Equivalent Thickness* (WET) of the material is the equivalent thickness of water that is needed to slow down the proton to the same energy, or stop it completely. The WET can be calculated as the ratio of the materials' to the waters' stopping powers and densities (Zhang et al., 2010):

$$\text{WET} = t_w = t_m \frac{\rho_m}{\rho_w} \frac{\overline{S}_m}{\overline{S}_w}, \tag{1.9}$$

where t_w is the water thickness, t_m is the material thickness, ρ_m is the density and $\overline{S}_m$ is the *mean* stopping power of material m. The ratio between the stopping powers are approximately energy independent, however the energy dependence should be taken into account when finding $\overline{S} = \overline{S(E)}$.

Another method, which is the one used throughout this study, is to consider look up tables of energy and range in known geometries. If the physical range is known, a look up table for the energy is needed in order to obtain that range, and, find based upon this, the range in water corresponding to this energy. By this method, the energy dependency of the WET is taken care of implicitly. In Section 2.2, we see that this WET calculation method is highly accurate when using cubic splines to interpolate between values.

---

[*]Often-used values are $\alpha = 0.0022$ cm/MeV and $p = 1.77$ (Bortfeld and Schlegel, 1996). In Section 2.2 the values $\alpha = 0.002\,62$ cm/MeV and $p = 1.736$ were found to be a better fit to the PSTAR data in the therapeutic energy range.

A material's Water Equivalent Path Length (WEPL) is the ratio of the WET to the physical range. It is a value that can be assigned to the voxels of the reconstructed image during a proton CT reconstruction, similar to the approach of assigning RSP values.

1.4.5 Range Straggling

Energy loss by ionization is a statistical process, and it follows that the final range of an ensemble of protons must be distributed with a finite width. From Bortfeld (1997), and, originally, from Livingston and Bethe (1937), we have that the so-called *range straggling* distribution from a mono-energetic proton beam, here a Gaussian with the RMS value σ_R, can be found by combining the Bohr's classical formula and the Bragg-Kleeman range-energy relationship, Eq. (1.8), with the result

$$\sigma_R^2 \simeq e^4 k_e e_d \, \frac{p^2 \alpha^{2/p}}{3 - 2/p} R^{3-2/p} \tag{1.10}$$

$$\sigma_R \simeq 0.0123 \, R^{0.924}, \tag{1.11}$$

with e, k_e and e_d as, respectively, the electron charge, the Coulomb constant and electron density. The factors α and p can be found from the Bragg-Kleeman relationship, and the values $\alpha = 0.002\,62$ cm/MeV and $p = 1.736$ as we will find in Section 2.2 are applied in the second line, as well as $[e^4 k_e e_d]_{\text{water}} \simeq 0.087$ MeV^2 cm. The result is that the range straggling is approximately equal to 1% of the range in water — this rule-of-thumb holds for different media, as well, given that the range is defined as the WET of the slab.

The increase in total range straggling $\sigma_{R,\text{tot}}$ due to a proton beam that has a non-zero energy spread, σ_E, can be included in Eq. (1.11) through the error propagation formula, where $\mathrm{d}R/\mathrm{d}E$ is calculated using the Bragg-Kleeman rule. We get

$$\sigma_{R,\text{tot}}^2 = \sigma_R^2 + \sigma_E^2 \, (\mathrm{d}R/\mathrm{d}E)^2 \tag{1.12}$$

$$= \sigma_R^2 + \sigma_E^2 \alpha^2 p^2 E^{2p-2}. \tag{1.13}$$

1.5 Computational Tools

1.5.1 Monte Carlo Simulations

The main project goals in this study require the information from theoretical calculations, results from experimental measurements in a proton beam line to calculate the expected properties of the planned proton CT scanner. Such properties can be quantifiable entities such as:

i) The spatial resolution, for accurate determination of the proton's most likely path.

ii) The accuracy of the reconstructed stopping power values. This accuracy is here determined on basis of the range resolution of reconstructed proton paths. The range resolution consists of the measurement uncertainty as well as a systematic error (bias).

These fundamental entities will have to be simulated through so-called Monte Carlo (MC) programs and measured experimentally during an optimization of the detector, in order to enable a further development of this detector; with the aim of obtaining a rapid detection and reconstruction of the deposited energy and the tracks of the traversing protons. Physical parameters for the protons will create the basis for these MC simulations: The proton beam energy (direction and momentum), the proton beam spread (the energy and momentum distributions), as well as details about the detector such as pixel size and sampling detector thickness. In addition, detailed information about the imaged body or a simplified phantom is required.

The MC simulations consist of propagating particles through the detailed geometry, during which the incoming protons undergo a high number of randomly (stochastically) distributed fundamental physical interactions. These interactions happen between the proton beam and the traversed materials, thus mimicking the real processes yielding results that can be utilized as benchmark results for later comparisons with measurements and vice versa.

For practical reasons, a *condensed* approach is used, where the average effect of a large number of small interactions is rather calculated on a macroscopic scale. Two such examples are the Bethe theory, where the gradual energy loss from a large number of inelastic Coulomb interactions is calculated as the average energy loss per unit length, and the Molière theory where the average angular deflection resulting from several elastic Coulomb interactions from a slab of the material is calculated. The *step size* is an important concept in MC simulations, which determines how far a particle should propagate before applying the condensed interactions. Another concept is the *production threshold*, which determines when secondary particles should be generated and tracked instead of the energy being deposited locally.

The MC simulation method is a common, powerful and versatile tool widely used in physics research where the study of interactions between ionizing radiation and matter is of importance. MC is a a valuable tool during the development and design phases of detectors due to its ability to assess the optimal design parameters prior to experimental efforts.
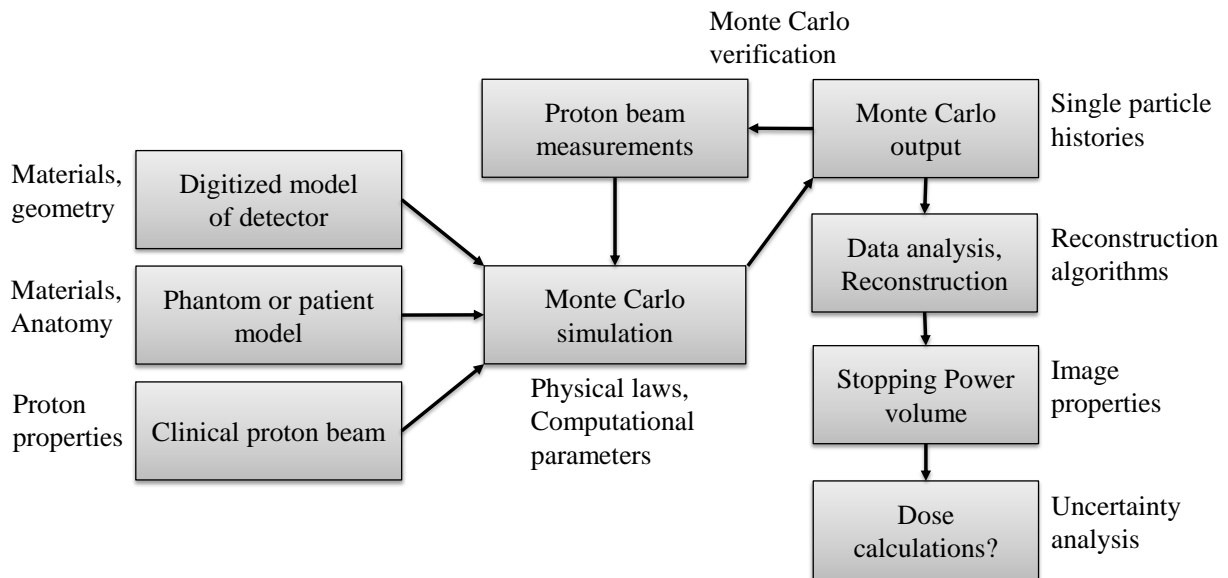
Figure 1.6: *The workflow for the Monte Carlo simulations and proton beam measurements.*

1.5.2 Analysis Workflow Using Monte Carlo

The workflow for obtaining the proton stopping power is illustrated in Fig. 1.6. As this diagram shows, the detector will be developed in a mutually dependent and continuous optimization process where the detector functionality is determined, improved and fine-tuned based upon results from both simulations and measurements. The MC simulation criteria, the geometry and setup need to be properly defined. Computational choices such as the interaction step length affect both the accuracy and the running time of the simulation. This process is described later in Section 2.1. The components that need to be defined are described below and in Fig. 1.7:

i) **A proton beam line** to obtain the correct energy spectrum characteristics, as well as the phase space distributions of the high energy protons. In the design optimization phase, as described in Chapter 5, a water phantom of varying thickness modulates a mono-energetic beam to decrease the energy and increase the energy spread in a realistic fashion

ii) **Two particle tracker planes** in front of the patient or phantom. This is usually a two-layer silicon strip detector (Bruzzi et al., 2007). Its omission may be possible, as discussed in Chapter 5.

iii) **The target**, which could be a simple object like a cubic water phantom or more complex geometries to test for basic image quality measures.

iv) **A calorimeter** for particle tracking and energy measurement: The DTC that is the
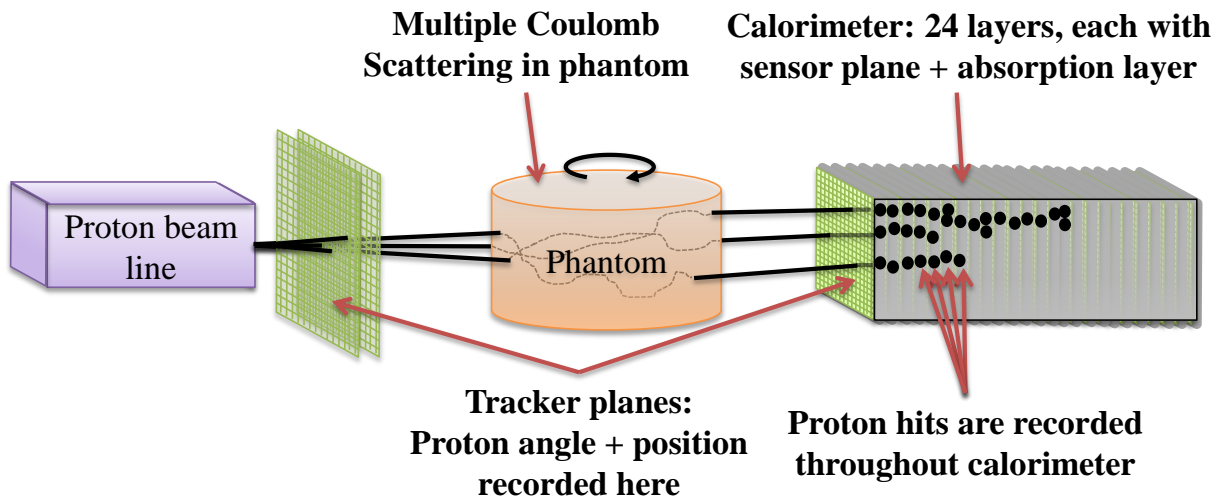
Figure 1.7: *The proton CT setup in the Monte Carlo simulations; The calorimeter (here shown as the ALICE-FoCal prototype) is placed in a virtual proton beam. The protons traverse through a phantom and the calorimeter placed behind the patient. The setup shown must be accurately modeled to match a realistic proton CT system where the path and deposited energy of each proton is used for proton stopping power reconstruction.*

topic of this thesis. The DTC measures the positions and directions of incoming protons, so the separate tracker planes distal to the patient are included in the tracking calorimeter.

In the DTC, each proton passing through one of the many pixels has a probability of registering as a *hit* in the pixel, which is a yes/no value. In the simulations, this behavior can be modeled to obtain a realistic detector response.

From the energy loss and proton tracking information in the tracking calorimeter; including proton tracking information from the additional tracking planes before the object, the complete proton path through the object needs to be reconstructed. There are algorithms to do this (Rit et al., 2013): These models use the limited information about entry and exit position and angles to reconstruct the complex path of the proton through the body.

With knowledge of the proton path through the object, the volumetric proton stopping power map can be reconstructed. Filtered Back Projection algorithms generalized from X-ray CT exist (Li and Liang, 2004), but they are noisy and poorly represent the imaged body. More advanced reconstruction methods must be considered (Penfold, 2010) before the image quality is of clinical value, and can be compared to clinical proton stopping power maps converted from X-ray CT.

1.5.3   Analysis Software

The MC program GATE (Geant4 Application For Tomographic Emission) is an application of the `C++` based MC framework Geant4 (Agostinelli et al., 2003). The GATE package is applied in the MC simulations as it simplifies the usage of Geant4, as well as adding features for simulations of detector functionality, such as the possibilities for simplified geometry building, readout logistics and triggering systems. The input to GATE is given through macro files which require no compilation before being executed.

At the end of a run involving hundreds of thousands of individual particle histories, the resulting output is saved to a file readable by simple graphing tools or through more advanced analysis suites such as ROOT (Brun and Rademakers, 1997). ROOT is an analysis framework distributed freely as a `C++` library. It includes functionalities such as file I/O, efficient data containers, least-squares fitting and powerful visualization tools.

See Section 2.1 for a comparison of the output from GATE as described above with other MC software packages such as MCNP6 and FLUKA, as well as with experimental and semi-empirical data from PSTAR and Janni (Janni, 1982).

1.6   Research Objective

In this introductory chapter, we have clarified the need for a clinical realization of a proton CT system. The main motivation for this is the reduction of treatment margins that are applied during proton therapy, thereby reducing the probability of development of secondary cancers and other side effects following proton treatment.

While several groups have designed prototype systems, proton CT is not currently available for clinical use, and there is little consensus regarding the optimal design specifications or technological base for a clinical proton CT. To this end, the research objectives behind this doctoral project are based on the benchmarking of a prototype tracking calorimeter for proton CT purposes, and can be summarized as

i)   Develop analysis tools for using a prototype tracking calorimeter in a proton CT context. Specifically, modeling of the in-pixel charge diffusion process for energy deposition calculations, the development and implementation of a proton track reconstruction algorithm and development of a range calculation scheme in order to obtain an accurate range calculation of each recorded proton in the proton beam.

ii) Perform experimental proton beam tests using the prototype tracking calorimeter from the ALICE-FoCal experiment and apply applicable post-processing and calibration. Model the geometry and perform MC simulations to complement the experimental data.

iii) Apply the analysis methodology from (i) on the experimental and simulated data, to benchmark the prototype tracking calorimeter in terms of range resolution, track reconstruction efficiency and limitations on the possible proton track densities that can be reconstructed.

iv) Apply the experience from (iii) together with MC simulations to propose a design for the next prototype tracking calorimeter, optimized specifically for proton CT. Find the expected relevant properties of the system, compared to the to existing prototype and to the requirements for a proton CT.

The work described in this thesis is an integral part of this larger collaborative project, where the required simulation and analysis framework to reconstruct the tracks originating from high-energy protons entering and then stopping inside the detector has been developed. This work has demonstrated the feasibility of the prototype Digital Tracking Calorimeter in the context of proton CT, in addition to revealing present shortcomings in terms of range resolution and readout speed (this due to its original design specification as a prototype High Energy Physics instrument).

1.7 Thesis Overview

Two studies seeking to validate the calculation tools and software applied in this thesis have been performed: First, the accuracy of the MC programs MCNP6, GATE and FLUKA is compared to each other and to experimental data.[*] Secondly, different calculation schemes for the individual proton range are compared. Both of these studies can be found in Chapter 2.

The prototype tracking calorimeter is introduced in Chapter 3, together with details on the performed experimental beam test as well as the necessary post-processing and calibration routines applied on the experimental data.

The design of the MC setup, the different parts of the developed analysis framework and the results obtained when applied on the experimental data are described in Chapter 4.

The optimization recommendations of the detector design for the next prototype, as well as the applied methodology, are found in Chapter 5, before ending with a compilation of the results, discussions and conclusions.

---

[*]Due to the multidisciplinary nature of the work that has been carried out, some specific contributions must be stated explicitly: In the MC program comparison study of Section 2.1, Jarle R. Sølie, Helge E. S. Pettersen and Ilker Meric designed the study and analysis. Jarle R. Sølie performed the FLUKA simulations and compiled the results. Ilker Meric performed the MCNP6 simulations. Helge E. S. Pettersen performed the GATE simulations, analysed the MC data and created the figures.

Chapter 2

Proton Range Calculations: Monte Carlo Simulations and Analytical Models

In the introductory chapter, proton therapy and the concept of the proton CT were described. An overview of the underlying physics was presented as well. Before continuing to the technical details about proton CT and the Digital Tracking Calorimeter, which is the main topic of this work, it is worthwhile to go into detail on some of the tools used in this thesis: Computer simulations using Monte Carlo (MC) software, and various analytical models of the proton range. This chapter consists of two parts:

In Section 2.1, we present a comparison of the results from the MC program GATE with published experimental and semi-empirical data and also with output from similar MC programs: this is done to benchmark the accuracy of the GATE MC program used in this project.[*]

In Section 2.2, we direct the focus towards the accuracy of different analytical and interpolation proton range calculation methods. A comparison of the accuracy of several calculation schemes has been performed. As in the former section, this is done as a check of the validity of the underlying calculations that are performed in this thesis.[†]

2.1 Proton Range Calculations with Monte Carlo Simulations

The results presented in this thesis rely on an extensive application of MC simulations. The choice of the particular MC program to be applied in a research project is often made

---

[*]This work has been submitted to *Radiation Physics and Chemistry* (Sølie et al., 2017).
[†]This work has been published in *Radiation Physics and Chemistry* (Pettersen et al., 2018).

arbitrarily, based on availability or on prior knowledge. In this section, we compare simulation results obtained through different MC programs: the results are compared to each other, and to results from the literature where applicable. In doing this, the physics output from the GATE MC program, which is applied in this thesis, are compared to results from similar software, with the dual purpose of testing the different results with the results from other programs and also to validate the approach by this way of double checking the work with definitions, geometry, and selection of physics and processes to be included in the simulations.

The parameters to be studied are: the proton ranges; the longitudinal and lateral variation of individual proton's ranges, respectively called beam straggling and transverse beam spread (induced mainly by multiple Coulomb scattering); and also the fraction of primary protons lost to nuclear interactions before the protons come to rest in the traversed matter.

2.1.1 Existing Literature

There exist numerous studies with focus on detailed comparisons of different MC programs. The transport of protons grazing a tungsten block has been modeled by Kimstrand et al. (2008), by applying Geant4.8.2, FLUKA2006 and MCNPX2.4.0. There it was found that while the energy spectrum of out-scattered protons agreed between the MC programs, dose-weighted out-scatter probability was highly dependent on user-defined settings, and quantitatively the deviation in out-scatter probability between simulations could reach up to 37%.

Other studies have shown discrepancies in the transverse beam spread between different MC programs and experimental data. Grevillot et al. (2010) reports that GATE underestimates the beam spread, attributed to the multiple Coulomb scattering model applied in GATE. One study (Bednarz et al., 2011) reports discrepancies in the multiple Coulomb scattering algorithms between MCNPX and Geant4, where Geant4 is more accurate in calculating the scattering angles and MCNPX is more accurate in calculating the lateral displacements, when compared to the theory of Molière and of Highland. Another study (Mertens et al., 2010) finds that MCNP overestimates the beam spread in low density (and low Z) targets, suggesting inaccuracies in the scattering cross-sections as a reason for the overestimation. Lin et al. (2017) have investigated the angular distributions of protons, when spread after hitting water and aluminum targets, as well as the Bragg peak position in a water phantom: They found similar inconsistencies in the lateral beam spread between the applied MC programs (FLUKA, Geant4 and MCNP6), but that there was agreement in the calculation of longitudinal Bragg peak positions.

There is little published information available concerning direct comparisons of pro-
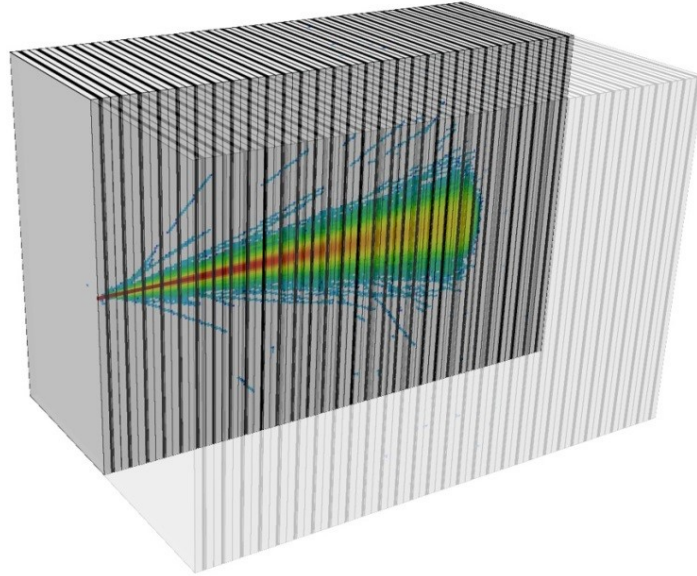
Figure 2.1: *The proton tracking detector geometry consisting of 30 layers, here it is overlaid with a MC simulated primary proton beam consisting of 10^5 protons traversing inside the middle of the detector, creating a shower of tracks of interactions leading to a halt of the protons as their energy is deposited in the detector.*

ton ranges and range straggling between the available MC programs, for studies performed at therapeutic energies. The results here represent an attempt to compare proton ranges and the range straggling calculated by the above-mentioned MC programs in a heterogeneous, layered calorimeter geometry such as the proton CT geometry studied in this thesis.

2.1.2   Monte Carlo Programs

Three general-purpose MC programs have been applied for the comparison: "Geant4 Application for Emission Tomography" (GATE) version 7.2 (using Geant4 version 10.2.2) (Agostinelli et al., 2003; Jan et al., 2004), "Monte Carlo N-Particle" (MCNP6) version 6.1 (Goorley et al., 2013) and "FLuktUierende KAskade" (FLUKA) version 2011.2c.5 (Ferrari et al., 2005).

Semi-empirical data of proton ranges from PSTAR (Berger et al., 2005), as well as data on the transverse beam spread and the amount of nuclear interactions from Janni (1982), are included in the comparisons where applicable. The analysis of the MC simulated data is carried out using the ROOT data analysis framework. The analysis code used in this work is made freely available in a GitHub repository (Pettersen, 2017b).

MC program	Applied physics package	Notes
GATE	`QGSP_BIC_EMY`: Using the "option 3" electromagnetic model.	Mean Ionization potential for water manually set to 75 eV to match PSTAR data tables
MCNP6	Cascade Exciton Model (CEM) for nuclear interactions. Vavilov straggling model for charged particle straggling.	The Bragg additivity rule (Thwaites, 1983) is used to calculate the mean ionization potential for mixtures and compounds.
FLUKA	The physics package `PRESICIO`	Particle transport threshold set at 100 keV. Mean Ionization potential for water manually set to 75 eV.

Table 2.1: *The applied physics packages and parameters of the MC software programs considered in this work.*

Physics Settings

In the simulations of the above-mentioned geometries, the incident proton beam is defined as an infinitely thin pencil beam, having its origin 1 mm proximal to the front surface of the target. The beam is mono-energetic and has no dispersion, with energies in the normal therapeutic span of 50–230 MeV in 10 MeV increments.

The beam consists of 10^5 primary protons for each of the simulated beam energies. The number of primaries per simulation was chosen for the following reasons: First, since many different energies and geometries were to be simulated, the total simulation time needed to be kept manageable. Secondly, the relevant output parameters are calculated from the available data since they are not located in the "tails" of the distributions, and therefore 10^5 primaries per setup was considered to be sufficient. The physics settings for each MC program, chosen with the aim of ensuring that the relevant physics processes and thresholds are accounted for in the simulations, are listed in Table 2.1.

In GATE, the physics builder list `QGSP_BIC_EMY` is applied.[*] This physics list is recommended for MC simulations in proton therapy and in proton imaging due to a variable maximum allowed step size that is decreasing towards and inside the Bragg Peak depth, and a high resolution binning of the pre-calculated stopping power tables (Grevillot et al., 2010; Jarlskog and Paganetti, 2008).

---

[*] `QGSP_BIC_EMY` uses the Quark-Gluon String Pre-compound model (`QGSP`), relevant above 12 GeV, the Binary Cascade (`BIC`) model for nuclear interactions, and high-resolution electromagnetic interaction data (`EMY`).

In MCNP6, nuclear interactions were modeled using the Cascade-Exciton Model (CEM) 03.03 which is the recommended model for nuclear interactions (Goorley et al., 2013). The use of tabulated cross-sectional data was turned off and nuclear interactions were treated using only interaction models.[*] The default Vavilov model for charged particle straggling was used. For multiple scattering, the default Fermilab angular deflection model was used (Mokhov and Striganov, 2002).

In FLUKA, the predefined physics setting PRECISIO is recommended for precision simulations with respect to transport thresholds and activation of processes as described in the FLUKA manual (Ferrari et al., 2005).

It is important to note that a manual adjustment of the ionization potentials of the different materials is possible in both GATE and FLUKA, whereas changing the automatically set, or calculated, ionization potentials in MCNP6 requires access to the source code (Seravalli et al., 2012): thus this has not been done in this work. All simulations using MCNP6 and FLUKA were run in the "proton-only" mode, thus ignoring the transport of all secondary particles other than protons. In GATE, the secondary protons were simulated but discarded during the analysis. This was done to decrease the time required for the MC simulations, and was made possible due to the fact that secondary particles do not contribute to the results obtained here.

Geometries Under Consideration

Three different geometries have been chosen for this study: two homogeneous phantoms consisting of, respectively, water and aluminum, and a more complex detector geometry similar to the proton CT calorimeter described in this thesis. The applied detector geometry is shown in Fig. 2.1, and its materials are listed in Table 2.2.

The water and aluminum phantoms have a cross sectional area of $10 \times 10 \, \text{cm}^2$ and a longitudinal depth of 40 cm, thus stopping all primary protons with energies up to 230 MeV. The more complex detector geometry, with a cross-sectional area of $10 \times 10 \, \text{cm}^2$ and a longitudinal depth of 15 cm, ensures that approximately all protons with energies up to 210 MeV will stop inside the detector. Note that while the energies of above 210 MeV are not applicable in the detector geometry, this limitation in range will not affect the outcome of this study, as the detector is implemented identically in the three MC programs.

---

[*]The tabulated data are only valid below 150 MeV, and models are used for higher energies (Chadwick et al., 1999). By forcing the use of models at all energies, the same calculation method is kept constant throughout.

Volume element name	Material	Thickness [µm]
Sensor Chip	Silicon	120
Glue	Silver glue	80
PCB	Cu / SiO$_2$ epoxy	160
Glue	Cyano-acrylate	70
Absorber	Aluminum	4300
Air gap	Air	245

Table 2.2: *Description of the geometry representing the proton tracking detector geometry. A single layer is modeled as a $10 \times 10\,cm^2$ and $4.975\,mm$ thick volume made up of each of the materials listed above in the given order. This geometry is sequentially repeated 30 times to obtain the complete detector geometry with 30 layers.*

2.1.3 Comparision of the Parameters Describing the Range Distribution

The coordinates of the *stopping position* of all primary protons are stored during the MC simulations. This is in contrast to the *energy loss* of the proton beam. Fig. 2.2 shows the relationship between the stopping position (range) and the energy loss distribution, as well as some of the parameters to be compared. Gaussian fits are applied to different parts of the obtained dataset, and the following values are obtained:

i) R: The mean value of the normal distribution of the protons' stopping depths, yielding the projected range.

ii) σ_R: The range straggling, defined as the standard deviation of the range distribution.

iii) σ_x/R: The lateral deflection of the stopping position, called the transverse beam spread in Makarova et al. (2017). It is the ratio of the standard deviation of the lateral distribution of stopping positions (measured in the x-direction), σ_x, to the proton range R.

iv) f_{NI}: The fraction of protons that undergo nuclear interactions. f_{NI} is calculated as the ratio of the number of nuclear interactions n_{NI} to the number of primary protons n_{tot}. The n_{NI} and n_{tot} values are found by utilizing the interaction-type metadata in the output files from the respective MC programs.

2.1.4 Comparison of the Results from the Different Simulations

The values for proton range, range straggling, transverse beam spread and the fraction of nuclear interactions have been obtained through simulations with the three MC programs
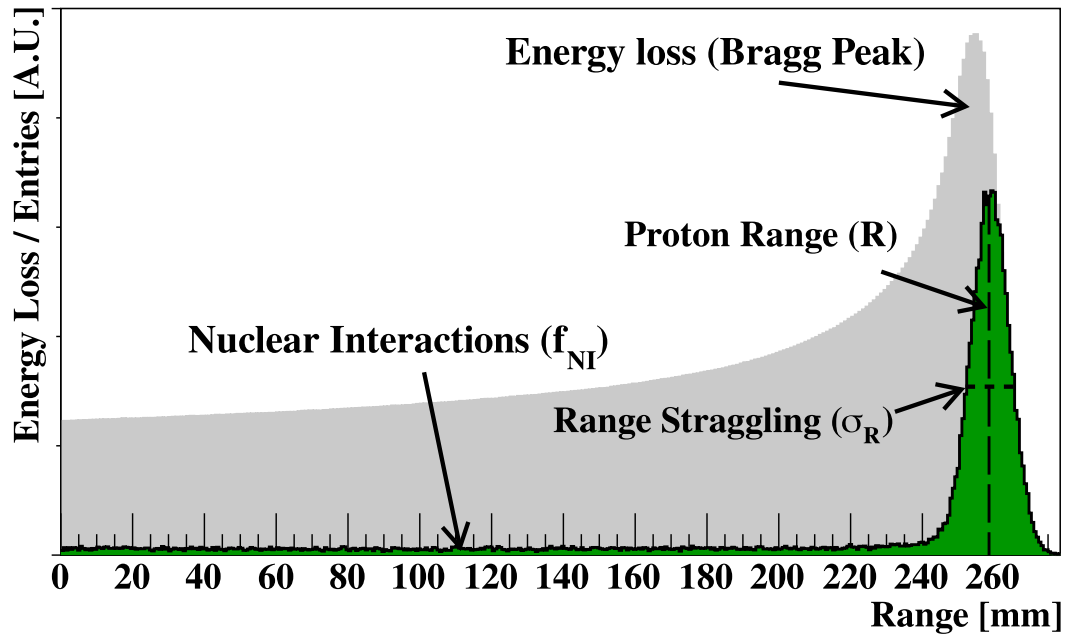
Figure 2.2: *The relationship between the proton beam's energy loss (light gray), and the protons' final stopping position R (green). Shown is also the range straggling σ_R and protons undergoing nuclear interactions. MC simulation results from a 200 MeV beam in water, MC simulated using GATE.*

for the three different geometries: they are listed below.

Proton Ranges

Table 2.3 lists MC simulated R values for a few selected initial primary proton energies, as well as the corresponding R_{PSTAR} values. In Fig. 2.4 (left), the range deviation $\Delta(R)$ is shown: For water and aluminum, $\Delta(R)_{m,i} = R_{m,i} - R_{\text{PSTAR}}$ is shown, where m is the medium, i is the MC program and "PSTAR" is the corresponding projected range from the PSTAR database. For the detector geometry, the deviation from the average results, $\Delta(R)_{\text{D},i} = R_{\text{D},i} - \sum_j R_{\text{D},j}/3$ is shown, as no accurate experimental values are available.

The largest deviation for water, $\Delta(R)_{\text{w}}$, is less than 1.7 mm (0.5% of the range) and $\Delta(R)_{\text{Al}}$ is below 0.2 mm (0.13% of the range). For the detector geometry, $\Delta(R)_{\text{D}}$ is below 0.2 mm (0.15% of the range). While FLUKA and GATE match each other quite well in water, and their $\Delta(R)_{\text{w}}$ values both are below 0.5 mm, results from MCNP6 show a larger range deviation as a function of increasing initial proton energy.

The Value of the Ionization Potential for Water

In Fig. 2.4, it is observed that the deviation $\Delta(R)_{\text{w,MCNP6}}$ is large compared to the $\Delta(R)$ values of GATE and FLUKA. A possible cause for this divergence is the ionization po-

Material	Energy [MeV]	GATE [mm]	MCNP6 [mm]	FLUKA [mm]	PSTAR [mm]
Water	50	22.2	22.2	22.2	22.2
	100	77.0	76.8	77.0	77.1
	150	157.3	156.9	157.3	157.6
	230	328.7	327.4	328.6	329.1
Aluminum	50	10.8	10.8	10.9	10.8
	100	37.0	36.9	37.1	37.0
	150	75.0	75.0	75.3	75.1
	230	155.8	156.1	156.3	156.0
Detector	50	11.1	11.1	11.1	-
	100	37.9	38.0	37.9	-
	150	76.8	76.8	77.1	-
	210	137.0	137.2	137.3	-

Table 2.3: *The proton ranges from MC simulations and PSTAR data for 50, 100, 150 and 230 MeV primary proton energies in water, in aluminum and in the detector geometry. The maximum energy applied for the simulations with the detector geometry is 210 MeV.*

tential of water, I_w, which is an important parameter in estimating the range of protons in low Z materials (Newhauser and Zhang, 2015). Five separate GATE simulations with varying I_w values were performed, and the resulting ranges are compared to the range predicted by MCNP6: Figure 2.3 shows different curves for $R_{w,GATE} - R_{w,MCNP6}$. Where applicable, MCNP6 uses the ICRU49-recommended values for the I of a material (Wyckoff, 1993; ICRU, 2016). For composite materials, MCNP6 uses the Bragg Additivity rule (Thwaites, 1983) to calculate I. The deviation $R_{w,GATE} - R_{w,MCNP6}$ is smallest for $I_w = 73$ eV.

Proton Range Straggling

The obtained results for the range straggling σ_R for some selected primary proton energies are listed in Table 2.4 and the complete MC simulation results are displayed in Fig. 2.4 (right). The values are compared to Janni (available for water and aluminum), and to each other.

The results from all three MC programs show a similar amount of range straggling, with a maximum difference between the MC programs for water at 0.48 mm (12.5% of σ_R), and for aluminum of 0.08 mm (4.5% of σ_R). The largest deviation compared to Janni is seen with the MCNP6 result, perhaps due to the I_w value as discussed above. The MC results in water agree well with the PSTAR values (within 0.1% on average),
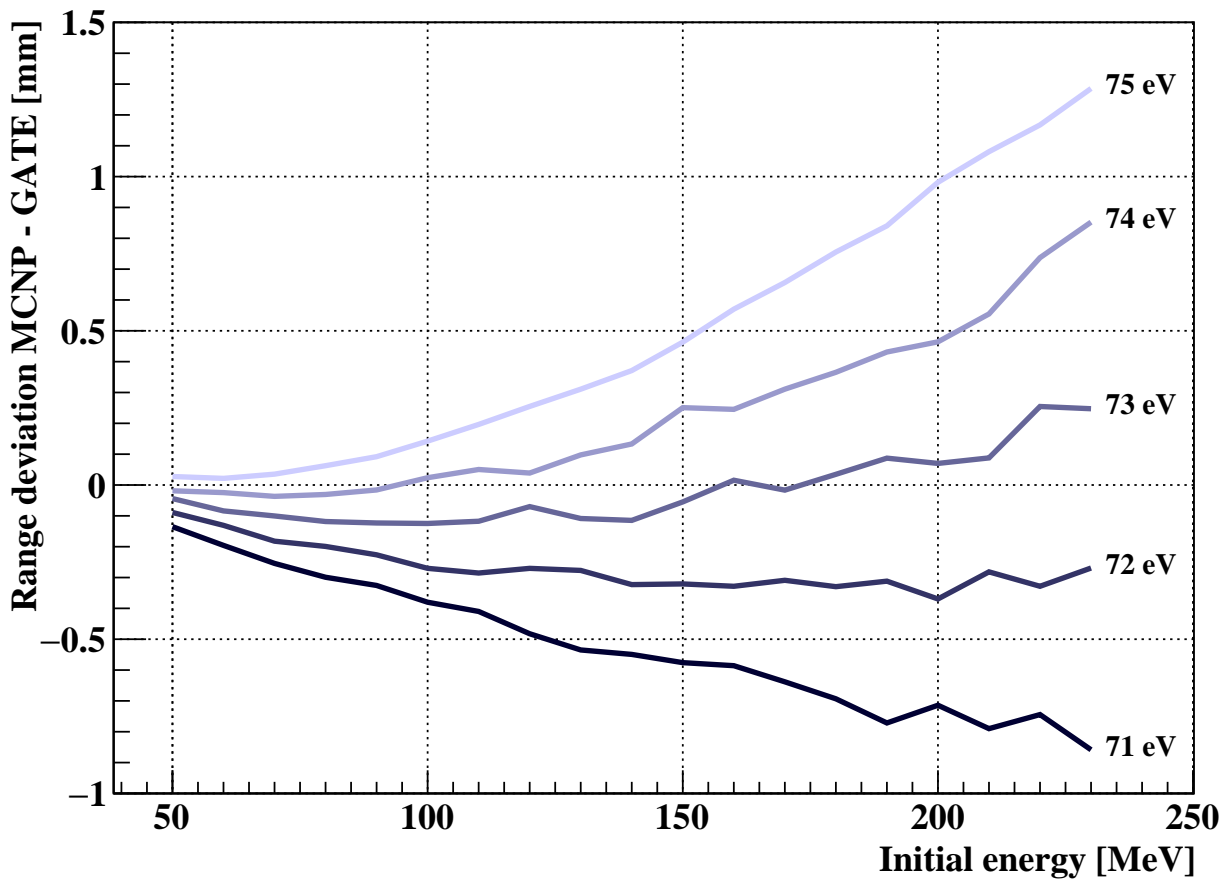
Figure 2.3: *Range deviation between MCNP6 and five separate GATE simulations. The GATE simulations are made using different values of the ionization potential in water, varying between 71 eV and 75 eV.*

and within 4% on average in aluminum. For the detector geometry, the largest difference between the MC programs is 0.24 mm (13.7% of σ_R). A higher variation in the range straggling is observed in the detector geometry, this is perhaps due to its longitudinal structure with different materials, with varying densities and material composition along the longitudinal axis.

Transverse Proton Beam Spread

The obtained results for the transverse beam spread, σ_x/R, are listed in Table 2.5 for some selected primary proton energies. Curves for σ_x/R are shown in Fig. 2.5 (left). There is a good agreement between MCNP6 and FLUKA. However, the results from the GATE simulations are 5%–20% lower compared to the average results from the other MC programs. This can also be seen in Fig. 2.6, where the lateral beam profiles of a 120 MeV proton beam incident on water are compared with respect to the three MC programs.
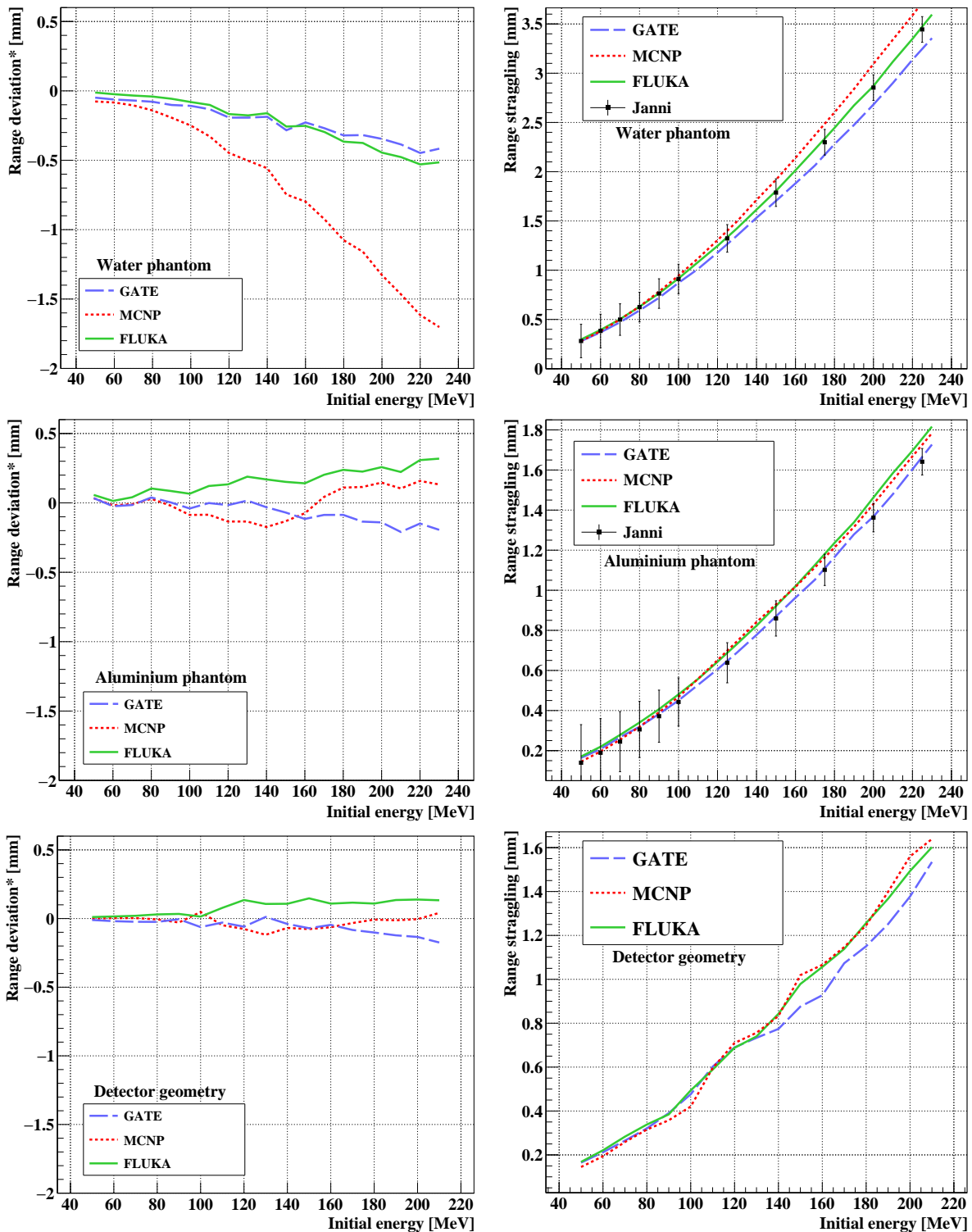
Figure 2.4: *The range deviation in different materials (left). *Range deviation: In water (top left) and aluminum (middle left), the range deviation is the deviation between MC and the PSTAR data. In the detector geometry (bottom left), it is the deviation from the average results from the three MC programs. The range straggling is also shown (right), with corresponding values from Janni for water and aluminum.*

Material	Energy [MeV]	GATE [mm]	MCNP6 [mm]	FLUKA [mm]	Janni [mm]
Water	50	0.25	0.27	0.27	0.28
	100	0.87	0.93	0.91	0.91
	150	1.70	1.90	1.79	1.79
	230	3.36	3.85	3.57	3.57*
Aluminum	50	0.16	0.15	0.17	0.14
	100	0.45	0.47	0.48	0.44
	150	0.87	0.93	0.92	0.86
	230	1.73	1.78	1.81	1.70*
Detector	50	0.16	0.14	0.17	-
	100	0.48	0.42	0.49	-
	150	0.88	1.02	0.98	-
	210	1.53	1.64	1.60	-

Table 2.4: *The range straggling values, σ_R, from MC results and data from Janni. *The 230 MeV values from Janni are interpolated using a spline approach. The maximum energy applied in the simulations of the detector geometry is 210 MeV.*

Material	Energy [MeV]	GATE [mm]	MCNP6 [mm]	FLUKA [mm]
Water	50	0.038	0.046	0.042
	100	0.026	0.033	0.031
	150	0.021	0.025	0.024
	230	0.015	0.016	0.016
Aluminum	50	0.047	0.051	0.052
	100	0.046	0.056	0.053
	150	0.035	0.042	0.047
	230	0.034	0.041	0.039
Detector	50	0.048	0.051	0.052
	100	0.044	0.051	0.048
	150	0.037	0.042	0.040
	210	0.031	0.033	0.032

Table 2.5: *The transverse beam spread σ_x/R from the MC programs. The maximum energy applied in simulations of the detector geometry is 210 MeV.*
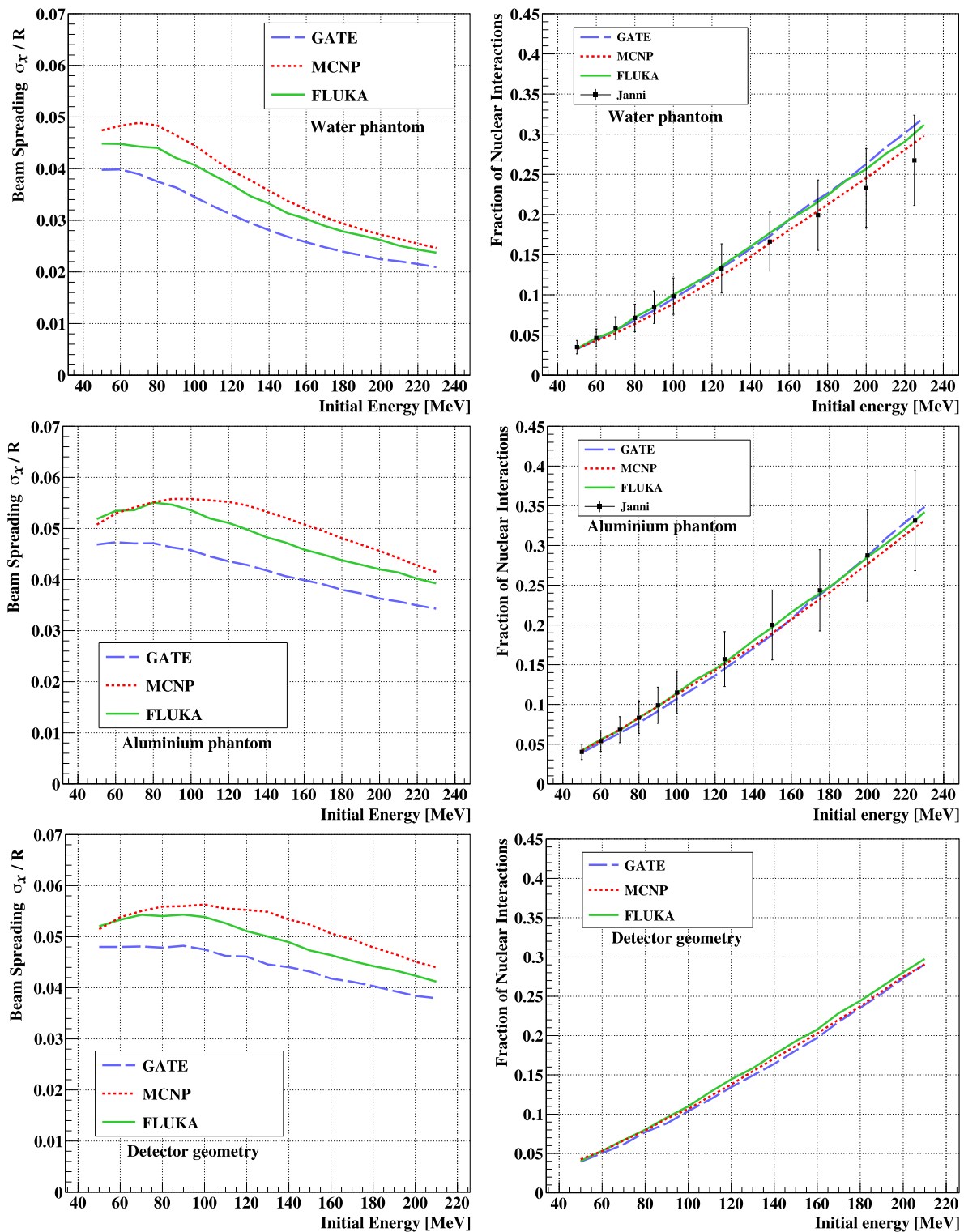
Figure 2.5: *The transverse beam spread σ_x/R, calculated in water (top left), in aluminum (middle left) and in the detector geometry (bottom left). The fractions of nuclear interactions, f_{NI}, are displayed in the right figures for the same geometries together with the data from Janni.*
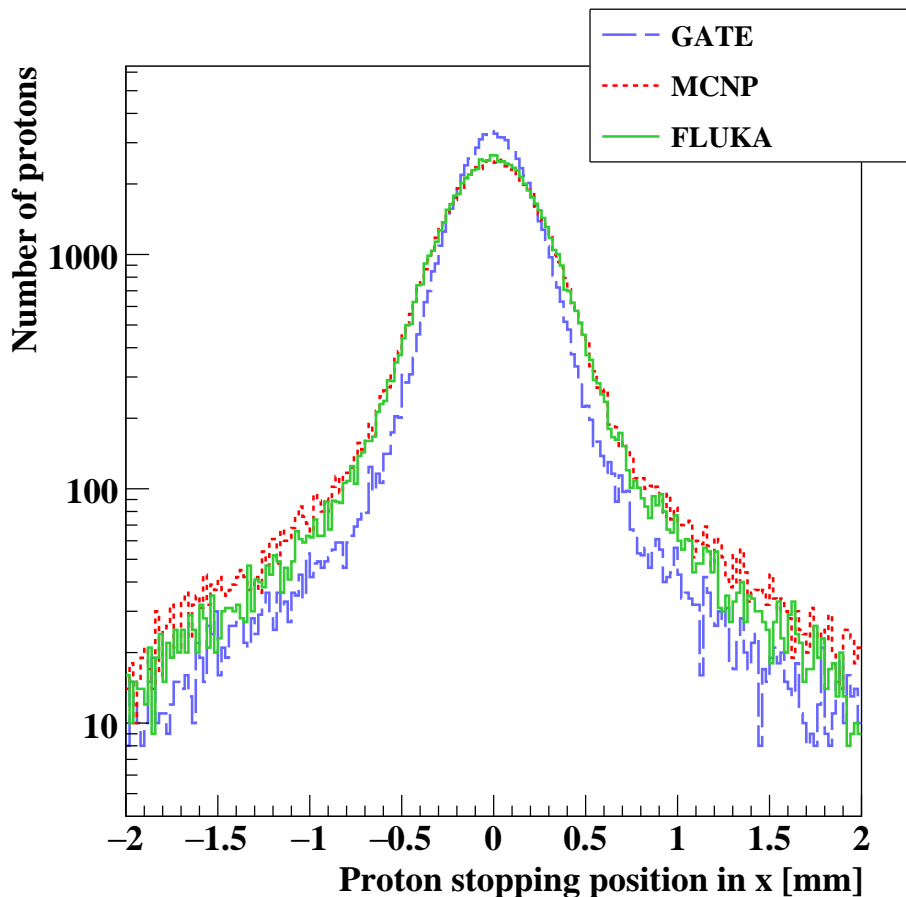
Figure 2.6: *The lateral profile of the Bragg Peak for the three MC programs. The lateral beam spread obtained from simulations with GATE is less compared to the other MC programs, a similar similar to the trend seen in Fig. 2.5 (left).*

Fraction of Nuclear Interactions

The simulated results for the fraction of nuclear interactions, f_{NI}, for some selected energies as well as corresponding data from Janni are collected in Table 2.6 and curves for all energies are shown in Fig. 2.5 (right).

The largest relative deviations of f_{NI} when compared to the data from Janni are 7.5% for water and 6.9% for aluminum. The MC results are on average 6% higher than Janni in water, and 1.3% lower than Janni in aluminum. For the detector geometry, the largest deviation between the MC results is 6.2%.

2.1.5   Stochastic Uncertainty of the Monte Carlo Results

In Tables 2.3 to 2.6, no results are presented that quantify the uncertainty of the values from the MC simulations. The uncertainty of the results are denoted as $\sigma_{fit}(R)$, $\sigma_{fit}(\sigma_R)$, $\sigma_{fit}(\sigma_x)$ and $\sigma_{fit}(f_{NI})$. The origin of the uncertainties can be thought to be stochastic uncertainties, uncertainties from the choice of histogram bin sizes and uncertainties from

Material	Energy [MeV]	GATE	MCNP6	FLUKA	Janni
Water	50	0.032	0.033	0.033	0.035
	100	0.096	0.089	0.100	0.098
	150	0.173	0.164	0.178	0.166
	230	0.321	0.298	0.312	0.274*
Aluminum	50	0.041	0.042	0.044	0.040
	100	0.108	0.113	0.116	0.115
	150	0.188	0.190	0.197	0.200
	230	0.348	0.331	0.340	0.340*
Detector	50	0.040	0.043	0.041	-
	100	0.104	0.106	0.110	-
	150	0.181	0.187	0.193	-
	210	0.291	0.291	0.297	-

Table 2.6: *Fraction of protons undergoing nuclear interactions. The maximum energy applied in simulations of the detector geometry is 210 MeV. Also given are the corresponding values from Janni in water and aluminum. *The 230 MeV values from Janni are interpolated using a spline approach.*

any non-Gaussian contributions.* They are here calculated by error propagation of the obtained fit errors of the parameters from the `TMinuit` fitting tool.

Uncertainty of the MC Proton Range

The uncertainty of the proton range is obtained directly from the `TMinuit` library as the error in the fitting of the normal distribution to the data. In aluminum and water, the relative range error $\sigma_{\text{fit}}(R)/R$ is always below 0.01%. In the detector geometry, $\sigma_{\text{fit}}(R)/R$ is below 0.1% for all initial energies.

Uncertainty of the MC Range Straggling

The uncertainties of the range straggling are similar to the uncertainties of the range. The absolute range straggling values σ_R are smaller, thus the relative uncertainty is increased. The relative errors, $\sigma_{\text{fit}}(\sigma_R)/\sigma_R$, are below 1% in aluminum and in water, and below 5% in the detector geometry for all initial energies: this higher uncertainty is most likely due to the longitudinally more complex structure of the detector.

---

*A non-Gaussian contribution to R, for example, would be elastic scattering events that cause a proximal asymmetry in the projected range.

Uncertainty of the MC Transverse Beam Spread

The uncertainty of the transverse beam spread, $\sigma_{\text{fit}}(\sigma_x/R)$, is calculated by propagating the errors from the values that enter into its calculation. We arrive at the error calculation

$$\sigma_{\text{fit}}(\sigma_x/R) = \sqrt{\left(\sigma_{\text{fit}}(\sigma_x)\frac{\partial(\sigma_x/R)}{\partial\sigma_x}\right)^2 + \left(\sigma_{\text{fit}}(R)\frac{\partial(\sigma_x/R)}{\partial R}\right)^2} \tag{2.1}$$

$$= \sqrt{\frac{\sigma_{\text{fit}}(\sigma_x)^2}{R^2} + \frac{\sigma_{\text{fit}}(R)^2\sigma_x^2}{R^4}} \tag{2.2}$$

Using the values obtained above for $\sigma_{\text{fit}}(R)$ and $\sigma_{\text{fit}}(\sigma_x)$, the relative uncertainty of the transverse beam spread, $\sigma_{\text{fit}}(\sigma_x/R)/(\sigma_x/R)$, is consistently below 0.5% for all the energies and for all the media studied here.

Uncertainty of the Fraction of Nuclear Interaction Values

The uncertainty of the fraction of nuclear interactions, $\sigma_{\text{fit}}(f_{\text{NI}})$, is calculated by error propagation on the Poisson uncertainty of n_{NI}. We find

$$\sigma_{\text{fit}}(f_{\text{NI}}) = \sigma_{\text{fit}}(n_{\text{NI}})\frac{\mathrm{d}f_{\text{NI}}}{\mathrm{d}n_{\text{NI}}} = \sqrt{n_{\text{NI}}}\cdot\frac{1}{n_{\text{tot}}} \tag{2.3}$$

The relative error is given as $\sigma_{\text{fit}}(f_{\text{NI}})/f_{\text{NI}} = 1/\sqrt{n_{\text{NI}}}$ and is below 2% in all the geometries and all the initial energies.

2.2 Proton Range Calculations with Analytical Models

In the first part of this chapter we saw that different MC programs are able to accurately reproduce the proton's range at different initial beam energies and in different geometries. For benchmarking purposes and for calibration purposes of proton CT systems, it is important to have an accurate conversion scheme between the ranges and energies of protons. It is, however, impractical to produce energy-range tables of high accuracy for a sufficiently large number of energy steps. The application of analytical models for calculation of the proton range is therefore necessary. In this section, we look at different approaches to calculations of the proton range. The analysis is performed using ROOT 5.34/19, and the applied program code is available through GitHub (Pettersen, 2017c).

Several parametrizations of the energy-range relationship exist, with different levels of complexity and accuracy. The mean range R of a proton beam with initial energy E_0 in arbitrary media can be parametrized with, as an example, the well-known Bragg-Kleeman formula, $R = \alpha E_0^p$. This is a simplification, and the resulting range has thus a limited accuracy. The model parameters are determined through a model fit to data tables from measurements of ranges in phantoms performed during commissioning and

quality assessment of a proton CT system, or during the design by employing MC simulations. The pristine Bragg curve shape of individual proton tracks can also be found as a differentiation of the energy-range parametrization.

Four models are considered in the following section: these are either semi-empirical or based on interpolation. The semi-empirical models are derived from the Bethe equation and fitted to experimental data in order to find the parameters of the particular parametrization scheme. The interpolation-based models use different approaches to interpolate from look-up-tables of tabulated energy-range data.

The four models are evaluated based on their ability to reproduce the proton range in water, and other media, at different energies, and also by comparing their resulting Bragg curves for individual proton tracks.

2.2.1   Proton Range Dataset

High-resolution energy-range tables are created using the PSTAR database. The energy-range tables for water are calculated with 1 μm range accuracy by numerical integration of the total stopping power. In contrast to the MC study of Section 2.1, the range is here calculated in the Continuous Slowing Down Approximation (CSDA) from the PSTAR database, which accounts for the curvature of the proton's path length due to scattering. This choice is made in order to facilitate comparisons with the literature, and also since it is the CSDA values that are obtained by numerical integration of the stopping power. The difference between the CSDA range and the projected range (depth) for a 230 MeV proton is only 0.02%, where the CSDA range is slightly longer.

The material used here, called "liquid water" in the PSTAR database, is defined as having a density of 1 g/cm^3 and a mean ionization potential of 75 eV, similar to the water used in the work described in Section 2.1. High-accuracy range values have also been calculated for A-150 Tissue Equivalent Plastic, aluminum and tungsten: the study has been repeated for these materials to further validate the approach.

It is not in the scope of this study to validate the accuracy of the experimental data from the literature, such as PSTAR, which uses semi-empirical values based on ICRU49 (Wyckoff, 1993); from SRIM (Ziegler et al., 2015); and from Janni (1982). Previous studies, such as Paul (2013), has estimated that the ICRU49 values should be accurate to the 0.5% level, depending on the value of the mean ionization potential I. The question in this study is thus: to which degree are the different models able to reproduce the tabulated data?

2.2.2 Analytical Models of the Proton Range

In order to calculate the proton range *a priori*, it is necessary to perform numerical integrations of the Bethe equation, given here as Eq. (1.1). However, this requires intimate knowledge of the input parameters, many of which exhibit a high level of uncertainty, as explained in Section 1.4. It is also possible to simplify the Bethe equation itself, which has been done in Grimes et al. (2017).

Semi-empirical models

An alternative to the numerical integration of the Bethe equation is to perform a series of approximations in order to obtain a simplified energy-range relationship. Several approximations have been suggested: The Bragg-Kleeman rule is the 1st term of the Taylor approximation. By inverting and differentiating the formula, one finds a simple expression for the energy loss (Bortfeld and Schlegel, 1996). The Bragg-Kleeman rule for a proton's range R with initial energy E_0, and energy loss curve, $\mathrm{d}E/\mathrm{d}z$ with respect to the depth z, is given as:

$$R = \alpha E_0{}^p \tag{2.4}$$

$$E(z) = \alpha^{-1/p}(R - z)^{1/p} \tag{2.5}$$

$$-\frac{\mathrm{d}E}{\mathrm{d}z} = p^{-1}\alpha^{-1/p}(R - z)^{1/p-1} \tag{2.6}$$

Here, α and p can be obtained from the Bethe equation or from model fits to energy-range data. The second analytical model applies a series of exponential terms (Ulmer, 2007) as a more accurate model for range calculations. Two separate approximations are here offered in order to calculate R and $E(z)$, respectively, and differentiation of the latter gives rise to the $\mathrm{d}E/\mathrm{d}z$ curve:

$$R = a_1 E_0 \left[1 + \sum_{k=1}^{N_1} (b_k - b_k \exp(-g_k E_0)) \right] \tag{2.7}$$

$$E(z) = (R - z) \sum_{k=1}^{N_2} c_k \exp(-\lambda_k (R - z)) \tag{2.8}$$

$$-\frac{\mathrm{d}E}{\mathrm{d}z} = \frac{E(z)}{R - z} - \sum_{k=1}^{N_2} \lambda_k c_k (R - z) \exp(-\lambda_k (R - z)) \tag{2.9}$$

The different parameters a_1, b_k, g_k, λ_k and c_k are described in Ulmer (2007). The parameters are here determined by fitting the model to the PSTAR energy-range data. A recommendation for the number of terms was also made in the same study, where $N_1 = 2$ and $N_2 = 5$ yielded a quite good accuracy while limiting the number of parameters to be determined. The same number of terms is therefore applied in this present work.

Data Interpolation Models

Another approach to the energy-range relationship is to directly use tabulated data in order to determine proton ranges at pre-computed energies in geometries of known media. However, interpolation is needed if the required pairs of energy-range data points are unavailable. The same holds for more complex geometries, such as detector geometries, where the tabulated data can be obtained through MC simulations.

Linear interpolation is the simplest interpolation scheme when working with a look-up-table. However, this approach does not account for any curvature of the underlying data. Spline interpolation is performed by calculating (here) a 3rd order polynomial function around each of the data points, linking them in a piecewise fashion. It is possible to extract dE/dz curves from energy-range tables by calculating the range difference between each energy step.

2.2.3   Evaluation Methods of Model Accuracy

In order to obtain the optimal model parameters, and to avoid over-fitting, 150 CSDA range values for protons in water are split into two groups. The training group ($N_T = 25$) is used to find the model parameters, while the remaining control group ($N_C = 125$) is used to evaluate the model calculations at small range intervals. The range values are in the therapeutic range and chosen from beam energies equidistantly spaced in the range 0–250 MeV. An example of the Bragg-Kleeman model is shown in Fig. 2.7, together with data points from both groups. The Bragg-Kleeman model has here a higher accuracy around 120 MeV compared to at around 50 MeV or at 250 MeV. The PSTAR data points are not displayed with their associated error bars, however the PSTAR data is estimated to be correct to within 0.5% (Paul, 2013).

The accuracy of a model is found by comparing each range in the control group to the corresponding model-calculated range at the same E_0. The 75th percentile value of the distribution of deviations between the estimated ranges and the PSTAR ranges is used as a single measure for the accuracy of a model at all energies.

The Bragg curve of a single proton incident in water is obtained from a differentiation of the energy-range relationship. The different parametrizations give rise to energy loss curves of slightly different shapes, which can be compared visually against PSTAR data.

2.2.4   Accuracy of the Models

After performing the model fitting, the resulting parameters for the Bragg-Kleeman model can be compared to those obtained by other studies: see Table 2.7. The parameters from
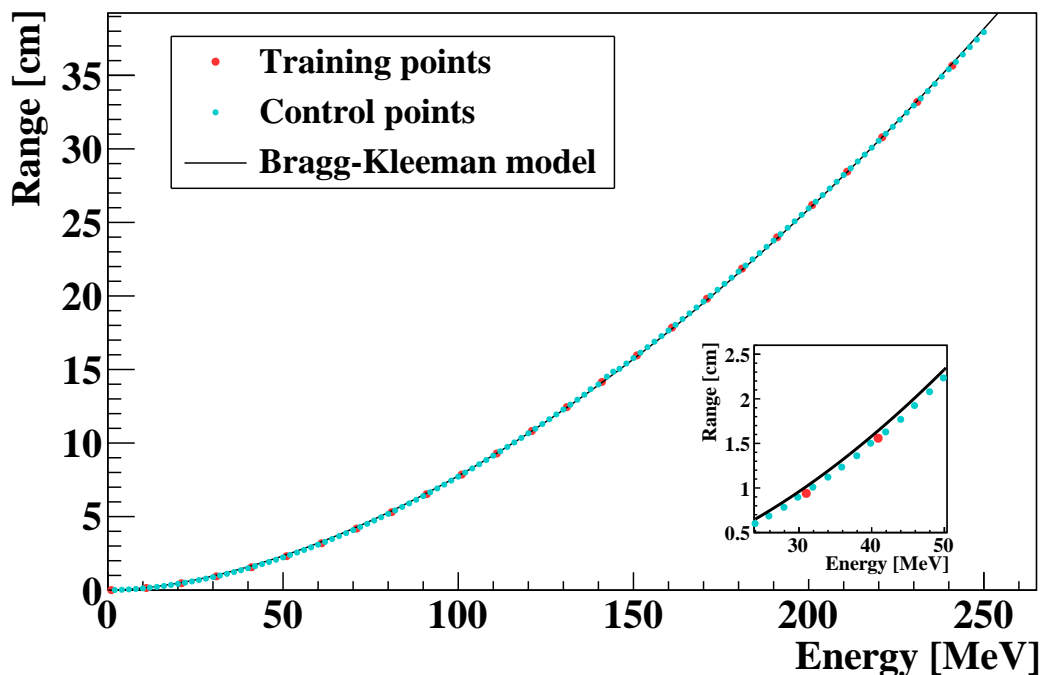
Figure 2.7: *Range as a function of the initial energy, and the PSTAR energy-range data from both the training group and the control group.*
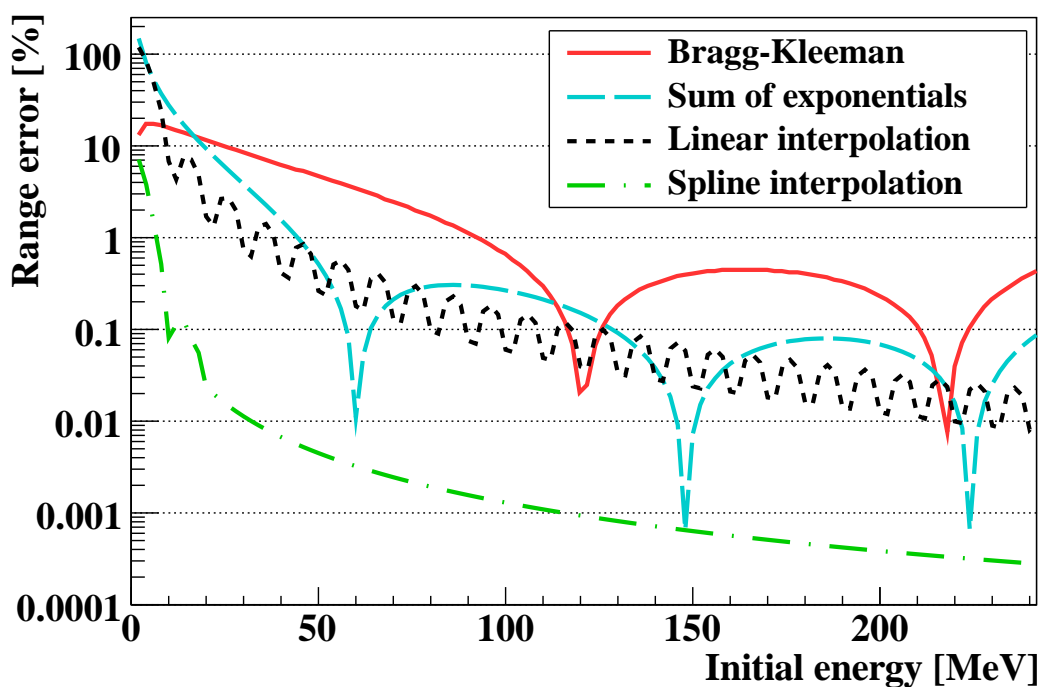
Figure 2.8: *The accuracy of the proton range calculations using different models. The range error as shown is the relative and absolute difference between the estimated range and the PSTAR data. The results are presented with respect to the control group, and are visually limited downwards by the PSTAR dataset accuracy of 1 μm. From Pettersen et al. (2018).*
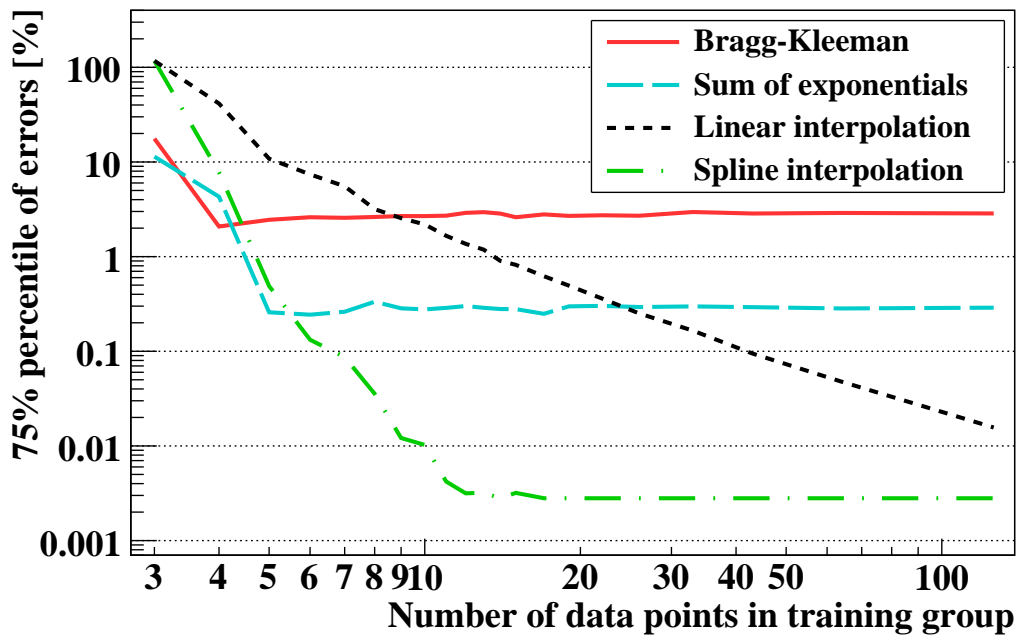
Figure 2.9: *The convergence of the models as a function of the number of data points used for model fitting. The error shown here is calculated as the 75th percentile of all the relative errors as shown in Fig. 2.8 for each of the models. The high accuracy of the spline interpolation is a result of its curvature. From Pettersen et al. (2018).*
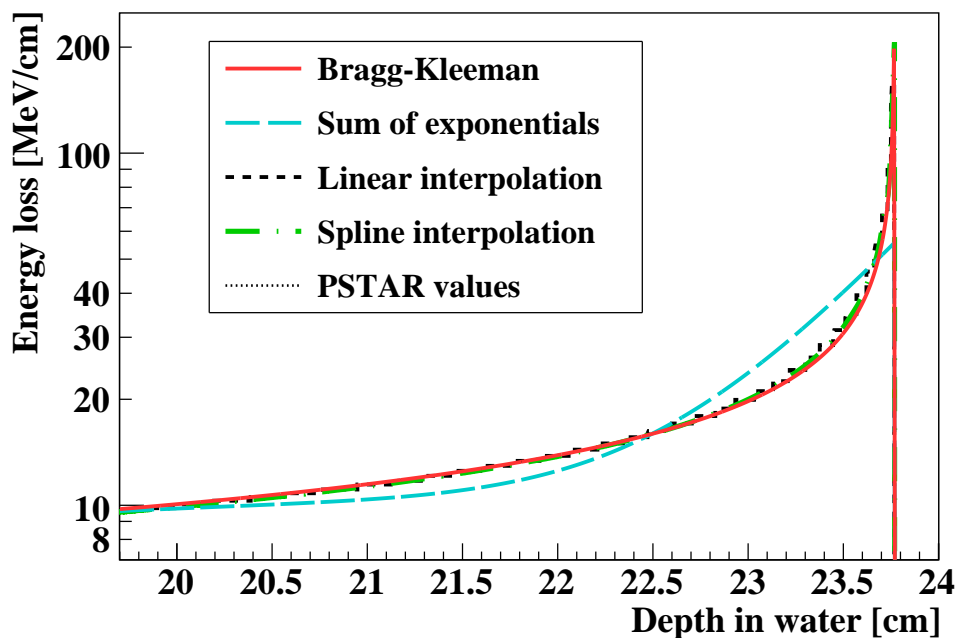
Figure 2.10: *The energy loss curves for individual (190 MeV) protons obtained by differentiating the models obtained with $N_C = 125$. The range is kept constant by the choice of R_0, in order to to facilitate a comparison between the curve shape. A curve showing the PSTAR energy loss data is also included. From Pettersen et al. (2018).*

	α [MeV/cm]	p	Error [mm]
This work	0.00262	1.736	0.69
Bortfeld (1997)	0.00220	1.770	0.85
Boon (1998)	0.00256	1.740	1.50

Table 2.7: *The parameters of the proton range calculation using the Bragg-Kleeman model, with the results found in this work and compared with other results. The (median) error between PSTAR ranges and the model-calculated ranges are included for each parameter set. From Pettersen et al. (2018).*

the fit of the "sum of exponentials" model in are not as easy to compare, due to the many terms linearly added; the values are therefore not reproduced here.

The accuracy of the proton range determination in water using different models is shown in Fig. 2.8, with the 75th percentile accuracy shown in Table 2.8. The Bragg-Kleeman model is the least accurate at a 75th percentile value of 3%. The "sum of exponentials" model and the linear interpolation model have a similar 75th percentile accuracy at around 0.3%, while the spline interpolation model has a 75th percentile accuracy of 0.003%. The spline interpolation model yields the highest accuracy. A sub-percent range calculation accuracy is obtained for all models above 90 MeV, and for the spline interpolation model above 10 MeV.

Energy loss curves resulting from the different models is shown in Fig. 2.10. The method described in this work has also been applied on a sample of other materials. The resulting deviations between the PSTAR ranges of different materials and the corresponding model-generated ranges are similar for the various materials, as shown in Table 2.8.

Range accuracy oscillation

An oscillatory behavior in the accuracy, with respect to the initial energy, is observed for three of the models, as seen in Fig. 2.8. The behavior has two different explanations, depending on the model in question. For the analytical models, the oscillation is due to the approximation of the energy-range relationship. Since the absolute error is shown, a sudden drop in the range error signifies that the model-calculated range curve "crosses" the PSTAR-calculated range curve. In the observed energy range, this happens twice for the Bragg-Kleeman model (with two parameters), and three times for the "sum of exponentials" model (with five parameters). The quick oscillation of the linear interpolation model is seen because the linear approximation does not reproduce the curvature of the underlying data, and thus any interpolated values between two sampled points have higher errors than values close to the sampled points. The spline interpolation model reproduces the curvature, and no similar oscillation is observed.

Material	Bragg-Kleeman	Sum of exp.	Linear interp.	Spline interp.
Liquid Water	2.98%	0.30%	0.26%	0.003%
A-150 T. E. P.	3.02%	0.25%	0.25%	0.003%
Aluminum	2.55%	0.49%	0.26%	0.006%
Tungsten	1.25%	0.36%	0.22%	0.003%

Table 2.8: *The deviation between the PSTAR control values and the model values for the models under study, applied on four different materials: Liquid Water, A-150 Tissue Equivalent Plastic (T. E. P.), aluminum and tungsten. The error shown is the 75th percentile of the absolute error over all energies in the range 1–250 MeV. The number of data points for model training is 25.*

Model convergence

The numbers of training points needed for convergence of the different models are shown in Fig. 2.9. A larger number of measurements at different energies is required for an interpolation-based range calculation scheme compared to using the simple Bragg-Kleeman rule with two parameters, or the "sum of exponentials" with five parameters. Using 25 data points for model fitting, the accuracy is kept at an acceptable level for all models, and the 75th percentile of the errors in the range calculation is at 0.1% of the range for both interpolation schemes and the sum of exponentials.

Bragg Curve Reproduction

The Bragg curves obtained from the interpolations and from differentiation of the Bragg-Kleeman model are similar in shape. The curve obtained by using the "sum of exponentials" model exhibits differences close to the Bragg Peak, mimicking an exponential decay. While the area under the curve is the same (due to that their integrals, yielding the energy-range relationship, are similar to within a few permille), the curve deviates around the true energy loss-curve.

2.3   Conclusions on the Range Calculations

The proton range deviation between the results from the compared MC programs is sub-millimeter in the therapeutic range 50–230 MeV. The exception are the ranges in water from MCNP6, which applies different values for the mean ionization potential for water I_w: the best correspondence between MCNP6 and GATE is achieved when the I_w value in GATE is set to 73 eV. This value is somewhat lower than $I_w = 78$ eV, which is the current recommended value by the ICRU (2016).

Other parameters obtained from the proton range distribution, such as the range straggling, transverse beam spread and the fraction of protons undergoing nuclear interaction, agree with the available experimental results. The results for the transverse beam spread in GATE is lower compared to the other MC programs, a conclusion that is also reflected in other studies.

There are important aspects to be aware of when planning MC simulations and during interpretation of the results (Paganetti, 2012). Awareness should be placed on how different MC programs handle the implementation of their respective models for physics interactions, which can be done either by theoretical models or through interpolation of experimental data depending on the energy region that is studied. In this regard, certain physics models and MC programs can be better suited to model a clinical proton beam than others.

Due to the general agreement between the output values from the different MC programs, the choice of simulation framework may be made on inter-project compatibility criteria, ease of use and the code availability and flexibility.

When comparing the analytical models of the proton range, the spline interpolation model yields the highest accuracy. A sub-percent range calculation accuracy is obtained for all models for energies above 90 MeV, and for the spline interpolation model above 10 MeV.

The simple analytical form of the differentiated Bragg-Kleeman formula is sufficiently accurate to be used as an approximation of the individual proton's energy loss.

The results of this work are applied throughout this thesis: Look-up-tables containing energy-range values are created using MC simulations, to be used in conjunction with spline interpolations. The differentiated Bragg-Kleeman formula is fitted to experimental and MC calculated energy loss values — the result is a high-accuracy range calculation of protons traversing the DTC.

Chapter 3

The Digital Tracking Calorimeter Prototype

In the last chapter, we explored the expected accuracy of proton range calculations using MC simulations and parametric calculation models. Over the next few chapters, the concept of the Digital Tracking Calorimeter (DTC) — application of a layer-by-layer pixel detector for proton CT purposes — will be further described and evaluated, both experimentally and by the use of MC simulations.

In this chapter, the first DTC prototype using the tracking calorimeter from the ALICE-FoCal experiment is described (Sections 3.1 and 3.2), followed by details about the experimental measurements in a proton beam line (Section 3.3) and the required post-processing of the acquired data (Section 3.4).

3.1   The Proof-of-Concept Prototype Detector

A high-granularity digital sampling pixel detector is made available through participation in the ALICE-FoCal collaboration at CERN (Rocco, 2016; Nooren, G. and Rocco, E., 2015). It is one of the proposed upgrades of the detector experiment carried out to provide an electromagnetic calorimeter for measurements of particle distributions at large rapidity. The high pixel granularity allows for discrimination of direct γ and π^0 particles at very high momenta. The detector's small Molière radius of 11 mm enables that the electromagnetic showers originating from the high energy particles can be fully contained within the full calorimeter of 24 telescopic sensor layers, sandwiched between tungsten absorbers. By counting the number of e^- and e^+ particles generated in the electromagnetic showers, the original energy of the incoming particle can be calculated.
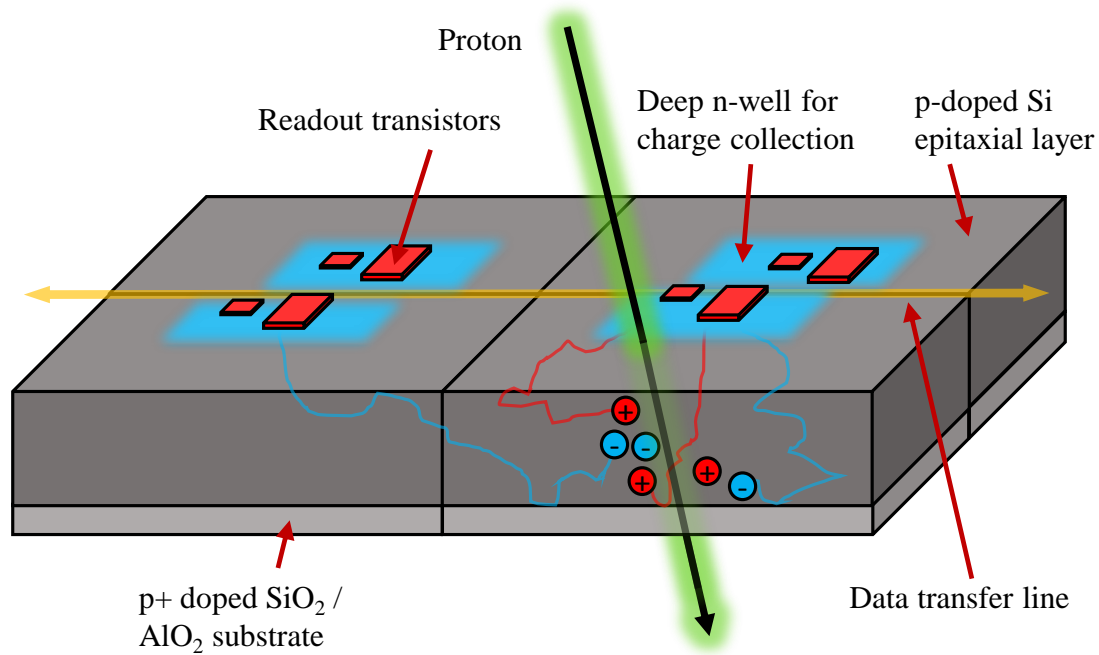
Figure 3.1: *Schematics of a Monolithic Active Pixel Sensor (figure by H. E. S. Pettersen, 2017). Electron-hole pairs are liberated from the traversing charged particle in the epitaxial p-doped silicon layer. The charge carriers diffuse to the deep n-wells in the closest neighboring pixels, where they are collected. The collected charge in the deep n-well is read out through transistors, and, depending on the design, the signal is digitized before being transmitted through the data lines.*

3.1.1   The MIMOSA23 Sensor Chip

The Monolithic Active Pixel Sensor chip PHASE-II MIMOSA23 is applied in the prototype electronics assembly in this work. This sensor is a Complimentary Metal-Oxide-Semiconductor (CMOS) based digital high-granularity pixel sensor, with a schematic design as shown Fig. 3.1. It is produced at the Institut Pluridiscipline Hubert Curien in Strasbourg in France (Himmi et al., 2008). The size of the active area is $19.5 \times 20.9 \, \text{mm}^2$, with a 640×640 array of $30 \times 30 \, \mu\text{m}^2$ pixels. The sensors have three different possible thickness configurations of the active epitaxial layer: $14 \, \mu\text{m}$, $15 \, \mu\text{m}$ and $20 \, \mu\text{m}$. They have a resistivity of either $10 \, \Omega \, \text{cm}$ or $400 \, \Omega \, \text{cm}$. The chips were manufactured with different thicknesses and resistivities in order to assess and quantify their performance with these different parameters.

The pixel data is read out line-by-line: The rolling shutter readout has a cycling time of $642 \, \mu\text{s}$. The readout is 1-bit digital with a programmable signal threshold to adjust for electronic noise. This programmable signal threshold and the sensitivity of the chip are configured by adjusting the voltages on the discriminators. In Nusselder (2014), the op-

timal settings for the two configurable voltages (called "Vref1" and "Vref2") were found by analyzing cosmic muon data. More details about the specifications and performance of the MIMOSA23 chips can be found in Rocco (2016) and Himmi et al. (2008).

Not all of the MIMOSA23 chips used in the experiment were working properly at the time. A fraction of the chips did not transmit any information about which pixels that were activated. The chips were either partially or completely dead, and may have been destroyed due to electronic or mechanical failures, however a possible cause is that the data transfer cables had broken, leading to a non-transmittal of the data. Such cables, rainbow colored, may be seen in Fig. 3.2.

3.1.2   Geometry and Materials

Two MIMOSA23 chips are mounted side-by-side to form a module. Such a module is shown in Fig. 3.2. Two modules are put on top of each other, thus one rotated at 180 degrees with respect to the other, one facing the other, enabling that four sensor chips are placed at approximately the same depth in the longitudinal direction of the detector, i.e. along the central beam axis. There is a 100 µm gap between the two chips in a module, and when two modules are placed on top of each other there is a 90 µm overlap of the sensitive areas of each module. The size of the sensitive area in a layer is $38.5 \times 38.5 \, \mathrm{mm}^2$ orthogonal to the beam direction.

Multiple sensor layers, there are 24 layers in total, are stacked behind each other, interleaved with 3.3 mm thick tungsten plates acting as energy conversion material between the layers. A detailed description of the materials in a single layer is listed in Table 3.1. By using the formula $X_0^{-1} = \sum_i V_i / X_{0,i}^{-1}$ (Olive, K. A. (Particle Data Group), 2014), where V_i are the volume fractions of each material, the resulting radiation length X_0 is 4.2 mm. The total thickness of a layer is 3.975 mm, or around 32 mm WET. The radiation thickness of a single layer is 0.97 X_0. In the first layer, the absorbing material in the front end of the detector is a 0.02 X_0 thick aluminum plate. In this way, the beam is less degraded and scattered prior to reaching the first sensor layer, compared to the situation when applying tungsten.

3.1.3   Detector Mounting and Trigger System

The calorimeter prototype is mounted onto a steel structure containing a system for liquid cooling of the electronics and mounting of the data readout electronics, as well as support for all the patch cables. The steel structure fixes three polyvinyl toluene scintillators to the system. A vertical $1 \times 4 \times 0.5 \, \mathrm{cm}^3$ scintillator, a horizontal $4 \times 1 \times 0.5 \, \mathrm{cm}^3$ scintillator and a $4 \times 4 \times 1 \, \mathrm{cm}^3$ front scintillator were placed, respectively, 17.4 cm, 16.6 cm and 6.5
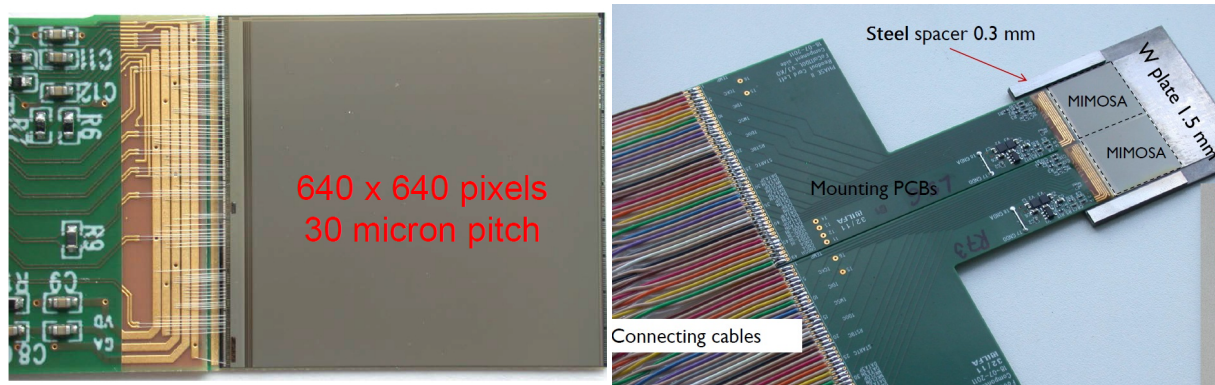
Figure 3.2: *Left: One MIMOSA23 chip connected to the Printed Circuit board (PCB). Right: Two MIMOSA23 chips mounted on PCB which is glued onto a tungsten absorber to form a module. The rainbow-colored readout cables are attached. Reprinted with permission from E. Rocco.*

Material	Thickness [µm]	Radiation thickness [X_0]	Density [g/cm^3]
W absorber	1500	0.428	19.30
Silver glue	40	0.001	3.2
PCB	160	0.002	1.85
Silver glue	40	0.001	3.2
MIMOSA23	120	0.005	2.33
Air gap	170	0.000 006	0.001
W absorber	300	0.086	19.30
Cyano-acrylate glue	70	0.0002	1.0
W absorber	1500	0.428	19.30
Air gap	75	0.000 003	0.001
Total	3975	0.97	17.7

Table 3.1: *The materials and their key properties, as used in the MC setup. The thicknesses are displayed both in terms of the geometric thickness and of the corresponding radiation thickness in units of the radiation length X_0. From Pettersen et al. (2017).*

cm upstream of the front face of the detector. The scintillators are used as suppliers for a trigger signal. Signals in coincidence from the scintillators trigger storage of an event. An image of the detector setup with all the layers and support structures is shown in Fig. 3.3, and schematically also in Fig. 4.1. A more detailed explanation about the setup and trigger logics can be found in Rocco (2016) and Fehlker et al. (2013).
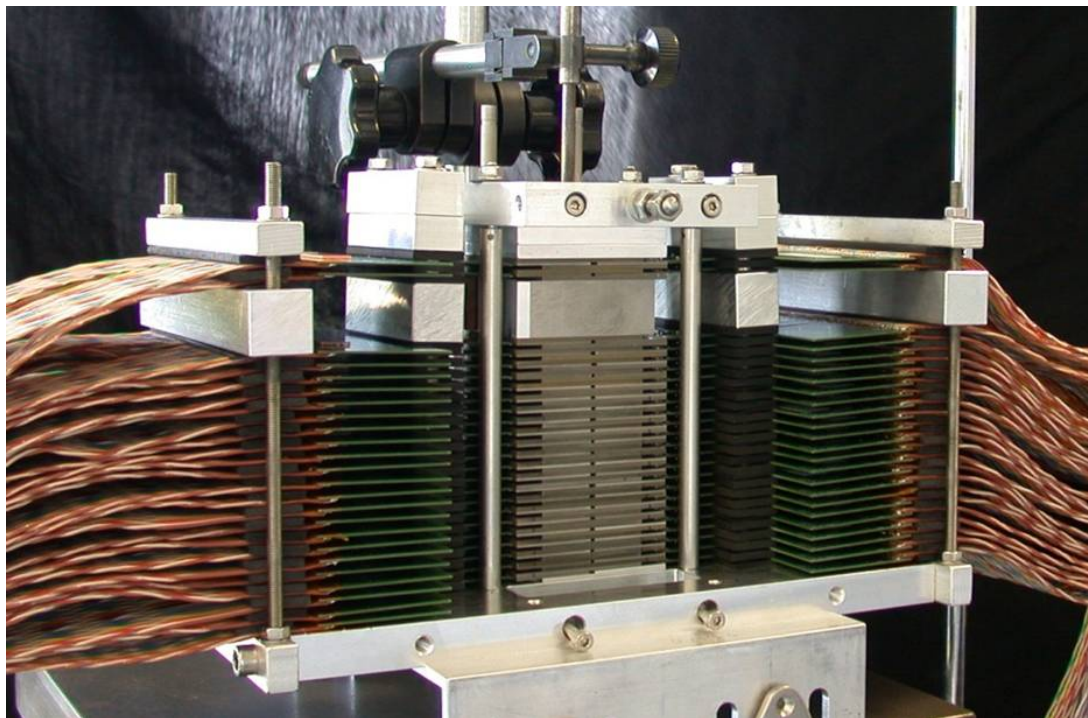
Figure 3.3: *The prototype detector setup. The modules are connected to the flat multi-colored readout cables. These are in turn connected to a patch-panel distribution unit, which facilitates the buffering and transmission of the 61 Gbps signal to FPGAs through the patch cables. The sensor layers are not visible in the figure, these are located inside the central part of the structure. From Rocco (2016).*

3.2   Electronics, Readout and Data Acquisition

The patch cables lead to four 96-port Spartan Field Programmable Gate Arrays (FPGA), which are further connected to two Virtex-6 FGPAs for triggering and multiplexing of the signal. For each readout cycle, 24 layers $\times$ 4 chips $\times$ (640$\times$640) 1-bit pixels are readout. This corresponds to a data size of 4.9 MB. The buffer size of the system is 4 GB, so in total 816 full readout cycles; called frames, can be read out in a single proton spill before the slower data transfer to the Data Acquisition (DAQ) computer is performed.

The 1-bit readout signal gives no information about the intensity of the detected signal from the traversing particles. A noise threshold determines if sufficient charge has been collected in each pixel for the pixel to transmit a signal. This threshold is configurable on a chip-to-chip basis.

The numbering scheme of the chips is: Chip $= 4\times$ Layer $+ q$, where q is the clockwise quadrant. Further details of the readout of this chip can be found in Fehlker et al. (2013).

Since the sensor chips are read out in a rolling shutter-fashion, an important aspect of the data quality is that no frames should be contaminated by earlier or later frames. In other words, when a proton travels through the detector stack, it may be recorded partially

by the current and by the next readout frame. A solution to this lies in the design of the triggering setup: Only events with no trigger signal in the neighboring frames (in time-wise ordering) are stored.

3.2.1 Readout Frequency and Proton Intensity Capacity

The high granularity of the pixels enables a high degree of proton event separation. The cycling time of the rolling shutter corresponds to a readout frequency of 2 kHz. However, a higher effective readout frequency f_{eff} can be achieved by accumulating n_p protons in a single readout cycle: $f_{\text{eff}} = n_p \times 2\,\text{kHz}$. The granularity together with the track reconstruction algorithm determines the saturation limit $n_{p,\text{max}}$. This saturation limit is found through MC simulations. Note that the upper limit $n_{p,\text{max}}$ depends on the spatial distribution of the proton beam. If they are all bunched together in a thin pencil beam, it is not possible to reconstruct as many tracks concurrently as in a uniformly spread out proton beam impinging the whole detector surface, since the *track density* is substantially higher.

3.2.2 Data Format and Conversion

The raw data format from the experiment is a multiplexed data stream containing trigger information and the output of each of the 96 sensor chips. Additionally, pedestal runs with information about sensor noise are also available. These data streams are de-multiplexed and the pedestal noise is subtracted from the readout signal for each of the sensor channels.

   This data conversion was performed on the beam test data during a stay at the Utrecht University in January 2015, by using the conversion software developed by Reicher (2016) at Utrecht University. The resulting output was stored as event-by-event objects containing the sensor layer number and pixel coordinates for each of the activated pixels in the ROOT framework. The output ROOT files were then applied in the analysis described in the following chapter. An example of the output of a partial single readout event (containing a single proton track) is shown in Table 3.2.

3.3 Experimental Test in a Proton Beam

The measurements reported upon in this study were performed in December 2014 at KVI-CART in Groningen, the Netherlands. The cyclotron at the AGOR facility for Irradiations of Materials (AGORFIRM) delivers proton beams with energies from 40 MeV and up to 190 MeV (Van der Graaf et al., 2009). The beam line is shown in Fig. 3.6.

Hit #	1	2	3	4	5	6	$\cdots$	418
Pixel X	308	-311	-313	-314	-320	-321	$\cdots$	-311
Pixel Y	412	-311	-32	-579	-575	514	$\cdots$	362
Layer #	8	5	21	20	0	12	$\cdots$	15

Table 3.2: *Example of the preprocessed output from a single detector event from the 188 MeV proton beam. The full event contained 418 hits (activated pixels), many of which were noise (isolated pixels) and parts of charge diffused pixel clusters where the proton track passed through. The four physical sensor chips correspond to the four quadrants in the coordinate system (-640,-640) $\rightarrow$ (640, 640).*

Energy [MeV]	Number of spills	Run numbers	Chip threshold
120	104	16, 17, 18, 19, 29, 31	$5 \cdot 10^{-4}$
139	12	45	$5 \cdot 10^{-4}$
151	23	43	$5 \cdot 10^{-4}$
160	20	41	$5 \cdot 10^{-4}$
170	112	12, 13, 21, 22, 24	$5 \cdot 10^{-4}$
180	23	39	$5 \cdot 10^{-4}$
188	75	4, 6, 9, 26	$5 \cdot 10^{-4}$
188	33	34, 37	10^{-5}

Table 3.3: *Overview over the beam test experiments performed using the calorimeter prototype at KVI-CART in Groningen. The chip threshold is given in units of fake activation probability per pixel.*

3.3.1 Overview over the Experiments

The beam tests lasted a week, and in the end 46 different experiments (runs) were performed, each run consisting of 5–50 *beam spills*. Of these, 21 consisted of usable data, the remainder being either pedestal (noise correction) data, inadequate proton beam quality or failed data acquisition. The extracted beam energies ranges from 120–188 MeV. An overview over the different runs at the different beam energies are given in Table 3.3.

3.3.2 Beam Specifications

The sensor layers have a surface area of approximately $4 \times 4\,\mathrm{cm}^2$, and during the experiment, the proton beam was shaped to this same field size. The intensity of the beam was set for delivering at most one proton per readout frame, with a detector readout frequency of $1/(642\,\mu s) \simeq 2\,\mathrm{kHz}$. The proton intensity in terms of particle rate is estimated to have been approximately 1350 protons/s, this value is deduced from the finding that
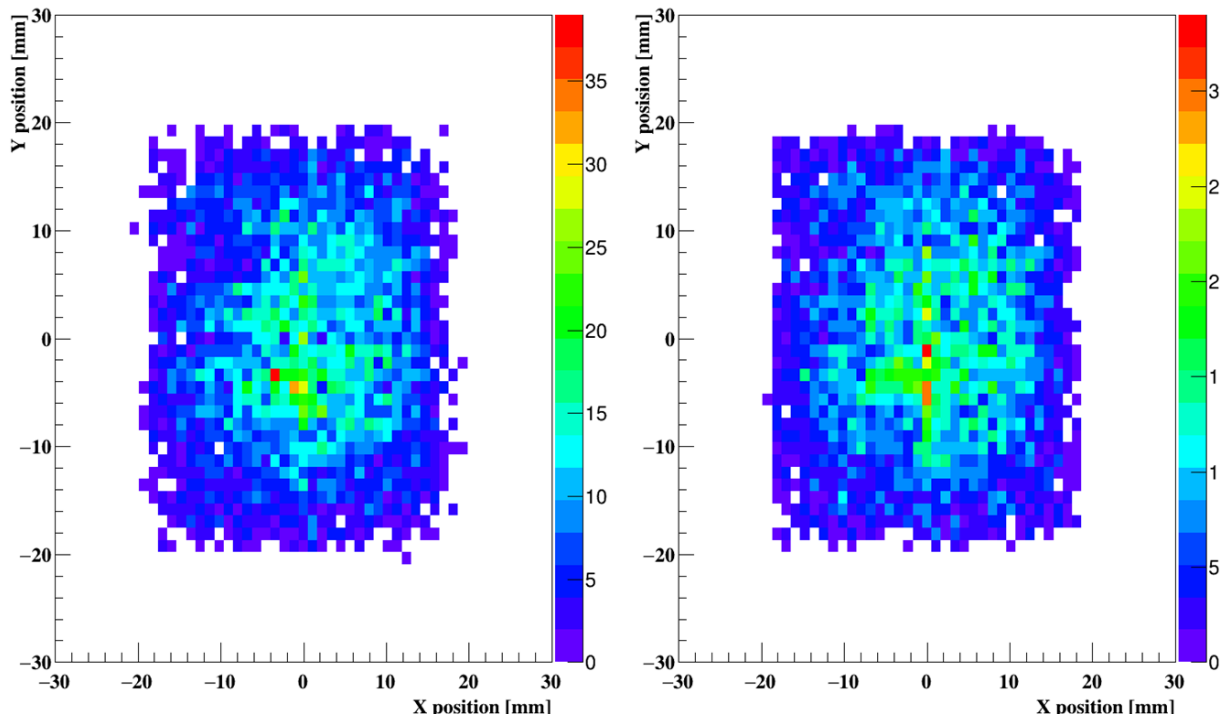
Figure 3.4: *Left*: *Lateral positions of the incoming protons at the front face of the detector.* **Right**: *Lateral positions of the protons at their stopping position inside the detector. Both figures are constructed with experimental data at all the available proton beam energies.*

about 67% of the readout frames contains proton tracks. See Table 3.4 for a comparison between the number of readout frames and the number of reconstructed tracks.

The beam profile at the detector front face, as well as the lateral stopping positions of the protons of all the beam energies is shown in Fig. 3.4. Each entry do not correspond to a hit, but to the position of a reconstructed track. Some features can be seen in the figure: A lower fraction of tracks are reconstructed in the upper right quadrant, this due to a dead sensor chip in that area, and the beam has a slightly increased spread in the deeper-laying layers: this is expected from the scattering.

The spatial distribution of the beam, in terms of the standard deviation of a fitted normal distribution, is 7.5 mm at the front face and 8 mm at the stopping position. This means that the increased beam spread, calculated by taking their quadratic difference, is in the order of 3 mm. Using the integral form of the Highland formula (Eq. (1.6)), we obtain a theoretical value for the scattering angle of $\theta_0 = 126$ mrad. This corresponds to a lateral deviation of 2.95 mm, which is very close to the measured value.

The test beam energies were chosen with the motivation of applying the maximum available energy, and thus measuring the corresponding maximum proton range, in the multi-layered detector. Due to the high Z absorber material, the 188 MeV proton beam is traversing through only the first 7 of the 24 layers: A beam energy of 450 MeV would
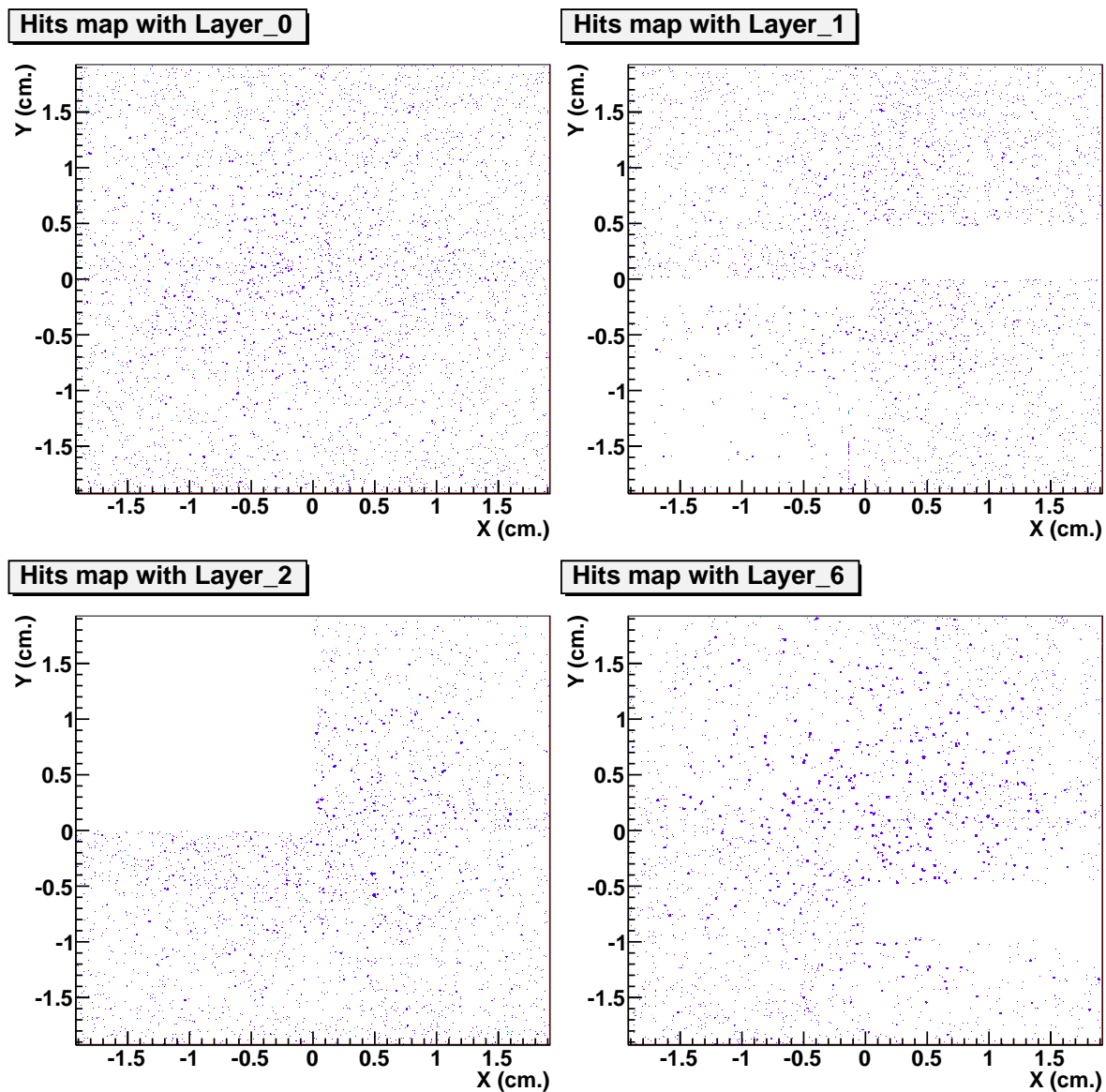
Figure 3.5: *Hitmaps from experimental data at 188 MeV. Each of the four figures represents a four-chip layer: The first three layers and the layer where the proton tracks come to rest. Note that fractional areas or even whole sensor chips do not contain any data: this is due to defect sensor chips, defect data cables or breaks in the connection between them. Note also that the size of the pixel hit clusters increase towards the Bragg peak, this can be due to the increased energy deposition.*

Aluminum degrader [mm]	60	45	35	27	17	8	0
Energy [MeV]	119.9	139.0	150.9	159.9	170.1	180.0	188.0
Energy spread [MeV]	1.4	1.1	1.0	0.9	0.7	0.5	~ 0
Readout frames	3719	241	819	762	4944	1334	2739
Reconstructed tracks	1576	87	408	408	3431	901	2010

Table 3.4: *List of the beam energies applied at the KVI-CART beam test, the number of readout frames as well as the number of reconstructed proton tracks at each energy. Adapted from Pettersen et al. (2017).*
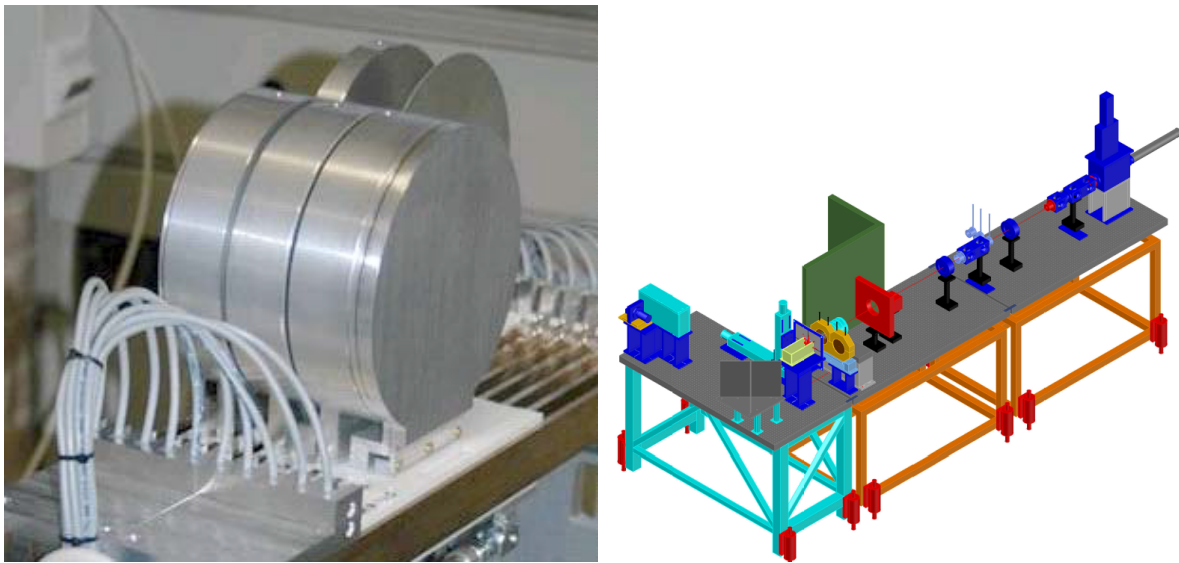
Figure 3.6: ***Left****: The proton beam-energy degrader at the AGOR facility at KVI-CART. Nine aluminum plates can be placed in the beam, controlled remotely.* ***Right****: Schematics of the beam test setup at the AGOR facility. Both figures from KVI AGORFIRM (2012).*

have been needed in order for the protons to traverse the whole detector (all the 24 layers) in the longitudinal direction.

In order to deliver the different beam energies, the beams were degraded by the presence by an aluminum absorber in the beam line. For details about the applied proton beams; energies, as well as the different degrader thicknesses and the number of recorded protons in each of the setups, see Table 3.4. An energy spread of up to 1.4 MeV is introduced by the degradation. This energy spread was calculated using GATE simulations. The energy spread increases with the thickness of the degrader following Eq. (1.11). The beam degrader as well a schematic drawing of the complete beam setup is shown in Fig. 3.6. More detailed beam specifications and the beam optics are described in Van der Graaf et al. (2009).

3.4 Data Post-Processing

3.4.1 Noise

There is a certain amount of unavoidable noise present in the beam test data. Prior to each change of the beam parameters, as well as during the run, pedestal values were read out in order to calibrate the noise level of the individual pixels. The process of pedestal removal on the MIMOSA23 chips is described in Maczewski (2010), and this was performed on the experimental data by using the readout software developed by Reicher (2016) at the time of data retrieval for our present use of the data files.

The clusters generated by the proton tracks typically activate a quite large pixel area due to the charge diffusion processes, as will be described and modeled in Section 4.3. Therefore, it is quite straightforward to remove all the remaining noise, which normally appears as isolated one- and two-pixel clusters.

3.4.2 Threshold Settings

A pixel in the MIMOSA23 chip is activated when its integrated photodiode charge has reached a preset threshold value. The electronic noise in MIMOSA23 has been estimated to be about 10 e^- Equivalent Noise Charge (ENC) (Winter, 2009). The threshold is defined as the signal intensity that is required for a pixel to be activated. In terms of electronic noise, the *fake rate* can be defined, which is the fake activation probability per pixel due to electronic noise. During the beam tests, different threshold values were applied, corresponding to fake rates ranging from 10^{-5} to $5 \cdot 10^{-4}$. A fake rate of 10^{-5} corresponds to 4 pixels per 640×640 chip per readout. This fake rate is equivalent to a signal threshold of about 26 e^- ENC, found by using a Poisson distribution with a noise level of 10 e^- ENC:

$$P(\lambda = 10, k) \approx 10^{-5} \quad \text{for } k = 26 \tag{3.1}$$

The choice of signal threshold determines the charge diffusion cluster size described in Section 4.3. A separate study (Hansen, 2017) uses an analytical model from Maczewski (2010) to determine the diffuse cluster size, this study confirmed the numbers presented in this section.

3.4.3 Chip Sensitivity Calibration

The physical chips exhibit variations in the epitaxial layer thicknesses and resistivities. A thicker epitaxial layer will increase the number of generated charge carriers and the area over which they are able to diffuse: differences in the charge collection area (cluster
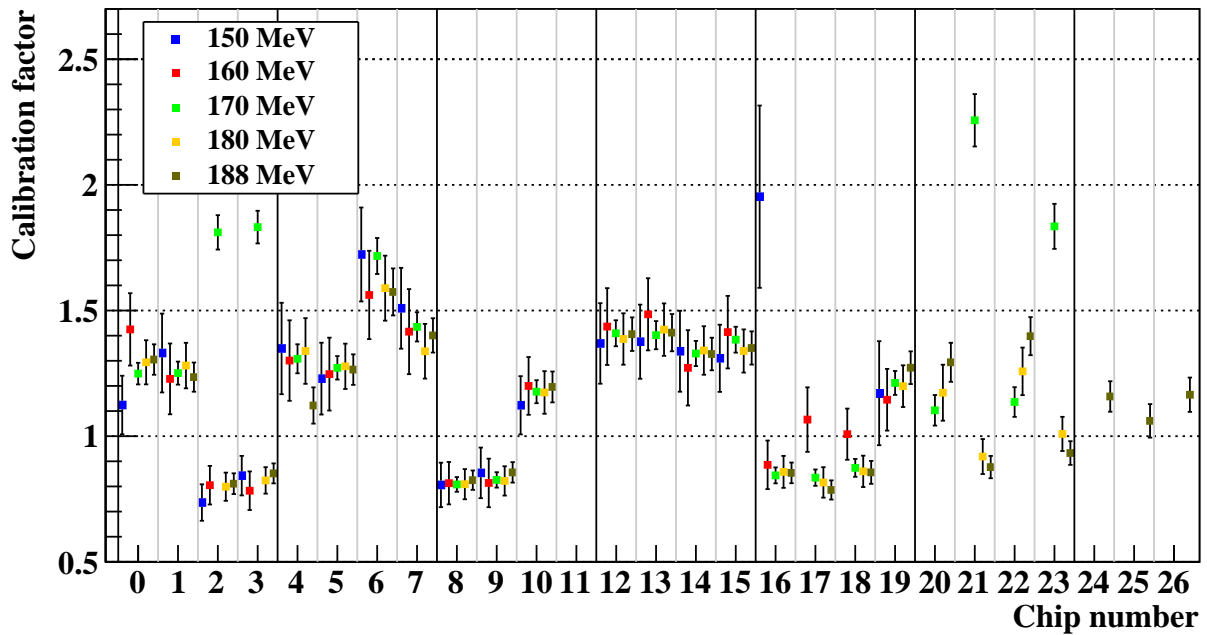
Figure 3.7: *The chip sensitivity calibration factors* $f(Chip)$, *applied for obtaining a relatively uniform cluster size distribution in the different layers. For stability-checking purposes, a set of calibration factors has been made for all datasets at different energies. It is found that the calibration factors have a higher variation in the Bragg peak area for each energy, since it is harder to accurately model the energy deposition when the energy deposition is high.*

sizes) are thus observed. This sensitivity calibration was performed in this project on proton data from the beam test runs.

Calibration of the sensitivity of each chip, i.e. a scaling factor in the E_{dep} calculation of Eq. (4.8), ensures that the responses of the physical chips are uniform throughout the whole calorimeter.

The sensitivity calibration of the sensors was here performed through identification of a scaling factor $f(Chip)$ for each of the 28 chips, corresponding to 7 layers, for which there exists data. In the first few sensor layers, the variation of energy deposition is small, so that the scaling factors for a given layer exhibit low variation between the datasets of different energies. In the Bragg peak regions of the different energies, the energy deposition variation is high, such that there is a lesser agreement between the scaling factors of the different energies. In Fig. 3.7, this is shown through a quite good agreement below chip number 16, and less agreement above.

A study from Zhang (2017) obtains calibration factors for the same detector using data from beam tests with 50 GeV and 100 GeV electrons: the calibration factors are of similar magnitudes to the ones found here.
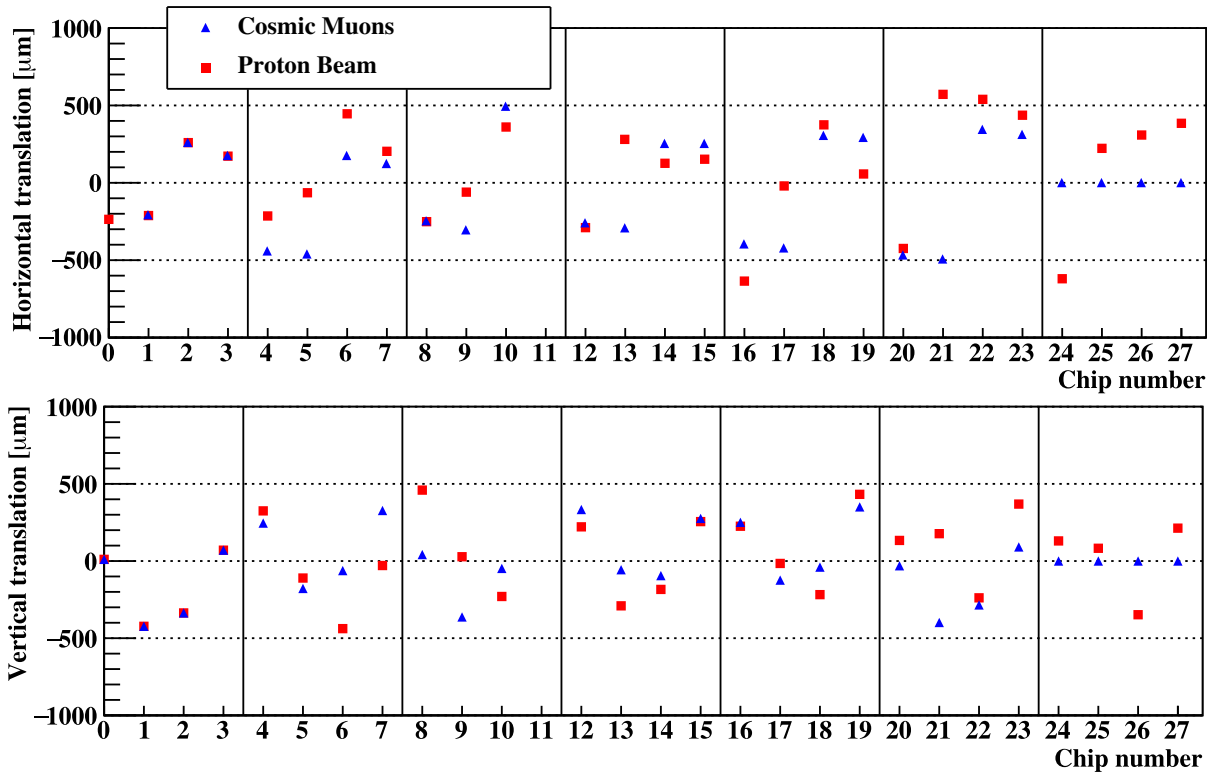
Figure 3.8: *Per-chip correction values applied for the lateral chip alignment, shown here in terms of lateral shifts in the x and y-directions. Values from cosmic muons taken at Utrecht University and from the proton tracks are shown.*

3.4.4   Chip Alignment Correction

In order to correct for misalignments from the fabrication process, the layers need to be aligned in software before the data analysis. Left unaligned, systematic lateral shifts would occur in the proton tracks between each layer, which would reduce the quality and efficiency of the track reconstruction.

Position calibration has been performed at Utrecht University by aligning the tracks of cosmic muons; this has resulted in alignment correction values for each chip. The alignment correction defines lateral shifts and rotations of the chips (Zhang, 2017).

In addition, it was here attempted to recreate the same chip alignment values with the proton beam data, by finding the values that would result in the smallest amount of lateral shift in the reconstructed proton tracks: the implemented method only considers translation and not rotation. The comparison between the two alignment methods is shown in Fig. 3.8: The values obtained using cosmic muons was applied on the experimental datasets for alignment correction.

3.4.5 Dead Sensor Chips

As described earlier, some of the sensor chips used were either completely or partially dead, i.e. they did not transmit any information about the activated pixels. A few examples of this can be seen in Fig. 3.5. In order to account for this deficiency in the data quality, the track reconstruction algorithm (as described in Section 4.4.1) must be able to correct for tracks traversing the dead areas. By extrapolating the track position through the dead areas, proton tracks can still be reconstructed through such regions. However, tracks ending in or near dead areas are discarded due to the importance of their last energy deposition position in the detector when in finding the residual range.

Chapter 4

Benchmarking the Digital Tracking Calorimeter Prototype

In the last chapter we introduced the Forward Calorimeter as a High Energy Physics prototype detector, along with a presentation of number of data post-processing techniques. In this chapter, we will describe the application of this detector for proton CT purposes.[*] The detector is suited for proton CT purposes due to many of its properties, such as the very high pixel granularity (precision), the layer-by-layer geometry (range determination) as well as the fast readout speed (speed matching the clinical workflow).

In this context, the detector and the detector readout system must be able to record data with a high enough quality, enabling the reconstruction of tracks of individual protons, yielding both the proton's initial velocity vector as well as its track length.

We begin with an overview of the software used in the study: the Monte Carlo software in Section 4.1 and the custom analysis framework developed for this project in Section 4.2. This is followed by the data analysis procedures: In Section 4.3 the process of modeling the charge diffusion in the sensor chip is described. The proton track reconstruction process is described in Section 4.4. The resulting reconstruction density capabilities are calculated in Section 4.5. The range calculation of individual and multiple protons are outlined in Section 4.6.

4.1   Monte Carlo Modeling

In the previous chapter we described the geometrical properties of both the DTC and the experimental setup during the beam test, i.e. with scintillator triggers and beam degraders. A MC simulation has been performed of the complete detector setup including the above-mentioned components, as described in Section 3.1.3. The MC software

---

[*]The results from this chapter have been published in Pettersen et al. (2017).
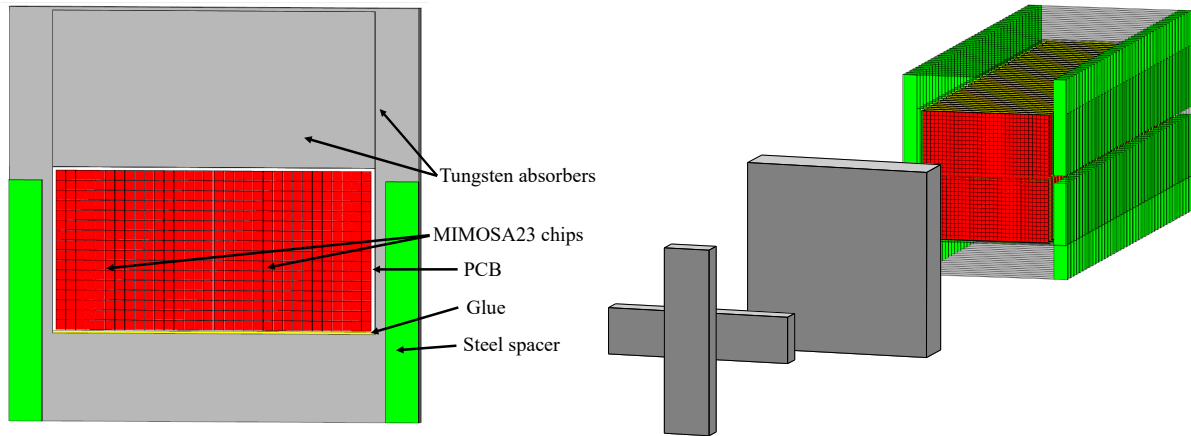
Figure 4.1: *Left: The MC implementation of a detector module.* ***Right****: The complete calorimeter consists of 24 sensor layers, also included are the three scintillators located upstream of the prototype detector. From Pettersen et al. (2017).*

GATE 7.0 for Geant4 9.6.4 was applied for this purpose.

Results from many different GATE simulations have been applied when developing the analysis framework. The same analysis methodology is applied to results from both MC simulations and experiments, the only differences being the readout format and whether or not the charge diffusion model described in Section 4.3 should be applied.

4.1.1   Geometry Implementation in GATE

The geometry applied in the simulations consists of three scintillators and the prototype DTC detector. The geometry of the detector setup is described in Section 3.1.3 and has been implemented in GATE accordingly. The detector setup as visualized in GATE is shown in Fig. 4.1.

Physics Builder List

In Section 2.1 different MC programs were presented, together with examples of how the physics settings were setup. The GATE program as applied in this chapter is set up similarly, using the `QGSP_BIC_EMY` physics builder list.

The values for the production thresholds are set to 0.1 mm, i.e. a new particle from a decay or collision is required to have an energy corresponding to at least this value in order for the particle to be generated, otherwise the energy is deposited locally. The minimum proton step size is set to 0.05 mm, and it decreases towards the Bragg peak depth. The adjustable mean excitation potential for water is set to $I_w = 75$ eV to match the I_w value used in the PSTAR data tables.

Beam Modeling by the use of a General Particle source

The proton beam at KVI-CART was described in Section 3.3. The beam model is simplified for analysis purposes (see Section 4.1.2), it is represented by a so-called source in the GATE simulations. The source is defined as a General Particle Source-based mono-energetic beam using the nominal energies of the beam test. The protons are emitted from a square $4 \times 4\,\text{cm}^2$ plane, with no angular deflection.

Monte Carlo Information Through Scoring

The *scoring* describes the variables that are stored during each MC simulation. Every interaction leading to an energy deposition event in a Sensitive Volume (SV) is written to an output file. The epitaxial layers of the 96 separate MIMOSA23 chips, each with a thickness of 14 µm, are defined as separate SVs. In total, there are 41 million pixels in the DTC. If they had all been defined as individual SVs, a rather large number of volumes would have had to be stored in the memory and the simulation performance would have been been degraded in terms of simulation time and memory usage.

Any comparison between MC and experimental data is here performed on a data set from the MC simulation with scoring only in the sensor layers. However, during the development of the analysis tools, it is helpful to have available fully scored MC simulations, so that it is possible to obtain information for calculation of entities such as scattering angles, accurate proton range distributions (lateral and longitudinal) and the distributions of the different interaction types occurring. In Fig. 4.2, an illustration of the two simulations with different scoring strategies are shown. In the simulation performed for the illustration, a 245 MeV proton beam with 50 000 primaries is used, and the DTC detector modeled with 3 mm tungsten energy absorber layers.

4.1.2   Simplifications in the Monte Carlo Design

Several simplifications were made during the design of the MC simulations of the experiment. While the geometry of the calorimeter itself is relatively accurately implemented (including estimations of the energy loss due to the trigger scintillators), no beam optics were included in the simulations.

The beam is implemented as a monoenergetic, uniformly spread proton beam. By ignoring the initial energy spread of the beam (due to the aluminum energy degraders), the uncertainty of the MC reconstructed proton range is only influenced by the detector construction and analysis methodology. The comparison between MC and the experimental data may suffer due to this simplification, however the properties of the detector become more transparent, and this is the motivation for such a simplification in this stage
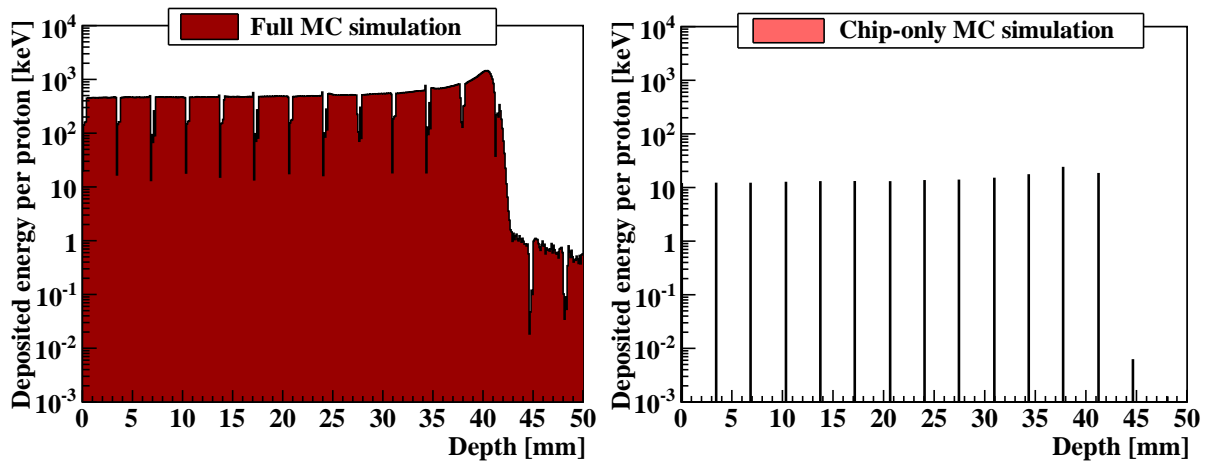
Figure 4.2: *Total energy deposition in "full" simulations (i.e., primaries and secondaries are scored in all volumes) and "chip-only" simulations (i.e., only the epitaxial layers of the sensor chips are scored).*

of the work. The effects on the range uncertainty by introducing a varying energy spread from energy-degrading water phantoms will be discussed in Chapter 5.

The beam is assumed to be uniformly distributed across the $\sim 4 \times 4\,\text{cm}^2$ sensor area in the MC simulations. This in contrast to the collimated, approximately Gaussian distributed beam used in the beam test experiment. This simplification was introduced in order to guide the development of the track reconstruction algorithm, as well as to find reliable numbers for the maximum possible beam intensity or *track density* that is possible to reconstruct with the implemented reconstruction algorithm.

Any variations in the thickness of the epitaxial layer between the different sensor were not implemented. The sensor chips come in different configurations, having 14 μm, 15 μm and 20 μm epitaxial thicknesses: the epitaxial layer of each sensor layer has been defined to be 14 μm. This effect, however, is assumed not to degrade the final data quality: differences in the charge collection sensitivity arising from a variation of epitaxial thickness are reduced through the per-chip sensitivity calibration, which was be discussed in Section 3.4.3.

4.2   The Developed Software Framework

A software framework was developed during this project for the management, processing, reconstruction, analysis and presentation of data from the beam test and from the MC simulations. It is of a modular design and it is object-oriented, such that it should be simple to extend the software with the following purposes in mind: to enable analysis of data from multiple sources such as the next-generation readout electronics and different

MC simulation software tools; to give the user a broad selection of different geometrical, physical and reconstruction models; to include a more extensive proton CT simulation with complex phantoms and positional trackers before and after the phantom or patient; and to facilitate further development and usage of the software by making it available as a analysis library.

The software framework is called the *Digital Tracking Calorimeter Toolkit*, and it is available for download at GitHub (Pettersen, 2015). The software is written in `C++` and ROOT, with some auxiliary tools written in `Python` and user scripts written in `bash`. Several hands-on teaching workshops have been held at the University of Bergen in order to demonstrate the usage of the software, and summaries of these are available at the GitHub project page. In total the framework, including tools consists of approximately 20 000 lines of code.

Some of the functionality in the code was already available in the existing ALICE-FoCal prototype framework designed by Reicher (2016). However, due to the differences between the data analysis requirements for electromagnetic showers and curved-path proton tracking, between the MC simulations and the desired output, and due to the fact that it is simpler to write code from scratch than to modify large parts of existing code, this framework was developed. In addition, the process was very helpful in developing appropriate analysis tools.

4.2.1 Overview over the Software Framework

The design of the software framework reflects the geometry of the detector, the structure of the data readout as well as the different parts of the analysis workflow, as shown in Fig. 4.3. The estimation of the proton path through the patient or phantom (the so-called Most Likely Path, or MLP) has not yet been implemented in the project as all the available experimental results were acquired without imaging phantoms. The so-called "simplified analysis" is a shortcut for validating the results by applying the MC generated proton identification tags for perfect track reconstruction, and is used extensively in Chapter 5. As an overview of the framework structure, the most used classes and their functionality are listed below:

- The `DataInterface` class: The interface to the beam test data in the data format specified in Section 3.2.2 as well as to the output ROOT files generated by the GATE software. Returns the data either as `Hit` objects or as histograms representing the sensor layers.

- The `Layer` and `CalorimeterFrame` are collections of histograms of hitmap data
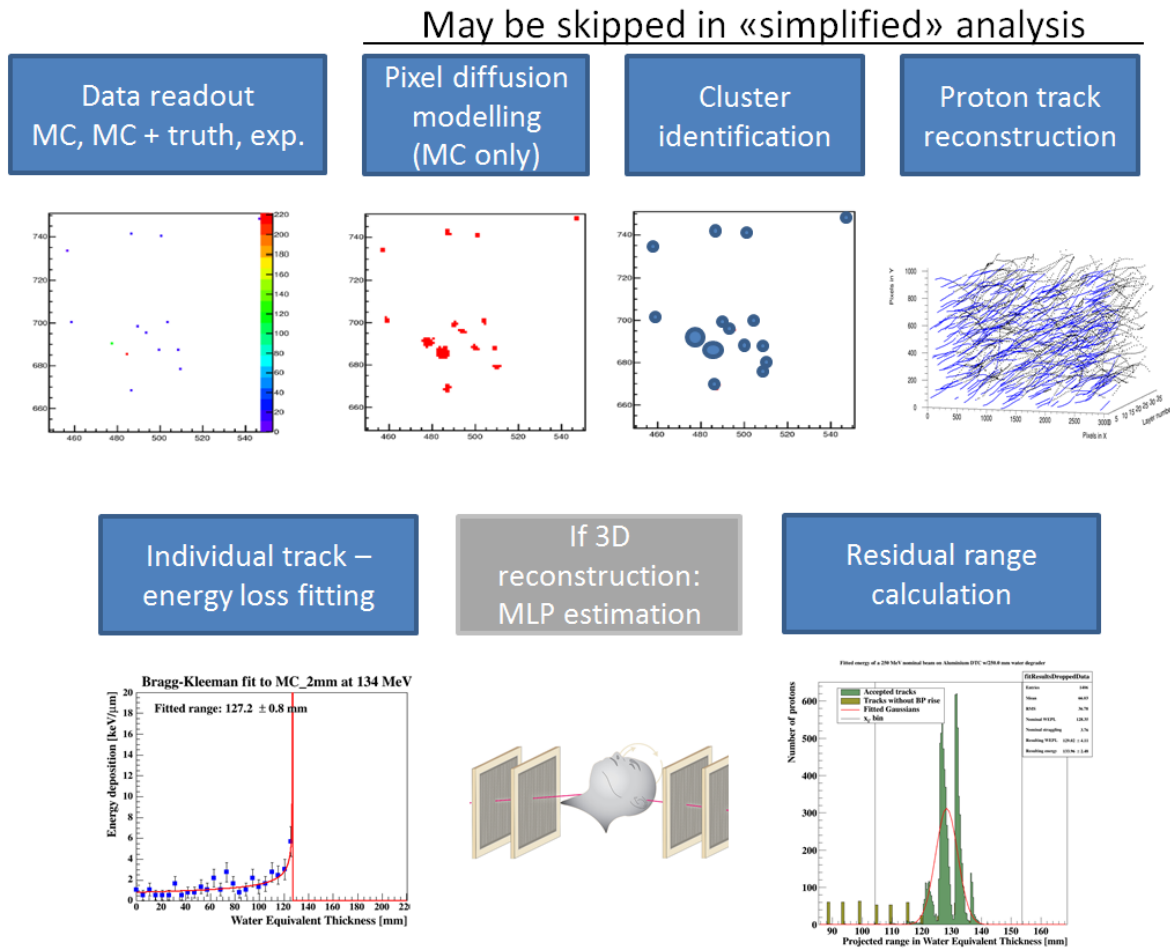
Figure 4.3: *The analysis chain in the software framework. The estimation of the proton path through the patient or phantom (the so-called Most Likely Path, or MLP), has not yet been implemented in the project.*

from a single layer and the complete calorimeter, respectively. A method is implemented to find all activated pixels in the histogram, returning `Hit` objects.

- The `Hit` class: An object representing a *hit*, a single activated pixel. The object includes the 3-dimensional position and (if originating from MC) the ID and the energy deposited by the activating proton. The available class methods are so-called "getters" and "setters" such as `Hit::getX()` and `Hit::setEventID(int)`. A container class `Hits` is available with organizational and optimization features, and methods to implement the hit clustering algorithm described in Section 4.3.7.

- The `Cluster` class: While the `Hit` object is a single activated pixel, the `Cluster` object represents a spatially connected group (called a cluster) of activated pixels. In addition to the spatial (positional) information of the center-of-gravity of all connected `Hit` objects, its member variables also include information about the *number* of pixels representing the cluster. The charge diffusion model, as described

in Section 4.3, is implemented in the `Cluster` class. A container class for multiple `Cluster` objects is available, it is called the `Clusters` class. Various track reconstruction algorithms have been implemented in the `Clusters` class.

- The `Track` class: All `Cluster` objects from a single physical (or simulated) proton track are collected in a single `Track` object. It is here that the many track analyses are implemented: The estimation of track properties such as scattering angles and interaction types (slowing-down or inelastic collision), the implementation of the Bragg curve model fit from Section 4.6.2 to calculate the residual range and thus the initial energy of the track and extraction of the initial vectors of the track.

- The `Tracks` class implements some optimizations which need such as removal of un-physical paths, tracks ending in known dead areas of a chip, tracks leaving the detector laterally and resolving colliding tracks (λ-shaped track segments).

By using the classes listed above, it is possible to write relatively compact user functions to perform all parts of the analysis. Tools that automate the track reconstruction have been developed, and different parts of the analysis are fully customizable using the `Constants.h` configuration file.

The automation tools enable a multi-threaded version of the code, working on separate data sets, through simultaneous execution of the program while altering both the program input and output. The automation tools are provided as `bash` script files.

See Appendix C for the different program files described together with their main functions. See Appendix D for examples of code, how to read the data files and how some of the algorithms are implemented.

4.2.2 The Modularity of the Framework

The framework is built as a class library in order to simplify the usage of and increase the readability of the analysis code. By using the inherent functionality of the ROOT framework, the most common objects have a rich I/O functionality. As an example, after the track reconstruction procedure, the `Tracks` object is automatically saved to disk, and the user may choose to load this file next time instead of performing the same track reconstruction multiple times. This is especially useful then analyzing a set of multiple tracks many times with small perturbations to the analysis technique.

Most of the implemented algorithms were originally developed for this project. As a result of this, there may be more than one applicable approach. In Section 4.3, multiple models for performing the charge diffusion are presented. Likewise, there are different ways to perform the track reconstruction described in Section 4.4.1. In the configuration
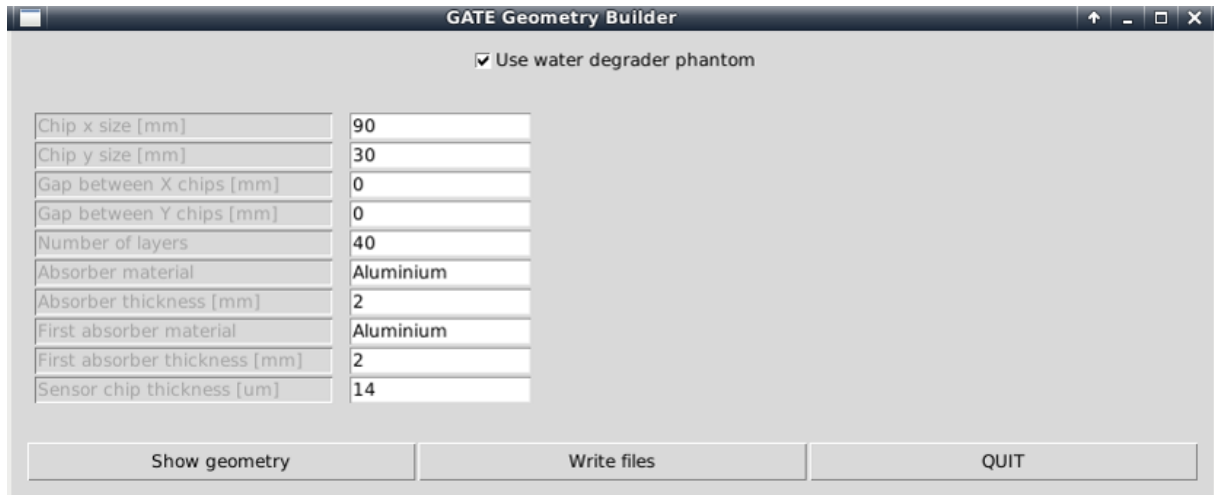
Figure 4.4: *The Python GUI for the creation of different DTC geometries. Based on the applied settings, a GATE* `.mac` *macro file is generated for the simulation of the defined geometry. The program code is available in the GitHub repository for the software framework (Pettersen, 2015).*

file `Constants.h` the user is given the possibility of choosing between all the different implemented models. Different geometries are also available, such as the Forward Calorimeter and the many different optimized geometries presented in Chapter 5.

4.2.3 Software Tools

Some of the auxiliary software tools developed for this project are described in this section:

Automatic Geometry Creation

A time-consuming task in GATE (and any MC program) is the definition of the geometry files. Small changes to e.g. the energy absorber thickness must be propagated to the other modules in the geometry, since they are sequentially defined in the same coordinate system. To that end, a `Python` program has been developed to automatically generate geometry files for the DTC. This is based on simple input variables such as energy absorber material and thickness, the number of layers and the thicknesses of other modules. A usage example of the program is shown in Fig. 4.4.

Energy Loss Calculations

One important calculation routinely performed is that of the proton's energy loss in different media. This calculation is used for finding the energy loss from components in
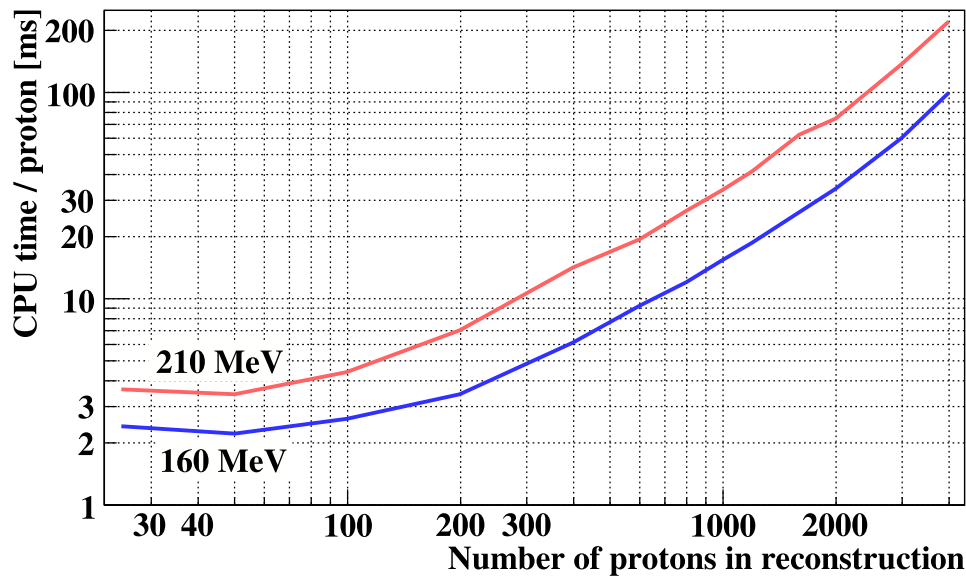
Figure 4.5: *Time requirements of the full MC processing including data retrieval, track reconstruction, track fitting and visualization. The time requirements for two different MC simulations are shown, both simulations are applying the 3.5 mm aluminum absorber geometry from Chapter 5.*

front of the detector, such as the scintillators or the initial energy absorber, or inside the sensor chips. These energy loss values are later used to correct the initial energy estimate of the individual tracks.

An accurate calculation of the energy loss requires full knowledge of all parameters that enters into the Bethe equation, Eq. (1.1), and then by performing a numerical integration. Alternatively, energy dependent stopping power values for a range of different media may be acquired from the PSTAR database (Berger et al., 2005).

A `Python` program was written for the simplification of this process: Look-up-tables (LUTs) of the energy loss values of different materials from PSTAR are loaded into the memory, and 3rd degree polynomial splines are made in order to perform accurate interpolations between the data values. In the program, the user defines the geometry and materials, and the range or energy loss is then calculated by numerically integrating the LUT values. The program is available on GitHub (Pettersen, 2017a).

4.2.4   Computational Efficiency

The software framework has been developed during the project to accommodate the requirements of the analysis workflow. Efforts have been made regarding the computational efficiency of the code. A typical track reconstruction task with MC data in an optimized geometry as will be described in Chapter 5 consists of a 160 MeV beam in-

teracting with 22 sensor layers before stopping. The time required for the concurrent analysis of 200 protons is about 0.7 seconds. Of these, 0.6 seconds are spent on the track reconstruction and the rest on visualization, data retrieval and analysis. See Fig. 4.5 for the dependency of the number of protons in the analysis on the reconstruction time. The numbers are found on a Xeon E5520 CPU at 2.27 GHz, utilizing a single core for the task. The reconstruction task can be executed in parallel on several CPU cores, decreasing the required time spent on the analysis.

4.3   Charge Diffusion of the Proton Track Signal

Large clusters with sizes varying normally between 1 and 35 pixels are activated by the charge diffusion of electron-hole pairs, the pairs being liberated in the epitaxial layer of the sensor chip by a passing proton and then thermally diffused. This diffusion effect cannot be modeled straightforwardly in MC simulations due to the low electron energies associated with the charge diffusion process.

The correct characterization of the charge diffusion process enables a conversion from the energy deposited by a passing proton in the epitaxial layer of the pixel (E_{dep}) and the number of pixels activated by the charge diffusion process (the *cluster size*). In this section, we will apply models of different complexities to describe the charge diffusion process, with the aim to find the relationship between the deposited energy and the cluster size. This relationship will then be used to guide the modeling of a Gaussian Diffusion function for generating realistic charge diffused clusters from the MC output.

It should be noted that this modeling is necessary due to the *digital* pixel readout scheme. The measured value is the *number* of pixels having a signal above a certain threshold, thus the charge diffusion process must be modeled in order to regain a measure of the initial total charge: that is a necessary property for identifying the proton's Bragg peak. This is in contrast to analog readout detectors (as described in Price et al. (2015) for a proton CT application) where the summed intensity of all pixels in a cluster is proportional to the energy loss of the passing proton.

4.3.1   Characterization of Cluster Size Distributions

The sizes of the clusters increase with the proton's energy deposition, and the shapes of the clusters are approximately Gaussian. A detailed view of a portion of the first layer is shown in Fig. 4.6.

In Fig. 4.7 several charge diffused clusters are shown, they are grouped as a function of their cluster size. It can be seen from Fig. 4.7 that the clustering identification method
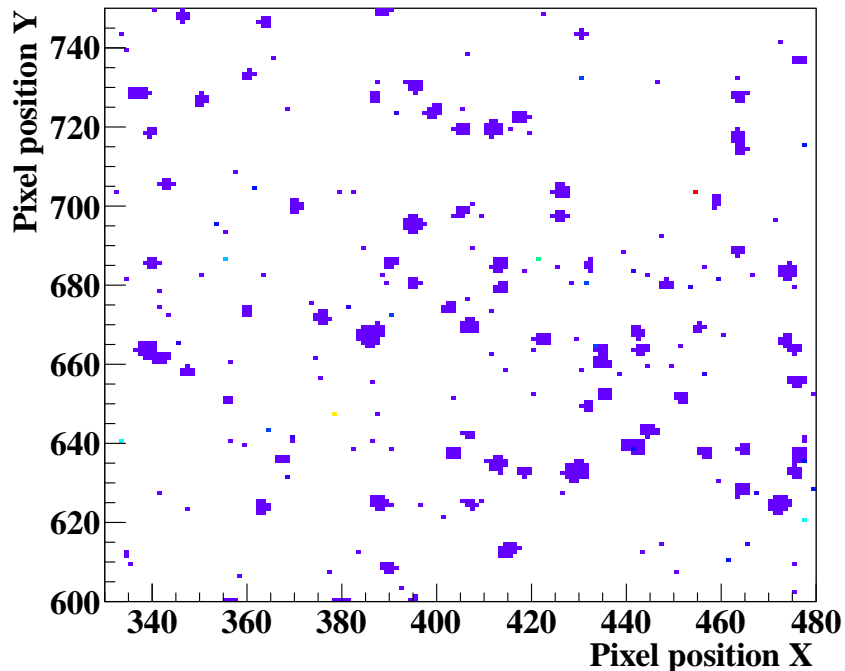
Figure 4.6: *A portion of the (1280×1280) pixel hit map from the first layer in the 170 MeV beam data. Each traversing proton activates a large pixel cluster. Note features such as hot (always-activated) pixels due to their high values (in red, green and yellow), summed over many data frames, and noise, identified as single-pixel hits.*

is not perfect, since several of the identified clusters are made up of smaller clusters merged together.

In Fig. 4.8, the cluster size distribution is shown for different detector layers, using beam test data extracted from the 170 MeV runs. The mean values of the distributions do not increase monotonically with layer depth, this is partly due to the different sensitivities of the sensor chips (see Fig. 3.7).

4.3.2   Modeling the Charge Diffusion

Ultimately, we must be able to calculate the energy deposited by the proton traversing through the sensor chip, so that it is possible to model the E_{dep} as a function of depth using the Bragg-Kleeman equation. In order to find a relationship between the E_{dep} and the resulting cluster size, we will require the following information:

i) Reconstructed proton paths, enabling the calculation of the remaining energy of the passing proton in each cluster. The remaining energy is the energy giving the proton its residual range from the position of the cluster depth to the proton's stopping depth, using the process as described in Section 4.6. This reconstruction process is discussed later, however the result is applied here.
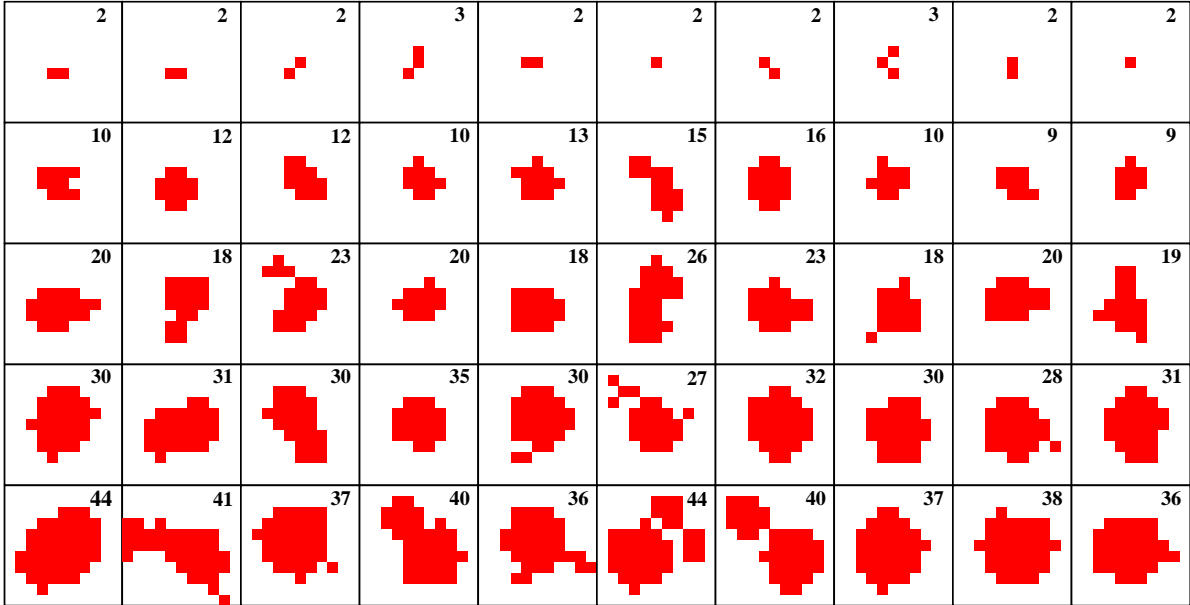
Figure 4.7: *Examples of charge diffused pixel clusters, grouped in rows by their cluster size (the number of activated pixels in cluster). Each sub-figure is a small portion of the hitmap (as exemplified in Fig. 4.6), with the individual pixels shown in the (x, y) axes. The cluster size is shown in the corner of each figure. Note that some of the larger clusters actually are combined smaller clusters, located very close to each other: a correction to this will have to be applied.*
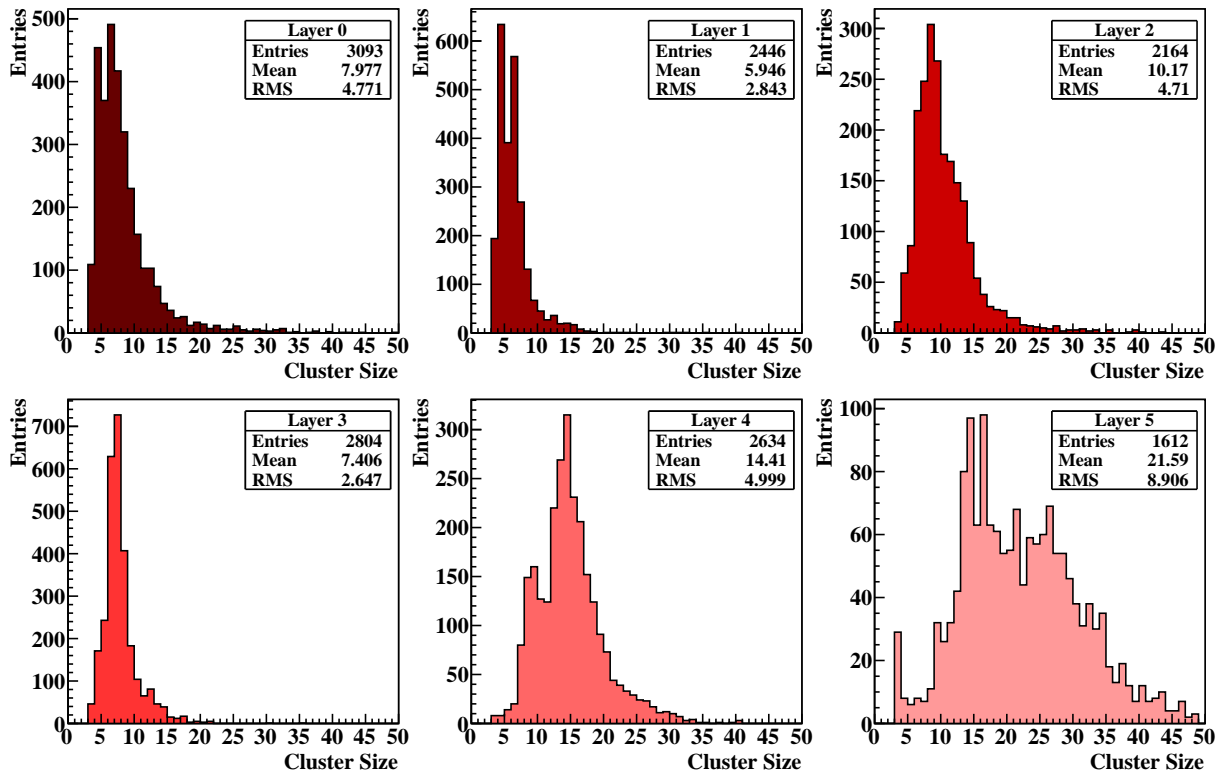
Figure 4.8: *Cluster size distributions in the various sensor layers, data from the 170 MeV beam test runs.*
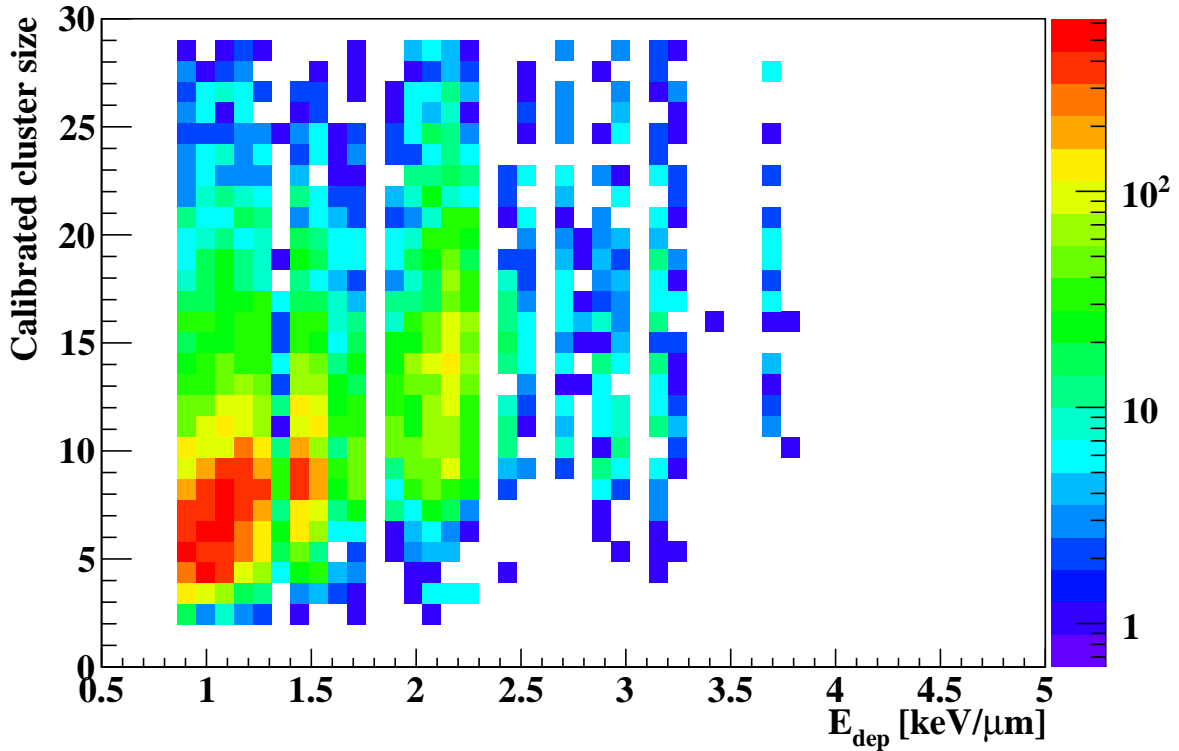
Figure 4.9: *Correlation plot between the E_{dep} and the cluster sizes. The cluster sizes are calibrated using the chip sensitivity calibration factors, and the E_{dep} is calculated using the energy-loss tables together with information about the sensor layer depth relative to the nominal range.*

ii) Sensitivity calibration factors, for each of the sensor chips in order to ensure a uniform response to the same signal throughout the detector: See Section 3.4.3.

iii) The E_{dep} in silicon, calculated from the remaining energy. A simple parametrization from the energy loss tables in Berger et al. (2005) yields

$$E_{\mathrm{dep,Si}} = 43.95 \cdot E^{-0.748}. \tag{4.1}$$

The analysis following these steps is performed using all available experimental data for all beam energies. For each reconstructed proton, its constituent clusters (one in each sensor layer) are calibrated with the calibration factor $f(\mathrm{Chip})$, and its local E_{dep} is calculated Eq. (4.1). The resulting two-dimensional histogram is shown in Fig. 4.9.

A Model of Charge Diffusion deduced from "First principles"

An analytical model of the charge diffusion process for MAPS chips was proposed in Maczewski (2010). This model was adapted to the MIMOSA23 chips used in the prototype calorimeter in a collaboration project together with a MSc student (Hansen, 2017).
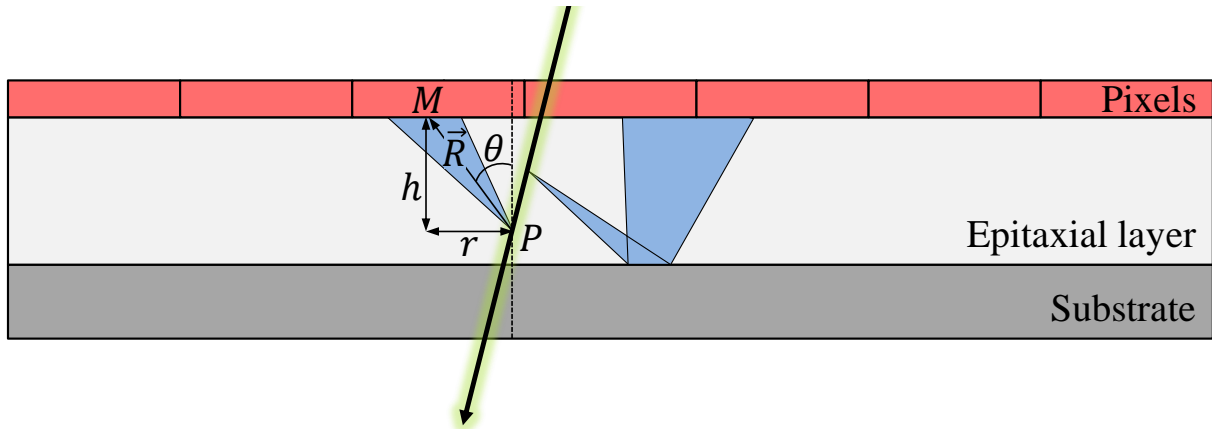
Figure 4.10: *Schematics of a proton's path through a MIMOSA23 chip (not to scale). Electron-hole-pair ionization events from the proton's path are shown as the shaded conical areas.*

It is in the model assumed that a traversing proton is ionizing the matter and releasing electron-hole pairs continuously in the epitaxial layer of the sensor. With reference to the variables displayed in Fig. 4.10, the probability ρ that a charge carrier ejected from P should hit the pixel layer at M, with $\vec{R}(r, \phi, \theta) = \overrightarrow{PM}$ is

$$\rho(\vec{R})\,\mathrm{d}r\mathrm{d}\phi = \frac{hr}{4\pi|\vec{R}|^3} \exp\left(-\frac{|\vec{R}|}{\lambda}\right) \mathrm{d}r\mathrm{d}\phi, \tag{4.2}$$

where h is the distance between the pixel layer and the ionization event, r is the distance between M and P, projected onto the pixel layer, and λ is the single free parameter to the model which accounts for the attenuation length in the epitaxial layer: it must be determined experimentally.

The E_{dep} distribution in each sensor layer has been computed using GATE simulations of the calorimeter geometry. The mean energy required to create electron-hole-pairs in silicon is $E_g = 3.6\,\mathrm{eV}$ (Michaelson, 1977), and consequently the number of ejected carriers is $N_c = E_{\mathrm{dep}}/E_g$. The typical E_{dep} of a proton in the 14 μm silicon epitaxial layer between 15 and 60 keV, and thus N_c is generally between 5000 and 15000.

The model was numerically integrated to account for all possible values of h, and multiplied by N_c. The resulting electron intensity was mapped to a (sub-) pixel mesh, where the incident position within the pixel was randomized. A lateral profile of the electron intensity is shown in Fig. 4.11. The intensity distribution assumes that one electron-hole pair is generated every μm. Each pixel consists of 9×9 sub-pixels of $3.3 \times 3.3\,\mathrm{\mu m}^2$.

From the two-dimensional intensity profile together with the knowledge about the number of electrons necessary in order to activate a pixel (the number 26 e^- was found in Section 3.4.2), it is possible to find the number of activated pixels. The resulting relationship between E_{dep} and the number of activated pixels, n, is shown in Fig. 4.12
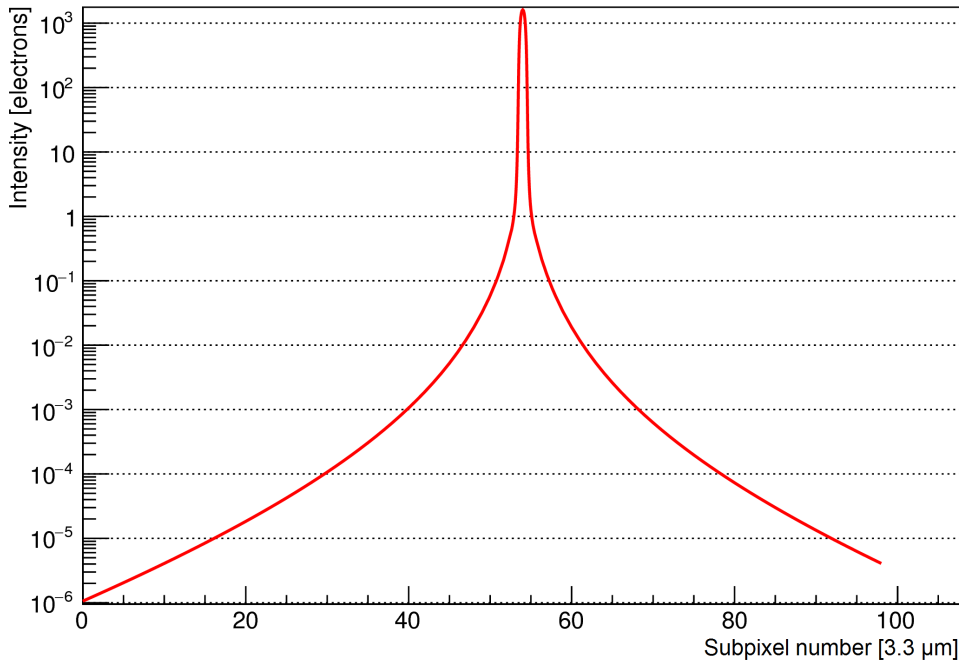
Figure 4.11: *Intensity distribution profile for an incident proton on a sensor chip. From Hansen (2017).*

for $\lambda = \infty$ μm[*] and it can be parametrized as:

$$n = 16.80 \cdot E_{\text{dep}}^{0.566}. \tag{4.3}$$

A study from Zhang (2017) applies the same analytical model to the ALICE-FoCal prototype studied in this work, using data from high energy electrons. The best correspondence between the model and the experimental data is there also obtained by using $\lambda = \infty$.

A "Gaussian Intensity" Model of Charge Diffusion

Another way of modeling the relationship between the cluster sizes and the deposited energy has been proposed in Spiriti et al. (2017), there applied for the (analog output) MIMOSA18 and the (digital output) MIMOSA26 sensor chips. With the assumption that the charge density per unit area $\mathrm{d}q(r)/\mathrm{d}S$ is Gaussian distributed, we can write

$$\frac{\mathrm{d}q(r)}{\mathrm{d}S} = \frac{Q_{\text{tot}}}{2\pi\sigma^2} \exp\left(-\frac{r^2}{2\sigma^2}\right), \tag{4.4}$$

where $Q_{\text{tot}} = E_{\text{dep}}/E_g$ is the total number of generated electron-hole pairs, E_g is the mean energy required to create an electron-hole pair, σ is the width of the charge diffused area

---

[*]This value yielded the lowest χ^2 value when compared with the data in Fig. 4.9. The physical interpretation is that the attenuation term can be neglected and only the isotropic diffusion is responsible for the describing the charge diffusion process.

and r is the distance from the center of the proton track. Only pixels having a charge density higher than a threshold T are activated (within $r \leq r_T$), and we get the relation

$$\frac{\mathrm{d}q(r_T)}{\mathrm{d}S} = T \implies r_T^2 = 2\sigma^2 \ln\left[\frac{E_{\mathrm{dep}}}{2\pi E_g T \sigma^2}\right] \tag{4.5}$$

and the number of activated pixels (each with size p) is

$$n = \frac{\pi r_T^2}{p^2} = 2\pi \frac{\sigma^2}{p^2} \ln\left[\frac{E_{\mathrm{dep}}}{2\pi E_g T \sigma^2}\right]. \tag{4.6}$$

Using the values $E_g = 3.6\,\mathrm{eV}$ and $p = 30\,\mu\mathrm{m}$, the most likely values for σ and T can be estimated by fitting the model to the experimental data shown in Fig. 4.9. This is done in the next section (see Fig. 4.12), with the resulting fit variables $\sigma = 32.9\,\mu\mathrm{m}$ and $T = 0.204$ charge carriers per $\mu\mathrm{m}^2$.

A Phenomenological Model of Charge Diffusion

Finally, a relationship between E_{dep} and the cluster sizes (n) can be modeled with the function $n = a \cdot E_{\mathrm{dep}}^b$, or, inversely, $E_{\mathrm{dep}} = a^{-1/b} n^{1/b}$. This is the function shape found from the "first principles" analytical model.

A least-squares fit is performed on the available experimental data. Each E_{dep} column in the 2D histogram of Fig. 4.9 is converted to a point in a scatter plot, using the mean value and asymmetric error calculated from the E_{dep} bins on the x axis in the 2D histogram. The points are, during the fitting procedure, weighted relative to the number of entries in the corresponding column. The curve fits are applied on this scatter plot, shown in Fig. 4.12, rather than on the 2D distribution in the histogram.[*] This procedure yields the parameters

$$n = 7.85 \cdot E_{\mathrm{dep}}^{0.727} \tag{4.7}$$

$$E_{\mathrm{dep}} = 0.0586 \cdot n^{1.376} \tag{4.8}$$

The curve given by Eq. (4.7) is shown in Fig. 4.12. The uncertainty of Eq. (4.8) is found by propagating the error in the two fitting parameters a, b. The covariance matrix from `TMinuit` gives the fit errors as $\sigma_a = 0.077$ and $\sigma_b = 0.022$. The covariance is $\sigma_{ab} = -0.0011$.

$$\sigma_{E_{\mathrm{dep}}}/E_{\mathrm{dep}} = \sqrt{\sigma_a^2 \left(\frac{\partial E_{\mathrm{dep}}}{\partial a}\right)^2 + \sigma_b^2 \left(\frac{\partial E_{\mathrm{dep}}}{\partial b}\right)^2 + 2\sigma_{ab}\left(\frac{\partial E_{\mathrm{dep}}}{\partial b}\right)\left(\frac{\partial E_{\mathrm{dep}}}{\partial a}\right)} \tag{4.9}$$

$$= \frac{1}{b^2}\sqrt{\sigma_a^2 (b-1)^2 + \sigma_b^2 \left(b - \ln(n/a)\right)^2 + 2\sigma_{ab}(b-1)(b - \ln(n/a)} \tag{4.10}$$

---

[*]The fitting procedure was performed on the scatter plot, since it is much more straightforward to fit scalar functions to scatter plots compared to fitting them on 2D histograms.

Model	Function shape	χ^2 value
First Principles	$n = 16.8 \cdot E_{\mathrm{dep}}^{0.57}$	0.16
Gaussian Intensity	$n = 7.56 \cdot \ln \frac{E_{\mathrm{dep}}}{5000}$	0.042
Power fit	$n = 7.85 \cdot E_{\mathrm{dep}}^{0.73}$	0.027

Table 4.1: *Different charge diffusion models: Function shapes and χ^2 values.*

Inserting these values we get a relative error of about 7% at $n = 5$ and 2% at $n = 25$. It must be noted that the error in E_{dep} at this stage will not be propagated further to the final range uncertainty that will be calculated in Section 4.6.3 — as that range uncertainty is calculated from the width of the observed distribution of the individual range calculations.

4.3.3   Comparison of the Different Charge Diffusion Models

A comparison of the charge diffusion models has been performed, with results in Fig. 4.12. The different models are evaluated in terms of how well they explain the data, such as with the χ^2 metric. The resulting χ^2 values that are obtained from the `TMinuit` library are listed in Table 4.1.

As the *phenomenological* model yielded the lowest χ^2 value, this relationship will be used to guide the modeling of the charge diffusion process using a Gaussian diffusion model in the next section. The Gaussian diffusion model will provide realistic cluster shapes from the MC simulation output. The correct cluster size distribution should then be obtained if the modeling is performed in concordance with Eq. (4.7).

Some caveats in the *First Principles* model were listed in Hansen (2017): The energy deposited by the passing proton was defined to be the most probable value in a Landau distribution, rather than sampling from the distribution itself: The error from this is asymmetrical, and the long tails in the distribution might increase the charge diffusion radius.

The calculation of E_{dep} for each of the cluster positions is sensitive to minuscule differences between the MC modeling and the experimental parameters during the beam test. The large spread in the correlation plot (Fig. 4.9) is a result of this. More experimental data at a larger span of E_{dep} values is needed in order to accurately model the charge diffusion process. A specialized beam test performed by gradually increasing the E_{dep} of the incoming protons, impinging on a single pixel layer, would provide a better suited dataset for the modeling performed in this section. At this stage, all the proposed models are able to adequately describe the data.
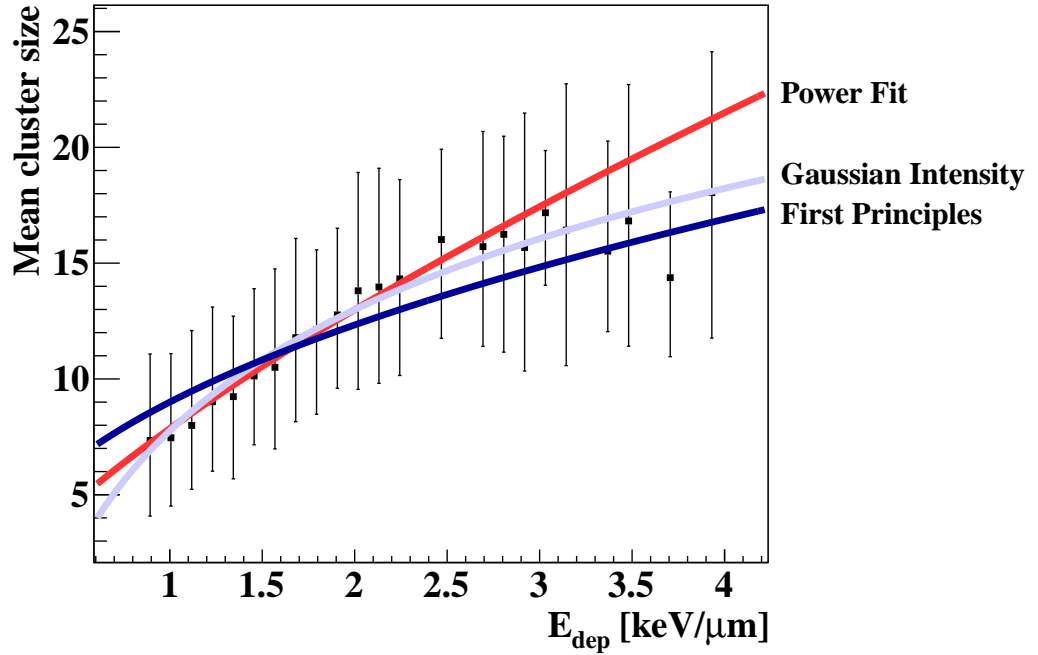
Figure 4.12: *Correlation data for the E_{dep} and the cluster sizes: E_{dep} is calculated using the energy-loss tables from Berger et al. (2005). In this graph the mean value and the asymmetric standard deviation values are shown for each of the E_{dep} bins in the histogram of Fig. 4.9, for purposes of curve fitting. Three curves are shown: The analytical charge diffusion model based on first principles, a Gaussian intensity charge distribution model and a power fit to the experimental data using Eq.* (4.7).

4.3.4 A Gaussian Diffusion Model for Monte Carlo Simulations

The MC simulations do not produce extended cluster areas, as the complete energy deposition process is approximated to occur inside a single pixel. An accurate model of this process would require a very detailed and time-demanding simulation of electrons down to thermal energies. A Gaussian diffusion model is proposed, with the goal to reproduce both the mean value of the experimental cluster sizes (Eq. (4.8)) and the distribution of shapes as seen in Fig. 4.7.

The main procedure in the Gaussian model is to convolute a 2D array of MC simulated hits with a Gaussian distribution, in which the σ parameter depends on the E_{dep} :

i) For each of the hits, generate a Gaussian distribution in (x, y) surrounding the hit. The standard deviation of the Gaussian should depend on the deposited energy in the pixel's epitaxial layer: we define $\sigma = \alpha E_{\text{dep}}^{\beta}$.

ii) The Gaussian is sampled N times in order to introduce statistical uncertainties, and thus $n \ll N$ pixels are defined to be activated in the pixel area surrounding the original pixel. n is the number of unique pixels from the N sampled positions.
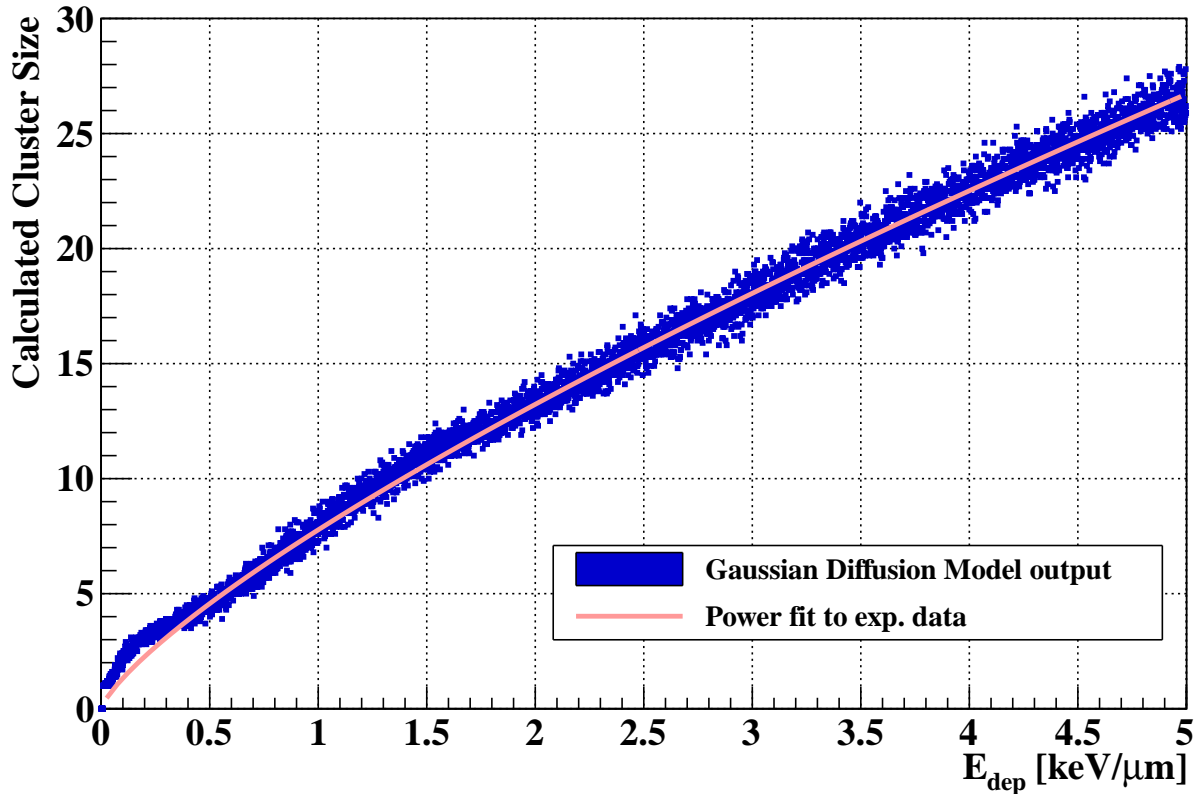
Figure 4.13: *Output cluster sizes using the Gaussian charge diffusion model.*

iii) This process is performed iteratively to correctly determine the values α, β and N. By matching the cluster size distributions arising from the above model with experimental data, the values $\alpha = 0.31 \, \text{keV}^{-1}$ and $\beta = 0.29$ are obtained.

iv) In the same way, by applying $N = E_{\text{dep}} \cdot 0.68 / (\text{keV}/\mu\text{m})$, the shapes of the generated clusters should have a distribution corresponding to the average sizes of the measured clusters in the experimental data.

The resulting cluster sizes generated from this model is shown in Fig. 4.13, where the procedure is performed multiple times at small E_{dep} increments. The results are presented there together with the curve defined by Eq. (4.7).

4.3.5 Results of the Chip Sensitivity Calibration

A model for the charge diffusion has been presented in this section. A comparison between the model and the experimental data is presented in Fig. 4.14, where the experimental data represents the measured values for the size of the charge diffused clusters, and the charge diffusion model is applied on the MC dataset. The different datasets used to this end were described in Section 3.3.2. In both cases, the cluster sizes have been converted into keV/μm, this to facilitate the chip sensitivity calibration which was performed on the E_{dep} values. The calibration factors have a higher variation in the Bragg
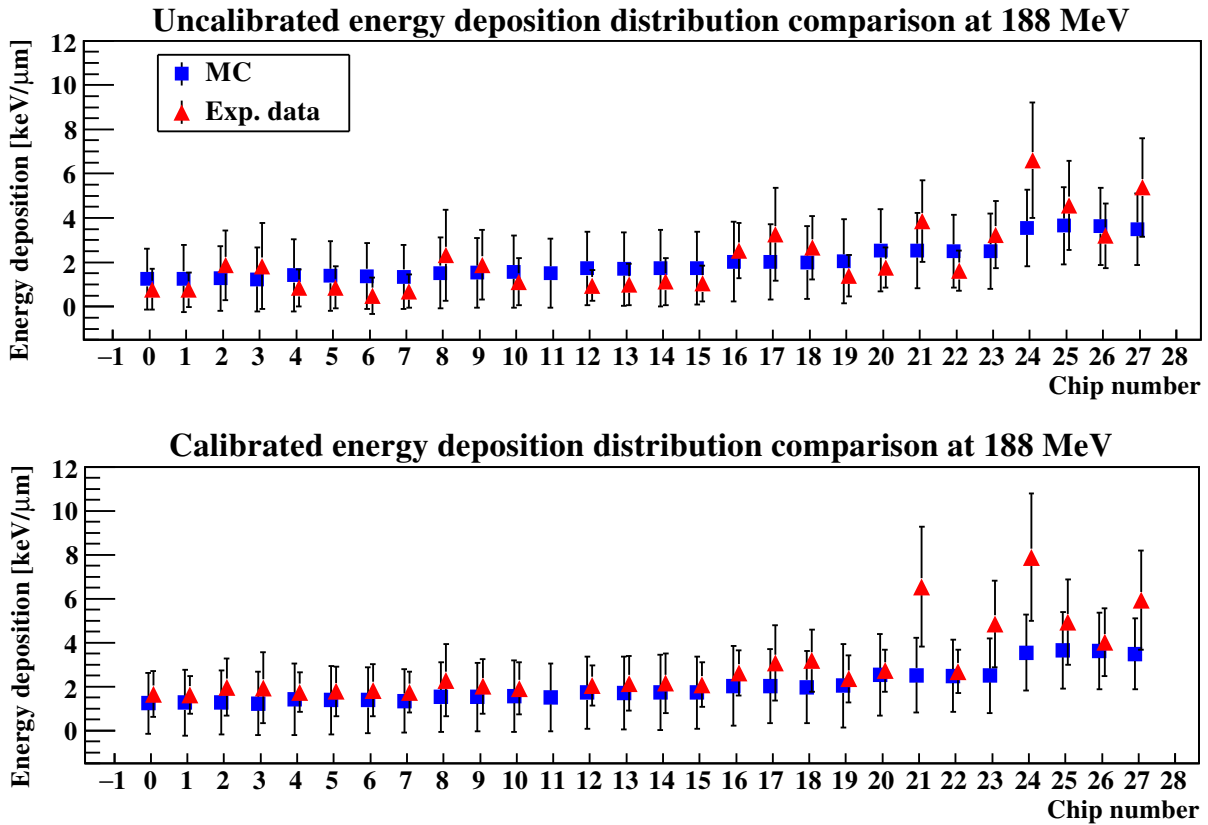
Figure 4.14: *Average energy deposition in each chip, applied as a validation of the charge diffusion model applied on the MC dataset and as a validation of the chip sensitivity calibration on the experimental data. From Pettersen et al. (2017).*

peak area for each energy, since it is harder to accurately model the E_{dep} when the energy loss gradient is high.

4.3.6 Effect of Signal Threshold on Cluster Sizes

Most of the data taken during the beam test was acquired using a preset signal threshold value of 26 e^- ENC. In addition to this dataset, a single run was acquired with a lower signal threshold of 22 e^- ENC. The lower threshold run contains approximately 700 protons with an initial energy of 188 MeV. Using this additional run it, is possible to calculate the effect of a lower signal threshold on the cluster size distribution.

The mean cluster size in each layer was found when comparing data taken with the normal threshold with data from the lower threshold run. The clusters in the lower-threshold run has a $23\% \pm 5\%$ increase in the number of activated pixels. The mean cluster size values from the two runs are listed in Table 4.2.

Layer	0	1	2	3	4	5
Normal Threshold	7.43	5.65	9.20	6.58	11.49	12.05
Lower Threshold	9.46	6.53	11.66	8.11	13.64	15.22
Relative increase	27.3%	15.6%	26.7%	23.3%	18.7%	26.3%

Table 4.2: *Mean cluster sizes (in terms of number of activated pixels) using normal (26 e^- ENC) and lower (22 e^- ENC) signal threshold values. The experimental data was acquired with a beam energy of 188 MeV.*

4.3.7 Cluster Identification Algorithm

Each traversing proton activates a cluster of pixels through charge diffusion process, and these clusters must be identified. All activated pixels, or hits, surrounding a proton track should be incorporated into a single cluster. Examples of different cluster shapes were shown in Fig. 4.7.

The clustering is performed through a simple neighboring algorithm: For each hit, check if any of the eight possible neighboring pixels have been activated. This algorithm is run recursively on all the activated neighboring pixels. The resulting `Cluster` object is then stored, having a defined center-of-mass position and the cluster size value.

Some of the larger identified clusters are actually composed of two or more smaller clusters located very close to each other. A more complex algorithm might be able to disentangle such features, such as a circle-locating Hough transform (Ballard, 1981) or an erosion-filtering approach, however due to the simplicity and efficiency of the simple neighboring algorithm, none of these algorithms have (yet) been implemented. The post-processing of the reconstructed tracks takes this into account, and when two tracks meet in a single identified cluster, the cluster is split into two new clusters: See Section 4.4.2 for more details.

4.4   Proton Track Reconstruction

The numerous clusters created throughout the many layers of the calorimeter are generated by the traversing protons. It is necessary to reconstruct all the intermingling tracks generated by the protons, in order to "connect the dots" and be able to calculate the endpoint of all incoming protons.[*] This task is made difficult by the many small atomic Coulomb scatter events, curving each trajectory slightly along its path. As a result of

---

[*]This approach is necessary in a tracking calorimeter, where all the recorded hits due to a single proton must be matched, and thus disentangled from tracks originating from different protons. This is in contrast to scintillator-based energy detectors, where a single proton event is time-matched using a trigger system to the corresponding tracker detector output.

this, it is not possible to apply conventional tracking methods such as straight-line fitting with a Kalman filter or Hough-based line-finding algorithms. Rather, a probability envelope of the angular deflection must be calculated in the search for the next track sector. In this section, the track reconstruction algorithm developed for this project is described.

4.4.1 Track Reconstruction Algorithms

A track-finding algorithm has been developed, modeled after the track following procedure in Strandlie and Frühwirth (2010):

i) Cluster pairs at approximately the same lateral position in the two first layers are identified. Multiple cluster pairs may originate from the same cluster in the first layer, to allow for tracks having different initial directional vectors. In Fig. 4.15 this process is visualized.

ii) Using the position and direction of each cluster pair as the starting point of a growing track candidate, further clusters are searched for at extrapolated anticipated positions in the subsequent layers.

iii) The expected RMS value of the multiple Coulomb scattering (MCS) angle distribution, θ_0, is found for each layer from the Highland equation (Eq. (1.6)).

iv) At each sensor layer, a search cone is applied in order to identify all possible matches. The radius of the search cone is calculated as the $k \cdot \theta_0$ value. The value k is used as a scaling factor.

v) Within this search cone, the cluster that is most adjacent to the anticipated position is added to the growing track. The angular deflection of the cluster is calculated as

$$\Delta\theta = \cos^{-1}\left[\frac{\vec{T}_{i-1} \cdot \vec{T}_i}{|\vec{T}_{i-1}||\vec{T}_i|}\right], \tag{4.11}$$

where the vectors are defined in Fig. 4.15.

vi) All candidate tracks originating from the same seed cluster in the first layer are compared, by searching for the highest scoring track. The track score is calculated as a function of the track length, the amount of angular scattering between each layer, and a check of whether the track contains a Bragg peak or not.

vii) The tracking algorithm is run twice, first with $k = 2.5$ and then with $k = 5$, so that, first, the relatively straight and most abundant $\Delta\theta < 2.5\,\theta_0$ tracks are found, and then one more time to ensure that all tracks with $2.5\,\theta_0 < \Delta\theta < 5\,\theta_0$ are found.

It turns out that a number of tracks are still incorrectly reconstructed by comparison with MC simulations, which is assumed to be the ground truth.
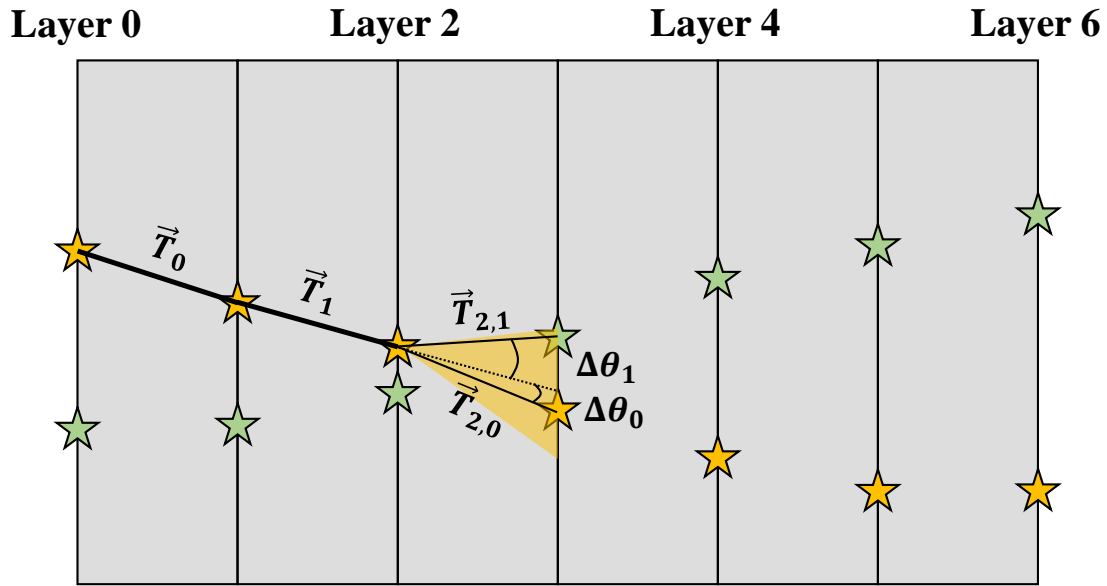
Figure 4.15: *A schematic example of the track reconstruction process, with hits from two proton tracks shown. Two track segments, $\vec{T}_0$ and $\vec{T}_1$, has been identified. The dashed line is the extrapolation of $\vec{T}_1$. In the continuation of the track, two possibilities ($\vec{T}_{2,0}$ and $\vec{T}_{2,1}$) are available within the search cone (shown in yellow). The angular deflections $\Delta\theta_i$ are calculated. Since $\Delta\theta_0 < \Delta\theta_1$, then $\vec{T}_{2,1}$ is chosen as the next track segment.*

4.4.2 Track Reconstruction Quality

Some track optimization methods are performed, in order to increase the accuracy of the proton track reconstruction. Due to the physics of proton interactions, a portion of the protons will stop abruptly due to nuclear interactions, prior to entering their Bragg peak region, in which the bulk of the protons come to rest. Such tracks do not contain a Bragg peak, and thus do not have an increased energy deposition in the deepest layer.

A cut based on the E_{dep} value of the cluster in the deepest layer of each reconstructed proton track ensures that the majority of such tracks are identified and removed from the analysis. The E_{dep} threshold should be around $2.5\,\text{keV/μm}$. This value has been found by recording two E_{dep} distributions:[*] one for protons stopping due to ionization energy losses and one for protons undergoing nuclear interactions, scored in the last reached sensor layer: see Fig. 4.16. A Landau distribution is fitted to each of the distributions using the ROOT library `TMinuit`. The E_{dep} value where the distributions are equal is defined to be the threshold value, and should give the best probability of correct classification. The Most Probable Value (MPV) of the energy loss of the nuclear interacting protons is $0.66\,\text{keV/μm}$, and the MPV of the gradually stopping protons is $4.21\,\text{keV/μm}$. The threshold value between the two is shown as the dashed line at $2.52\,\text{keV/μm}$.

---

[*]Determined using a GATE simulation of 20 000 protons with an initial energy of 230 MeV and tracking their histories throughout the detector setup.

Tracks that leave the detector laterally, and thus for this reason do not contain a Bragg peak, are also removed from the analysis by identifying outwards-pointing tracks that end near a detector side.

As presented in Section 3.1.1, some of the sensor chips were not able to transfer all of the hits to the DAQ system. In addition, there is a 100 μm dead area between the two chips in a module. The track reconstruction software needs to be able to handle missing clusters due to dead chips, bad data channels and gap areas. If the reconstruction algorithm cannot find a cluster to append to the growing track, it extrapolates the track one layer further, based upon the track position in the last layer with an identified cluster. If there is a cluster close to the extrapolated position in this next layer, the track continues from there. In this way, tracks that are lacking a cluster in a single layer are still reconstructed. The survival rate of the protons is still lower in the experimental dataset compared to the MC results: Areas with fewer reconstructed tracks near the projected position of the bad chips can be observed in Fig. 3.5.

Due to charge diffusion, separate hits with a shower of diffused charge surrounding them may be identified as a single cluster that is merged and kept as a single cluster. Two crossing protons can produce a single merged cluster with the result that only one of the reconstructed tracks may be incorporated in it, resulting in a track with a missing cluster in the layer where the protons crossed. Therefore, a cluster splitting algorithm is applied: The algorithm locates all the crossing track pairs in the layer where one of the tracks is missing a cluster. It then divides the supposedly merged cluster into two, and connects the new cluster to the track without a cluster. Each of the new clusters has a smaller size than that of the merged cluster: The size is chosen according to Eq. (4.8) such that the total amount of deposited energy is conserved.

4.4.3   Track Loss

Loss of tracks may occur due to protons leaving the detector geometry, due to dead sensor areas and tracks may cease due to inelastic nuclear interactions in the detector. Tracks that are incorrectly reconstructed due to mismatch errors will be discussed in Section 4.5.

The overall percentage of track loss from all recorded beam energies is 40%. These tracks are cut from the analysis, examples of this are tracks identified as undergoing an inelastic nuclear interaction, these have been subtracted since they do not contribute to the range calculation, likewise also for tracks ending outside the detector or in a dead sensor area.
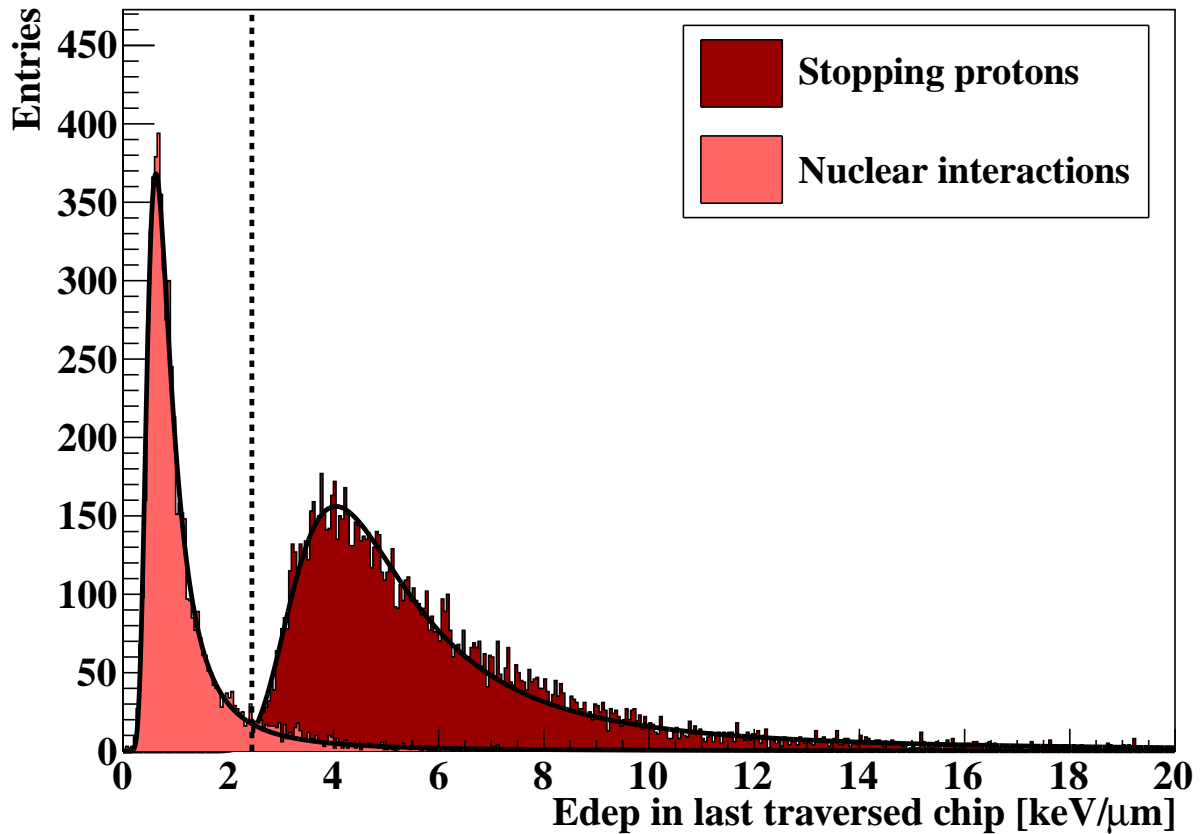
Figure 4.16: *Energy loss distributions of protons stopping due to ionization energy loss and due to nuclear interactions, respectively, each fitted with a Landau curve. The dotted line shows the E_{dep} where the contributions from the two processes are equal, and it is used for discrimination between the two.*

Track Loss due to Nuclear Interactions

A fraction of the tracks end before their expected range, this is mainly due to nuclear interactions. About 33% of the tracks stop prior to their mean projected range (accounting here also for the range straggling), in addition to those having a cluster size distribution with no identifiable Bragg peak. These results are higher than the fraction of protons undergoing nuclear interactions obtained from Janni (1982) and from MC simulations, where the values across the energy range is found to be about 19%. The discrepancy may arise from tracks that resemble inelastic scattering, but are instead incorrectly reconstructed tracks from protons undergoing other processes or tracks from secondary particles.

Track Loss due to Dead Sensor Areas

If a slowing-down track is found to stop in a dead sensor area, it is discarded. The fraction of tracks discarded in this manner is 5% across the detector area and the beam energies.

Track Loss due to Protons Leaving the Detector

Some of the protons leave one of the lateral detector sides. This is either due to multiple scattering processes or due to the proton's initial direction when entering the front face of the detector. Protons leaving the detector before coming to rest are removed from the analysis. This effect is proportional to the proton range, and in average 4% of the protons exit from the detector this way.

4.5   Proton Intensity Capacity

During the beam test, the intensity of the beam was adjusted ensuring that the rate of protons was a little below the readout frequency of the calorimeter, so that at maximum one proton was contained in each readout. Due to the high granularity of the MIMOSA23 sensors, it is possible to reconstruct a large number of proton tracks concurrently. Considering this, n_p readout frames have been accumulated in the track reconstruction step.

The detector occupancy is the ratio of the number of activated pixels to the total number of pixels in the detector. The detector occupancy increases linearly with n_p, and at $n_p = 500$ the detector occupancy is 0.42% in the last active layer, containing the largest fraction of protons with a Bragg peak. This corresponds to 13.5 activated pixels per proton track in that layer.

A higher detector occupancy decreases the probability that all hits in a given reconstructed track originates from the same primary proton. The number of correctly reconstructed tracks has been found through checks against the primary proton identification ID tag obtained from MC simulations, which indicates the primary proton responsible for the cluster. The saturation limit of the detector, $n_{p,\,max}$, is calculated according to the accuracy goal of the proton tracking. Fig. 4.17 shows the portion of tracks which are identified as correctly reconstructed, i.e. they originate from the same primary particle, at different n_p values. Three curves are shown according to different definitions of a correctly reconstructed track. Tracks lost due to the effects described in Section 4.4.3 are not included in this figure.

The resulting saturation limit where 80% of the tracks are correctly reconstructed is $n_{p,max} = 235$, resulting in a proton intensity capacity corresponding to 470 000 protons/s. However, the misidentification of a track introduces errors that are potentially small, such as a small shift in the angular orientation and in the lateral position determination. With an allowance of small deviations of $\pm 0.5°$ and ± 0.5 mm on the misidentified track in the first layer, the resulting saturation limit at 80% accuracy is $n_{p,max} = 480$, corresponding to 960 000 protons/s, or 60 000 protons/cm²/s. This number has been found with MC simulations where the beam is uniformly spread across the complete detector area. This
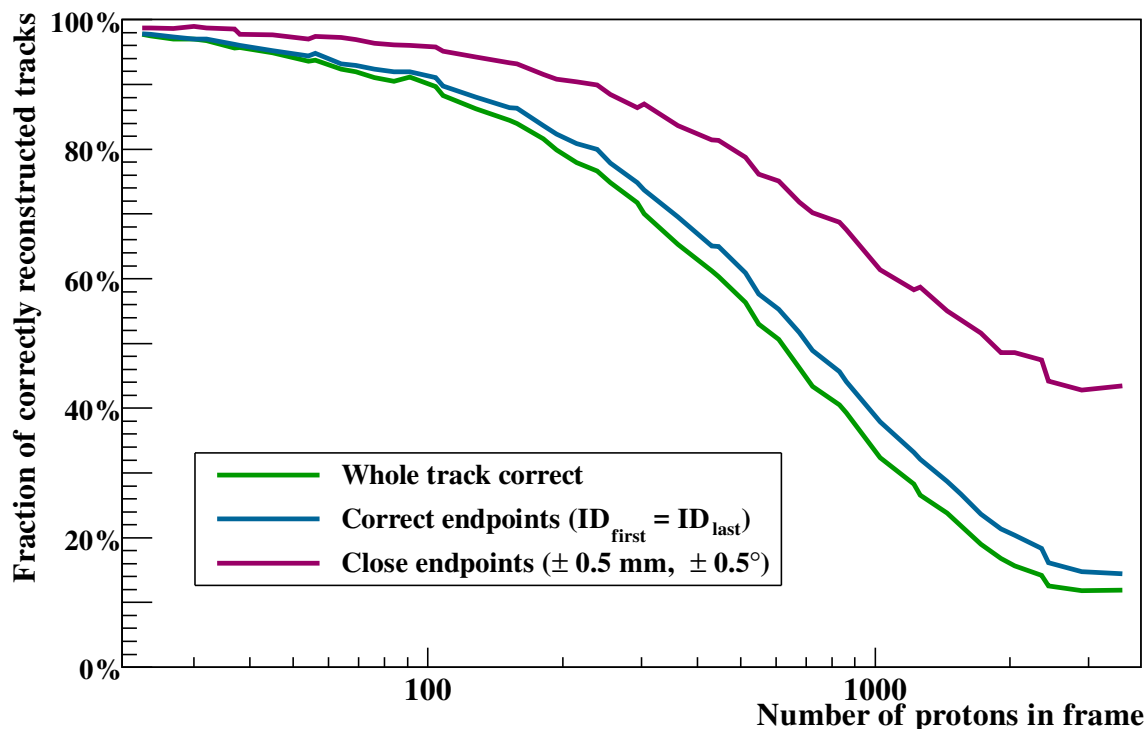
Figure 4.17: *The fraction of correctly reconstructed tracks, benchmarked using MC simulations. Three curves are shown according to different definitions of a correct track reconstructed. From Pettersen et al. (2017).*

may not be true for all applications, such as during pencil beam scanning. The results in Figs. 4.21 and 4.23 as well as the resulting range uncertainties are obtained with $n_p = 500$.

4.6   Range Calculation

There are several components in the range calculation workflow of the DTC, as shown in Fig. 4.18 and in Fig. 4.19. First, the expected range R at a given initial energy E_0 needs to be calculated: this is found using fully scored GATE simulations, retrieved using the spline interpolated look up tables.

Using information about the energy-range relationship obtained from the simulations, a model of the Bragg curve is fitted to the calculated depth-dependent energy loss. In this way, the individual range $\hat{R}$ for each tracked proton is estimated. This process is explained in Section 4.6.2.

The mean value $\langle \hat{R} \rangle$ of the distribution of all the individual ranges can be compared to the "MC truth" R. At this step, some care must be taken to extract a "mean" value from the distribution, as the layered geometry does not produce a simple Gaussian range distribution. This process is discussed in Section 4.6.3.

Then we are able to find the accuracy of the calorimeter (and of the analysis proce-

```
┌─────────────────────────────┐
│ MC simulations with 'full scoring' │
└─────────────────────────────┘
              │
              ▼
┌─────────────────────────────┐
│ 'MC truth' Range distributions │
└─────────────────────────────┘
              │
              ▼
┌─────────────────────────────┐        ┌──────────────────────────────┐
│ Look up tables: E₀ → R, σ_R    │───────▶│ Spline interpolation: find R, σ_R in │
└─────────────────────────────┘        │ look up tables from arbitrary E₀ │
              │                         └──────────────────────────────┘
              ▼                                        ▲
┌─────────────────────────────┐                       │
│ Bragg-Kleeman parameters α, p  │                       ▼
└─────────────────────────────┘        ┌──────────────────────────────┐
              │                         │ Compare to find accuracy ΔR and │
              ▼                         │ uncertainty Δσ_R               │
┌─────────────────────────────┐        └──────────────────────────────┘
│ Bragg-Kleeman + reconstructed tracks │                  ▲
│ = individual proton ranges R̂   │                       │
└─────────────────────────────┘                          ▼
              │                         ┌──────────────────────────────┐
              ▼                         │                              │
┌─────────────────────────────┐        ┌──────────────────────────────┐
│ Measured Range distributions   │───────▶│ Calculate ⟨R̂⟩, ⟨σ̂_R⟩          │
└─────────────────────────────┘        └──────────────────────────────┘
```
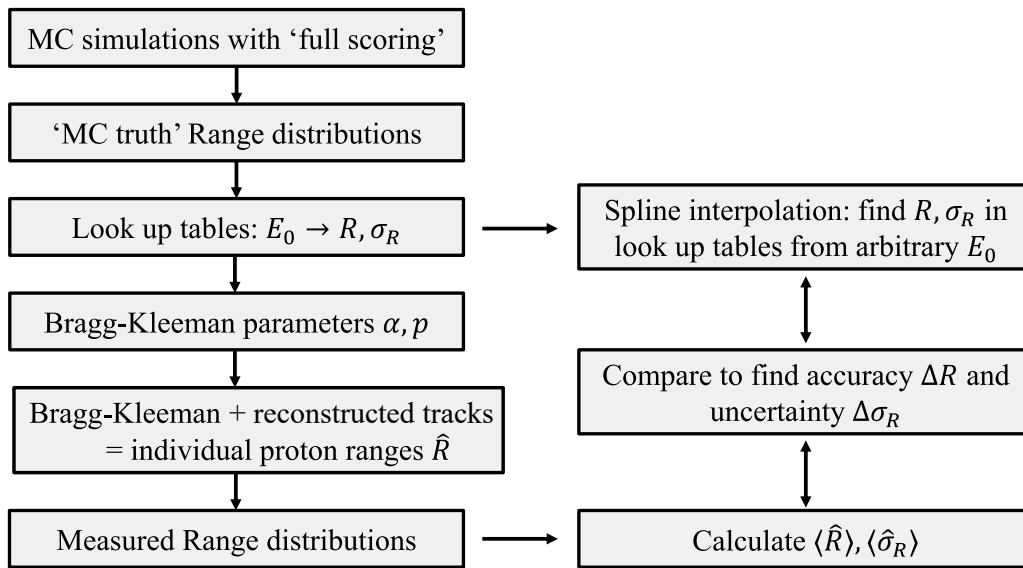
Figure 4.18: *Workflow of the range calculation procedure.*

dure), and this is here defined as the average deviation $\langle\langle\hat{R}\rangle - R\rangle$. The range uncertainty is the total width of the calculated range distribution, $\langle\hat{\sigma}_R\rangle$, and can be compared to the compared to the "true" range straggling in the simulated data σ_R.

4.6.1   The Expected Proton Range

In order to identify the relationship between initial proton energies and the corresponding range of the protons in the calorimeter, LUTs have been generated for the MC simulations of the beamline experiments and for the design optimization of Chapter 5. The most accurate range calculation scheme is the one where pre-calculated values are stored in a spline-based LUT (Section 2.2). Each time a conversion needs to be performed between the initial energy and the range of the proton, or between the range and the WET (via the initial energy), the spline is evaluated at that point.

These LUTs are generated using output data files from MC simulations where all interactions are stored (example in Fig. 4.2), this approach is in contrast to only storing interactions in the sensor chips. In this manner, the "MC truth" range R is found as the mean value of the range distribution of all simulated proton histories. By modulating the initial proton energy in steps of 1 MeV in the range of initial energies that was used in the experimental beam test, an accurate LUT connecting the initial proton energies and final proton ranges is created.

A look-up-table for proton ranges in pure water is also created in order to calculate the WET of a given proton in the DTC: This is done by calculating the energy from the proton range, and then calculate the WET from the energy. Note that this procedure is more accurate compared to using a constant stopping power ratio between water and the
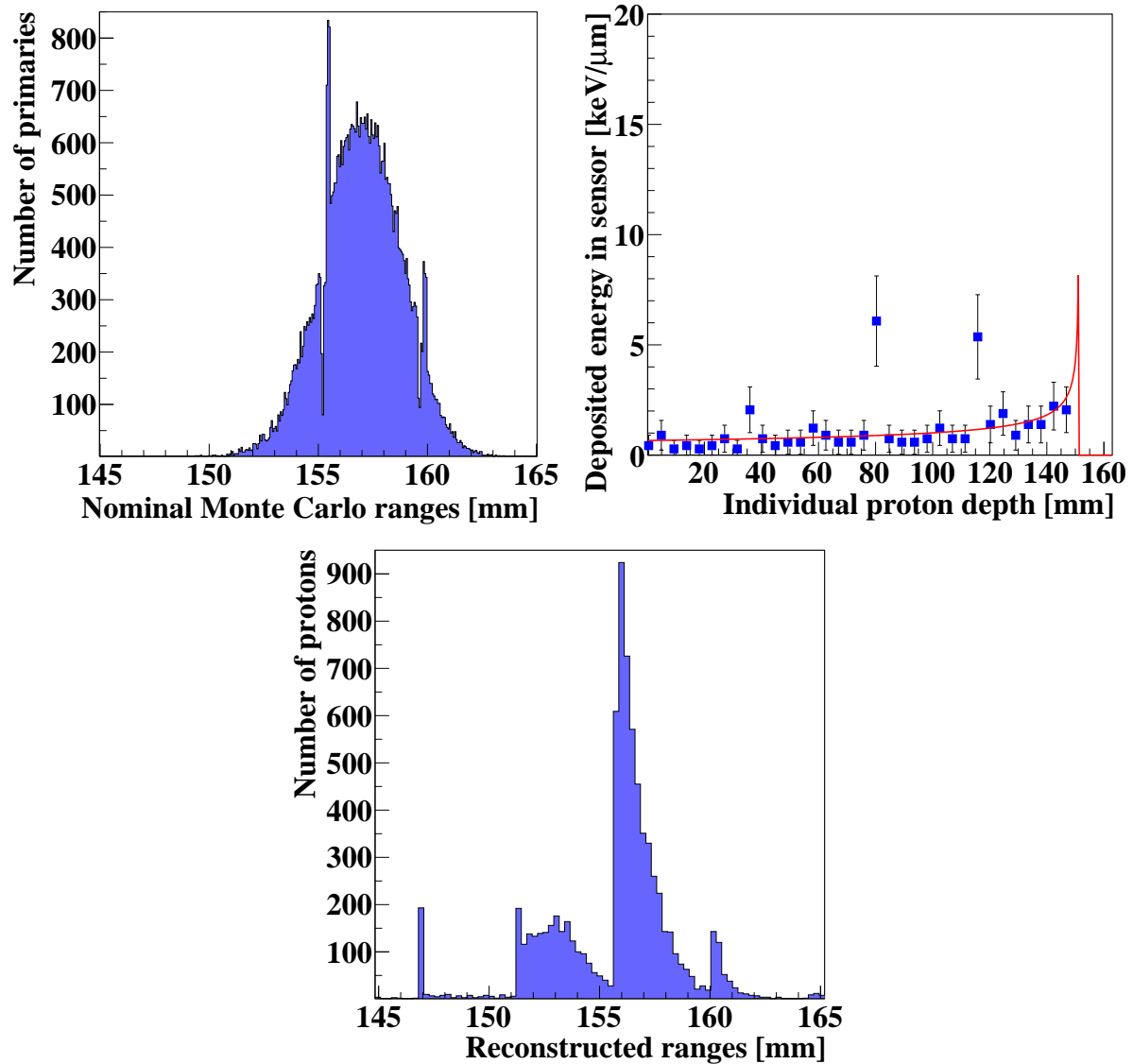
Figure 4.19: *Components of the range calculation procedure.* **Left:** *The "MC truth" range distribution from GATE simulations (the visible artifacts are due to the fact that few protons stop in the air gap layer).* **Right:** *The energy-loss plot from a single proton, used to find the proton's range.* **Bottom:** *The resulting distribution of all individual proton ranges, to be compared to the "MC truth" range distribution. The data is from MC simulations of a geometry defined in Chapter 5, where the energy absorber is a 4 mm aluminum layer.*

detector materials, since the stopping power ratio is only approximately energy independent.

Error Estimation of the Range due to the Absorber Thickness

The error in the range measurements is dominated by the large sampling spacing between the sensor layers. Assuming uniform hit distributions throughout each layer, a first estimation of the error can be calculated as $\Delta z/\sqrt{12} = 3.975\,\text{mm}/\sqrt{12} = 1.15\,\text{mm}$, corresponding to 9.2 mm WET. This error is visualized as the horizontal error bars in Fig. 4.20. While this error is not propagated further in the analysis, it should be compared to the error in the reconstructed range $\langle \hat{\sigma}_R \rangle$ as defined in Section 4.6.3.

4.6.2 Range Calculation of Individual Protons by Bragg Curve Fitting

Each track is constructed from a connected collection of clusters; there is maximum one cluster in each layer for each proton track. The cluster sizes are converted into estimated deposited energy using the method described in Section 4.3. By fitting a Bragg curve to the deposited energy in each layer, the estimated proton range, $\hat{R}$, of a single proton track can be calculated with an improved accuracy compared to that of using the last traversed sensor layer in the track as representing the range of that proton (see the discussion in Section 6.5 for more details). While the spline-based method from Section 2.2 is very accurate when used for the calculation of the range based upon information about the initial energy of the proton, a simpler function such as the differentiated Bragg-Kleeman rule (Bortfeld, 1997) has a smoother behavior around the Bragg peak and is as such more suitable for approximating the energy loss curve:

$$D_{\text{BP}}(z) = -\frac{1}{\rho}\frac{\text{d}E}{\text{d}z} = \frac{1}{\rho p \alpha^{1/p}(\hat{R} - z)^{1-1/p}} \tag{4.12}$$

Here, z is the traversed depth and $\hat{R}$ is the range estimate that best describes the data during the fitting procedure. Furthermore, $\rho = 17.7\,\text{g\,cm}^{-3}$ is the average density of the DTC, and the parameters p and α are found in a similar fashion to those described in Section 4.6.1: by fits to MC simulated ranges in the energy range between 150 and 250 MeV one obtains the values $\alpha = 0.0446\,\text{cm/MeV}$ and $p = 1.668$ in the geometry. Eq. (4.12) exhibits errors at large $(\hat{R} - z)$ values due to the underlying simplifications. However, the estimation is quite accurate near the Bragg peak where $z \to \hat{R}$.

It should be noted that the range estimation takes into account the energy loss of the incident protons in the scintillators providing trigger signal (see Section 4.1.1). The number of traversed scintillators is estimated from an extrapolation of the initial proton

position[*], and a pre-sensor energy loss was estimated and added to the energy of each proton crossing these scintillators.

4.6.3   Estimating the Range from Multiple Proton Tracks

By performing the range fitting procedure as described in Section 4.6.2, an estimate of the range $\hat{R}$ is obtained for each reconstructed proton track. The validity of this estimate depends to a large degree on the position of the Bragg peak relative to the position of the sensor layer where the proton comes to rest. In a longitudinally segmented detector setup, depending on whether the energy of the protons is such that the Bragg peak depth is located within one sensor layer, or as also will happen, if the Bragg peak depth is located between two sensor layers, results with different levels of uncertainties are obtained. If the Bragg peak is located within a sensor layer, the resulting distribution of reconstructed ranges is normally distributed with a central value at the sensor layer depth. By increasing the beam energy slightly, the distal deepest reaching end of the $\hat{R}$ distribution reaches into the next, deeper, sensor layer. In this latter case, two separate distribution appear, each representing the central position of the two sensor layers most adjacent to the center value of the physical Bragg peak.

A Gaussian fit is performed around the depth of each sensor layer in order to identify the distributions of the $\hat{R}$ values. The histogram has bins x_i with widths 2.5 mm and weights w_i. Each fit is evaluated based on the sum n of the bin values in the $\mu \pm 3\sigma$ region, as well as its χ^2/n value. Fits that are positioned in areas with high noise or low statistics are rejected: the cut criteria have been chosen as $n < 0.2N$ and $\chi^2/n > 8$. Here, N is the total number of entries in the histogram.

The resulting Gaussian distributions are determined by (μ_1, σ_1) and potentially (μ_2, σ_2) if a second distribution is found, where $\mu_1 < \mu_2$. This procedure is performed in order to find the histogram bin with the lowest range value $x_{i'}$ in the Bragg peak region. The range value for the bin is defined relative to the first Gaussian, where $x_{i'} \equiv \mu_1 - 3\sigma_1$. This cut on the range will further ensure that the overall range estimate is based only on proton tracks slowing down to low speed and stopping in the matter, thus generating a Bragg peak.

The reconstructed range $\langle \hat{R} \rangle$ is calculated as the weighted average from the histogram bins. The corresponding range uncertainty $\langle \hat{\sigma}_R \rangle$ is the empirical standard deviation of the

---

[*]The initial proton vectors are assumed to be parallel. Any measurement of the initial angular deviation, using information from the the first two sensor layers, is dominated by the scattering in the detector materials.

same histogram. These parameters are calculated by

$$\langle \hat{R} \rangle = \frac{\sum_{i=i'}^{\infty} w_i x_i}{\sum_{i=i'}^{\infty} w_i}, \qquad \langle \hat{\sigma}_R \rangle = \sqrt{\frac{\sum_{i=i'}^{\infty} w_i (x_i - \langle \hat{R} \rangle)^2}{[\sum_{i=i'}^{\infty} w_i] - 1}} \qquad (4.13)$$

By calculating the standard deviation of the reconstructed range, without making any assumptions of the shape of the distribution of the data or by performing any fits to the data, the range uncertainty $\langle \hat{\sigma}_R \rangle$ for a given dataset can be estimated in a direct way, avoiding the propagation of errors that are introduced when adding multiple Gaussian distributions.

4.7   Accuracy and Uncertainty of the Range Calculations

After performing the range fitting as described in Section 4.6.2, estimates of the range $\hat{R}$ are obtained for each individual proton track. The Bragg curve fit to three individual protons tracks are displayed in Fig. 4.20. In that figure, the displayed "$\pm$" accuracy is the output from the least-square method applied on an individual proton, and it is not representative for a proton beam of that energy. Some of the tracks are missing measurements in some of the layers, this is due to bad readout channels.

The range uncertainty $\langle \hat{\sigma}_R \rangle$ is always larger than the inherent range straggling. This lower limit of the accuracy can be estimated to be $\langle \hat{\sigma}_R \rangle_{\min} = 0.017 R^{0.935}$, in units of WET. This is the range straggling as it is observed in MC simulations where the full detector volume has been scored. This value is slightly larger than the range straggling occurring in pure water, which is approximately $0.012 R^{0.935}$ (Bortfeld and Schlegel, 1996).

A summarizing figure with the range accuracy and range uncertainty results from both the MC simulations and experimental data can be seen in Fig. 4.23.

4.7.1   Experimental Data

As described in Section 4.6.3, the range distribution from multiple proton events is approximately Gaussian distributed around each sensor layer. A Gaussian fit procedure is applied in order to estimate the reconstructed range $\langle \hat{R} \rangle$ of protons with different individual ranges $\hat{R}$. The available range distributions for the experimental datasets of different energies are shown in Fig. 4.21. Note the short ranges due to identified nuclear interaction processes: these are removed from the analysis. A comparison between the experimental data and MC simulations at 188 MeV is also shown in Fig. 4.22. A table showing the different results can be found in Table 4.3.

The expected range straggling is 2.6–2.8 mm WET, found from the proton range in the detector and the initial energy spread of the beam in accordance to Eq. (1.12).
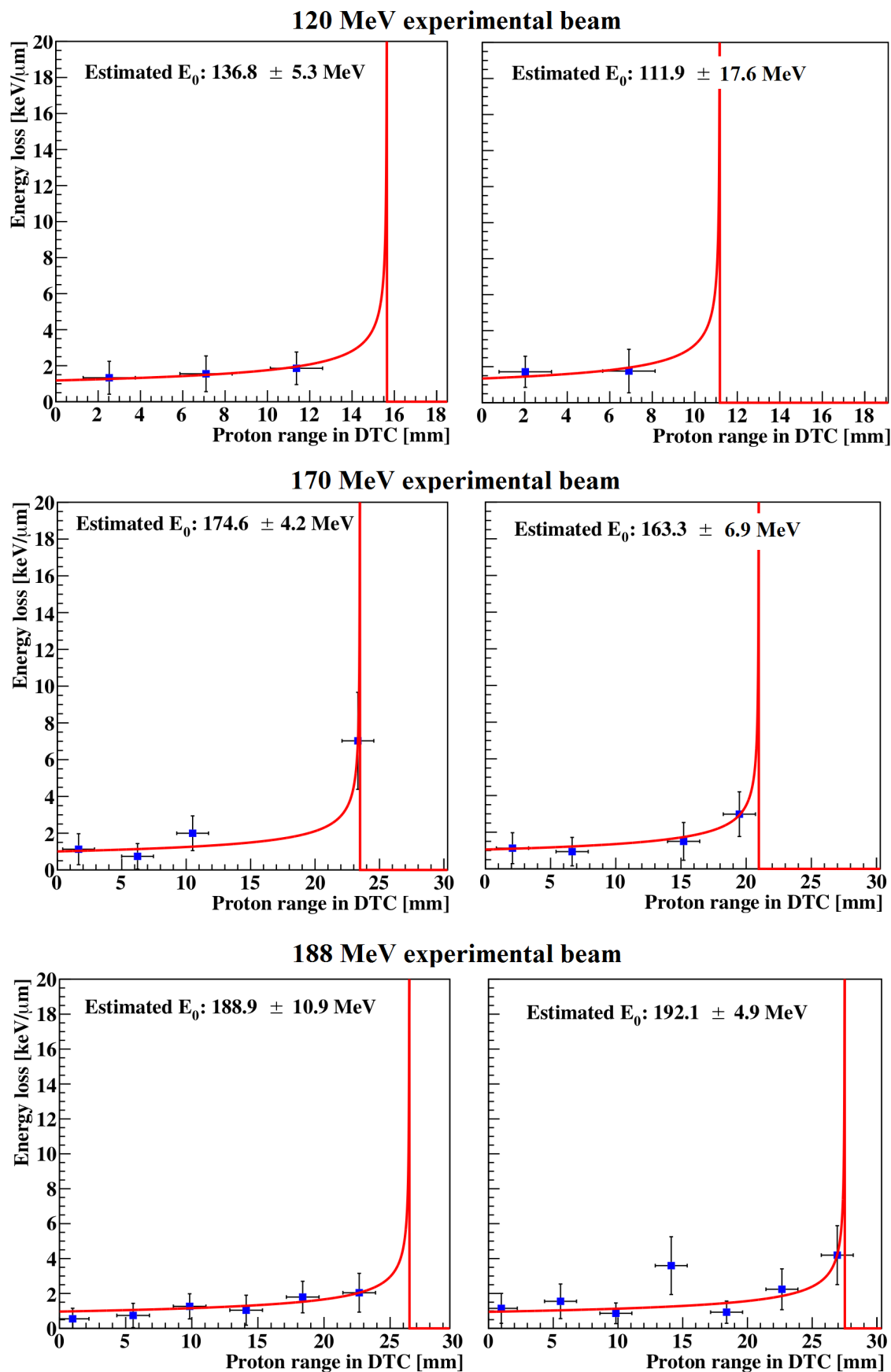
Figure 4.20: *Bragg curve fit (solid line) to individual proton tracks from the experimental data. The data points display the proton's depth and energy loss in each traversed layer.*

The range uncertainty and range accuracy (systematic error) depends on whether one or more sensor layers are covered by the range straggling distribution.[*] The measured range uncertainty is on average 6.8 mm WET (4.4%) with one sensor layer included (120 MeV, 160 MeV and 180 MeV), and 20.1 mm WET (11%) with two or more sensor layers included (139 MeV, 170 MeV and 188 MeV). The latter is perhaps more indicative of the reality. Conversely, as expected, the range accuracy is low when one sensor layer is covered, at $\langle \langle \hat{R} \rangle - R \rangle = -13.4$ mm WET, and higher when two layers are covered, at $\langle \langle \hat{R} \rangle - R \rangle = -4.7$ mm WET.

4.7.2   Monte Carlo Simulations

A set of MC simulations was performed with beam energies varying from 145 MeV to 200 MeV, increasing the beam energy in steps of 1 MeV. The reconstructed ranges $\langle \hat{R} \rangle$ from each dataset are shown in Fig. 4.23.

For beam energies between 145 MeV and 200 MeV, the average estimation error $\langle \hat{\sigma}_R \rangle$ based on Eq. (4.13) is 9.4 mm WET (4.6%), and the average absolute deviation from the expected range $\langle \langle \hat{R} \rangle - R \rangle$ is -3.3 mm WET (1.7%). The values for $\langle \hat{R} \rangle - R$ vary from -7.9 mm WET to 0.3 mm WET due to an oscillatory behavior of the estimation (see Fig. 4.23). The oscillatory pattern is thought to be due to the under-sampling of the Bragg curve, with a spacing between the sensor layers of approximately 32 mm WET: this will be a consequence of protons depositing a significant part of their energy, forming a Bragg peak in an absorption layer. In other words, in Fig. 4.23 it is observed that beam energies resulting in a Bragg peak that covers two sensor layers are more accurate, with a dip in the range accuracy when only one sensor layer is covered.

In the next chapter we will further explore this oscillatory pattern, together with the limits for both the resolution accuracy and the range uncertainty when the large thickness of the energy absorbers is reduced in a MC study.

4.8   Conclusions on the DTC Benchmarking

The materials used in the current version of the DTC are optimized for applications in a high energy physics experiment. Due to this, every sensor layer is separated by tungsten absorbers of 32 mm WET. This sets an upper limit to the accuracy with which the range and energy of protons can be determined in the present prototype.

The measured range uncertainty is 14 mm WET (8.2%) on average, depending on whether one or two sensor layers are covered by the beam. The obtained range uncer-

---

[*]At least 20% of the total entries must be located around a sensor layer for it to be included in the calculation, to reduce noise from lower-energy tracks
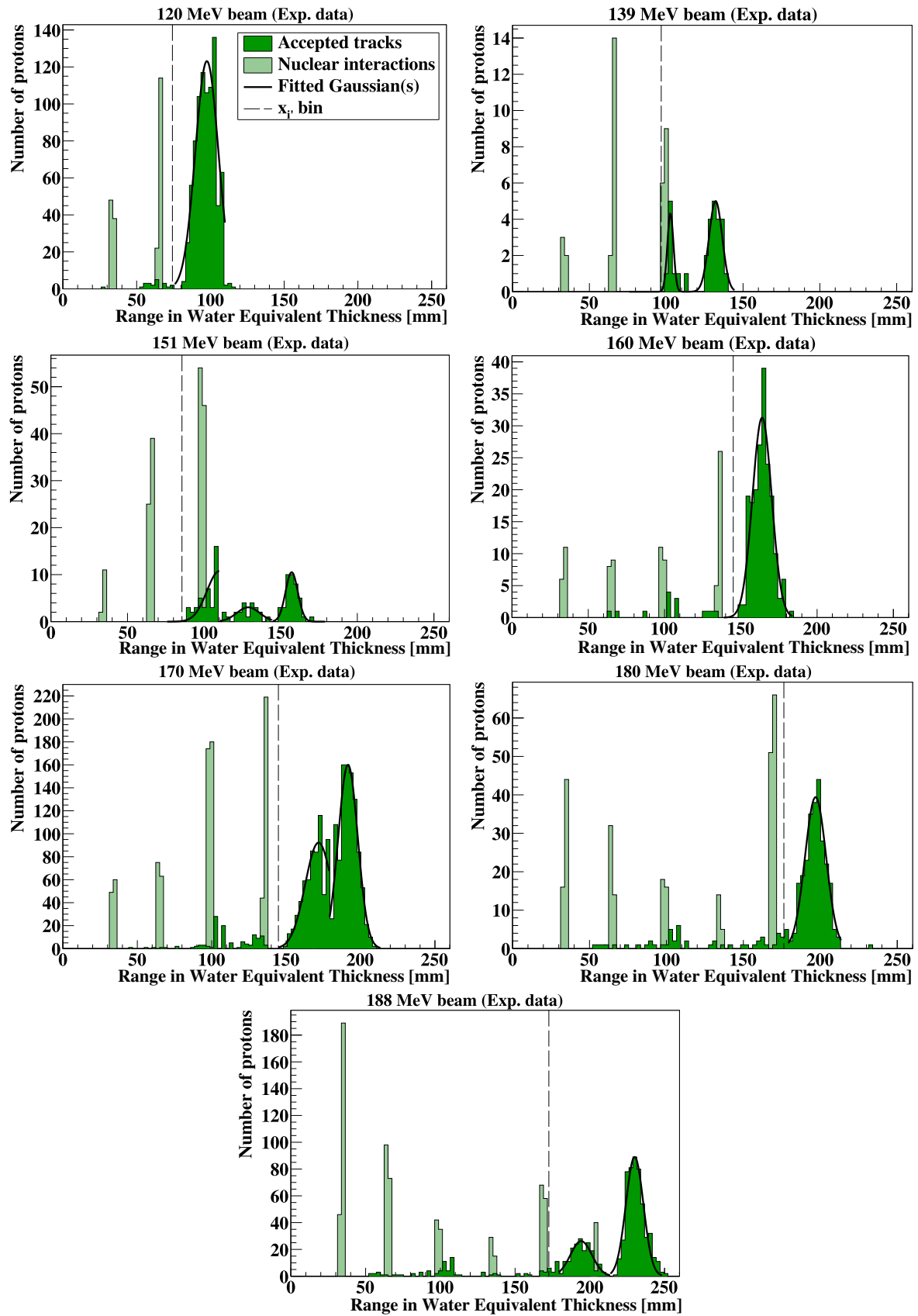
Figure 4.21: *Range ($\hat{R}$) distributions from Bragg curve fits. The dashed line indicates the lowest-range bin used for the range estimation (see the text). The 32 mm WET spacing between the peaks correspond to the spacing between the sensor layers.*
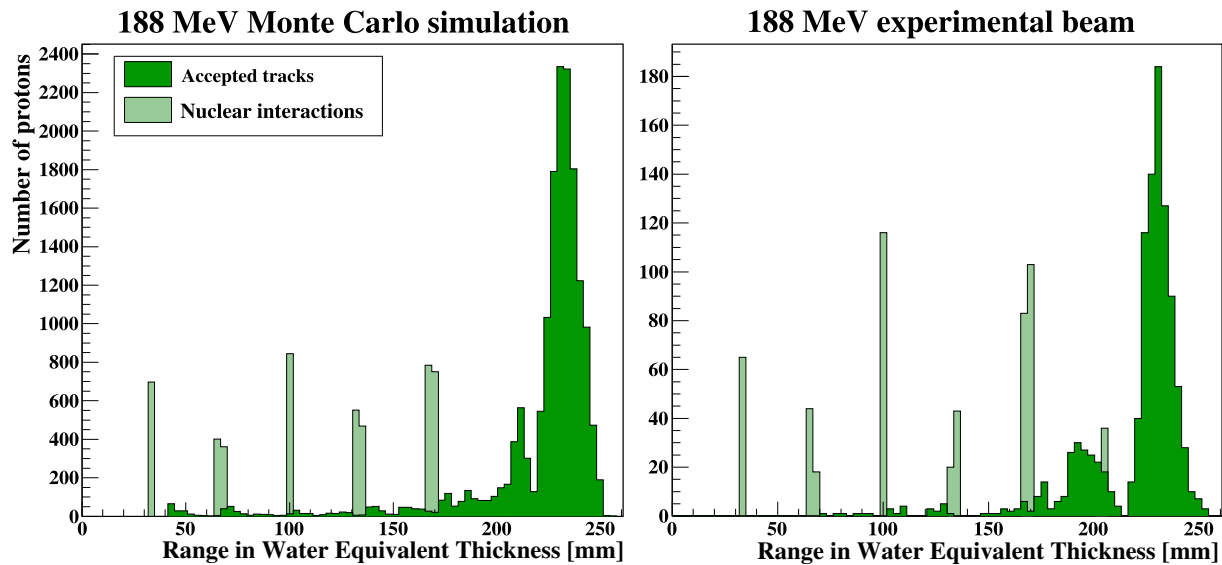
Figure 4.22: *Range estimation distributions from Bragg curve model fits — comparison between the MC simulations and the experimental beam at 188 MeV. Adapted from Pettersen et al. (2017).*
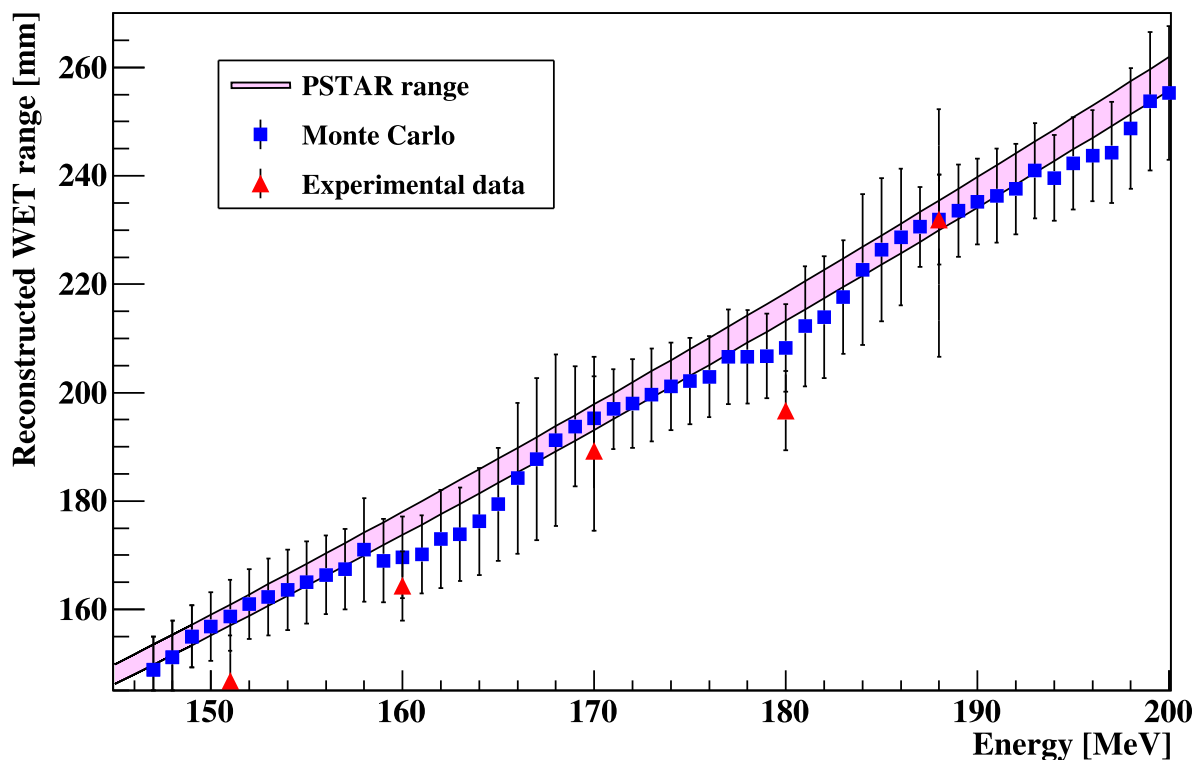
Figure 4.23: *Reconstructed WET ranges of proton beams with different energies, with data from both the MC simulations and from the experimental measurements. The PSTAR (water) range is displayed using a band representing the expected range straggling. From Pettersen et al. (2017).*

Beam energy [MeV]	120	160	180	139	170	188	151
Layers covered	1	1	1	2	2	2	3
Nominal range R [mm]	105.9	175.7	215.9	137.5	195.7	232.7	158.8
Reconstructed range $\langle \hat{R} \rangle$ [mm]	97.0	164.0	196.2	132.2	188.5	231.1	137.8
Range error $\langle \langle \hat{R} \rangle - R \rangle$ [mm]	-8.9	-11.7	-19.6	-5.2	-7.2	-1.6	-21.0
Rel. range error [%]	-8.4	-6.7	-9.1	-3.9	-3.7	-0.7	-13.2
Nom. range straggling σ_R [mm]	2.6	2.8	2.8	2.6	2.8	2.8	2.7
Range uncertainty $\langle \hat{\sigma}_R \rangle$ [mm]	6.5	6.3	7.5	19.1	16.3	25.1	17.4
Rel. range uncertainty [%]	6.1	3.6	3.5	13.9	8.3	10.8	11.0

Table 4.3: *Range accuracy and uncertainty of the experimental data. Ranges and range accuracies are given in WET. The nominal range straggling is calculated from the energy straggling of the proton beam added to the expected range straggling from the detector. The "Layers covered" number reflects how many sensor layers that are covered by the range straggling distribution (see Fig. 4.21), the table is sorted by this value.*

tainty varies with different incident energies, from around 6.3 mm WET from the 160 MeV beam test to 25 mm WET from the 188 MeV beam test.

The results of this work indicate that the DTC can be used for track reconstruction and range estimation for a significant number of concurrent proton tracks at therapeutic energies. The proof-of-concept tracking calorimeter shows that a next version with a more optimized prototype has the potential of enabling fast and accurate determination of the ranges of individual protons in a therapeutic proton beam.

The intensity capacity of a uniformly distributed beam was found to be in the order of 10^6 protons/s, or 60 000 protons/s/cm². The number depends on the performance of the tracking algorithm and the spatial distribution of the proton beam. An improved algorithm would increase the accuracy of the track reconstruction, and would enable for separation of a higher number of protons in each readout frame.

The intensity capacity presented in this work is at the high end of the capacities of existing prototypes, where the current fastest proton CT systems are able to handle 2×10^6 protons/s (Johnson et al., 2016; Uzunyan et al., 2013a), and DeJongh (2017) aiming for a readout speed of 10^7 protons/s.

Chapter 5

Design Study of the Digital Tracking Calorimeter

In this work, the performed data analysis have been based upon a experimental results from a prototype of the Digital Tracking Calorimeter (DTC) made for the ALICE-FoCal experiment. This work has been performed as a proof-of-concept for the DTC.

In this chapter, we will apply the experience from this first prototype in order to propose a design for the next prototype of the DTC. As the next prototype of the DTC will follow similar design principles as the ALICE-FoCal prototype: large-area arrays of pixel sensor layers are to be stacked in the longitudinal direction of the detector, the layers being interleaved with energy absorbing layers.

The aim for the design study to be outlined here is to optimize the various properties of a DTC for its use as an integral part of a detector for proton CT purposes. The simultaneous optimization is performed of the following metrics: high accuracy of the range determination; low uncertainty (a low standard deviation) in the range determination, this is limited by the proton beam's range straggling; high track reconstruction efficiency, i.e. the ability to disentangle and reconstruct all the protons in a single read-out frame; and other constraints such as economy (the number of layers), cooling and mechanical stability.

The range accuracy will have impact on to which degree the Relative Stopping Power (RSP) map for the patient's body is correctly identified, while a high range certainty and an efficient track reconstruction enables that fewer protons are needed during the scan, i.e. a lower dose to the patient and a shorter scan time and a higher signal to noise ratio.

The design optimization is here performed through the determination of an optimized thickness of the energy absorber material between the sensor layers, as well as the choice of the absorber material itself. We are considering several different values for the thickness and will carry out the analysis as presented in the former chapters on Monte Carlo

(MC) simulated data.

5.1   The ALPIDE Sensor Chip

One of the design choices that was made early in the planning phase of the next proto-type of this detector, was that of the sensor chip type: the chip ALPIDE (ALICE Pixel Detector) (Mager, 2016) is to be used. This choice reflects that the planned upgrade of the ALICE Inner Tracking System (ITS), is based on the ALPIDE chip which has been developed for that specific purpose.

This ongoing development process for the ALICE experiment simplifies many of the tasks also for the next DTC prototype development: chip wafer production, mechanical and electrical integration of the chips as well as the design of the readout electronics, software and chip testing regimes.

The ALPIDE chip can be compared to the MIMOSA23 chips used in the first DTC prototype: It is a Monolithic Active Pixel Sensor with digital threshold readout, it has approximately the same chip dimensions ($3 \times 1.5\,\mathrm{cm}^2$) and pixel dimensions ($28 \times 28\,\mathrm{\mu m}^2$). However, in many respects, it is a significant upgrade with favorable properties for proton CT usage: A fast integration time of $5\,\mathrm{\mu s}$ with a readout chain capable of handling a continuous readout at that rate is achieved by the reduction of data, through: the regional pixel readout via a priority encoder, a multi-event memory and a so-called *zero-suppression* technique, where only activated pixels send a signal. The integration time of $5\,\mathrm{\mu s}$ can be compared to the readout capabilities of the MIMOSA23 chip, where the integration time for continuous readout was set to be $642\,\mathrm{\mu s}$.

In Fig. 5.1, a prototype of the ALPIDE chip can be seen mounted to a carrier board. In a proposed setup, using design elements from the ITS Inner Barrel project, nine ALPIDE chips are mounted horizontally to a single carrier board. Several such carrier boards can then be stacked vertically, enabling a detector area of $27 \times (n \times 1.5\,\mathrm{cm}^2)$.

The design constraints from the the planning work discussed above is used for the MC optimization in this chapter. However, as the details are preliminary they might not reflect the final DTC to be constructed. More details on the ALPIDE chip can be found in Mager (2016), and in the MSc thesis of Grøttvik (2017) where a proton CT readout system using the ALPIDE chip is explored.

5.2   Design Guidelines of the Next DTC Prototype

By considering several different values for the spacing and carrying out the analysis as described in Chapter 4, potential geometries are explored through through MC simula-
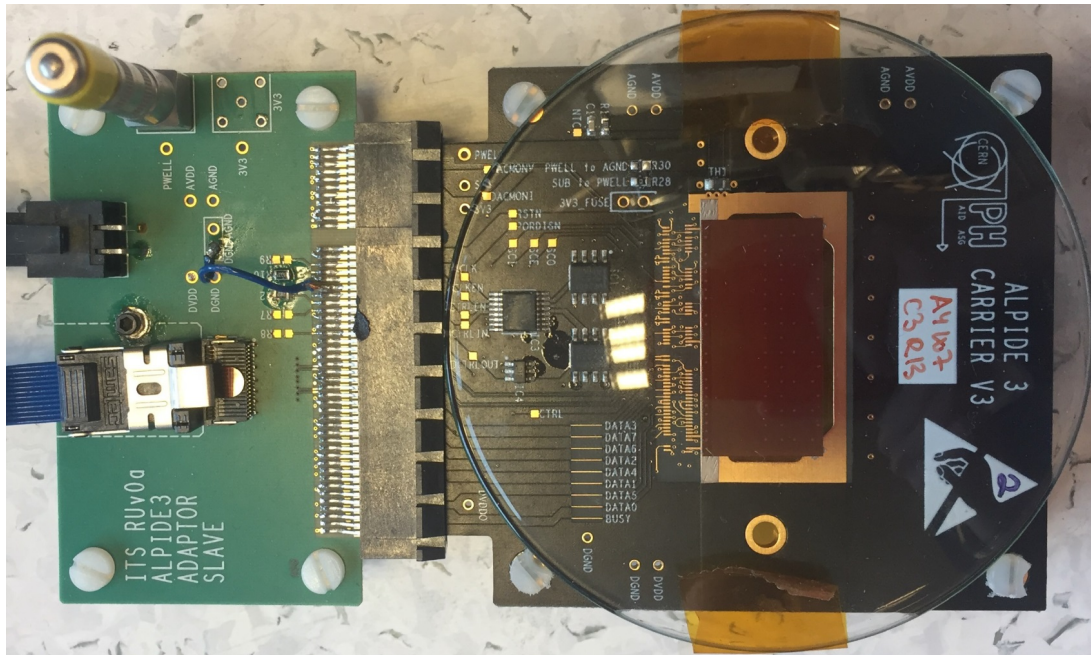
Figure 5.1: *The ALPIDE chip, mounted to a carrier board (right), here protected by a glass disc, and the adapter slave connection to the DAQ. From ALICE-ITS / Grøttvik (2017).*

tions with respect to the of the range accuracy (systematic bias of range determination), range uncertainty (in addition to the inherent range straggling), tracking efficiency as well as economy: driven by the number of layers and the number of chips per layer needed.

Several geometrical configurations are needed in order to compare and evaluate the desired detector metrics. It is possible to define a large number of potential designs for the DTC, and therefore some constraints must be put on the degrees of freedom in this work. A baseline design based on the original ALICE-FoCal prototype from Chapter 3 is shown in Fig. 5.2. While the geometry of the sensor chips and electronic components are unaltered, the energy absorbers between the sensor layers are chosen to be between 2 mm and 6 mm aluminum (the choice of aluminum is discussed below).

In order to achieve a high accuracy in the measurement of the initial proton vectors, the two first layers should contain as little mass as possible. To this end, the first absorber layer is removed and the cavity is filled with air.

Details such as chip bonding, aspects related to the mechanical structure, heat sink design and the readout electronics are out of scope of this work and, also, not yet finally decided upon. As a result of this, the exact results of the simulations will not reflect the detailed final prototype. Several simplifications are made during the geometrical designs for the MC simulations, such as using homogeneous slabs of materials rather than implementing accurate designs with details such as the ALPIDE chips bonded to
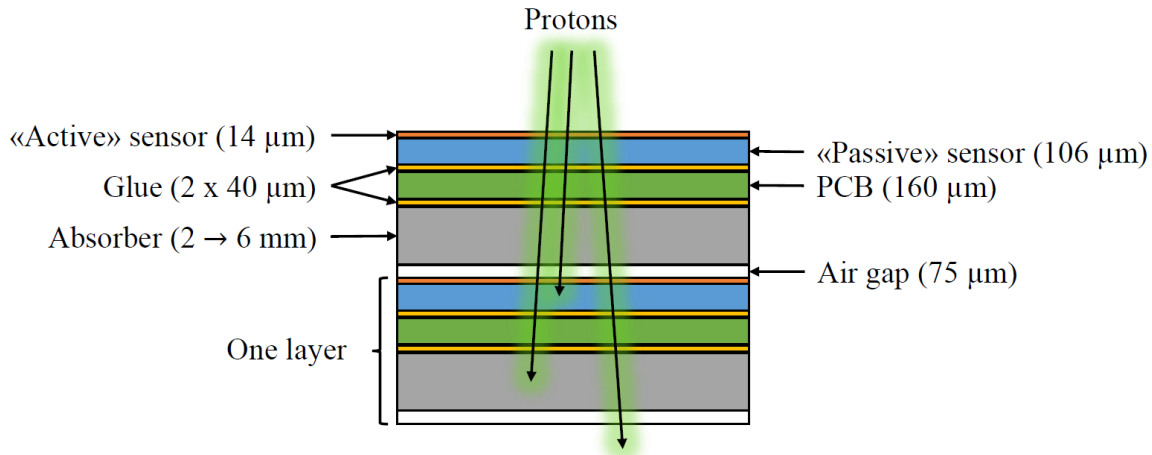
Figure 5.2: *The design to be optimized: Different thicknesses (2–6 mm) for the energy absorbers are considered, and evaluated through the MC simulations. Only the "active" sensor volumes are scored in the MC simulations.*

the PCB, glued to a backing together with absorbers and heat sinks, all mounted to a scaffolding. Nevertheless, the longitudinal distribution of materials will be modeled and included to the level of available knowledge.

Different materials are available for application as the absorber material. Material properties such as proton stopping- and scattering power, durability, ease of machining and mounting, thermal conductivity, thermal expansion of the absorber material and secondary neutron production must be considered, as well as the interface between the absorber and the aluminum carrier board for the sensor chips (e.g. having similar thermal expansion coefficients). See Table 5.1 for a list of different properties: the WET is found by finding the thickness which yields the same stopping power as 4 mm water. The scattering angle is calculated with the Highland equation (Eq. (1.7)) for a 150 MeV proton through a 4 mm WET slab. The neutron yield is the number of neutrons produced per incoming proton, and is accurate to 6% from Poisson statistics (150 MeV beam in a slab of 4 mm WET, found in the GATE simulations by using the `QGSP_BIC_HP`[*] physics list and 10^5 primaries).

Based on these, and in particular that the flexible PCB cables connected to the ALPIDE sensors are mounted to an aluminum backing, the material of choice for the absorber is aluminum. The MC simulations that are reported on here focus on aluminum as the absorber material, however MC simulations using graphite as the absorber material were also conducted. They did not yield any substantial differences in terms of track reconstruction quality and range resolution, and are therefore not reported upon.

---

[*]HP: High Precision Neutron calculations down to thermal energies.

Material	PMMA	Graphite	Aluminum	Copper	Tungsten
4 mm WET equivalent [mm]	3.46	2.24	1.9	0.66	0.4
Scattering angle [mrad]	3.25	4.7	6.0	9.2	15.3
Neutron yield [10^{-4}]	69.2	71.9	80.9	74.1	26.9
Thermal conductivity [W/mK]	0.25	25–240	205	401	174
Thermal Expansion [10^{-6} K^{-1}]	70	4–8	21–24	16	4.5

Table 5.1: *Properties of the potential absorber materials (Particle Data Group, 2015; Touloukian et al., 1971; Goodfellow Inc., 2018).*

5.3 Monte Carlo Simulations of Different Geometries

To perform the data analysis to the level required to calculate the desired performance metrics, the MC simulations must contain the following: A proton beam with realistic spatial and (adjustable) spectral characteristics, and an sufficiently accurate geometrical implementation of a stack of ALPIDE chips fixed to absorber layers of adjustable thicknesses.

A water phantom of variable thickness is used to modulate the a monoenergetic beam to different energies. The stochastic energy loss throughout the beam ensures that the resulting energy and spatial distribution incident on the detector is realistic.

The overall design of the setup is similar to the one described in Section 4.6.1: The beam is placed in front of the water phantom, uniformly distributed from a plane, with an area of $100 \, cm^2$, parallel to the sensor area.

The MC software GATE version 7.2 has been applied, together with the physics builder list `QGSP_BIC_EMY`, using default settings for step length and particle threshold (Grevillot et al., 2010). The mean ionization potential for water is set to 75 eV in order to facilitate comparisons with the PSTAR database (Berger et al., 2005).

The "GATE Geometry Builder" software tool developed for this project was described in Section 4.2.3 and it is used here for the purpose of generating DTC geometries with different absorber thicknesses. The purpose is dual: First to rapidly generate different geometries without manually calculating and propagating all the necessary geometrical parameters, and secondly to ensure that the geometries do not contain errors from the input or manual calculations.

When the GATE software has been configured for a single geometry, a number of scenarios are defined by generating MC simulations of proton beams with realistic energy spectra and a fine stepwise variation of the initial energy in order to characterize the linearity of the range determination accuracy.

5.4   Analysis Workflow

In order to obtain the best possible estimates of the performance of the different DTC designs, the different parts of the analysis are treated separately: The track reconstruction step is omitted during the evaluation of the residual range calculation, where the tracks are obtained directly from the "MC truth" using the primary proton identification ID from GATE.

Using a perfect track reconstruction, the Bragg curve fitting methodology as described in the last chapter is applied to find the reconstructed range $\hat{R}$. The mean range $\langle \hat{R} \rangle$ and the corresponding range uncertainty $\langle \hat{\sigma}_R \rangle$ are found for each beam energy using a modified version of the method described in the last chapter. These results from the different geometries under study are compared.

Then, a modified version of the tracking algorithm from the last chapter, optimized for a denser layer geometry, is applied on the data. Here, the track reconstruction efficiencies from the different geometries are compared.

5.4.1   Proton Range from "MC Truth"

The final results from the range calculations that emerge from the following sections need to be compared to a ground truth, and separate MC simulations are made for this purpose.

The methodology for comparing the calculated proton range to the "MC truth" is similar to the one described in Section 4.6, however a energy degrading water phantom is modeled in order to obtain a better estimate of the energy spectra. A short summary is given below:

A mono-energetic 250 MeV beam is modulated to represent realistic energy spectra with residual proton ranges that span the complete DTC in depth. The water phantom thicknesses vary from 0 cm to the maximum water equivalent range of the beam, approximately 38 cm, in steps of 1 mm. The beam is uniformly distributed from a plane source, with an area of $100\,\mathrm{cm}^2$, parallel to the sensor area. In Fig. 5.3 the simulated setup is shown. A look-up-table containing phantom thicknesses, proton energy incident on DTC and residual DTC range is created, by using the geometrical input files as described above and recording the interactions in all volumes. This is repeated for all design variants and water phantom thicknesses.
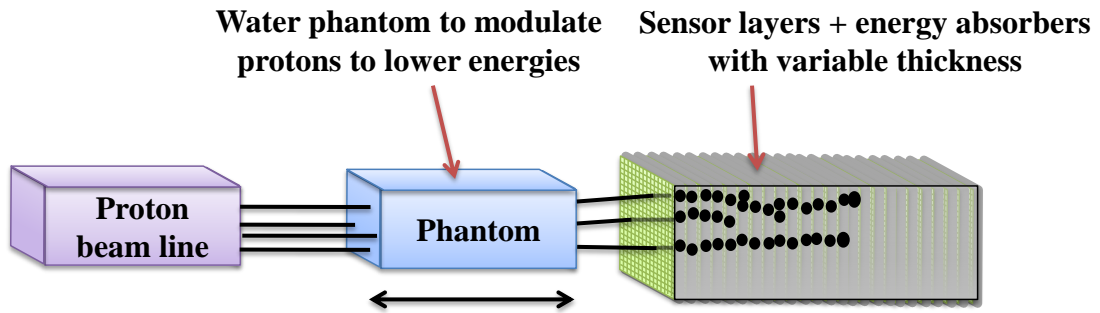
Figure 5.3: *Schematic setup of the range calculation geometry. In order to obtain a spectrum of different proton beams to hit the DTC, the thickness of the energy degrading water phantom is modulated from 0 cm to the maximum range of a 250 MeV beam, which corresponds to a water phantom length of approximately 38 cm.*

5.4.2   Range Accuracy and Range Uncertainty

The range accuracy and range uncertainty resulting from a specific design variant can be found by comparing the *nominal* proton range distribution R to the *reconstructed* proton range distribution $\langle \hat{R} \rangle$. See Fig. 4.18 for an comparison between the two. The *range accuracy*, or $\langle \langle \hat{R} \rangle - R \rangle$, is found by comparing the systematic error of the mean value of the range distribution throughout the full dynamic range of the detector (in terms of proton range). The *range uncertainty* is found by comparing the widths of the two distributions, respectively, σ_R and $\langle \hat{\sigma}_R \rangle$. Any added width in the reconstructed range distribution is due to the degrading effects of the detector and to the analysis routine.

Since the range uncertainty due to range straggling is known from theory (Eq. (1.11)) and from the MC simulations, the intrinsic range uncertainty from the analysis can be calculated by subtracting in quadrature the expected range straggling from the measured range uncertainty.

It is not expected that the uncertainty and accuracy for a given geometry are the same at different incident proton energies, as the values are dependent on the relative position between the proton range position versus the sensor layer position: This effect was clearly seen in the ALICE-FoCal prototype, as described in Chapter 4.

It is also of interest to calculate other system properties: The fluctuation of the range accuracy relative to the proton range relative to the sensor layer depth, and the effect on the proton trajectory estimation error of the scattering in the first layer material.

5.4.3   Track Reconstruction

One of the strengths of the DTC design is the ability to disentangle and reconstruct a large number of concurrent traversing proton tracks. To this end, a track reconstruction method
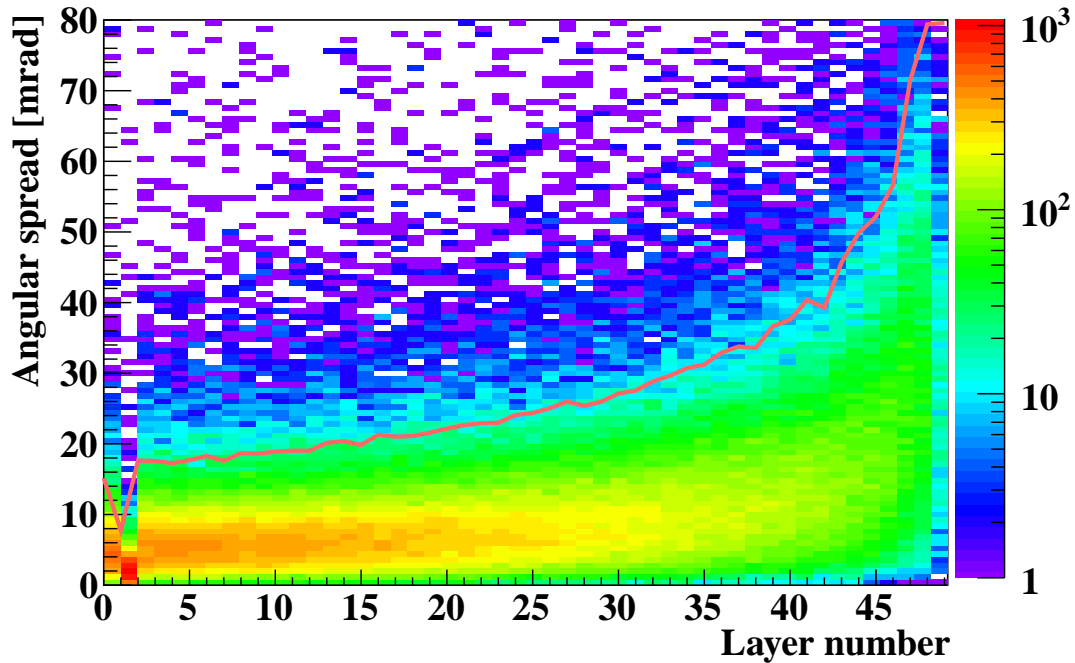
Figure 5.4: *Proton track angular change at different layers, using a 3 mm aluminum geometry with a 250 MeV beam modulated by a 1 cm water phantom. The solid line is the fitted "3σ" value of the distribution at each layer.*

was developed, as described in Chapter 4 for the ALICE-FoCal prototype geometry. The methodology needs some adjustments in order to be efficient for the thin-absorber geometries:

To find values for the *search radius* (defined in Chapter 4) that better represent the actual scattering power, an empirical approach was chosen: For each DTC design (and for each incident energy), a large number of "MC truth" tracks are found using the primary proton identification ID from GATE. Then, for each layer, the scattering distribution is found, e.g. a distribution of angular deviations. The "3σ" value of a fitted Gaussian distribution is used for choosing the search radius in a given scenario. See Fig. 5.4 for a distribution of angular change values in a geometry with 3 mm aluminum absorbers. The angular changes are smaller in the second layer, since it is a "tracking" layer without the aluminum absorbers.

If the individual incident proton energy is unknown (as often is the case with experimental data), an alternative approach is to choose a constant scattering angle threshold based on the distributions — the value of $k_i \cdot 50$ mrad is chosen for this purpose. The track-following scheme is performed two consecutive times using different values for k_i: $k_1 = 2$ and $k_2 = 3$. Due to the fact that the protons are subject to a higher scattering power towards the Bragg peak, the track reconstruction is performed two more times starting at the last identified hit towards the Bragg peak: This time the values $k_3 = 5$ and $k_4 = 7$ are chosen as to include proton paths with a high degree of scattering.

The Correctly Reconstructed Track

In order to benchmark the precision and efficiency of the track reconstruction algorithm as described above, a definition of a correctly reconstructed track must be made. The constraints are defined as: the first and last entry in a track must originate from the same proton history, and the last hit from a proton history must be included. By following this definition, track objects have the correct incoming vector and the correct residual range, which is the required values for volumetric reconstruction of the stopping power map for proton CT purposes.

The *efficiency* of the track reconstruction is defined to be the ratio of correctly reconstructed tracks to the total number of identified tracks. Tracks that are stopping due to inelastic collisions should not degrade the efficiency; they can be identified due to a lack of an increase in the deposited energy at the distal part of the track due from the Bragg peak (see Section 4.4.2). The efficiency is found as a function of an increasing number of protons that are reconstructed simultaneously.

5.4.4   Range Calculation

Least-square fits are performed using the Bragg curve on the track's energy loss measurements in each sensor layer to obtain $\hat{R}$. Examples from the different geometries are shown in Fig. 5.5. Note that the range found using thinner absorber designs yields a visibly higher range determination accuracy of individual proton tracks. The mean value and the standard deviation are calculated from the resulting range distributions, shown in Fig. 5.6. The ranges of all protons in a beam (or a voxel, if used for image reconstruction) contribute to a histogram with bin values x_i and bin heights w_i. The lower and upper limits, respectively, x_1 and x_2 for the range distribution is defined as the $\mu \mp 4\sigma$ values. Then, we have

$$\langle \hat{R} \rangle = \frac{\sum_{i=x_1}^{x_2} w_i x_i}{\sum_{i=x_1}^{x_2} w_i}, \qquad \langle \hat{\sigma}_R \rangle = \sqrt{\frac{\sum_{i=x_1}^{x_2} w_i (x_i - \langle \hat{R} \rangle)^2}{\left[\sum_{i=x_1}^{x_2} w_i\right] - 1}} \tag{5.1}$$

The above procedure is similar to the analysis for the ALICE-FoCal prototype, described in detail in Section 4.6, with the difference being the method of fitting the Gaussian distributions to the histogram values. In the geometries described here, a higher number of sensor layers are contained within a range distribution, and as such it is possible to fit a single distribution to the distribution of $\hat{R}$ values. The results of these calculations are compared to the ground truth obtained from separate MC simulations.
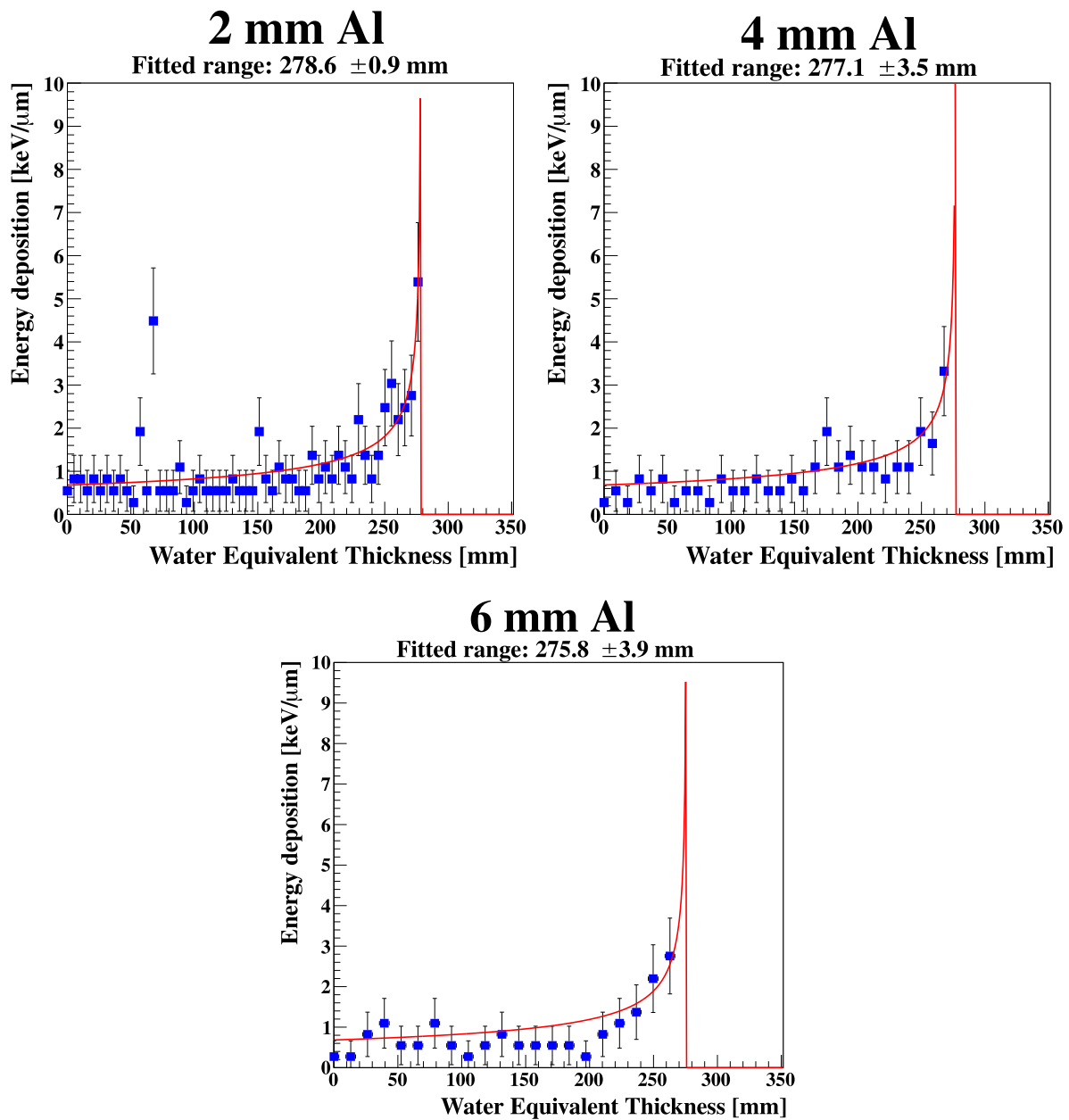
Figure 5.5: *Individual 250 MeV proton tracks in three different geometries, degraded by a 10 cm water phantom, overlaid with a Bragg curve fit. The displayed "±" accuracy is the output from the least-squares method applied on an individual proton, and it is not representative for a proton beam of that energy. MC data taken with a 250 MeV beam degraded using a 10 cm water phantom.*
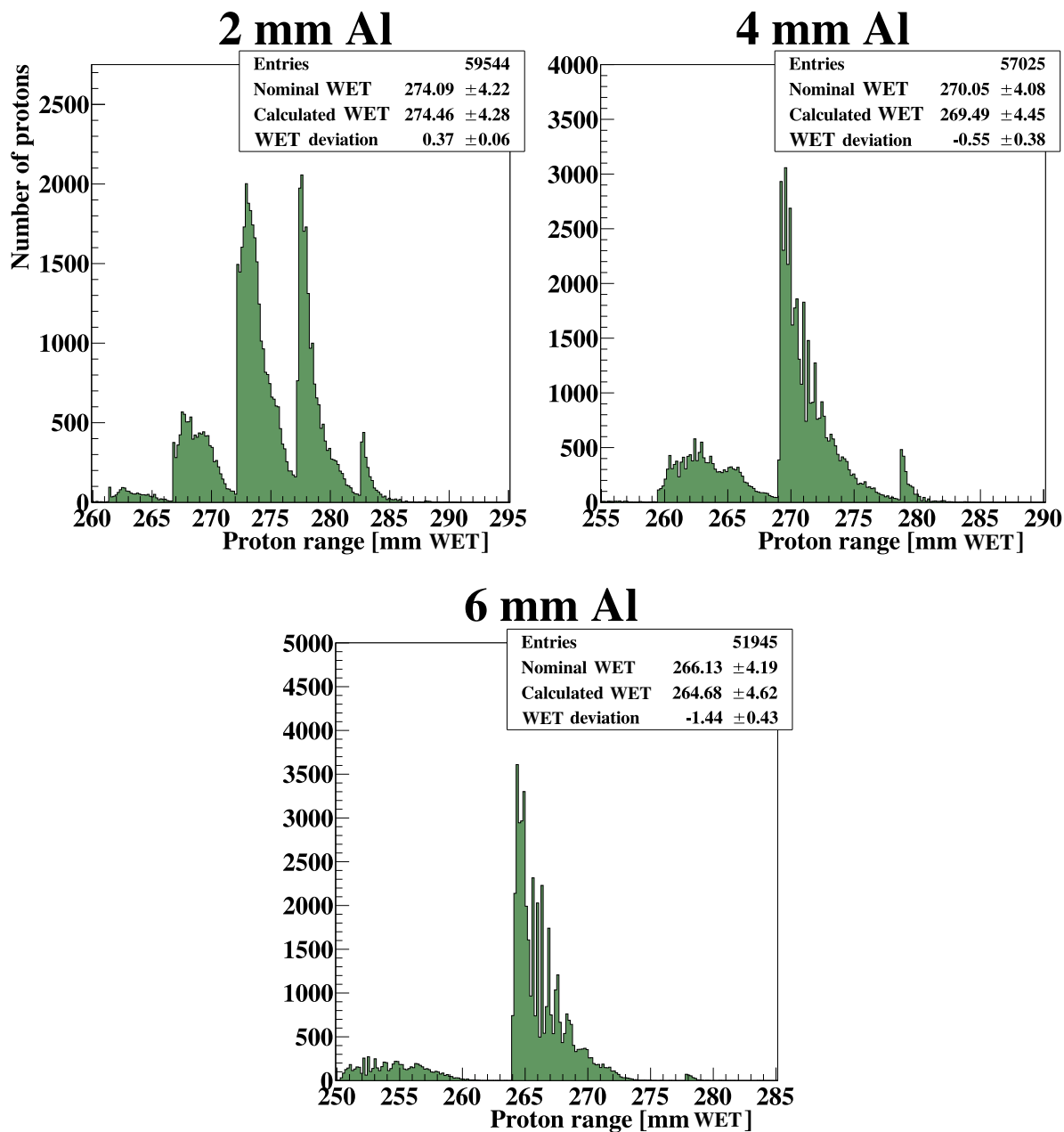
Figure 5.6: *Distribution of the individual estimated ranges. From this distribution the residual range ⟨R̂⟩ and range straggling ⟨σ̂_R⟩ of a proton beam is calculated, shown in the text box as "⟨R̂⟩ ± ⟨σ̂_R⟩". The characteristic pattern of the distribution, with regular sudden rises, can be seen in the figure. Each rise in the distribution is in coincidence with the beam reaching a new sensor layer. MC data taken with a 250 MeV monoenergetic proton beam degraded using a 10 cm water phantom.*
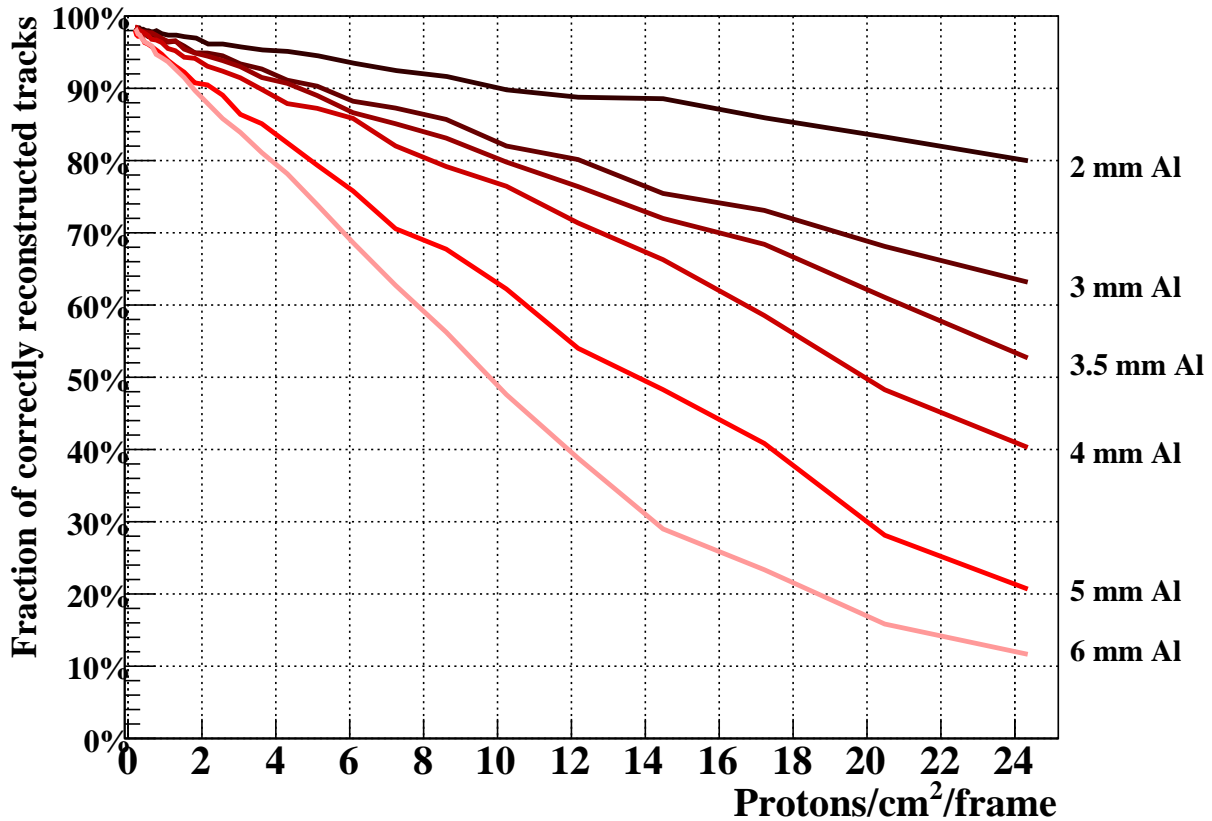
Figure 5.7: *The tracking efficiency of the different geometries. In order for a track to be regarded as correctly reconstructed, it must have the correct stopping depth, and the start- and endpoints must originate from the same incoming proton.*

5.5   Optimization Results

5.5.1   Efficiency of the Track Reconstruction

The efficiency of the track reconstruction, as defined in Section 5.4.3, is shown in Fig. 5.7 for the different designs under consideration. For the 4 mm design, the efficiency is 90% at a beam intensity of 4 protons/cm^2 per reconstruction frame, and 80% at a beam intensity of 8 protons/cm^2 per reconstruction frame. With a proton beam of that intensity, covering the full detector area of approx. 400 cm^2 and with a continuous readout of 5 μs, the proton reconstruction capabilities at 80% efficiency corresponds to 640 million protons/s.

The efficiency numbers are obtained with a *uniform* particle density in the MC simulations. A clinical proton beam is usually Gaussian distributed, with $\sigma_{xy} \sim 5$ mm before entering the patient (Rescigno et al., 2015). In Fig. 5.8 the lateral profile of a beam with the parameters $\sigma_x = 4$ mm, $\sigma_y = 2$ mm and an angular spread of ~ 4 mrad is shown, first after exiting a 10 cm phantom in the first traversed DTC layer, and then after the last traversed DTC layer. It is evident that it is in the beam core that most efforts must be put for
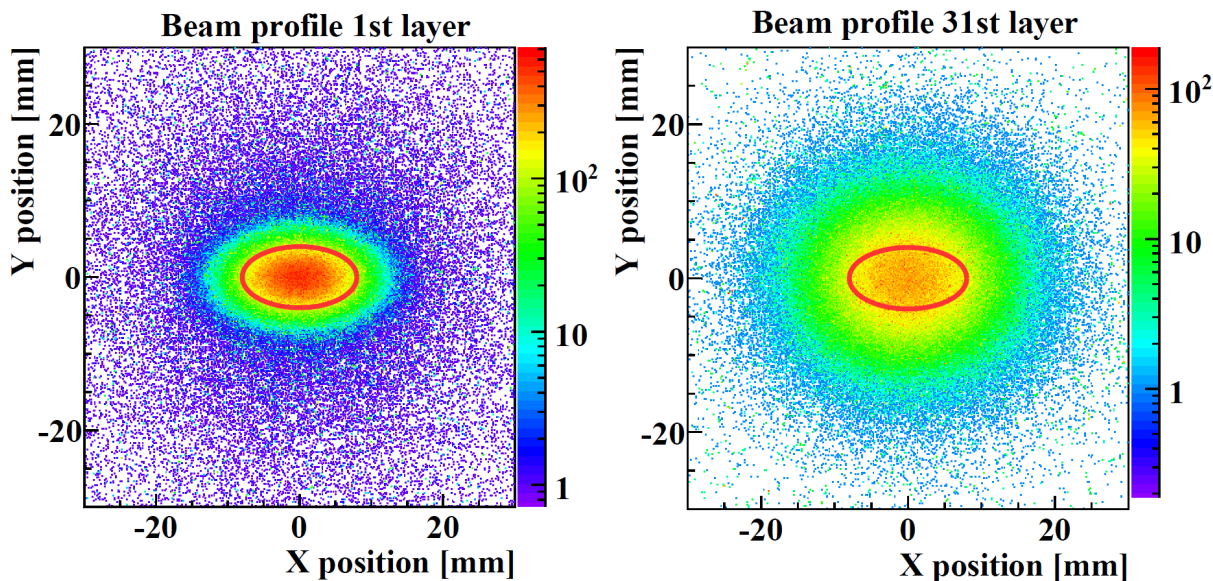
Figure 5.8: *Beam profiles in the DTC at two different positions. A 250 MeV pencil beam is shown first after traversing 10 cm water, then after traversing 30 layers of the DTC. The pencil beam is defined by the parameters $\sigma_x = 4\,mm$, $\sigma_y = 2\,mm$ and an angular spread of $\sim 4\,mrad$. The red ellipse is the 2σ value of the original pencil beam profile.*

an efficient efficient track reconstruction, since the track density and thus the difficulty of correct reconstruction, is highest in that area. The 2σ area of the beam, proximal to the energy degrading water phantom, is $1\,cm^2$. The 2σ area of the beam incident on the detector is $1.3\,cm^2$ and in the layer containing the Bragg peak the 2σ beam profile area is $4.5\,cm^2$.

Of the results presented in this chapter, the track reconstruction efficiency is the one that is most dependent on improvements of the algorithm. In Chapter 7, several improvement strategies will be discussed, such as simultaneous layer-by-layer reconstruction, back-to-front reconstruction and techniques based on graph theory and also on machine learning. The optimization of the track reconstruction algorithm will ensure that the reconstruction can be performed at higher beam intensities at high efficiencies.

Lastly, in the analysis of the ALICE-FoCal prototype data, a small relaxation was made for tracks that were not perfectly reconstructed, due to a mismatch with nearby tracks within 0.5° and 0.5 mm. No quantitative results for such tracks are presented here.

5.5.2   Accuracy of the Range Calculation

The range accuracy is the systematic bias on the calculated proton range, found by from the reconstructed ranges $\langle \hat{R} \rangle$ and the nominal ranges R through the relation $\langle \langle \hat{R} \rangle - R \rangle$
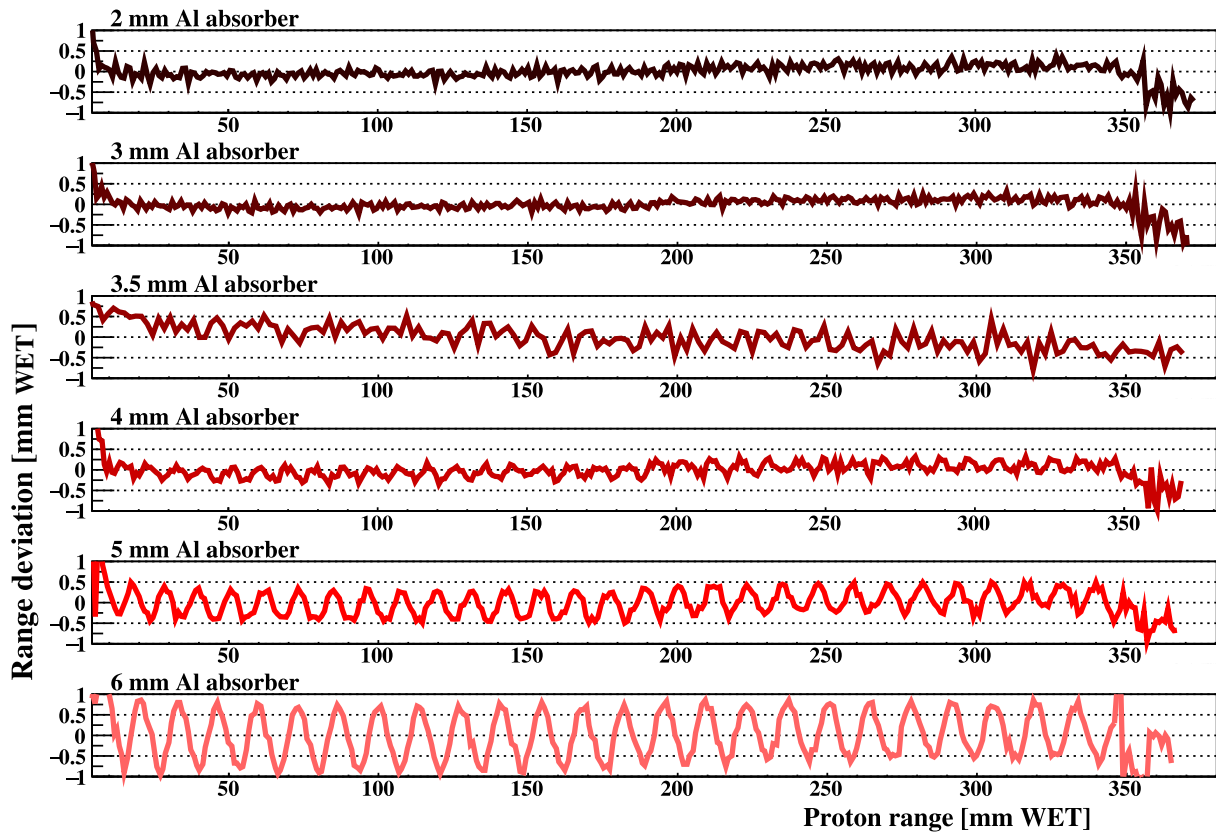
Figure 5.9: *The range determination accuracy shown as the deviation between the "MC truth" range, and the reconstructed range $\langle \hat{R} \rangle$. For visualization purposes, a calibration constant has been added to all ranges within a given geometry: this constant is below 1 mm (below 2 mm for the 5 and 6 mm thicknesses).*

for each of the incident proton energies. In Fig. 5.9 the range accuracy is shown for increasing incident energies in different designs of the DTC. Some key aspects can be seen in Fig. 5.9: The systematic errors are kept within 0.5 mm WET throughout the DTC, for the designs having a 5 mm aluminum absorber or less. Note that, for visualization purposes, a calibration constant has been added to all ranges within a given geometry in the figure: this constant is below 1 mm (below 2 mm for the 5 and 6 mm thicknesses).

Oscillating Error in the Range Accuracy

There is an oscillation artifact in the range accuracy. It is especially pronounced for the designs with 4 mm and thicker absorbers, and in the 2 mm and 3 mm designs it is negligible. The artifact is characterized by a sinusoidal shaped perturbation of the range accuracy.

The origin of the artifact is that the range straggling distribution of a proton beam spans several sensor layers (see Fig. 5.6). The range accuracy depends on the number of sensor layers covered, and on the position of the mean value of the range distribution
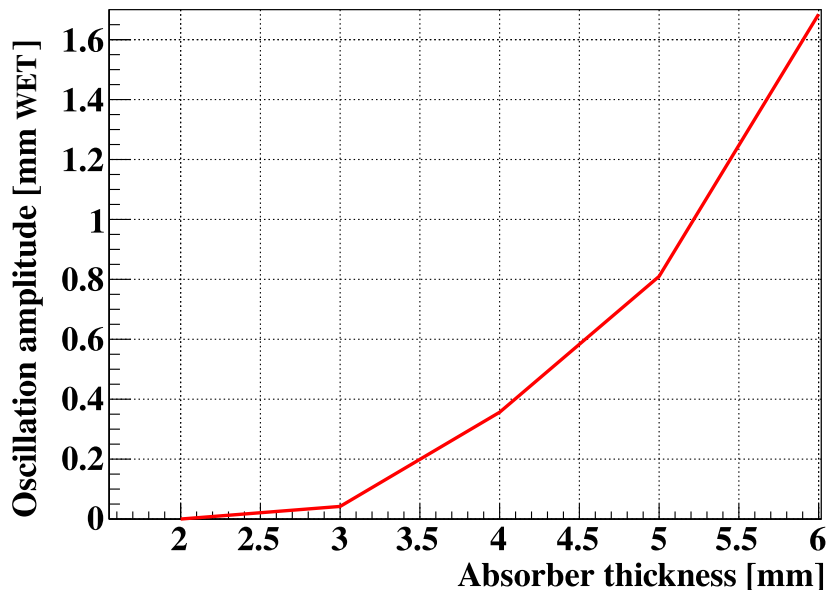
Figure 5.10: *Measurements of the peak-to-peak amplitude of the oscillation artifact and the normalized Fourier amplitude.*

relative to the position of the adjacent sensor layers. The more sensor layers that are covered by the range straggling distribution (e.g. thinner energy absorbers), the smaller the oscillation artifact. This was also seen in the ALICE-FoCal geometry, where range distributions that spanned two sensor layers had a significantly higher range accuracy compared to range distributions that only spanned one sensor layer (for a discussion, see Section 4.7).

A quantitative measurement of the effect can be performed through a spectral analysis of the range accuracy distributions shown in Fig. 5.9: see Appendix B for more details. In general the amplitudes of the oscillation are kept to within 0.5 mm WET if the absorber is thinner than 4.5 mm aluminum, and below 0.2 mm WET for the 3.5 mm aluminum geometry: see Fig. 5.10 for the relationship between the absorber thickness and the oscillation amplitude.

5.5.3   Uncertainty of the Range Calculation

The uncertainty of the range calculation is highly dependent on its lower physical limit, which is the statistical range straggling of the proton beam. As can be seen in Fig. 5.11, the range uncertainty $\langle \hat{\sigma}_R \rangle$ is dominated by the inherent range straggling, with an increase in the uncertainty of high energy protons traversing a higher fraction of the DTC material. The range straggling shows an oscillating variation with a wavelength correlated with the spacing of the sensor layers, similar to the effects described in the last section.

The dynamic range of the DTC, given by the region with uniform range uncertainty
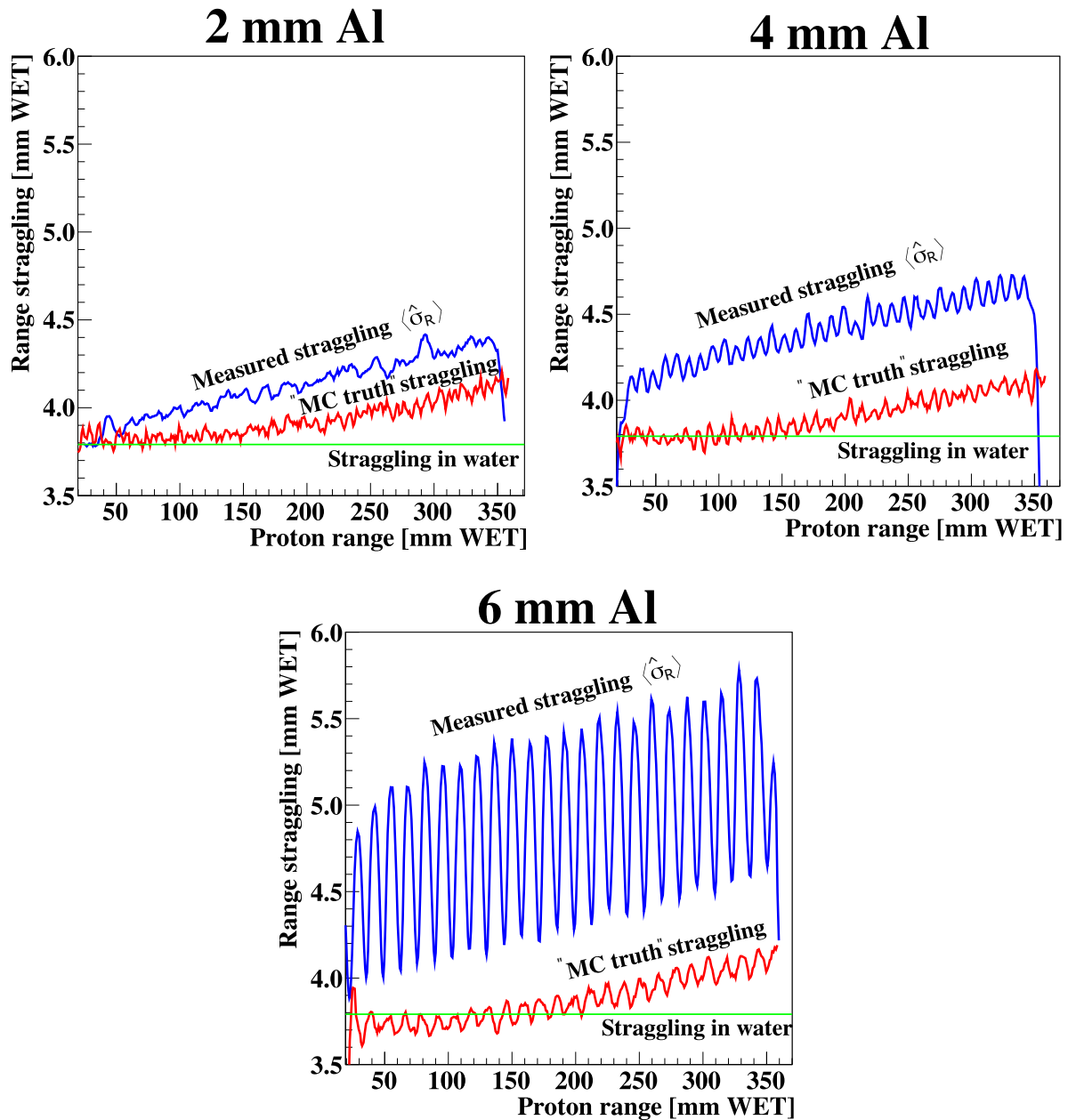
Figure 5.11: *The measured range straggling $\langle\hat{\sigma}_R\rangle$, together with the actual straggling and the baseline straggling in water. An oscillating systematic error occurs when using thick absorbers, due to the large spacing between the measurements in subsequent layers.*
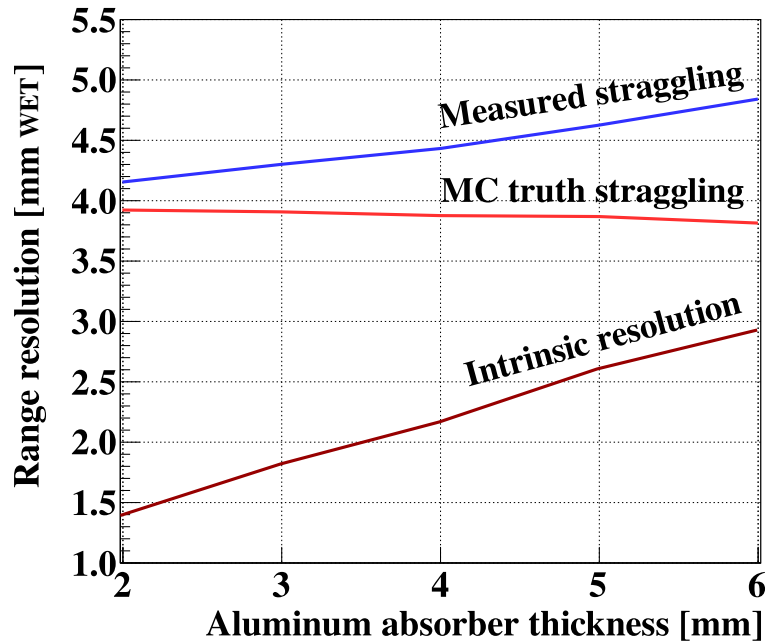
Figure 5.12: *The range uncertainties of the proposed designs. Shown in the figure is the total uncertainty (measured as the mean value of $\langle\hat{\sigma}_R\rangle$ in Fig. 5.11), the range straggling from the MC truth as well as the added uncertainty which is the quadratic difference between the two. See Table 5.2 for the number of required layers for the shown designs.*

and uniform range accuracy, is approximately between 20 mm WET and 350 mm WET in the detector, or in terms of energy, between 50 MeV and 240 MeV. See Table 5.2 for the correspondence between the energies and the required number of layers.

Inherent and Total Range Uncertainty

The *average* measured range straggling $\langle\hat{\sigma}_R\rangle$ ranges from 4.15 mm WET measured in the 2 mm geometry, to 4.8 mm WET measured in the 6 mm geometry. This is the expected overall uncertainty of the whole system. However, we need to consider that only a small portion of this number actually is due to the properties of the reconstruction process and the simulation of the detector. The range straggling as predicted during fully scored MC simulations, here denoted as $\sigma_{R,\text{MC}}$, ranges from 3.92 mm WET measured in the 2 mm geometry to 3.8 mm WET measured in the 6 mm geometry.[*] The added *intrinsic* uncertainty of the reconstruction process and simulation of the detector can be calculated as the subtraction between the two in quadrature:

$$\sigma_{R,\text{Intrinsic}} = \sqrt{\langle\hat{\sigma}_R\rangle^2 - \sigma_{R,\text{MC}}^2} \tag{5.2}$$

---

[*]The increased fraction of aluminum relative to the copper contents in the PCB reduces the straggling in the thicker absorber geometries.

Absorber thickness [mm]	2	2.5	3	3.5	4	4.5	5	5.5	6
Layers needed (230 MeV)	66.6	55.2	47.1	41.1	36.5	32.8	29.7	27.2	24.4
Layers needed (200 MeV)	52.8	43.8	37.4	32.6	29	26	23.6	21.6	20

Table 5.2: *The number of layers needed to contain a 230 MeV and a 200 MeV beam, respectively, in the different geometries, when a necessary extra margin corresponding to a distance of three times the range straggling is added.*

The values for the average intrinsic uncertainty are now 1.4 mm WET in the 2 mm geometry, 2.15 mm WET in the 4 mm geometry and 2.9 mm WET in the 6 mm geometry. These values are shown in Fig. 5.12.

5.5.4   Required Number of Sensor Layers

The number of layers required to contain the complete proton beam has been found for the different designs studied here. A 230 MeV mono-energetic proton beam has been applied in this part of the work. The necessary dynamic range is defined as the range plus 3 times the range straggling (to accurately measure the tails of a 230 MeV beam): This leads to the required number of layers, listed in Table 5.2. For each layer, the energy is degraded from the sensor chips, flexible PCB board with glue as well as the aluminum absorber (see Fig. 5.2, the latter varying in thickness.

5.5.5   Impact on the Tracking Resolution In Patient due to Scattering

One of the required measurements during the proton CT image acquisition is that of the direction of the incoming proton, by using measurements from the first two sensor layers. Any material in the first two sensor layers (i.e. the sensor chips, PCB and carrier backing material) will scatter the incoming protons. The scatter angle is here denoted as the RMS angle θ_0 found by the Highland equation (Eq. (1.7)). We need to estimate the resolution degradation as a function of different carrier backing material thicknesses, in order to define a maximum thickness for the design specification.

We assume that the scattering a single event taking place near the first sensor layer, and that the first sensor layer is positioned 15 cm after the the patient. In Bopp et al. (2014), the distance between the patient and the first sensor layer is 10 cm, however we increase this number somewhat in order to spread the beam for tracking purposes.

Moreover, we simplify the geometry, so that the PCB consists of 40 μm aluminum and 60 μm silicon (aluminum-based flexible PCB) and that the ALPIDE chip layer is 10 μm aluminum and 40 μm silicon. The carrier board backing, which can be of different thicknesses, is added to this. The degraded resolution due to scattering in the first two
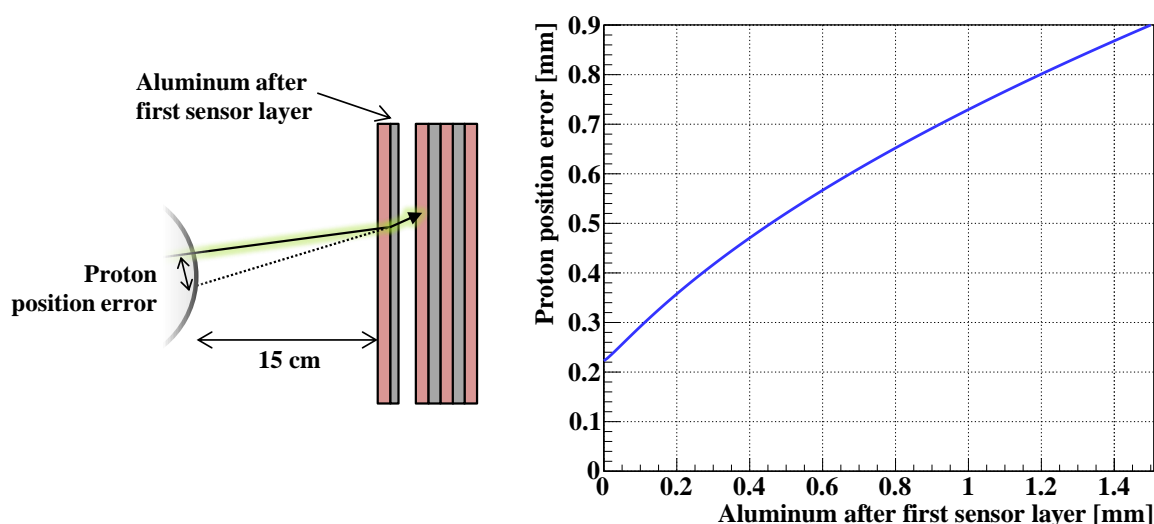
Figure 5.13: *The proton position determination error on phantom due to scattering on aluminum carrier board between the first two sensor layers. **Left:** Schematics of the calculation. **Right:** Errors from different carrier board thicknesses (and contributions from sensor chips and PCB).*

sensor layers is most precisely calculated by performing a full Most Likely Path study, however it can also be estimated by using the proxy variable "RMS lateral deflection of proton vector on phantom".

This lateral deflection should be kept as low as possible, and below 0.5 mm. The value is found by projecting θ_0 onto the phantom 15 cm away. In Fig. 5.13 the positional errors are shown as a function of the thickness of aluminum after the sensor layer, a number which includes the contributions from the sensor chip and flexible PCB components.

The amount of aluminum added as a structural backing to the sensor chip and flexible PCB between between the two first tracking layers should be kept below 450 μm.

Chapter 6

Results and Discussion

6.1 The Digital Tracking Calorimeter Applied for Proton CT Purposes

The Digital Tracking Calorimeter (DTC) concept is that of concurrent reconstruction of multiple proton tracks, in order to measure the range of the protons in the traversed calorimeter layers. The DTC concept has been explored in this work through the development of an analysis framework, which has been applied on both Monte Carlo (MC) simulated DTC geometries as well as on experimental data from beamline measurements performed with a DTC prototype built for a high energy physics experiment (the ALICE-FoCal experiment).

Detector Design

The readout and data acquisition from a proton CT detector needs to be able to record information about each proton traversing the patient: each individual proton's position- and direction coordinates when entering and exiting the patient, and also the proton's residual range after exiting the patient. These measurements must be of high resolution, and the proton CT scan should be performed sufficiently rapid as this is a part of the clinical workflow where minimizing the patient's time lying on the treatment table is essential.

The required specifications for a proton CT and an overview over the properties of the DTC, as well as results obtained through MC simulations and results from experimental data, have been presented in this work. The proof-of-concept calorimeter prototype was originally destined for applications in a high energy physics regime for the ALICE-FoCal experiment. As a result, the choice of materials and of the geometrical layout is not optimal for use as a proton CT detector. However, the results presented in this work

convey that the DTC is a detector concept with a promising potential in the proton CT context.

Among the key features of the DTC is an "all-in-one" design where the entrance layers of the calorimeter can function as the proton tracker and also a high acquisition rate capability due to that the technology enables tracking and reconstruction of hundreds of simultaneous proton tracks.

Range Accuracy and Uncertainty

The range uncertainty (resolution) requirements of a proton CT system is estimated to be around 1% (Poludniowski et al., 2015). Prototype proton CT scanners meeting this requirement have been constructed (Johnson et al., 2016). Several other prototype scanners have a range uncertainty of 2%–3% (Uzunyan et al., 2013b; Scaringella et al., 2014; Price et al., 2015).

The geometrical sampling spacing between the active sensor layers in the prototype studied in this present work is approximately 3.3 mm tungsten, corresponding to 32 mm Water Equivalent Thickness (WET). This is a very large sensor layer separation, and we do not expect the range resolution, obtained when applying the detector with this design, to be adequate for proton CT.

The measured range uncertainty is 14 mm WET (8.2%) on average. The value of the range uncertainty varies with different incident energies, from around 6.3 mm WET from the 160 MeV beam test to 25 mm WET from the 188 MeV beam test.

The results show systematic errors of up to 21 mm WET in range deviation, depending on the initial proton energy. These errors propagate into other parts of the analysis (that depend on the proton energy at different depths in the detector): to the charge diffusion modeling and chip sensitivity calibration. When such errors are introduced in the simulation, systematic errors are introduced in the calculation of the *nominal* proton ranges, and the calculated deviation is therefore biased. In addition, the oscillation of the range accuracy due to the thick absorbers increases both the average systematic error and its variation. This effect is also seen in the optimization study.

The results may be split into several categories regarding the quality of the underlying data. If the runs with few reconstructed tracks are removed (such as the 151 MeV one), and if the remaining data is divided into range distributions covering *one* sensor layer and *two* sensor layers (see Table 6.1), we see that:

i) Beams covering one sensor layer have high systematic errors. The average range is measured to be 13.4 mm WET below the respective nominal ranges. Conversely, since all protons are observed to stop close to each other, the measured range uncertainty is artificially low with an average value of 6.8 mm WET.

Beam energy [MeV]	120	160	180	139	170	188	151
Layers covered	1	1	1	2	2	2	3
Rel. range accuracy [%]	-8.4	-6.7	-9.1	-3.9	-3.7	-0.7	-13.2
Rel. range uncertainty [%]	6.1	3.6	3.5	13.9	8.3	10.8	11.0

Table 6.1: *Range accuracy and uncertainty of the experimental data. The "Layers covered" number reflects how many sensor layers that are covered by the range straggling distribution. This table is an excerpt of Table 4.3.*

ii) Beams covering two sensor layers have relatively low systematic errors, with an average value of 4.7 mm WET below the respective nominal ranges. In these cases, the range is calculated as the relative number of protons stopping in one of the two adjacent sensor layers, and thus the estimate is more accurate. The measured range uncertainties are in these cases larger, with an average value of 20.1 mm WET. This is, perhaps, more indicative of the reality.

Proton Intensity Capacity

In order to perform a 10 second proton CT scan, a proton intensity capacity of at least 10 million protons/s is required (Poludniowski et al., 2015). One of the advantages of the DTC concept is that hundreds to thousands of proton tracks can be reconstructed concurrently from a single readout frame. The ALICE-FoCal prototype has a readout frequency of approximately 2 kHz, and if the reconstruction algorithm is able to disentangle n_p protons tracks in a single readout frame, then the *effective* readout capacity is $n_p \cdot 2000$ protons/s.

The effective readout capacity has here been defined to be the beam intensity where 80% of the protons can be correctly reconstructed. The effective readout capacity is calculated by reconstructing batches of MC-generated proton beams with an increasing number of uniformly spread-out protons.

The intensity capacity of a uniformly distributed beam has been found to be in the order of 1 million protons/s, or 60 000 protons/s/cm^2. The number depends on the performance of the tracking algorithm as well as on the spatial distribution of the proton beam. An improved algorithm would increase the accuracy of the track reconstruction, and would enable for the separation of a higher number of protons in each readout frame.

The intensity capacity presented in this work is at the high end of the intensity capacities of existing prototypes, where the current fastest proton CT systems are able to handle 2 million protons/s (Johnson et al., 2016; Uzunyan et al., 2013a), and DeJongh (2017) aiming for a readout speed of 10 million protons/s.

6.2 Design Specifications for the Next DTC Prototype

A research project is currently ongoing in a joint effort between research institutions in Bergen. The project receives financial support from Bergen Research Council, the Norwegian Research Council and the University of Bergen (TOPPFORSK). The goal of the research project is to bring a proton CT detector into the clinic for imaging during particle therapy, through gradual improvement of thoroughly tested prototypes. At present the aim is to design, construct and evaluate the next DTC prototype — based on experiences from the first prototype.

The next version of the DTC applied in this project, as explored in Chapter 5, will be designed with proton CT as its main purpose. While the design philosophy from the first prototype is preserved, energy absorbers of less dense materials, i.e. with less proton stopping power, will facilitate improvements of the track reconstruction as well as of the range calculation. The next generation of sensor chips (using the "ALPIDE" chips) and readout systems are expected to increase the proton rate capabilities significantly.

By considering several different designs and carrying out the analysis as done for the ALICE-FoCal prototype, the simulated geometries have here been evaluated in terms of the range accuracy, range uncertainty, tracking efficiency and economy.

6.2.1 Range Accuracy and Uncertainty

The results presented here show that both systematic errors and range uncertainties are not far from their theoretical limits, this applies for several of the proposed designs: i.e. the systematic errors are within 0.2–0.5 mm WET for the geometries with up to 4 mm thick absorber layers. The range uncertainty is limited by the physically inherent range straggling: Results from MC simulations shows the uncertainty to be 4.4 mm WET (using 3.5 mm thick absorber plates), compared to the 3.8 mm WET range straggling. The uncertainty is thus 15% above the range straggling imposed limit for range determination.

In the geometries where the aluminum energy absorber plates are 4 mm or thicker, an oscillating artifact in the range determination increases the systematic range deviation to more than 1 mm WET. The range accuracy depends on the number of sensor layers that are within the proton beam's range straggling, and on the position of the mean value of the range distribution relative to the position of, and thus the distance to, the most adjacent sensor layers. The more sensor layers that are covered by the range straggling distribution (e.g. the thinner the energy absorber layers are), the smaller this effect is. These results reflect those of the ALICE-FoCal prototype, where range distributions covering two sensor layers showed a higher range accuracy compared to range distributions

covering only one sensor layer.

The uncertainty of the range measurements has been found through MC simulations to be uniform throughout the whole dynamic range of the detector (from a residual range of approx. 20 mm WET). This is a property of range telescope detectors when having sufficient number of layers. Scintillation based calorimeters have an energy-dependent uncertainty. In Bashkirov et al. (2016) this energy dependence is mitigated by the application of several consecutive plastic scintillators coupled to photomultipliers. The range accuracy and range uncertainty capabilities of the optimized DTC are comparable to current proton CT prototypes based on such staged scintillators and parallel plate ionization chambers (Rinaldi et al., 2014).

6.2.2   Proton Intensity Capacity

We found in Chapter 5 that by requiring that 80% of the tracks should be reconstructed correctly, 8 protons per cm^2 can be tracked for each detector "snapshot", or readout frame. Using realistic assumptions about the attainable performance and the capacity of the electronic readout system (5 μs readout cycle) of the DTC design at present under consideration, the number of protons that can be reconstructed concurrently is 1.6 million protons/s/cm^2. This number is higher than the minimum requirements of a proton CT if the beam incident on the detector is distributed over a few cm^2, and this may enable scan times limited by other factors such as gantry or patient rotation speeds (if seated). If the DTC is used for applications where the beam is distributed throughout the full detector area, the reconstruction capacity is in the order of 640 million protons/s. Current prototypes have reported readout speeds of 1–10 million protons/s (Scaringella et al., 2014; Bashkirov et al., 2016; Naimuddin et al., 2016; DeJongh, 2017).

The reconstruction efficiency is dependent on both the applied reconstruction algorithm, where significant improvement is possible, and on the specific design of the detector, i.e. the geometry, materials and optimized positioning of the material components. The track reconstruction is simpler to design and perform with thin absorber layers, this is reflected in the maximum proton densities that can be reconstructed with a certain efficiency for each layout.

6.2.3   Design Recommendation

We recall that in the last chapter, we defined the optimal design of the DTC to fulfill the following ambitions: High accuracy of the range determination; low uncertainty (standard deviation) of the range determination, limited by the inherent proton range straggling; high track reconstruction efficiency, i.e. the ability to disentangle and reconstruct

all the protons in a single readout frame; and other constraints such as economy (number of layers), cooling and mechanical stability.

Based on these requirements and constraints, as well as on the results in Chapter 5, we arrive at the following:

i) The lateral size of the sensor layers should be approximately $15 \times 27\,\text{cm}^2$: This corresponds to 90 ALPIDE chips per layer. The reasoning behind this is mainly comparisons with other proton CT projects. The added value of doubling the detector's vertical dimensions is however small compared to the corresponding improved range accuracy associated with a doubling of the number of layers in the longitudinal direction.

ii) The longitudinal size of the detector should be designed with aluminum energy absorption layers between the sensor layers, this layer should be 3.5 mm thick, corresponding to approx. 7.5 mm WET. With this thickness, around 41 layers are needed (with 3690 chips in total) in order to fully contain the range of a 230 MeV proton beam within the detector, including a 3 sigma range straggling longitudinal extension.

Using this geometry, the *intrinsic* range uncertainty is 2 mm WET, compared to the range straggling of 3.8 mm WET that is added to this number in quadrature. The oscillating pattern introduced to the range determination accuracy, due to the layer structure of the detector, is kept below 0.2 mm WET. The track reconstruction efficiency increases rapidly with decreasing absorber thickness, and from this perspective the thickness should be kept below 4 mm and as low as possible.

iii) Any material in and between the first two sensor layers, i.e. the aluminum carrier board, should be kept as thin as possible and below 0.45 mm. A thicker slab leads to higher amounts of multiple Coulomb scattering, and the positional errors on the proton position projected onto a phantom would be in excess of 0.5 mm.

6.3 Applications of the DTC as a Proton CT Detector

6.3.1 Proton CT in a Broad Beam

If the proton beam is uniformly spread over the proposed detector area (in the order of $400\,\text{cm}^2$), then 640 million protons/s can be reconstructed. However, this is not feasible due to the requirement that the protons path through the patient must be reconstructed with position information from measurements from tracker layers located before and after the patient — it would have been very difficult to match the measured proton vectors.

For application in a broad (scattered) beam, the proton density would need to be reduced significantly. By using separate track detectors it would be possible to reconstruct the tracks of individual protons in a beam with information about where, and with the direction, the protons entered and exited the patient.

The separate track detectors would need to be of a "massless" design, i.e. with as little material as possible in order to reduce both energy loss (before the energy measurement) and, more importantly, the total amount of induced scattering. The error resulting from the presence of material in the tracking layers are discussed in Section 5.5.5.

6.3.2   Proton CT in a Pencil Beam

An alternative to the broad beam proton therapy is to use the detector when applying Pencil Beam Scanning with IMPT-enabled proton beam therapy. If the proton beam is sufficiently narrow and well defined on the upstream side of the patient, e.g. precisely measured by beam profile monitors or DTC-type sensor layers, it will be possible to track protons from the assumed upstream beam position, through the patient, and to their measured exit position from the patient.

If the upstream positions of individual protons are estimated on basis of the lateral distribution of the proton beam, before entering the patient, an uncertainty is added to the individual proton's path in the calculation of the Most Likely Path of the proton through the patient. This uncertainty would need to be investigated further before this approach is considered.

In Section 5.5.1 we saw that the lateral beam profile, at the front face of the DTC, originating from a realistic, thin pencil beam (with $\sigma_x = 4\,\text{mm}$ and $\sigma_y = 2\,\text{mm}$), has a 2σ elliptic area of approximately $1.3\,\text{cm}^2$, in which 95% of the protons are contained. With the incorrect assumption of a uniform beam intensity within that area, this number corresponds to a beam intensity capacity of 2 million protons/s. A study of the track reconstruction performance using Gaussian beam profiles should be conducted in order to obtain the expected efficiency values in a pencil beam setup, however the actual value is expected to be somewhat lower without improvements in the track reconstruction algorithm.

6.3.3   Helium CT

The thesis as a whole has been concentrated on applications of the DTC as a *proton* CT detector. An emerging field is that of *particle* CT where especially helium CT is under consideration due to its favorable properties regarding the reduced multiple Coulomb scattering.

In Hansen et al. (2014) the two modalities are compared: in terms of spatial resolution, an ideal Helium CT reaches MTF_{10}[*] at 18.2 lp/cm, whereas proton CT has an MTF_{10} at 9.4 lp/mm. The significantly higher resolution (at a similar CT Dose Index of 10 mGy) indicates that helium CT is a promising modality.

The DTC should be suitable for reconstruction of particles in a helium beam. Measurements of the pixel charge clustering is expected to yield information about particle charge (which is highly correlated to the energy loss), and therefore, particle species (Aricò et al., 2017). This would be an effective discrimination of secondary particles, a necessity in helium CT due to the high proton content of the beam. The particle reconstruction should be simpler than with protons, since the helium ions scatter less. Last, while having higher energies, the range of the helium beam is equal to the range of the proton beam. As a result, the DTC could be applied in a helium beam without having to increase or decrease the thickness of the energy absorbers.

6.3.4   Proton CT with Laser Accelerated Protons

Another potential application for the DTC concept is its application in combination with laser accelerated protons (LAP) (Daido et al., 2012). While no clinical implementation of LAP has been shown, several feasibility studies of beam delivery (Scuderi et al., 2014) and treatment quality (Hofmann et al., 2015) are available. LAP is in principle expected to deliver protons of therapeutic energies in very short picosecond bursts with kHz repetition rates. The DTC might be capable of resolving the resulting bursts of a few thousand protons per readout cycle by exploiting the high-granularity of the sensors which allows simultaneous tracking of individual protons as presented in this work.

6.4   Calculations of the Proton Range

In Chapter 2 the accuracy of MC simulations and analytical proton range calculation models was evaluated.

6.4.1   Accuracy of the MC Simulated Proton Range Distributions

The objective of the MC comparison study has been to compare simulated range distributions of protons traversing different materials, obtained with the three general purpose MC programs GATE, MCNP6 and FLUKA. This was performed by assessing the agreement between the results for the mean projected proton range, the range straggling, the

---

[*]Modular Transfer Function: The MTF_{10} value expresses the resolution (in terms of line pairs per cm) where the line pair contrast is degraded to 10% of its original value.

transverse beam spread, and the fraction of protons lost from the primary beam due to nuclear interactions. The MC results were also compared to data from PSTAR (Berger et al., 2005) and to data from Janni (1982).

The proton ranges agree within 0.5%, both between the MC programs and to the experimental data. The range at 230 MeV predicted by MCNP6 in water deviates by 1.3 mm from the proton ranges calculated by FLUKA and GATE. A possible reason for this is the ionization potential of water value used by MCNP6. Although it is reported that MCNP6 uses the recommended value of 75 eV as the ionization potential of water, the results between GATE and MCNP6 agree better at an ionization potential value of about 73 eV.

The range straggling values exhibit some discrepancies: the maximum relative difference is 12.5% in water, 4.5% in aluminum and 13.7% in the detector geometry. In the case of water and aluminum, the average values from the MC programs are consistent with the experimental data. The results for the fraction of nuclear interactions in water and aluminum agree with Janni within the uncertainties of the experimental data, and within 7.5% to each other. The results for the transverse beam spread show some discrepancies, and the GATE beam spread is significantly smaller compared to MCNP6 and FLUKA: this is consistent with existing studies (Bednarz et al., 2011; Kimstrand et al., 2008; Grevillot et al., 2010; Lin et al., 2017; Mertens et al., 2010).

6.4.2   Accuracy of the Analytical Proton Range Models

For benchmarking purposes and for the calibration of proton CT systems, it is important to have an accurate calculation scheme between proton initial energies and ranges. Several parametrizations of the energy-range relationship are available, with different levels of complexity and accuracy. In Section 2.2 four different models were compared and evaluated on their accuracy in reproducing tabulated energy-range data from the PSTAR database (Berger et al., 2005).

The Bragg-Kleeman model is the least accurate at a 75th percentile error of 3%, across different initial energies. The "sum of exponentials" model and linear interpolation model are similar at around 0.3%, while the spline interpolation model has a 75th percentile error of of 0.003%.

The parameter values used for the Bragg-Kleeman model in this work differs from both Bortfeld (1997) and Boon (1998), as shown in Table 2.7. The median range error using the model parameters obtained here is lower compared to the median error on this dataset using the other model parameters. The discrepancy might arise from small differences between the semi-empirical PSTAR data values used here and the ICRU49 data tables used by the above-mentioned studies, and from the selection of data points to

use for fitting.

6.5   Resolution Improvement by Bragg Curve Fitting of Individual Proton Tracks

One topic that has not yet been addressed is to what degree the Bragg curve model fitting increases the accuracy of the range accuracy and range uncertainty. In this section, a short re-analysis of the data from Chapter 5 has been performed: With the exception that the estimated range from each proton track history is defined to be the position of its last traversed layer.

Effects on Range Uncertainty

In order to characterize the effect of the Bragg curve fitting on the range uncertainty, we study the added width of the reconstructed range distribution due to the analysis and detector geometry. By using the simple last-layer estimator for the proton range, the intrinsic (added) uncertainty in the optimization geometries (energy absorbers consisting of 2–6 mm aluminum) increases by 20%–45%. Specifically, for the geometry with 4 mm absorbers, the increase in the intrinsic uncertainty is from 2.1 mm to 3.0 mm. This uncertainty is still below the inherent range straggling, and thus the increase in absolute range uncertainty is smaller (5%–10% increase).

Effects on Range Accuracy

For the range accuracy determination, we consider the amplitude of the oscillation artifact that we have seen in both experimental data from the ALICE-FoCal prototype, and during the geometry optimization process. This choice of variable was made because any systematic range inaccuracies that are constant throughout the complete detector can be removed by calibration, and the remaining inaccuracies are due to the relative positioning between the Bragg peak position and the sensor layers.

By using the simple last-layer estimator for the proton range, the increase in the wobbling is strongly dependent on the geometry under consideration. In the 4 mm aluminum absorber geometry, the increase in amplitude is from 0.3 mm WET with Bragg curve fitting, to 0.4 mm WET without (10% increase). For the 6 mm aluminum absorber case, the increase is from 2.2 mm WET to 3.1 mm WET (40% increase).

Chapter 7

Conclusion

7.1 The Proof-of-Concept Prototype Detector

In this thesis, the feasibility of applying a proof-of-concept version of the Digital Tracking Calorimeter (DTC) in a proton CT system has been shown. Methods have been developed for the purpose of calculating the energy deposited by protons, by modeling of the charge diffusion process of electron-hole pairs liberated by traversing protons in digital pixel sensors; for performing the subsequent track reconstruction through multiple sensor layers separated by energy absorbers; and for reconstruction of the initial energy of the proton tracks through the fitting of Bragg curve models. The above methods have been presented and evaluated, using results from both Monte Carlo simulations and experimental measurements.

The results of this work lead to the conclusion that the DTC can be used for track reconstruction and range estimation for a significant number of concurrent proton tracks at therapeutic energies. The materials used in the current version of the DTC are optimized for applications in a high energy physics experiment. Due to this, every sensor layer is separated by tungsten absorbers of 32 mm Water Equivalent Thickness (WET). This sets an upper limit to the accuracy with which the range and energy of protons can be determined in the existing prototype.

The results from this proof-of-concept tracking calorimeter shows that a next version that is optimized for proton CT purposes has the potential of enabling fast and accurate determination of the ranges of individual protons in a therapeutic proton beam.

7.2 Optimization for the Next Prototype

In Chapter 5 we investigated the performance of different conceptual designs of the next generation Digital Tracking Calorimeter (DTC) using MC simulations together with the

analysis framework developed for the proof-of-concept DTC prototype.

The analysis was performed by combining individual proton tracking in a high-granularity pixel sensor range telescope and Bragg curve modeling of each proton's energy loss. The DTC has the capability of tracking more than 1.6 million protons/s/cm^2, assuming realistic electronics- and design proposals. The range uncertainties are close to the range straggling limit, and systematic errors in the range determination are kept below 0.3 mm WET throughout the complete detector. By considering the presented results, the optimal conceptual design is 3.5 mm aluminum.

The first two layers of the DTC are used both for tracking and determination of the proton's incoming vector. An aluminum slab is required for mechanical stability and cooling purposes, however due to proton scattering, this slab should have a thickness of maximum 0.45 mm for the error in the projected position determination not to exceed 0.5 mm.

The improvement achieved by using absorbers of thicknesses 3 mm or less is negligible due to the inherent range straggling limit for the range uncertainty. Thicker absorbers, however, yield a systematic oscillating artifact in accuracy of the the range determination, and at thicknesses of 5 mm and higher this effect will degrade the accuracy. In terms of the reconstruction efficiency, a thinner absorber improves the efficiency: The thickness should not be significantly above 3 mm in order to avoid a degrading of the efficiency and of the range resolution accuracy. However, when considering realistic construction constraints, a 4 mm absorber requires fewer sensor layers (39 layers) compared to the 3 mm (48 layers) design, and thus the 3.5 mm design with 41 layers could represent an optimal trade-off between efficiency/accuracy and construction constraints.

These results provide input to the conceptual design of the next generation DTC in a proton CT detector assembly, currently under development at the University of Bergen and at the Western Norway University of Applied Sciences.

7.3   Proton Range Calculations

In Chapter 2, the proton range accuracy calculation using different approaches were described. First, several different Monte Carlo software packages were compared in terms of proton range, range straggling, lateral scattering and also with respect to the nuclear interactions taking place. Similar results were obtained for the different frameworks compared, however by using GATE, a reduced amount of scattering was observed. The proton range deviation between the MC programs is of the order of sub-millimeter in the therapeutic range between 50 MeV and 230 MeV. The exceptions here are the ranges in water from MCNP6, which applies different values for the mean ionization potential

for water compared to the other software packages: the best correspondence between MCNP6 and GATE is achieved when the mean ionization potential value for water in GATE is set to 73 eV.

Secondly, regarding analytical models of the proton range, it was found that a look-up-table approach combined with spline interpolation between initial proton energies and the corresponding proton ranges is superior in accuracy, compared to using the Bragg-Kleeman relationship, however a differentiation of the latter yields an accurate energy loss curve for the individual protons.

7.4   Outlook

In this last Outlook section, we look towards the future and the upcoming work. We ask here which efforts that need to be carried out in order to ensure that a clinical proton CT scanner — based on the Digital Tracking Calorimeter concept — is realized? Several paths are proposed below, either as improvements to some of the techniques presented in this thesis, or as generalizations of these tailored to the next prototype.

7.4.1   The Next DTC Prototype

Efforts are currently being made in order to develop the next prototype of the DTC. To this end, a conceptual design was proposed in Chapter 5 to optimize the pertinent scanner properties in regards to the track reconstruction efficiency and range resolution. However, research and development of this detector is not a trivial project, and the recommendations only touch upon a small fraction of the overall system design. Several other key aspects needs further exploration: Regarding the physical design of the scanner, the heat sink design for cooling and the actual cooling requirements, mechanical stability, scanner mounting, the bonding process between the ALPIDE chips and carrier boards, readout cables and connector design, readout architecture, FPGA and bandwidth requirements. Regarding the software and analysis; development of fast enough and stable on-line image reconstruction — including proton tracking inside the calorimeter — and improved an Monte Carlo design, proton range modeling, calibration routines and a new charge diffusion model taking into account the specific properties of the ALPIDE chip.

7.4.2   Proton Track Reconstruction

The proton track reconstruction system introduced in this thesis, both for the DTC prototype using the ALICE-FoCal detector and for the next DTC prototype, has limitations

on the track density that can be reconstructed correctly. Several improvement strategies are possible for further development, and an improved track reconstruction algorithm will benefit the DTC concept by allowing for higher beam intensities before saturation of the reconstruction process due to too high particle density. Some of the strategies are outlined here:

i) Optimization based on forward and backward reconstruction (Strandlie and Frühwirth, 2010). Since the track density is lower towards the distal part of the detector, it might be valuable to start the tracking process in that area. In addition, if the tracking is performed simultaneously in both directions, track segments that match in both directions are stored, and track segments that do not match can be treated with more care.

ii) Weighted recursion track following. Due to computational limits, a large number of tracks are discarded during the track-following of a single track. As presented here, only the "best" next-step candidate is kept at each step. The extreme alternative is to perform a full recursive tracking, splitting the track when multiple possibilities are available, before evaluating all possible tracks at the end: This procedure is quite computationally demanding. A possible combination of the two, proposed as the winning contribution to the "RAMP Machine Learning for Track Reconstruction" data challenge (Amrouche et al., 2017), is such: Follow all tracks recursively (within a given search radius) while keeping score on each track candidate, tallying a score based on e.g. total angular change relative to the expected scattering. If a single track exceeds the maximum score value allowed, discard it. This way, the computational demand is limited, while exploring a larger fraction of the following track combinations.

iii) Using mathematical techniques from graph theory; Siklér (2017) suggests constructing a set of nodes representing the detector hits. The parts of the track that are simple to reconstruct are represented as nodes with few connections, and "bridge" nodes with many connections are ambiguous track portions with many solutions. An optimization routine can be applied to minimize the χ^2 value throughout the complete graph.

iv) Another approach is to connect two and two complete layers: Instead of finding the most-probable-connection between two and two hits separately, based on extrapolation from one direction, two neighboring layers can be simultaneously optimized through the minimization of the sum of angular change coming from both directions. This approach reduces the problem of deciding too early on a track candidate.

v) Approaches based on machine learning and so-called deep neural networks: The details of such an approach is not yet clearly defined, however in many track reconstruction contexts neural networks are of value and several frameworks for implementation exist — such as outlaid in Farrell et al. (2017).

7.4.3 Charge Diffusion Modeling

The charge diffusion models presented in Section 4.3 are important since they contribute to an increase of the resolution of the proton range calculation. However, attempts to model the process analytically (work performed in a project together with Hansen (2017)) did not lead to results that sufficiently explain the experimental data. In Chapter 4, some shortcomings of the model were discussed. In addition, the measurement data of the proton's instantaneous energy loss is not trivial to understand and model. It is desirable to extend this model, and to include more experimental data, to enable an analytical model of the charge diffusion process.

In addition, the modeling was performed on data from the MIMOSA23 sensor chip. The next DTC prototype is based on the ALPIDE chip, with different characteristics. Carefully designed experiments should be performed to record data at a known spectrum of energy loss values, and the resulting charge diffused clusters from different particle species should be compared to their energy loss.

A last point in this section is that by calculating the E_{dep} values of the particle track, it should be possible to perform particle identification (PID). This is because the E_{dep} value is proportional to the projectile charge, and therefore the plateau E_{dep} value would help identify differently charged particles. If used in an helium or carbon beam, a PID system would be valuable in removing secondary particles such as protons.

7.4.4 The Clinical Proton CT Scanner

Last but not least, it is a long way from a prototype proton CT to a clinical proton CT. While not in the scope of this thesis, it is worth reflecting upon some of the clinical requirements: Gantry mounting, rotation of imaging system (or even rotation of the patient, if possible without organ motion, such as rotation of a seated patient in the horizontal plane), system footprint and radiation hardness of the sensor. These requirements are secondary in the current design of the next prototype, however they need to be considered during the project before arriving at the design of a clinical proton CT system based on the Digital Tracking Calorimeter concept.

Bibliography

Aadnevik, D. (2014). *Extremely high-granularity digital tracking calorimeter for the detection of scattered protons in pCT*. MSc, University of Bergen, Norway. 12

Agostinelli, S., Allison, J., Amako, K., Apostolakis, J., et al. (2003). Geant4—a simulation toolkit. *Nuclear Instruments and Methods in Physics Research Section A: Accelerators, Spectrometers, Detectors and Associated Equipment*, 506(3):250–303. 22, 27

Ahlen, S. P. (1980). Theoretical and experimental aspects of the energy loss of relativistic heavily ionizing particles. *Rev. Mod. Phys.*, 52:121–173. 14

Amrouche, S., Braun, N., Calafiura, P., Farrell, S., Gemmler, J., Germain, C., Gligorov, V. V., Golling, T., Gray, H., Guyon, I., Hushchyn, M., Innocente, V., Kégl, B., Neuhaus, S., Rousseau, D., Salzburger, A., Ustyuzhanin, A., Vlimant, J.-R., Wessel, C., and Yilmaz, Y. (2017). Track reconstruction at LHC as a collaborative data challenge use case with RAMP. *EPJ Web Conf.*, 150. 134

Aricò, G., Gehrke, T., Jakubek, J., Gallas, R., Berke, S., Jäkel, O., Mairani, A., Ferrari, A., and Martišíková, M. (2017). Investigation of mixed ion fields in the forward direction for 220.5 MeV/u helium ion beams: comparison between water and PMMA targets. *Physics in Medicine and Biology*, 62(20):8003. 128

Austreim, K. (2015). *Proton Beam Test Of A High Granularity Calorimeter For Proton Computed Tomography*. MSc, University of Bergen, Norway. 12

Ballard, D. H. (1981). Generalizing the hough transform to detect arbitrary shapes. *Pattern recognition*, 13(2):111–122. 83

Bashkirov, V. A., Schulte, R. W., Hurley, R. F., Johnson, R. P., Sadrozinski, H. F.-W., Zatserklyaniy, A., Plautz, T., and Giacometti, V. (2016). Novel scintillation detector design and performance for proton radiography and computed tomography. *Medical Physics*, 43(2):664–674. 11, 12, 125

Bednarz, B., Chen, G., Paganetti, H., Han, B., Ding, A., and Xu, X. G. (2011). Comparison of particle-tracking features in Geant4 and MCNPX codes for applications in mapping proton range uncertainty. *Nuclear technology*, 175(1):2–5. 26, 129

Berger, M. J., Coursey, J., Zucker, M., and Chang, J. (2005). ESTAR, PSTAR, and ASTAR: Computer Programs for Calculating Stopping-Power and Range Tables for Electrons, Protons, and Helium Ions. 17, 27, 71, 75, 80, 105, 129

Besemer, A., Paganetti, H., and Bednarz, B. (2013). The clinical impact of uncertainties in the mean excitation energy of human tissues during proton therapy. *Phys Med Biol*, 58(4):887–902. 14

Bethe, H. (1930). Zur Theorie des Durchgangs schneller Korpuskularstrahlen durch Materie. *Ann. Phys.*, 397(3):325–400. 14

Bichsel, H. (1990). Barkas effect and effective charge in the theory of stopping power. *Phys. Rev. A*, 41:3642–3647. 15

Bichsel, H. (1992). Stopping power and ranges of fast ions in heavy elements. *Phys. Rev. A*, 46:5761–5773. 15

Boon, S. N. (1998). *Dosimetry and quality control of scanning proton beams*. PhD thesis, University of Groningen, Groningen. 45, 129

Bopp, C., Colin, J., Cussol, D., Finck, C., Labalme, M., Rousseau, M., and Brasse, D. (2013). Proton computed tomography from multiple physics processes. *Physics in Medicine and Biology*, 58(20):7261–7276. 10

Bopp, C., Rescigno, R., Rousseau, M., and Brasse, D. (2014). The impact of tracking system properties on the most likely path estimation in proton CT. *Physics in Medicine and Biology*, 59(23):N197–N210. 118

Bortfeld, T. (1997). An analytical approximation of the Bragg curve for therapeutic proton beams. *Med Phys*, 24(12):2024–2033. 18, 45, 92, 129

Bortfeld, T. and Schlegel, W. (1996). An analytical approximation of depth-dose distributions for therapeutic proton beams. *Physics in medicine and biology*, 41(8):1331. 17, 41, 94

Bragg, W. H. and Kleeman, R. (1905). XXXIX. On the α particles of radium, and their loss of range in passing through various atoms and molecules. *Philosophical Magazine Series 6*, 10(57):318–340. 17

Brun, R. and Rademakers, F. (1997). ROOT — An object oriented data analysis frame-
    work. *Nuclear Instruments and Methods in Physics Research Section A: Accelerators,
    Spectrometers, Detectors and Associated Equipment*, 389(1):81–86. 22

Bruzzi, M., Blumenkrantz, N., Feldt, J., Heimann, J., Sadrozinski, H. F.-W., Seiden, A.,
    Williams, D. C., Bashkirov, V., Schulte, R., Menichelli, D., Scaringella, M., Cirrone,
    G. A. P., Cuttone, G., Randazzo, N., Sipala, V., and Lo Presti, D. (2007). Prototype
    Tracking Studies for Proton CT. *IEEE Transactions on Nuclear Science*, 54(1):140–
    145. 20

Bucciantonio, M., Amaldi, U., Kieffer, R., Sauli, F., and Watts, D. (2013). Develop-
    ment of a fast proton range radiography system for quality assurance in hadronther-
    apy. *Nuclear Instruments and Methods in Physics Research Section A: Accelerators,
    Spectrometers, Detectors and Associated Equipment*, 732:564–567. 11

Chadwick, M. B., Young, P. G., Chiba, S., Frankle, S. C., Hale, G. M., Hughes, H. G.,
    Koning, A. J., Little, R. C., MacFarlane, R. E., Prael, R. E., and Waters, L. S. (1999).
    Cross-section evaluations to 150 MeV for accelerator-driven systems and implemen-
    tation in MCNPX. *Nuclear Science and Engineering*, 131(3):293–328. 29

Collins-Fekete, C.-A., Brousmiche, S., Hansen, D. C., Beaulieu, L., and Seco, J. (2017).
    Pre-treatment patient-specific stopping power by combining list-mode proton radiog-
    raphy and x-ray CT. *Physics in Medicine and Biology*, 62(17):6836–6852. 9

Craft, D. L., Halabi, T. F., Shih, H. A., and Bortfeld, T. R. (2006). Approximating convex
    pareto surfaces in multiobjective radiotherapy planning. *Medical Physics*, 33(9):3399–
    3407. 8

Daido, H., Nishiuchi, M., and Pirozhkov, A. S. (2012). Review of laser-driven ion
    sources and their applications. *Reports on Progress in Physics*, 75(5):056401. 128

Das, I. J. and Paganetti, H. (2015). *Principles and Practice of Proton Beam Therapy*.
    Number 37 in AAPM Monograph. NPP Medical Physics Publishing, 1st edition. 4

DeJongh, F. (2017). A fast monolithic system for proton imaging (for ProtonVDA Inc.).
    Lomda Linda proton imaging workshop. 99, 123, 125

Dionisi, F. and Ben-Josef, E. (2014). The Use of Proton Therapy in the Treatment of
    Gastrointestinal Cancers: Liver. *The Cancer Journal*, 20(6). 2

Emfietzoglou, D., Garcia-Molina, R., Kyriakou, I., Abril, I., and Nikjoo, H. (2009). A
    dielectric response study of the electronic stopping power of liquid water for energetic

protons and a new I -value for water. *Physics in Medicine and Biology*, 54(11):3451. 16

Esposito, M., Anaxagoras, T., Evans, P., Green, S., Manolopoulos, S., Nieto-Camero, J., Parker, D., Poludniowski, G., Price, T., Waltham, C., and Allinson, N. (2015). CMOS Active Pixel Sensors as energy-range detectors for proton Computed Tomography. *Journal of Instrumentation*, 10(06):C06001–C06001. 12

Fano, U. (1963). Penetration of Protons, Alpha Particles, and Mesons. *Annual Review of Nuclear Science*, 13(1):1–66. 14, 15

Farrell, S., Andersen, D., Calafiura, P., Cerati, G., Gray, L., Kowalkowski, J., Mudigonda, M., Prabhat, Spentzouris, P., Spiropoulou, M., Tsaris, A., Vlimant, J.-R., and Zheng, S. (2017). The HEP.TrkX Project: deep neural networks for HL-LHC online and offline tracking. volume 150, page 12, Paris, France. EPJ Web of Conferences. 135

Fehlker, D., Alme, J., Brink, A. v. d., Haas, A. P. d., Nooren, G. J., Reicher, M., Röhrich, D., Rossewij, M., Ullaland, K., and Yang, S. (2013). Electronics for a highly segmented electromagnetic calorimeter prototype. *Journal of Instrumentation*, 8(03):P03015. 52, 53

Ferrari, A., Sala, P. R., Fasso, A., and Ranft, J. (2005). FLUKA: A multi-particle transport code (Program version 2005). 27, 29

Filipak, M. (2012). Comparison of dose profiles for proton vs x-ray radiotherapy. `https://commons.wikimedia.org/w/index.php?curid=27983203`. CC BY-SA 3.0, Accessed: 2017-11-20. 2

Gehrke, T., Amato, C., Berke, S., and Martisikova, M. (2018). Theoretical and experimental comparison of proton and helium-beam radiography using silicon pixel detectors. *Physics in Medicine and Biology*. 12

Goodfellow Inc. (2018). Polymethylmethacrylate material information. 105

Goorley, J. T., James, M. R., Booth, T. E., Brown, F. B., Bull, J. S., Cox, L. J., Durkee, J. W. J., Elson, J. S., Fensin, M. L., Forster, R. A. I., et al. (2013). *Initial MCNP6 Release Overview - MCNP6 version 1.0*. 27, 29

Gottschalk, B. (2010). On the scattering power of radiotherapy protons. *Medical Physics*, 37(1):352. 16

Grevillot, L., Frisson, T., Zahra, N., Bertrand, D., Stichelbaut, F., Freud, N., and Sarrut, D. (2010). Optimization of GEANT4 settings for Proton Pencil Beam Scanning simulations using GATE. *Nuclear Instruments and Methods in Physics Research Section B: Beam Interactions with Materials and Atoms*, 268(20):3295–3305. 26, 28, 105, 129

Grimes, D. R., Warren, D. R., and Partridge, M. (2017). An approximate analytical solution of the Bethe equation for charged particles in the radiotherapeutic energy range. *Scientific Reports*, 7(1). 14, 15, 41

Grøttvik, O. S. (2017). *Design of High-Speed Digital Readout System for Use in Proton Computed Tomography*. MSc, University of Bergen, Bergen, Norway. 12, 102, 103

Hansen, D. C., Bassler, N., Sørensen, T. S., and Seco, J. (2014). The image quality of ion computed tomography at clinical imaging dose levels. *Medical Physics*, 41(11):111908. 128

Hansen, E. (2017). *Charge diffusion modelling for a Monolithic Active Pixel Sensor Detector with application to proton CT*. MSc, NTNU, Trondhjem. 12, 59, 75, 77, 79, 135

Highland, V. L. (1975). Some practical remarks on multiple scattering. *Nuclear Instruments and Methods*, 129(2):497 – 499. 16

Himmi, A., Bertolone, G., Brogna, A., Dulinski, W., Colledani, C., Dorokhov, A., Hu, C., Morel, F., and Valin, I. (2008). PHASE-1 User Manual. Technical report, Tech. report, Institut de Recherches Subatomiques IN2P3-CNRS/ULP, Strasbourg, France. 50, 51

Hofmann, K. M., Masood, U., Pawelke, J., and Wilkens, J. J. (2015). A treatment planning study to assess the feasibility of laser-driven proton therapy using a compact gantry design. *Medical physics*, 42(9):5120–5129. 128

ICRU (2016). 5. Recommended Values for Key Data. *Journal of the International Commission on Radiation Units and Measurements*, 14(1):31–48. 14, 32, 46

Jan, S., Santin, G., Strul, D., Staelens, S., Assie, K., Autret, D., Avner, S., Barbier, R., Bardies, M., Bloomfield, P. M., and others (2004). GATE: a simulation toolkit for PET and SPECT. *Physics in medicine and biology*, 49(19):4543. 27

Janni, J. F. (1982). Energy loss, range, path length, time-of-flight, straggling, multiple scattering, and nuclear interaction probability PART 1. *Atomic Data and Nuclear Data Tables*, 27(4):341–529. 22, 27, 40, 87, 129

Jarlskog, C. Z. and Paganetti, H. (2008). Physics Settings for Using the Geant4 Toolkit in Proton Therapy. *IEEE Transactions on Nuclear Science*, 55(3):1018–1025. 28

Jermann, M. (2017). Particle Therapy Statistics (per end of 2016). *PTCOG*. 1

Jette, D. and Chen, W. (2011). Creating a spread-out bragg peak in proton beams. *Physics in Medicine and Biology*, 56(11):N131. 5, 6

Johnson, R. P., Bashkirov, V., DeWitt, L., Giacometti, V., Hurley, R. F., P., P., Plautz, T. E., Sadrozinski, H. F. W., Schubert, K., Schulte, R., Schultze, B., and Zatserklyaniy, A. (2016). A Fast Experimental Scanner for Proton CT: Technical Performance and First Experience With Phantom Scans. *IEEE Transactions on Nuclear Science*, 63(1):52–60. 99, 122, 123

Johnson, R. P., DeWitt, J., Holcomb, C., Macafee, S., Sadrozinski, H. F.-W., and Steinberg, D. (2013). Tracker Readout ASIC for Proton Computed Tomography Data Acquisition. *IEEE Transactions on Nuclear Science*, 60(5):3262–3269. 11

Kimstrand, P., Tilly, N., Ahnesjö, A., and Traneus, E. (2008). Experimental test of Monte Carlo proton transport at grazing incidence in GEANT4, FLUKA and MCNPX. *Physics in Medicine and Biology*, 53(4):1115. 26, 129

Kumazaki, Y., Akagi, T., Yanou, T., Suga, D., Hishikawa, Y., and Teshima, T. (2007). Determination of the mean excitation energy of water from proton beam ranges. *Radiation Measurements*, 42(10):1683–1691. 14

KVI AGORFIRM (2012). KVI Agorfirm webpage. `http://agorfirm.nl/`. 58

Leeman, J. E., Romesser, P. B., Zhou, Y., McBride, S., Riaz, N., Sherman, E., Cohen, M. A., Cahlon, O., and Lee, N. (2017). Proton therapy for head and neck cancer: expanding the therapeutic window. *The Lancet Oncology*, 18(5):e254–e265. 2

Li, T. and Liang, J. Z. (2004). Reconstruction with most likely trajectory for proton computed tomography. pages 2067–2074. 21

Lin, Y.-C., Pan, C., Chiang, K., Yuan, M., Chu, C., Tsai, Y., Teng, P., Lin, C., Chao, T., Lee, C., Tung, C., and Chen, A. (2017). Monte Carlo simulations for angular and spatial distributions in therapeutic-energy proton beams. *Radiation Physics and Chemistry*. 26, 129

Livingston, M. S. and Bethe, H. A. (1937). Nuclear physics c. nuclear dynamics, experimental. *Rev. Mod. Phys.*, 9:245–390. 18

Maczewski, L. (2010). *Measurements and simulations of MAPS (Monolithic Active Pixel Sensors) response to charged particles - a study towards a vertex detector at the ILC*. PhD. arXiv: 1005.3710. 59, 75

Mager, M. (2016). ALPIDE, the Monolithic Active Pixel Sensor for the ALICE ITS upgrade. *Nuclear Instruments and Methods in Physics Research Section A: Accelerators, Spectrometers, Detectors and Associated Equipment*, 824:434–438. 102

Makarova, A., Gottschalk, B., and Sauerwein, W. (2017). Comparison of Geant4 multiple Coulomb scattering models with theory for radiotherapy protons. *Physics in Medicine and Biology*, 62(15):5959. 30

Marafini, M., Gasparini, L., Mirabelli, R., Pinci, D., Patera, V., Sciubba, A., Spiriti, E., Stoppa, D., Traini, G., and Sarti, A. (2017). MONDO: a neutron tracker for particle therapy secondary emission characterisation. *Physics in Medicine and Biology*, 62(8):3299. 9

McGowan, S. E., Burnet, N. G., and Lomax, A. J. (2013). Treatment planning optimisation in proton therapy. *The British Journal of Radiology*, 86(1021):20120288. 6, 8

Meric, I. (2017). Personal Communication. 9

Mertens, C. J., Moyers, M. F., Walker, S. A., and Tweed, J. (2010). Proton lateral broadening distribution comparisons between GRNTRN, MCNPX, and laboratory beam measurements. *Advances in Space Research*, 45(7):884–891. 26, 129

Michaelson, H. B. (1977). The work function of the elements and its periodicity. *Journal of Applied Physics*, 48(11):4729–4733. 76

Ministry of Finance (2017). Agreement for the national budget 2018. Technical report, Norwegian Ministry of Finance. 3, 12

Mokhov, N. V. and Striganov, S. I. (2002). Implementation of MARS hadron production and Coulomb scattering modules into LAHET. *Los Alamos Natl. Lab.*, Los Alamos -UR-03-4264. 29

Naimuddin, M., Coutrakon, G., Blazey, G., Boi, S., Dyshkant, A., Erdelyi, B., Hedin, D., Johnson, E., Krider, J., Rukalin, V., Uzunyan, S., Zutshi, V., Fordt, R., Sellberg, G., Rauch, J., Roman, M., Rubinov, P., and Wilson, P. (2016). Development of a proton Computed Tomography detector system. *Journal of Instrumentation*, 11(02):C02012. 11, 125

Newhauser, W. D. and Zhang, R. (2015). The physics of proton therapy. *Physics in Medicine and Biology*, 60(8):R155–R209. 13, 32

Nooren, G., Haas, A. P. d., Peitzmann, T., Reicher, M., Rocco, E., Röhrich, D., Ullaland, K., Brink, A. v. d., van Leuuven, M., Wang, H., Yang, S., and Zhang, C. (2018). The FoCal prototype - an extremely fine-grained electromagnetic calorimeter using CMOS pixel sensors. *Journal of Instrumentation*, 13(01):P01014. 12

Nooren, G. and Rocco, E. (2015). A particle counting EM calorimeter using MAPS. *Journal of Physics: Conference Series*, 587(1):012061. 49

Nusselder, R. (2014). *FoCal chip calibration with cosmic rays*. BSc, Utrecht University, Utrecht. 50

Olive, K. A. (Particle Data Group) (2014). Review of Particle Physics. *Chinese Physics C*, 38(9):090001. 51

Paganetti, H. (2002). Nuclear interactions in proton therapy: dose and relative biological effect distributions originating from primary and secondary particles. *Physics in medicine and biology*, 47(5):747. 13

Paganetti, H. (2012). Range uncertainties in proton therapy and the role of Monte Carlo simulations. *Physics in Medicine and Biology*, 57(11):R99–R117. 6, 7, 8, 9, 10, 14, 47

Palm, Å., Nilsson, E., and Herrnsdorf, L. (2010). Absorbed dose and dose rate using the Varian OBI 1.3 and 1.4 CBCT system. *Journal of Applied Clinical Medical Physics*, 11(1). 10

Parodi, K. and Enghardt, W. (2000). Potential application of PET in quality assurance of proton therapy. *Physics in Medicine and Biology*, 45(11):N151. 9

Particle Data Group (2015). Atomic and Nuclear Properties of Materials for more than 300 materials. Accessed: 2018-01-12. 105

Paul, H. (2007). The mean ionization potential of water, and its connection to the range of energetic carbon ions in water. *Nuclear Instruments and Methods in Physics Research Section B: Beam Interactions with Materials and Atoms*, 255(2):435–437. 14

Paul, H. (2013). On the Accuracy of Stopping Power Codes and Ion Ranges Used for Hadron Therapy. In *Theory of Heavy Ion Collision Physics in Hadron Therapy*, volume 65 of *Advances in Quantum Chemistry*, page 23. 40, 42

Penfold, S. N. (2010). *Image reconstruction and Monte Carlo simulations in the development of proton computed tomography for applications in proton radiation therapy*. PhD, University of Wollongong. 21

Penfold, S. N., Schulte, R. W., Censor, Y., and Rosenfeld, A. B. (2010). Total variation superiorization schemes in proton computed tomography image reconstruction. *Medical Physics*, 37(11):5887. 10

Pettersen, H., Alme, J., Biegun, A., van den Brink, A., Chaar, M., Fehlker, D., Meric, I., Odland, O., Peitzmann, T., Rocco, E., Ullaland, K., Wang, H., Yang, S., Zhang, C., and Röhrich, D. (2017). Proton tracking in a high-granularity Digital Tracking Calorimeter for proton CT purposes. *Nuclear Instruments and Methods in Physics Research Section A: Accelerators, Spectrometers, Detectors and Associated Equipment*, 860C:51–61. 52, 58, 63, 64, 82, 89, 98

Pettersen, H. E. S. (2015). GitHub - digital tracking calorimeter toolkit. `https://github.com/HelgeEgil/focal`. 67, 70

Pettersen, H. E. S. (2017a). GitHub - energy loss from pstar. `https://github.com/HelgeEgil/energylossFromPSTAR`. 71

Pettersen, H. E. S. (2017b). GitHub - MC Comparison. `https://github.com/HelgeEgil/compareMCcodes`. 27

Pettersen, H. E. S. (2017c). GitHub - range model comparison code. `https://github.com/HelgeEgil/comparisonOfProtonRangeModels`. 39

Pettersen, H. E. S., Chaar, M., Meric, I., Odland, O. H., Sølie, J. R., and Röhrich, D. (2018). Accuracy of parameterized proton range models; a comparison. *Radiation Physics and Chemistry*, 144C:295–297. 25, 43, 44, 45

Petterson, M., Blumenkrantz, N., Feldt, J., Heimann, J., Lucia, D., Seiden, A., Williams, D. C., Sadrozinski, H.-W., Bashkirov, V., Schulte, R., and others (2006). Proton radiography studies for proton CT. In *Nuclear Science Symposium Conference Record, 2006. IEEE*, volume 4, pages 2276–2280. IEEE. 10

Plautz, T., Bashkirov, V., Feng, V., Hurley, F., Johnson, R. P., Leary, C., Macafee, S., Plumb, A., Rykalin, V., Sadrozinski, H. F.-W., Schubert, K., Schulte, R., Schultze, B., Steinberg, D., Witt, M., and Zatserklyaniy, A. (2014). 200 MeV Proton Radiography Studies With a Hand Phantom Using a Prototype Proton CT Scanner. *IEEE Transactions on Medical Imaging*, 33(4):875–881. 10

Poludniowski, G., Allinson, N. M., Anaxagoras, T., Esposito, M., Green, S., Manolopou-los, S., Nieto-Camero, J., Parker, D. J., Price, T., and Evans, P. M. (2014). Proton-counting radiography for proton therapy: a proof of principle using CMOS APS tech-nology. *Physics in Medicine and Biology*, 59(11):2569–2581. 12

Poludniowski, G., Allinson, N. M., and Evans, P. M. (2015). Proton radiography and tomography with application to proton therapy. *The British Journal of Radiology*, 88(1053):20150134. 10, 11, 122, 123

Price, T., Esposito, M., Poludniowski, G., Taylor, J., Waltham, C., Parker, D., Green, S., Manolopoulos, S., Allinson, N., Anaxagoras, T., Evans, P., and Nieto-Camero, J. (2015). Expected proton signal sizes in the PRaVDA Range Telescope for proton Computed Tomography. *Journal of Instrumentation*, 10(05):P05013–P05013. 72, 122

PTCOG (2017). Particle therapy facilities in operation. Accessed: 2017-11-28. 5

Quiñones, C. T., Létang, J. M., and Rit, S. (2016). Filtered back-projection reconstruction for attenuation proton CT along most likely paths. *Physics in Medicine and Biology*, 61(9):3258–3278. 10

Raaymakers, B. W., Raaijmakers, A. J. E., and Lagendijk, J. J. W. (2008). Feasibility of MRI guided proton therapy: magnetic field dose effects. *Physics in Medicine and Biology*, 53(20):5615. 9

Reicher, M. (2016). *Digital Calorimetry Using Pixel Sensors*. PhD thesis, Utrecht Uni-versity. 54, 59, 67

Reinhart, A. M., Spindeldreier, C. K., Jakubek, J., and Martišíková, M. (2017). Three dimensional reconstruction of therapeutic carbon ion beams in phantoms using single secondary ion tracks. *Physics in Medicine and Biology*, 62(12):4884. 9

Rescigno, R., Bopp, C., Rousseau, M., and Brasse, D. (2015). A pencil beam approach to proton computed tomography. *Medical Physics*, 42(11):6610–6624. 112

Rinaldi, I., Brons, S., Jäkel, O., Voss, B., and Parodi, K. (2014). A method to increase the nominal range resolution of a stack of parallel-plate ionization chambers. *Physics in Medicine and Biology*, 59(18):5501–5515. 125

Rit, S., Dedes, G., Freud, N., Sarrut, D., and Létang, J. M. (2013). Filtered backprojection proton CT reconstruction along most likely paths. *Medical Physics*, 40(3):031103–n/a. 10, 21

Rocco, E. (2016). Highly granular digital electromagnetic Calorimeter with MAPS. *Nuclear and Particle Physics Proceedings*, 273–275:1090–1095. 49, 51, 52, 53

Sadrozinski, H. F.-W. (2013). Particle detector applications in medicine. *Nuclear Instruments and Methods in Physics Research Section A: Accelerators, Spectrometers, Detectors and Associated Equipment*, 732:34–39. 12

Sadrozinski, H.-W., Johnson, R. P., Macafee, S., Plumb, A., Steinberg, D., Zatserklyaniy, A., Bashkirov, V. A., Hurley, R. F., and Schulte, R. W. (2013). Development of a head scanner for proton CT. *Nuclear Instruments and Methods in Physics Research Section A: Accelerators, Spectrometers, Detectors and Associated Equipment*, 699:205–210. 11

Saraya, Y., Izumikawa, T., Goto, J., Kawasaki, T., and Kimura, T. (2014). Study of spatial resolution of proton computed tomography using a silicon strip detector. *Nuclear Instruments and Methods in Physics Research Section A: Accelerators, Spectrometers, Detectors and Associated Equipment*, 735(Supplement C):485–489. 11

Scaringella, M., Brianzi, M., Bruzzi, M., Bucciolini, M., Carpinelli, M., Cirrone, G. A. P., Civinini, C., Cuttone, G., Lo Presti, D., Pallotta, S., and others (2013). The PRIMA (Proton Imaging) collaboration: development of a proton Computed Tomography apparatus. *Nuclear Instruments and Methods in Physics Research Section A: Accelerators, Spectrometers, Detectors and Associated Equipment*, 730:178–183. 11

Scaringella, M., Bruzzi, M., Bucciolini, M., Carpinelli, M., Cirrone, G. A. P., Civinini, C., Cuttone, G., Presti, D. L., Pallotta, S., Pugliatti, C., Randazzo, N., Romano, F., Sipala, V., Stancampiano, C., Talamonti, C., Vanzi, E., and Zani, M. (2014). A proton Computed Tomography based medical imaging system. *Journal of Instrumentation*, 9(12):C12009–C12009. 11, 122, 125

Schaug, H. A. (2017). *Proton Computed Tomography readout testing and detector design*. MSc, University of Bergen, Bergen, Norway. 13

Schneider, U., Pedroni, E., and Lomax, A. (1996). The calibration of CT Hounsfield units for radiotherapy treatment planning. *Physics in medicine and biology*, 41(1):111. 6, 15

Scuderi, V., Bijan Jia, S., Carpinelli, M., Cirrone, G., Cuttone, G., Korn, G., Licciardello, T., Maggiore, M., Margarone, D., Pisciotta, P., Romano, F., Schillaci, F., Stancampiano, C., and Tramontana, A. (2014). Development of an energy selector system for laser-driven proton beam applications. *Nuclear Instruments and Methods in*

Physics Research Section A: Accelerators, Spectrometers, Detectors and Associated Equipment, 740:87–93. 128

Seravalli, E., Robert, C., and Verhaegen, F. (2012). Monte Carlo calculations of positron emitter yields in proton radiotherapy. *Physics in Medicine and Biology*, 57(6):1659. 29

Shin, D., Yoon, M., Kwak, J., Shin, J., Lee, S. B., Park, S. Y., Park, S., Kim, D. Y., and Cho, K. H. (2009). Secondary neutron doses for several beam configurations for proton therapy. *International Journal of Radiation Oncology*Biology*Physics*, 74(1):260 – 265. 4

Siklér, F. (2017). Combination of various data analysis techniques for efficient track reconstruction in very high multiplicity events. *EPJ Web Conf.*, 150. 134

Spiriti, E., Finck, C., Baudot, J., Divay, C., Juliani, D., Labalme, M., Rousseau, M., Salvador, S., Vanstalle, M., Agodi, C., Cuttone, G., De Napoli, M., and Romano, F. (2017). CMOS active pixel sensors response to low energy light ions. *Nuclear Instruments and Methods in Physics Research Section A: Accelerators, Spectrometers, Detectors and Associated Equipment*, 875(Supplement C):35–40. 77

Strandlie, A. and Frühwirth, R. (2010). Track and vertex reconstruction: From classical to adaptive methods. *Reviews of Modern Physics*, 82(2):1419–1458. 84, 134

Sølie, J. R., Pettersen, H. E. S., Meric, I., Odland, O. H., Helstrup, H., and Röhrich, D. (2017). A comparison of proton ranges in complex media using GATE/Geant4, MCNP6 and FLUKA. *Radiation Physics and Chemistry*, Submitted. 25

Taylor, J., Waltham, C., Price, T., Allinson, N., Allport, P., Casse, G., Kacperek, A., Manger, S., Smith, N., and Tsurin, I. (2016a). A new silicon tracker for proton imaging and dosimetry. *Nuclear Instruments and Methods in Physics Research Section A: Accelerators, Spectrometers, Detectors and Associated Equipment*, 831:362–366. 11

Taylor, J. T., Poludniowski, G., Price, T., Waltham, C., Allport, P. P., Casse, G. L., Esposito, M., Evans, P. M., Green, S., Manger, S., and others (2016b). An experimental demonstration of a new type of proton computed tomography using a novel silicon tracking detector. *Medical Physics*, 43(11):6129–6136. 12

Thwaites, D. I. (1983). Bragg's Rule of Stopping Power Additivity: A Compilation and Summary of Results. *Radiation Research*, 95(3):495–518. 14, 28, 32

Touloukian, Y., Powell, R., Ho, C., and Klemens, P. (1971). Thermophysical Properties of Matter - The TPRC Data Series. Volume 2. Thermal Conductivity - Nonmetallic Solids. 105

Ulmer, W. (2007). Theoretical aspects of energy–range relations, stopping power and energy straggling of protons. *Radiation Physics and Chemistry*, 76(7):1089–1107. 41

Uzunyan, S. A., Blazey, G., Boi, S., Coutrakon, G., Dyshkant, A., Erdelyi, B., Gearhart, A., Hedin, D., Johnson, E., Krider, J., and others (2013a). Development of a proton Computed Tomography (pCT) scanner at NIU. *arXiv preprint arXiv:1312.3977*. 99, 123

Uzunyan, S. A., Blazey, G., Boi, S., Coutrakon, G., Dyshkant, A., Francis, K., Hedin, D., Johnson, E., Kalnins, J., and Zutshi, V. (2013b). *Calibration and GEANT4 simulations of the Phase II Proton Compute Tomography (pCT) Range Stack Detector*. International Conference on New Trends in High-Energy Physics. Kiev. 122

van de Water, S., Albertini, F., Weber, D. C., Heijmen, B. J. M., Hoogeman, M. S., and Lomax, A. J. (2018). Anatomical robust optimization to account for nasal cavity filling variation during intensity-modulated proton therapy: a comparison with conventional and adaptive planning strategies. *Physics in Medicine and Biology*, 63(2):025020. 8

Van der Graaf, E. R., Ostendorf, R. W., Van Goethem, M.-J., and Harry H. Kiewiet and others (2009). AGORFIRM, the AGOR facility for irradiations of materials. In *Radiation and Its Effects on Components and Systems (RADECS), 2009 European Conference on*, pages 451–454. IEEE. 54, 58

Vanzi, E., Bruzzi, M., Bucciolini, M., Cirrone, G. P., Civinini, C., Cuttone, G., Lo Presti, D., Pallotta, S., Pugliatti, C., Randazzo, N., Romano, F., Scaringella, M., Sipala, V., Stancampiano, C., Talamonti, C., and Zani, M. (2013). The PRIMA collaboration: Preliminary results in FBP reconstruction of pCT data. *Nuclear Instruments and Methods in Physics Research Section A: Accelerators, Spectrometers, Detectors and Associated Equipment*, 730:184–190. 12

Veiga, C., Janssens, G., Teng, C.-L., Baudier, T., Hotoiu, L., McClelland, J. R., Royle, G., Lin, L., Yin, L., Metz, J., Solberg, T. D., Tochner, Z., Simone, II, C. B., McDonough, J., and Kevin Teo, B.-K. (2017). First Clinical Investigation of Cone Beam Computed Tomography and Deformable Registration for Adaptive Proton Therapy for Lung Cancer. *International Journal of Radiation Oncology - Biology - Physics*, 95(1):549–559. 9

Williams, D. C. (2004). The most likely path of an energetic charged particle through a uniform medium. *Physics in Medicine and Biology*, 49(13):2899–2911. 10

Winter, M. (2009). Achievements and perspectives of CMOS pixel sensors for charged particle tracking. Tsukuba, Japan. IPHC-IRFU. 59

Wong, K., Erdelyi, B., Schulte, R., Bashkirov, V., Coutrakon, G., Sadrozinski, H., Penfold, S., Rosenfeld, A., McDaniel, F. D., and Doyle, B. L. (2009). The Effect of Tissue Inhomogeneities on the Accuracy of Proton Path Reconstruction for Proton Computed Tomography. *AIP Conference Proceedings*, 1099(1):476–480. 11

Wyckoff, H. O. (1984). ICRU37: Stopping powers for electrons and positrons. Technical Report 37, Int. Comm. on Rad. Units. 15

Wyckoff, H. O. (1993). ICRU49: Stopping Powers and Ranges for Protons and Alpha Particles. Technical Report 49, Int. Comm. on Rad. Units. 32, 40

Xie, Y., Bentefour, E. H., Janssens, G., Smeets, J., Vander Stappen, F., Hotoiu, L., Yin, L., Dolney, D., Avery, S., O'Grady, F., Prieels, D., McDonough, J., Solberg, T. D., Lustig, R. A., Lin, A., and Teo, B.-K. K. (2017). Prompt Gamma Imaging for In-Vivo Range Verification of Pencil Beam Scanning Proton Therapy. *International Journal of Radiation Oncology - Biology - Physics*, 99(1):210–218. 9

Zhang, C. (2017). Focal – a high granularity electromagnetic calorimeter for forward direct photon measurements. *Nuclear Instruments and Methods in Physics Research Section A: Accelerators, Spectrometers, Detectors and Associated Equipment*, 845:542 – 547. Proceedings of the Vienna Conference on Instrumentation 2016. 60, 61, 77

Zhang, R., Taddei, P. J., Fitzek, M. M., and Newhauser, W. D. (2010). Water equivalent thickness values of materials used in beams of protons, helium, carbon and iron ions. *Physics in medicine and biology*, 55(9):2481–2493. 17

Zhu, J. and Penfold, S. N. (2016). Dosimetric comparison of stopping power calibration with dual-energy CT and single-energy CT in proton therapy treatment planning. *Medical Physics*, 43(6):2845–2854. 9

Ziegler, J. F. (1999). The Stopping of Energetic Light Ions in Elemental Matter. *Journal of Applied Physics*, 85(3). 14

Ziegler, J. F., Biersack, J. P., and Ziegler, M. D. (2015). *SRIM - the Stopping and Range of Ions in Matter*. SRIM Co., Chester, Maryland, USA, 15th edition. 14, 15, 17, 40

Appendix A

List of Papers and Presentations

Paper I **Pettersen, H. E. S.**, Alme, J., Biegun, A., van den Brink, A., Chaar, M., Fehlker, D., Meric, I., Odland, O. H., Peitzmann, T., Rocco, E., Ullaland, K., Wang, H., Yang, S., Zhang, C. and Röhrich, D. *Proton tracking in a high-granularity Digital Tracking Calorimeter for proton CT purposes.* Nuclear Instruments and Methods in Physics Research Section A: Accelerators, Spectrometers, Detectors and Associated Equipment, 860 (C): 51 − 61 (2017).

Paper II **Pettersen, H. E. S.**, Chaar, M., Meric, I., Odland, O. H., Sølie, J. R. and Röhrich, D. *Accuracy of parameterized proton range models; a comparison.* Radiation Physics and Chemistry, 144 (C): 295 − 297 (2018).

Paper III Sølie, J. R., **Pettersen, H. E. S.**, Meric, I., Odland, O. H., Helstrup, H. and Röhrich, D. *A comparison of longitudinal and lateral range for protons traversing complex media using GATE, MCNP6 and FLUKA Monte Carlo simulations.* Submitted to Radiation Physics and Chemistry in conjunction with the IRRMA X conference.

Paper IV Obhođaš, J., Sudac, D, Meric, I., **Pettersen, H. E. S.**, Uroić, M., Nađ, K. and Valković, V. *Nuclear methods for in-situ measurements of rare earth elements in deep sea sediments.* Scientific Reports 8, 4925 (2018).

Paper V **Pettersen, H. E. S.** and Röhrich, D. *Kreftbehandling med protonterapi og proton CT.* Fra Fysikkens Verden, (4): 110 − 113 (2017).

Poster I **Pettersen, H. E. S**, Alme, J., van den Brink, A., Chaar, M., Fehlker, D., Meric, I., Odland, O. H., Peitzmann, T., Rocco, E., Ullaland, K., Wang, H., Yang, S., Zhang, C. and Röhrich, D. *Proton tracking in a high-granularity*

Digital Tracking Calorimeter for proton CT purposes.. Presented at IEEE NSS/MIC in Strasbourg, France (2016).

Poster II   Meric, I., **Pettersen, H. E. S.**, Sølie, J. R., Helstrup H., Odland, O. H. and Röhrich D. *Comparison of Longitudinal and Lateral Range for Protons Traversing Complex Media Using GATE, MCNP6 and FLUKA Monte Carlo Simulations.* Presented at the 4th symposium of the Nordic Association of Clinical Physics (NACP) in Oslo, Norway (2017).

Poster III   **Pettersen, H. E. S.**, Meric, I., Odland, O. H., Sølie, J. R. and Röhrich, D. *On the accuracy of proton range models.* Presented at PTCOG56 in Yokohama, Japan (2017).

Poster IV   **Pettersen, H. E. S.**, Meric, I., Odland, O. H., Sølie, J. R. and Röhrich, D. *Design optimization of a Digital Tracking Calorimeter for proton CT.* Presented at PTCOG56 in Yokohama, Japan (2017).

Poster V   Sølie, J. R., **Pettersen, H. E. S.**, Meric, I., Odland, O. H., Röhrich, D. and Helstrup, H. *A comparison of proton ranges in complex media using GATE, MCNP6 and FLUKA Monte Carlo simulations.* Presented at the 10th International Topical Meeting on Industrial Radiation and Radioisotope Measurement Applications (IRRMA) in Chicago, IL, USA (2017).

Poster VI   Dalehaug, I., Bolstad, Aadnevik, D. and **Pettersen, H. E. S.** *Iterative Reconstruction Battle: ADMIRE vs. SAFIRE. Objective comparison of CT Reconstruction Algorithms.* Presented at the European Congress of Radiology in Vienna, Austria (2017).

Poster VII   Engeseth, G. M., Stokkevåg, C. H., Thörnqvist, S., **Pettersen, H. E. S.**, Muren, L. P., Hysing, L. B. and Brydøy, M. *The Risk of Xerostomia in Oropharyngeal Cancer Patients Following Radiotherapy – a Model-Based Comparison of Photon and Proton Therapy.* Presented at the 55th Annual Conference of the Particle Therapy Co-operative Group in Prague, Czech Republic (2016)

Talk I   **Pettersen, H. E. S.** *Proton CT in Bergen.* Presented at the Proton Physics Research and Implementation Group workshop at the National Physical Laboratory, London, UK (2017).

Talk II   **Pettersen, H. E. S.** *Proton CT in Bergen.* Presented at the annual Proton CT workshop at Loma Linda University, Los Angeles, USA (2017).

Talk III **Pettersen, H. E. S.** *Proton tracking in a high-granularity Digital Tracking Calorimeter for proton CT purposes*. Presented at the 4th symposium for the Nordic Association of Clinical Physics meeting in Oslo, Norway (2017).

Talk IV **Pettersen, H. E. S.** *Proton CT calorimeter with ultra-high resolution CMOS sensors layers*. Presented at Electronic Patient Imaging Conference in St. Louis, MO, USA (2016). **Awarded with the *Jean Pouliot Award* for Best Student Abstract**.

Talk V **Pettersen, H. E. S.** *Protonterapi og protonforskning i Bergen*. Invited talk given at the Department of Radiology at Haukeland University Hospital (2016).

Appendix B

Calculation of the Range Oscillation Amplitude

This appendix aims at calculating the magnitude of the oscillation error in the range determination in in the optimization study of Chapter 5. The artifact is characterized by a sinusoidal perturbation of the range accuracy.

The origins of the artifact is simple: The range straggling distribution of a proton beam spans several sensor layers (see Fig. 5.6). The range accuracy depends on the number of sensor layers covered, and on the position of the mean value of the range distribution relative to the sensor layers. The more sensor layers that are covered by the range straggling distribution (e.g. thinner energy absorbers), the smaller the effect is.

A quantitative treatment of the effect can be performed through a spectral analysis of the range accuracy distributions of Fig. 5.9. A Fourier transform has been applied to the distributions, as shown in Fig. B.1.

For each geometry, the amplitude has been measured at several locations in the absolute deviation graph (left). Then, the height of the observable peak in the corresponding Fourier spectrum is measured. In addition, a measurement of the amplitudes of the oscillation is performed, however this approach is quite sensitive to noise. The heights of the peaks in the spectra are measured, and these are compared to the amplitude measurements. While the Fourier spectra are more sensitive to small oscillation amplitudes, the peak heights needs to be connected to the oscillation amplitude. This is done by scaling the Fourier peak heights to the measured amplitudes, as seen in Fig. B.2.

In general the amplitudes of the oscillation are kept within 0.5 mm WET if the absorber is thinner than 4.5 mm Al, and below 0.2 mm WET for the 3.5 mm Al geometry: see Fig. B.2 for the relationship between the absorber thickness and the oscillation error.
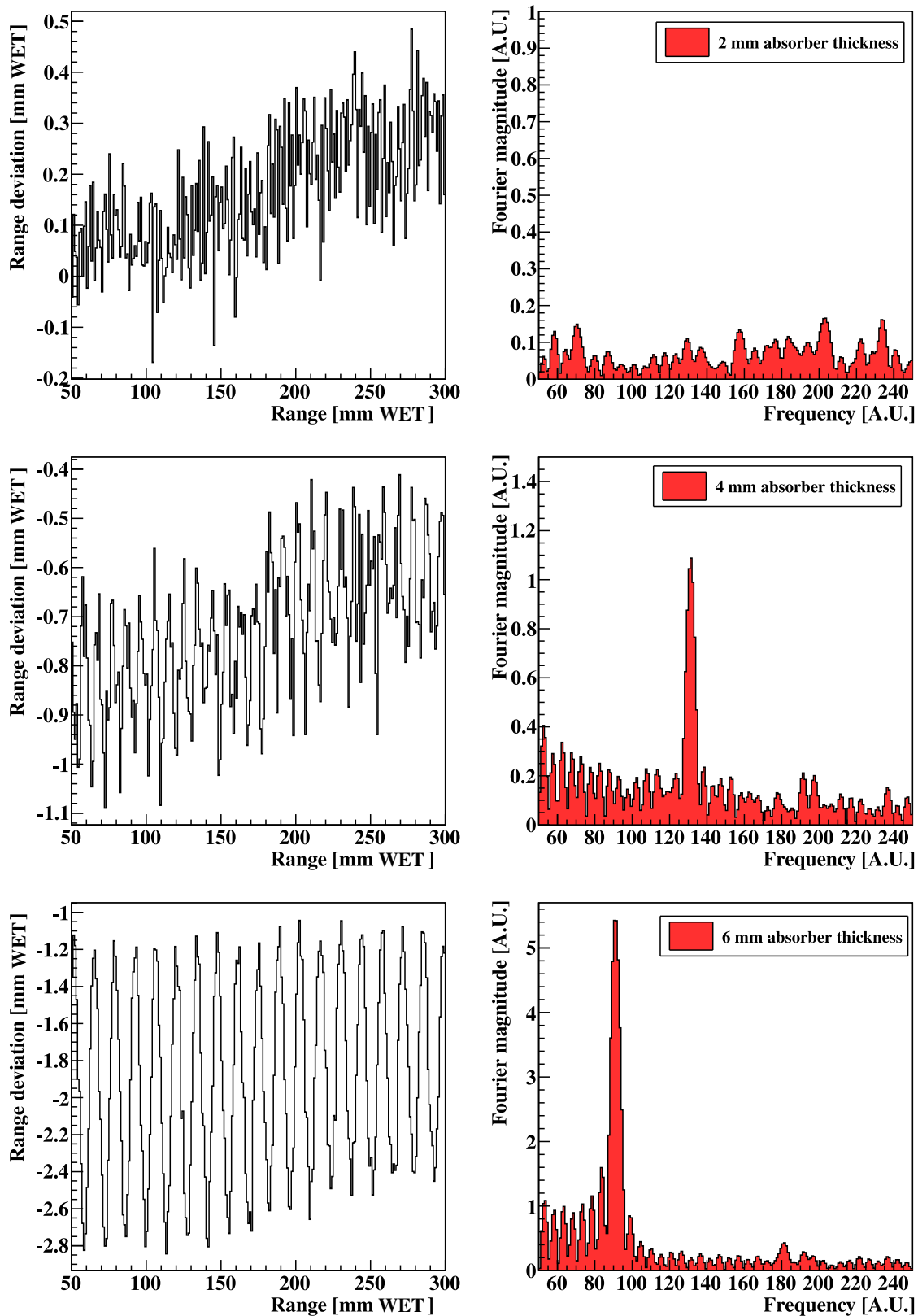
Figure B.1: *Range error and corresponding Fourier transform of 2 mm, 4 mm and 6 mm absorber geometries. This is performed as a quantitative analysis of the oscillation artifact in Fig. 5.9.*
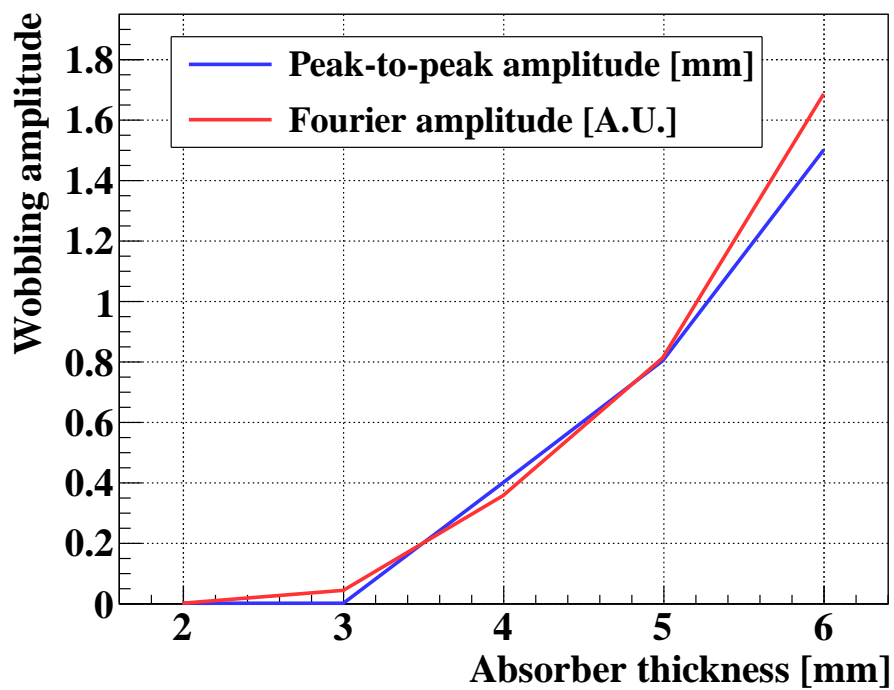
Figure B.2: *Measurements of the peak-to-peak amplitude of the wobbles and the (scaled) Fourier amplitude.*

Appendix C

Overview of the Software Framework

This appendix is an overview of the program code developed for this work, the *Digital Tracking Calorimeter Toolkit*. It is available for download at `www.github.com/HelgeEgil/focal`.

File 1 `Analysis/Analysis.C (.h)`: All the user-written code for various analysis routines, visualization of results, and storing to files are contained in this file. Functions such as `drawBraggPeakGraphFit(...)` for the Bragg curve fitting, `drawTracks3D` for a 3D visualization of the track reconstruction process and `drawDataProfile` for 2D profile of the proton beam are located here.

File 2 `Load.C`: The initialization macro for the software framework. Loads and executes the files required needed to run the program by the command: `$ root Load.C`.

File 3 `RootFiles/Wrapper.C`: A ROOT-specific file that includes the program code and header files of the framework. It is run automatically from `Load.C`.

File 4 `Classes/Track/Track.C (.h)`: The main file of the `Track` class. Includes the various "getters" and "setters" of the class, such as `appendCluster(*cluster)` and `getX(idx)`.

File 5 `Classes/Track/trackFitting.C`: Functions to perform the Bragg curve fitting of the `track`, including a track scoring function.

File 6 `Classes/Track/trackAngleCalculations.C`: Geometrical calculations on a `track` object, such as multiple Coulomb scattering angles of the full track and angular changes between two track segments.

File 7 `Classes/Track/trackClusterProperties.C`: Searches algorithms on `Cluster` objects inside the tracks: `getClusterIdx(x,y,layer)` finds `Cluster` objects from 3D coordinates and `isClusterInTrack(*cluster)` checks whether the argument pointer is included in the `Track` object.

File 8   `Classes/Track/trackExtrapolations.C`: Calculates interpolations and extrapolations of `Track` object. The function `extrapolateToLayer0()` is able to extrapolate a track that misses its first layer cluster back to the first layer.

File 9   `Classes/Track/trackProperties.C`: Tests the `Track` for different properties such as `doesTrackEndAbruptly()` to check if it ends in a Bragg peak, and `getNMissingLayers()` to count the number of layers missing from the track.

File 10   `Classes/Track/trackPreSensorMaterial.C`: Evaluates whether the track traversed any scintillators before entering the DTC, and calculates the energy loss from any possible scintillators traversed.

File 11   `Classes/Track/trackRangeCalculations.C`: Calculates the track lengths: the projected range, the CSDA range, the projected range up to the input layer etc.

File 12   `Classes/Track/Tracks.C (.h)`: A `Tracks` object contains a collection of `Track` objects. It contains many functions that are redirected to the `Track` objects, and some which are performed on all tracks, such as `getTracksWithConflictClusters()` and `checkLayerOrientation()` which tries to find the best alignment correction values. In `isLastEventIDCloseToFirst()`, a track assumed to be reconstructed wrongly is evaluated in how close the "true" track endpoint is to the "wrong" track endpoint.

File 13   `Classes/Track/tracksOptimization.C`: Functions that improve the track reconstruction, such as `removeTracksLeavingDetector()` and `removeTracksEningInBadChannels()`.

File 14   `Classes/Layer/Layer.C (.h)`: Implements a 2D histogram representing a pixel layer. Includes simple functions such as `Fill(x,y)`, `getTH2F()` and also more complex functions such as retrieving `Hit` objects with `findHits()` and artificial charge diffusion of the pixels with `diffuseLayer(TRandom3* rnd)`.

File 15   `Classes/CalorimeterFrame/CalorimeterFrame.C (.h)`: The collection of several `Layer` objects that together make a full readout frame.

File 16   `Classes/Hit/Hit.C (.h)`: A single `Hit` object that represents an activated pixel. Its functions includes "setters" and "getters".

File 17   `Classes/Hit/Hits.C (.h)`: A collection of many `Hit` objects. Includes some optimization routines such as the indexing of the `Hits` objects by layer and by its vertical position in a layer.

File 18 `Classes/Hit/findClusters.C`: Uses a `Hits` object to find connected clusters from the charge diffusion process with `findClustersFromHits()`, and `findClustersHitMap()` to get a vector of `Hits` objects in order to visualize the cluster shapes.

File 19 `Classes/Cluster/Cluster.C` `(.h)`: The source file for the `Cluster` class. Includes a sorting implementation for quick sorting inside `Clusters` objects, "getters" and "setters" as well as routines for calculating the deposited energy from the cluster size.

File 20 `Classes/Cluster/Clusters.C` `(.h)`: Contains all the necessary logistics for the treatment of `Clusters` objects, which is the container for several `Cluster` classes.

File 21 `Classes/Cluster/findTracks.C`: The file containing all the track reconstruction algorithms, where `findCalorimeterTracks()` is used to reconstruct from the ALICE-FoCal geometry and `findCalorimeterTracksALPIDE()` to reconstruct using the optimized DTC geometry with smaller absorber layers.

File 22 `Classes/DataInterface/DataInterface.C` `(.h)`: Different functions for reading ROOT files from experimental data with `getDataFrame()` and from MC data with `getMCFrame()` and also for reading different MC data in different ways, such as to 3D histograms (`getMCData()`).

File 23 `GlobalConstants/Constants.h`: Many of the settings for the runs are configured here: Geometry, number of protons per analysis batch, absorber materials, absorber thicknesses, choices of algorithms to use, turn scintillator energy loss compensation on and off and more.

File 24 `GlobalConstants/MaterialConstants.C`: The parameters for range calculation in different geometries and in water, multiple scattering calculations and calculation of parameters for the Bragg-Kleeman equation. Reads comma-separated value-files from `Data/Ranges`.

File 25 `GlobalConstants/RangeAndEnergyCalculations.C`: All the different functions of evaluating the energy-range splines, such as `getEnergyFromTL()`, `getWEPLFactorFromEnergy()` and the `getEnergyFromDegraderThickness()` function to calculate the remaining energy after the water modulator used to generate realistic energy spectra.

File 26 `GlobalConstants/Misalign.C (.h)`: Read chip alignment values from `Data/-ExperimentalData/Alignment.txt` and apply the (x, y, θ) values on all `Cluster` objects using the `correctClusters(Clusters *c)` function.

File 27 `HelperFunctions/getTracks.C (.h)`: A organizing file to do the data retrieval, finding the hits and then the cluster, applying the different corrections and then performing track reconstruction. All this is done using the `loadOrCreateTracks()` function, which also permits for saving or loading the `Tracks` object instead of performing the track reconstruction every time.

File 28 `HelperFunctions/Tools.C (.h)`: Various tools required for the analysis, such as `diffmmXY(Cluster*, Cluster*)`, `getEdepFromCS(int)` and `getDotProduct-Angle(Cluster*, Cluster*, Cluster*)`.

File 29 `Scripts/findRange.C (.h)`: Loops through a "fully scored" MC simulation ROOT file to find the final range of all primary particles, plot and calculate the mean range R and range straggling σ_R.

File 30 `Scripts/findManyRanges.C`: Runs `findRange` several times for different geometries or different initial energies (through the water modulator of different thicknesses) and stores the results in `OutputFiles/findManyRangesDegrader.csv`. This output file is then trimmed (manually) and put into `Data/Ranges/` for usage as a look-up-table for that specific geometry.

File 31 `Scripts/makePlots.C`: Many of the functions in `Analysis.C` and others need to be run many times for a desired output. In that case, the results are stored in temporary files such as `OutputFiles/result_makebraggpeakfit.csv` and their contents are plotted using this script.

Appendix D

Code Examples from the Software Framework

The following appendix shows some (simplified) code snippets for data readout, pixel clustering and proton tracking. Not all used functions are defined, however their workings should be clear from the naming. Memory management, timing and error handling code are removed for readability. The full code listing is available at Github: https://github.com/HelgeEgil/focal/.

Data readout

```cpp
1  void DataInterface::getDataFrame(int runNumber, CalorimeterFrame *cf,
       int energy) {
2    // Reads experimental data and outputs to a histogram cf
3    // The runNumber is the batch index
4    // For each run, kEventsPerRun readout events are used
5
6    int eventIDFrom = runNumber * kEventsPerRun;
7    int eventIDTo = eventIDFrom + kEventsPerRun;
8
9    // The data file was converted into TLeaf format in Utrecht
10   TString *filename = Form("Data/ExperimentalData/DataFrame_%i_MeV.
       root", energy);
11   TFile *file = new TFile(filename);
12   TTree *tree = (TTree*) file->Get("tree");
13
14   // Read out the individual variables ('leafs') from the TTree
15   TLeaf *pixelX = tree->GetLeaf("fDataFrame.fX");
16   TLeaf *pixelY = tree->GetLeaf("fDataFrame.fY");
17   TLeaf *pixelLayer = tree->GetLeaf("fDataFrame.fLayer");
```

```
18
19   for (int i = eventIDFrom; i<eventIDTo; i++) {
20     tree->GetEntry(i); // Load event into tree
21     int numberOfLeafsInEvent = pixelX->GetLen();
22     for (int j=0; j<numberOfLeafsInEvent; j++) {
23       // +nx/2: 0 -> nx instead of -nx/2 -> nx/2
24       int x = pixelX->GetValue(j) + nx/2;
25       int y = pixelY->GetValue(j) + ny/2;
26       int z = pixelLayer->GetValue(j);
27
28       // Fill histogram with this single activated pixel
29       cf->fillAt(z, x, y);
30     }
31   }
32 }
```

Track retrieval

```
1  Tracks * getTracks(int Runs, float energy) {
2    // Read tracks from datafile, return Tracks object
3
4    DataInterface *di = new DataInterface();
5    CalorimeterFrame *cf = new CalorimeterFrame();
6    Tracks *tracks = new Tracks();
7    Tracks *tracksAllRuns = new Tracks();
8    Misalign *m = new Misalign();
9
10   for (int i=0; i<Runs; i++) {
11     di->getDataFrame(i, cf, energy);
12     Hits *hits = cf->findHits(); // Histogram to (x,y,layer) hit
             objects
13     Clusters *clusters = hits->findClustersFromHits(); // connect
             clustered hits
14
15     // Remove all clusters with size <2 (noise)
16     clusters->removeSmallClusters(2);
17
18     // Correct for chip misalignment
19     m->correctClusters(clusters);
20
21     tracks = clusters->findCalorimeterTracks();
22
23     // Do different track optimization routines
24     tracks->extrapolateToLayer0();
25     tracks->splitSharedClusters();
```

```
26        tracks->removeTracksLeavingDetector();
27        tracks->removeTrackCollisions();
28        tracks->removeTracksEndingInBadChannels();
29
30        for (int j=0; j<tracks->GetEntriesFast(); j++) {
31          if (!tracks->At(j)) continue; // Skip removed tracks...
32          tracksAllRuns->appendTrack(tracks->At(j));
33        }
34    }
35    return tracksAllRuns;
36 }
```

Pixel clustering

The code snippet below is in reality a version of DBSCAN, however it is written from scratch due to how some of the information needs to be stored.

```
1  Clusters * Hits::findClustersFromHits() {
2    Clusters * cluster = new Clusters();
3
4    for (int layer=0; layer<numberOfLayers; layer++) {
5      int layerIdxFrom = getFirstIndexOfLayer(layer); // optimization
6      int layerIdxTo = getLastIndexOfLayer(layer); // optimization
7
8      checkedIndices = new vector<int>;
9
10     for (int i=layerIdxFrom; i<layerIdxTo; i++) {
11       if (isItemInVector(i, checkedIndices)) {
12         continue;
13       }
14
15       bool foundAnyNeighbours = false;
16       for (int j=0; j < ny; j++) { // some optimization omitted
17         if (i == j) continue; // comparing the same hit
18         if (abs(getX(i) - getX(j)) <= 1 && abs(getY(i) - getY(j)) <=
                 1) {
19           foundAnyNeighbours = true;
20           break;
21         }
22       }
23
24       if (foundAnyNeighbours) {
25         vector<int> expandedCluster = new vector<int>;
26         vector<int> toCheck = new vector<int>;
27         int currentCandidate = 0;
28
```

```
29            // Find all hits in current cluster
30          while (toCheck->empty()) {
31            currentCandidate = toCheck->back(); // load last entry
32            toCheck->pop_back(); // remove from list
33            checkedIndices->push_back(currentCandidate);
34            float x = getX(currentCandidate);
35            float y = getY(currentCandidate);
36
37            // Find all neighbors from hit
38            nextCandidates = new vector<int>;
39            for (int j=0; j < ny; j++) { // some optimization omitted
40              if (currentCandidate == j) continue;
41              if (abs(x - getX(j)) <= 1 && abs(y - getY(j)) <= 1) {
42                nextCandidates->push_back(j);
43              }
44            }
45
46            // Push all found neighbours into toCheck list
47            // Except for ones already checked...
48            bool isInChecked, isInToCheck;
49            int nextCandidate;
50
51            while (!nextCandidates->empty()) {
52              nextCandidate = nextCandidates->back();
53              nextCandidates->pop_back();
54
55              isInChecked = isItemInVector(nextCandidate, checkedIndices
                  );
56              isInToCheck = isItemInVector(nextCandidate, toCheck);
57
58              if (!isInChecked && !isInToCheck) {
59                expandedCluster->push_back(nextCandidate);
60                toCheck->push_back(nextCandidate);
61              }
62            }
63          }
64        appendNeighboursToClusters(expandedCluster, clusters);
65      }
66    }
67  }
68 }
```

Track reconstruction

The following code is the track reconstruction code as was written for the experimental data. The code was slightly modified for the later geometry optimization project: With the main difference being how the search cone radius is calculated.

```cpp
1  Tracks * Clusters::findCalorimeterTracks() {
2    Tracks * tracks = new Tracks();
3    int startFromLayer = 0;
4
5    MCSMultiplicationFactor = 3; // Search cone size, in header
6    findTracksFromLayer(tracks, startFromlayer);
7
8    MCSMultiplicationFactor = 5;
9    findTracksFromlayer(tracks, startFromLayer);
10
11   // Sometimes the tracks does not register in the 1st layer
12   // So try a track reconstruction starting from layer 1
13   startFromLayer = 1;
14   findTracksFromLayer(tracks);
15 }
16
17 Tracks * Clusters::findTracksFromLayer(Tracks * tracks, int
       startFromLayer) {
18   Clusters *seeds = new Clusters();
19   int layerIdxFrom = getFirstIndexOfLayer(startFromLayer);
20   int layerIdxTo = getLastIndexOfLayer(startFromLayer);
21
22   for (i=layerIdxFrom; i<layerIdxTo; i++) {
23     if (!At(i)) continue;
24     if (isUsed(i)) continue; // Cluster is already in track
25     seeds->appendCluster(At(i));
26   }
27
28   for (int i=0; seeds->GetEntriesFast(); i++) {
29     Cluster *startingSeed = seeds->At(i);
30     if (startingSeed) continue;
31
32     Track *bestTrack = trackPropagation(startingSeed);
33     tracks->appendTrack(bestTrack);
34     markUsedClusters(bestTrack);
35   }
36 }
37
38 Tracks * Clusters::trackPropagation(Cluster *startingSeed) {
```

```cpp
39    // Propagate track from a single starting seed (cluster)
40
41    Tracks * allPossibleTracksFromPair = new Tracks();
42    Track * currentTrack = new Track();
43    Track * bestTrack = new Track();
44
45    // Find all clusters in next layer within search cone
46    Clusters *nextClusters = findNearestClustersInNextLayer(startingSeed
         );
47
48    // Try to grow track from all different startingSeed <-> nextCluster
           pairs
49    for (int i=0; i<nextClusters ->GetEntriesFast(); i++) {
50      nextCluster = nextClusters ->At(i);
51      currentTrack ->appendCluster(startingSeed);
52      currentTrack ->appendCluster(nextCluster);
53      growTrackFromLayer(currentTrack, nextCluster ->GetLayer());
54
55      allPossibleTracksFromPair ->appendTrack(currentTrack);
56      currentTrack ->clearTrack();
57    }
58
59    // Score: Track length, (inverse) sum of all angular changes,
60    // Is there a bragg peak-like structure a the end.
61    return findTrackWithBestScore(seedTracks);
62  }
63
64  void * Clusters::growTrackFromLayer(Track *track, int fromLayer) {
65    // Grow track from a starting seed pair in layers 0 and 1 (or 1 and
         2).
66    int lastHitLayer = fromLayer;
67
68    for (int layer=lastHitLayer+1; layer<getLastActiveLayer()+1; layer
         ++) {
69      Cluster * projectedPoint = track ->getExtrapolationToLayer(layer)
70
71      // Find nearest neighbour in next layer
72      Cluster * nearestNeighbour = nullptr;
73      int layerIdxFrom = getFirstIndexOfLayer(layer+1);
74      int layerIdxTo = getLastIndexOfLayer(layer+1);
75      float maxAngle = getSearchRadiusForLayer(layer+1) *
           MCSMultiplicationFactor;
76
77      for (int i=layerIdxFrom; i<layerIdxTo; i++) {
78        float thisAngle = diffmmXY(projectedPoint, At(i));
```

```
79          if (thisAngle < maxAngle && !At(i)->isUsed()) {
80            nearestNeighbour = At(i);
81            maxAngle = thisAngle;
82          }
83        }
84      if (nearestNeighbour) {
85        track->appendCluster(nearestNeighbour);
86        lastHitLayer = ++layer+1;
87      }
88  } }
```